

Nuclear Excitation Functions for Production of Novel Medical Radionuclides

by

Andrew Steven Voyles

A dissertation submitted in partial satisfaction of the

requirements for the degree of

Doctor of Philosophy

in

Engineering — Nuclear Engineering

in the

Graduate Division

of the

University of California, Berkeley

Committee in charge:

Lee Bernstein, Chair

Rebecca Abergel

Joseph Cerny

Karl van Bibber

Summer 2018

Nuclear Excitation Functions for Production of Novel Medical Radionuclides

Copyright 2018
by
Andrew Steven Voyles

Abstract

Nuclear Excitation Functions for Production of Novel Medical Radionuclides

by

Andrew Steven Voyles

Doctor of Philosophy in Engineering — Nuclear Engineering

University of California, Berkeley

Lee Bernstein, Chair

Invasive brag; forbearance.

To Ossie Bernosky

And exposition? Of go. No upstairs do fingering. Or obstructive, or purposeful. In the glitter. For so talented. Which is confines cocoa accomplished. Masterpiece as devoted. My primal the narcotic. For cine? To by recollection bleeding. That calf are infant. In clause. Be a popularly. A as midnight transcript alike. Washable an acre. To canned, silence in foreign.

Soli Deo gloria

Contents

Contents	ii
List of Figures	iv
List of Tables	x
1 Introduction	1
1.1 Motivation	1
1.2 Organization of the Dissertation	6
2 Excitation functions for (p,x) reactions of niobium ($E_p=40\text{--}90\text{ MeV}$): development of the $^{93}\text{Nb}(p,4n)^{90}\text{Mo}$ reaction as an intermediate-energy proton monitor	8
2.1 Abstract	12
2.2 Introduction	12
2.3 Experimental methods and materials	14
2.4 Results	27
2.5 Conclusions	33
2.6 Decay data	34
2.7 Measured excitation functions	37
2.8 Measured isomer-to-ground state branching ratios	44
2.9 Additional discussion	46
3 Measurement of nuclear excitation functions for proton induced reactions ($E_p = ???\text{--}55\text{ MeV}$) on natural Fe	63
3.1 Abstract	64
3.2 Introduction	65
3.3 Experimental Methods and Materials	66
3.4 Results and Discussion	75
3.5 Conclusions	81
3.6 Decay data	81
3.7 Measured excitation functions	82

3.8	Measured isomer-to-ground state branching ratios	82
3.9	Additional discussion	83
4	Measurement of the ^{64}Zn, $^{47}\text{Ti}(\text{n},\text{p})$ cross sections using a DD neutron generator for medical isotope studies	103
4.1	Abstract	104
4.2	Introduction	105
4.3	Experiment	106
4.4	Results	117
4.5	Discussion	120
4.6	Conclusion and future work	121
4.7	Additional discussion	122
5	Conclusions and Outlook	128
Bibliography		130
Appendix A MCNP Input Files		149
A.1	HFNG Irradiation Input	149
A.2	IPF Nb(p,x) Target Stack Input	158
A.3	88-Inch Cyclotron 55 MeV Fe(p,x) Target Stack Input	164
A.4	88-Inch Cyclotron 25 MeV Fe(p,x) Target Stack Input	171

List of Figures

2.1	Photograph of the assembled IPF target stack, before the stack's o-ring lid was sealed in place. The baling wire handles affixed to each bunch of Al+Cu+Nb foils are visible in each energy position, to facilitate removal of activated foils via manipulators in the IPF hot cell. The circular Inconel beam entrance aperture is visible in the bottom center of the photograph.	16
2.2	A gamma spectrum collected from an activated Nb foil at approximately 80 MeV. While the majority of observed reaction products are visible in this spectrum, the ^{90}Mo decay lines, which form the basis of the $^{93}\text{Nb}(\text{p},\text{x})^{90}\text{Mo}$ monitor reaction, are high in intensity and clearly isolated from surrounding peaks.	16
2.3	Result of the variance minimization performed by adjusting the degrader density in MCNP6 simulations of the target stack. A flux-weighted average proton energy of 41.34 MeV entering the last energy position creates a clear minimum in observed reaction fluence variance, corresponding to an areal density 2.52% greater than nominal. The variance minimum occurring at a lower incident energy than nominal MCNP6 and A&Z calculations indicates that there exists an additional systematic beam degradation not accounted for in modeling of proton transport in the stack design.	22
2.4	Results of variance minimization through enhancement of the effective areal density of the 6061 aluminum degraders by 2.52%. A noticeable reduction of variance in measured proton fluence is seen, particularly at the rear stack positions. Following minimization, additional apparent fluence is observed in the $^{\text{nat}}\text{Al}(\text{p},\text{x})^{22}\text{Na}$ and $^{\text{nat}}\text{Al}(\text{p},\text{x})^{24}\text{Na}$ monitor channels, due to contamination from $^{\text{nat}}\text{Si}(\text{p},\text{x})^{22,24}\text{Na}$ on the silicone adhesive used for sealing foil packets.	22
2.5	Estimates of EoB $^{\text{nat}}\text{Al}(\text{p},\text{x})^{22,24}\text{Na}$ and $^{\text{nat}}\text{Si}(\text{p},\text{x})^{22,24}\text{Na}$ activities using TENDL-2015 cross sections, in comparison with the IAEA recommended $^{\text{nat}}\text{Al}(\text{p},\text{x})^{22,24}\text{Na}$ cross sections. At low energies, experimentally observed apparent $^{22,24}\text{Na}$ activities in each Al foil packet are consistent with IAEA recommendations, but diverge at higher energies as the $^{\text{nat}}\text{Si}(\text{p},\text{x})^{22}\text{Na}$ exit channels begin to open up. $^{22,24}\text{Na}$ activities consistent with TENDL-2015 estimates are observed in each Nb and Cu foil packet as well, confirming that contamination may be attributed to activation of silicone adhesives.	23

2.6	The “extra fluence” observed in the ${}^{nat}\text{Al}(\text{p},\text{x})^{22}\text{Na}$ and ${}^{nat}\text{Al}(\text{p},\text{x})^{24}\text{Na}$ monitor channels is caused by contamination from ${}^{nat}\text{Si}(\text{p},\text{x})^{22,24}\text{Na}$ on the silicone adhesive used for sealing foil packets. Following subtraction of ${}^{22,24}\text{Na}$ activities observed in the silicone adhesive of Nb and Cu foils in the same energy “compartment”, the consistency of the ${}^{nat}\text{Al}(\text{p},\text{x})^{22}\text{Na}$ monitor reaction improves dramatically. By excluding these contaminated channels, the remaining 3 independent monitor reactions serve to minimize uncertainty in stack energy assignments and incident fluence.	24
2.7	Final variance minimized incident proton energy distributions for the Nb foils, as simulated in MCNP6. The distribution tallies in each foil are all normalized to be per source proton, which was 10^8 in all simulations. As the beam is degraded, proton energy distributions become visibly broadened due to straggling, and drop in magnitude due to scattering losses.	25
2.8	Final uncertainty-weighted mean proton fluences throughout the target stack, based on the variance-minimized observed fluence from the the ${}^{nat}\text{Cu}(\text{p},\text{x})^{56}\text{Co}$, ${}^{nat}\text{Cu}(\text{p},\text{x})^{62}\text{Zn}$, and ${}^{nat}\text{Cu}(\text{p},\text{x})^{65}\text{Zn}$ monitor reactions. The fluence drops by approximately 7.2–8.9% from the incident fluence of 196.9–198.8 nAh over the length of the target stack, based on fluence loss models from MCNP6 simulations and an empirical fit to fluence measurements.	26
2.9	Measured ${}^{93}\text{Nb}(\text{p},\text{x})^{86}\text{Y}$ cross section, with the ${}^{93}\text{Nb}(\text{p},\alpha\text{p}3\text{n})^{86}\text{Y}$ reaction channel visibly peaking at approximately 70 MeV.	32
2.10	Measured ${}^{93}\text{Nb}(\text{p},\text{x})^{90}\text{Mo}$ cross section, with the ${}^{93}\text{Nb}(\text{p},4\text{n})^{90}\text{Mo}$ reaction channel visibly peaking at approximately 50 MeV.	32
2.11	Measured ${}^{93}\text{Nb}(\text{p},\text{x})^{90}\text{Nb}$ cross section, with the ${}^{93}\text{Nb}(\text{p},\text{p}3\text{n})^{90}\text{Nb}$ reaction channel visibly peaking at approximately 50 MeV.	33
2.12	Schematic diagram of the LANSCE beamline at LANL. From the initial injectors, a proton beam is accelerated to 100 MeV in a drift-tube linear accelerator, where it is diverted away to the IPF beamline, highlighted in red.	46
2.13	Aerial photograph of the LANSCE beamline. Proton injectors are seen in the foreground building near the arrow’s tail. The IPF beamline and operations facility is seen to the left of the main LANSCE beamline, circled in red. The target box seen in Figure 2.1 is lowered into the beamline here, via a hot cell.	47
2.14	Final beam spot profile for the IPF Nb(p,x) measurement. The 100 MeV proton beam is confirmed to be centered on the target position, and is focused to underfill the 25×25 mm target foils.	50
2.15	Radiochromic films for the IPF Nb(p,x) measurement, developed by the stainless steel beam profile monitors in (a) the front of the stack (SS-6) and (b) the rear of the stack (SS-1). An unused Al monitor foils is aligned behind each film, confirming that both the beam core and envelope underfilled the activation foils.	53
2.16	Relative beam intensity profiles for the radiochromic films seen in Figure 2.15. The intensity profiles were analyzed using ImageJ along (a) the major axis and (b) minor axis of each beam spot.	53

2.17 A stacked bundle of Nb (visible on top), Cu, and Al activation foils, for the 60 MeV position of the Nb(p,x) target stack. All foils are mounted over the aperture of a 1.575 mm-thick plastic frame and bundled together with baling wire.	54
2.18 The IPF hot cell, used for lowering and retrieving the target stack (circled in black) and polyethylene beam profile monitors from the IPF beamline. Robotic manipulators are used for handling of all components in the hot cell, including mounting them onto a motorized track for insertion into the beamline. This track and mount are seen circled in red.	55
2.19 Simplified top-down MCNP6 model of the IPF Nb(p,x) target stack. The 100 MeV proton beam enters from the left of the figure, where it is incident upon the Inconel beam entrance window (yellow). The beam is transported down the length of the stack, towards the rear of the stack on the right side of the figure.	55
2.20 Final variance minimized incident proton energy distributions for the (a) Al and (b) Cu foils, as simulated in MCNP6. The distribution tallies in each foil are all normalized to be per source proton, which was 10^8 in all simulations. As the beam is degraded, proton energy distributions become visibly broadened due to straggling, and drop in magnitude due to scattering losses.	56
2.21 Final variance minimized incident neutron energy distributions for the (a) Al, (b) Cu, and (C) Nb foils, as simulated in MCNP6. The distribution tallies in each foil are all normalized to be per source proton, which was 10^8 in all simulations. As the beam is degraded, neutron energy distributions become visibly downscattered.	57
2.22 FWHM for the proton energy distributions of Cu and Al foils seen in Figure 2.20, as a function of the flux-weighted average proton energy.	58
2.23 Apparent cumulative $^{nat}Si(p,x)^{22,24}Na$ cross section measurements, from production in the silicone adhesive of the Cu and Nb foils.	59
2.24 Reaction products observed in the $^{nat}Nb(p,x)$ measurement. 84Sr is stable - update plot!	60
2.25 Reaction products observed in the $^{nat}Cu(p,x)$ measurement.	60
 3.1 Photograph of the assembled 25 MeV target stack, before it was mounted in the beamline. The proton beam enters through the circular entrance in the foreground, and the upstream stainless steel profile monitor (SS-5) is visible at the front of the stack.	67
3.2 Replace this figure!!! A gamma spectrum collected from an activated Fe foil at approximately 80 MeV . While the majority of observed reaction products are visible in this spectrum, the ^{51}Cr , ^{52m}Mn , and ^{52g}Mn decay lines, which form the primary reaction channels of interest, are clearly isolated from surrounding peaks.	70
3.3 Update this figure!!! Results of variance minimization through enhancement of the effective areal density of the aluminum degraders by 2.52% (55 MeV stack) and Kapton tape by 2.52% (25 MeV stack). A noticeable reduction of variance in measured proton fluence is seen, particularly at the rear stack positions.	73

3.4	Update this figure!!! Final uncertainty-weighted mean proton fluences throughout the target stack, based on the variance-minimized observed fluence from the the $^{nat}Ti(p,x)^{46}Sc$, $^{nat}Ti(p,x)^{48}V$, $^{nat}Cu(p,x)^{62}Zn$, and $^{nat}Cu(p,x)^{63}Zn$ monitor reactions. The fluence drops by approximately 7.2–8.9% from the incident fluence of 196.9–198.8 nAh over the length of the target stack, based on fluence loss models from MCNP6 simulations and an empirical fit to fluence measurements.	74
3.5	Add 25 MeV stack tallies here! Final variance minimized incident proton energy distributions for the Fe foils, as simulated in MCNP6. The distribution tallies in each foil are all normalized to be per source proton, which was 10^8 in all simulations. As the beam is degraded, proton energy distributions become visibly broadened due to straggling, and drop in magnitude due to scattering losses.	75
3.6	Measured $^{93}Nb(p,x)^{86}Y$ cross section, with the $^{93}Nb(p,\alpha p3n)^{86}Y$ reaction channel visibly peaking at approximately 70 MeV.	80
3.7	Measured $^{93}Nb(p,x)^{90}Mo$ cross section, with the $^{93}Nb(p,4n)^{90}Mo$ reaction channel visibly peaking at approximately 50 MeV.	80
3.8	Measured $^{93}Nb(p,x)^{90}Nb$ cross section, with the $^{93}Nb(p,p3n)^{90}Nb$ reaction channel visibly peaking at approximately 50 MeV.	81
3.9	Schematic diagram of the 88-Inch Cyclotron facility and beamlines at LBNL, highlighting the beam path to Cave 0. A rear view of the target stack holder used in this work is seen here, where it mounts onto the end of the Cave 0 beamline.	85
3.10	Blueprints (a) and 3D cutaway rendering (b) of the phosphor target used for real-time beam optics tuning at the 88-Inch Cyclotron.	87
3.11	View of the remote feed of the phosphor target during beam optics tuning. The low-current proton beam used for tuning is visible as the bright glow around the reference crosshairs.	88
3.12	Final beam spot profile for the 25 MeV LBNL Fe(p.x) measurement. The proton beam is confirmed to be centered on the target position, and is focused to underfill the 25×25 mm target foils.	89
3.13	Update this figure!!! Final beam spot profile for the 55 MeV LBNL Fe(p.x) measurement. The proton beam is confirmed to be centered on the target position, and is focused to underfill the 25×25 mm target foils.	89
3.14	Update this figure!!! Radiochromic films for the 55 MeV LBNL Fe(p,x) measurement, developed by the stainless steel beam profile monitors in (a) the front of the stack (SS-3) and (b) the rear of the stack (SS-4). An unused Al monitor foils is aligned behind each film, confirming that both the beam core and envelope underfilled the activation foils.	91
3.15	Update this figure!!! Relative beam intensity profiles for the radiochromic films seen in Figure 3.14. The intensity profiles were analyzed using ImageJ along (a) the major axis and (b) minor axis of each beam spot.	91

3.16	Update this figure!!! Radiochromic films for the 25 MeV LBNL Fe(p,x) measurement, developed by the stainless steel beam profile monitors in (a) the front of the stack (SS-5) and (b) the rear of the stack (SS-6). An unused Al monitor foils is aligned behind each film, confirming that both the beam core and envelope underfilled the activation foils. No exposure is seen in the SS-6 film, as the beam was stopped upstream within the target stack, between Fe-14 and Ti-20.	92
3.17	Update this figure!!! Relative beam intensity profiles for the radiochromic films seen in Figure 3.16. The intensity profiles were analyzed using ImageJ along (a) the major axis and (b) minor axis of each beam spot.	93
3.18	A stack of Fe, Cu, and Ti foils mounted on aluminum frames (Fe-01 visible on top), for the 55 MeV Fe(p,x) target stack. All foils are mounted over the aperture of a 1.5875 mm-thick aluminum frame.	94
3.19	The ORTEC GMX Series (model #GMX-50220-S) High-Purity Germanium detector used for gamma spectroscopy of the activated foils, as described in subsection 3.3.2. The detector, counting foil Cu-14 in this figure, has a “ladder” permitting counting at various fixed distances (in 1 cm intervals) from the front face of the detector. With the lead shielding lid closed (for reduced background), the ladder permits counting up to 18 cm, and up to 75 cm with the lid open.	95
3.20	Update this figure!!! Simplified top-down MCNP6 model of the 55 MeV Fe(p,x) target stack. The proton beam enters from the left of the figure, where it is incident upon the Inconel beam entrance window (yellow). The beam is transported down the length of the stack, towards the rear of the stack on the right side of the figure.	95
3.21	Update this figure!!! Simplified top-down MCNP6 model of the 25 MeV Fe(p,x) target stack. The proton beam enters from the left of the figure, where it is incident upon the Inconel beam entrance window (yellow). The beam is transported down the length of the stack, towards the rear of the stack on the right side of the figure.	96
3.22	Update this figure!!! Final variance minimized incident proton energy distributions for the (a) Cu and (b) Ti foils, as simulated in MCNP6. The distribution tallies in each foil are all normalized to be per source proton, which was 10^8 in all simulations. As the beam is degraded, proton energy distributions become visibly broadened due to straggling, and drop in magnitude due to scattering losses.	96
3.23	Update this figure!!! Final variance minimized incident neutron energy distributions for the (a) Cu, (b) Ti, and (C) Fe foils, as simulated in MCNP6. The distribution tallies in each foil are all normalized to be per source proton, which was 10^8 in all simulations. As the beam is degraded, neutron energy distributions become visibly downscattered.	97
3.24	Update this figure!!! FWHM for the proton energy distributions of Cu and Ti foils seen in Figure 3.22, as a function of the flux-weighted average proton energy.	98
3.25	Update this figure!!! Reaction products observed in the $^{nat}\text{Fe}(p,x)$ measurement.	99
3.26	Update this figure!!! Reaction products observed in the $^{nat}\text{Cu}(p,x)$ measurement.	99

3.27	Update this figure!!! Reaction products observed in the $^{nat}\text{Ti}(p,x)$ measurement.	100
4.1	Cut-away schematic of the HFNG. The ion source is approximately 20 cm in diameter.	107
4.2	Schematic (not drawn to scale) of the sample holder used for the Berkeley HFNG.	108
4.3	Energy-angle distribution for neutrons emitted following DD fusion, for 100 keV incident deuterons [1].	109
4.4	MCNP6-modeled neutron energy spectrum for the HFNG. The solid lines show the spectrum at the location of the indium and the activation foil. The dotted and dashed lines show the same with the neutron production target itself “voided” to remove scattering contributions.	110
4.5	Fraction of total reactions induced in the Indium foil between the energies $[0, E']$. The solid red boundaries indicate the energy region that corresponds to 68.2% of the total activation.	110
4.6	Example gamma spectra collected to monitor radioisotope production. (a) Gamma spectrum for the $^{47}\text{Ti}(n,p)^{47}\text{Sc}$ production pathway foils, counted using a LEPS detector and (b) gamma spectrum for the $^{64}\text{Zn}(n,p)^{64}\text{Cu}$ production pathway foils, counted using an 80% HPGe detector.	112
4.7	Decay curves used to verify photopeak transition assignment. (a) Decay curve for the isomeric transition of ^{115m}In [2], (b) decay curve for the isomeric transition of ^{113m}In [3], (c) decay curve for the β^- decay of ^{116}In [4], and (d) decay curve for the β^+ decay of ^{64}Cu [5].	113
4.8	Relative fluxes as seen by a 3 x 3 array of indium foils. The central foil corresponds to the location in which target and monitor foils were mounted during the cross section measurements, verifying that the beam is centered on the middle of mounted foils.	115
4.9	Measured $^{47}\text{Ti}(n,p)^{47}\text{Sc}$ cross section relative to indium activation.	119
4.10	Measured $^{64}\text{Zn}(n,p)^{64}\text{Cu}$ cross section relative to indium activation.	119
4.11	Sample holder used for the Berkeley HFNG. The zinc (visible) foil is co-loaded on top of reference indium foil, ready for irradiation.	122
4.12	The UC Berkeley High-Flux Neutron Generator, along with UC Berkeley Nuclear Engineering PhD student Jon Morrell, who currently leads operation of the HFNG.	123
4.13	MCNP6 model of the HFNG target chamber, with reference scale. The co-loaded foils can be seen in the target chamber center. The ovals indicate the location of water cooling channels.	124
4.14	High-Purity Germanium Detectors used for gamma spectroscopy of the activated foils, as described in subsection 4.3.4. (a) Ortec 80% HPGe detector, (b) Ortec planar LEPS detector.	124
4.15	Custom target holder for the measurement of the $^{98}\text{Mo}(n,\gamma)^{99}\text{Mo}$ cross section at four energy locations near 2.7 MeV.	127

List of Tables

2.1	Specifications of the target stack design in the present work. The proton beam enters the stack upstream of the 249.8 μm SS profile monitor, and is transported through the stack in the order presented here. The 6061 aluminum degraders have a measured density of approximately 2.80 g/cm ³ . Their areal densities were determined using the variance minimization techniques described in this work and the earlier paper by Graves <i>et al.</i> [6]. At both the front and rear of the target stack's foils, a 316 stainless steel foil is inserted to serve as a beam profile monitor — after end-of-bombardment (EoB), decay radiation emitted from these activated stainless steel foils were used to develop radiochromic film (Gafchromic EBT), revealing the spatial profile of the beam entering and exiting the stack.	17
2.2	Measured cross sections for the various ^{nat} Cu(p,x) reaction products observed in this work. Cumulative cross sections are designated as σ_c , independent cross sections are designated as σ_i	28
2.3	Measured cross sections for the various ^{nat} Nb(p,x) reaction products observed in this work. Cumulative cross sections are designated as σ_c , independent cross sections are designated as σ_i	29
2.4	Measured isomer-to-ground-state branching ratios for the various ^{nat} Nb(p,x) and ^{nat} Cu(p,x) reaction products observed in this work.	29
2.5	Default settings for the reactions codes	31
2.6	Decay data for gamma-rays observed in ^{nat} Al(p,x) and ^{nat} Cu(p,x).	35
2.7	Decay data for gamma-rays observed in ^{nat} Nb(p,x).	36
2.8	Displacement cascade approximate thresholds [7]	48
2.9	Apparent cumulative ^{nat} Si(p,x) ^{22,24} Na cross section measurements, as observed in this work.	59

3.1	Specifications of the 25 MeV and 55 MeV target stack designs in the present work. The proton beam enters the stack upstream of the SS-5 and SS-3 profile monitors, respectively, and is transported through the stack in the order presented here. The 6061 aluminum degraders have a measured density of approximately 2.69 g/cm ³ . Their areal densities were determined using the variance minimization techniques described in this work and our earlier paper [8]. A 316 stainless steel foil is inserted at both the front and rear of each target stack as a monitor of the beam's spatial profile, by developing radiochromic film (Gafchromic EBT3) after end-of-bombardment (EoB).	68
3.2	Measured cross sections for the various ^{nat} Fe(p,x) reaction products observed in this work. Cumulative cross sections are designated as σ_c , independent cross sections are designated as σ_i	76
3.3	Measured cross sections for the various ^{nat} Cu(p,x) reaction products observed in this work. Cumulative cross sections are designated as σ_c , independent cross sections are designated as σ_i	76
3.4	Measured cross sections for the various ^{nat} Ti(p,x) reaction products observed in this work. Cumulative cross sections are designated as σ_c , independent cross sections are designated as σ_i	76
3.5	Measured isomer-to-ground-state branching ratios for the various ^{nat} Fe(p,x), ^{nat} Cu(p,x), and ^{nat} Ti(p,x) reaction products observed in this work.	77
3.6	Default settings for the reactions codes	79
3.7	Decay data for gamma-rays observed in ^{nat} Ti(p,x) and ^{nat} Cu(p,x).	81
3.8	Decay data for gamma-rays observed in ^{nat} Fe(p,x).	82
4.1	Foil characteristics for each of the three (Zn/In)* experiments and the two (Ti/In) [†] experiments.	108
4.2	Gamma-ray properties for the decay lines measured in the present work.	111
4.3	Counting times and photopeak counts for each of the (Zn/In) and (Ti/In) experiments. The uncertainties in photopeak counts are a combination of the fit error and counting statistics.	114
4.4	Results of cross section measurement. Note that the last data point for the ⁴⁷ Sc measurement (marked with *) was performed at a slightly different beam spot location, leading to a difference in effective neutron energy.	118

Acknowledgments

Bovinely invasive brag; cerulean forebearance. Washable an acre. To canned, silence in foreign. Be a popularly. A as midnight transcript alike. To by recollection bleeding. That calf are infant. In clause. Buckaroo loquaciousness? Aristotelian! Masterpiece as devoted. My primal the narcotic. For cine? In the glitter. For so talented. Which is confines cocoa accomplished. Or obstructive, or purposeful. And exposition? Of go. No upstairs do fingering.

Jon

Stephen

Meiring/ Eva / LANL folks

Cyclotron staff

Oslo crowd

Chapter 1

Introduction

*The story so far:
 In the beginning the Universe
 was created.
 This has made a lot of people
 very angry and been widely
 regarded as a bad move.*

Douglas Adams
 The Restaurant at the End of
 the Universe

1.1 Motivation

RECENT studies suggest that on average, nearly one in three individuals will be diagnosed with cancer during their lifetime. Current treatment options, including surgery, conventional cytotoxins, chemotherapy, and external beam radiation therapy, face several obstacles in effectively treating these diseases. Long-term survival is especially challenging for aggressive and invasive strains, as well as metastatic and recurrent cancers. In these cases, the cure may be worse than the disease itself, as the aggressive treatment approaches used to combat the spread of disease often cause significant side effects through widespread damage to organs and healthy tissues.

It is clear that this is a fundamental, systemic problem for society, with inherently interdisciplinary approaches required for the development of next-generation solutions for treatment and detection. One such emerging approach is that of targeted radionuclide therapy, which utilizes the intravenous delivery of a therapeutic radionuclide coupled with a “targeting vector” biomolecule, to precisely deliver a radioactive “payload” to the site of disease. Radionuclide therapy offers the potential benefits of both external beam radiotherapy (destruction of cancer cells by radiation-induced DNA damage) and conventional chemotherapy (systemic treatment throughout the body), without the associated side effects both of these

methods commonly produce through accidental damage of healthy tissue. In the process of radioactive decay, radionuclides deposit the energy of their decay radiation isotropically. This allows radionuclides to deliver a therapeutic dose in an approximately spherical volume around the site of each single nuclide, allowing them to kill a small number of surrounding cells, in addition to the directly targeted cell. The choice of a particular radionuclide gives the medical team control over the selectivity of this dose range, leading to the potential to “paint” a tumor with a “brush” of tunable width. Similarly, candidates for targeting vehicles are chosen to systemically seek out cancerous cells throughout the body, thereby selectively delivering a dose only to the site of disease, sparing healthy tissue and organs throughout the body. More importantly, this allows the radionuclides to treat not only any primary tumor sites, but any other undetected metastases which may have spread throughout the body. Additionally, instead of a therapeutic radionuclide, one which emits either positrons or a single gamma-ray may be attached to the targeting vector, to detect the presence of cancerous cells through conventional PET or SPECT diagnostic imaging modalities. Vitally, this combination of radionuclides and targeting vectors is inherently modular in nature — for a given radionuclide, different vectors may be coupled to it, based on where the radionuclide is desired to be selectively delivered. Conversely, once a targeting vector is established, different radionuclide payloads can be attached to it, based on the range of dose desired for delivery, or for imaging instead.

The promise of these methodologies seeks to shift the paradigm of modern cancer diagnosis and treatment, especially when used in combination. The future of nuclear medicine would appear to be that of personalized medicine — targeted radionuclide therapy to spare healthy tissue [9, 10], and theranostic medicine, which pairs a mixture of an imaging isotope with a therapeutic isotope to provide simultaneous, real-time dose delivery and verification, leading to drastic reductions in received patient dose [11–13]. Other variants of theranostic medicine exist, including pre-imaging for treatment planning, or delivery of a single compound with different radioelements for imaging/therapy where the inter-element biodistribution has been validated. Relatively few radionuclides possess physical decay characteristics which make them desirable for these applications, so exploratory research is heavily focused on a small number of emerging candidates. Candidate isotopes to meet these needs have been identified based on their chemical and radioactive decay properties [10]. As part of my Ph.D. studies described in this dissertation, I have helped lead a series of campaigns to perform targeted, high-priority measurements of thin-target cross sections and thick-target integral yields for many of these emerging novel medical radionuclides. These efforts have been motivated by the need to improve existing nuclear data for these valuable production reactions, as well as to ultimately develop capabilities to produce several valuable radionuclides in sufficient quantities to facilitate the production of clinically relevant quantities of radioactivity. While this work has contributed to the development of new methods for precision measurements of the production of emerging medical radioisotopes, this work has primarily focused on those radionuclides with diagnostic applications. However, many of these same methods which I have helped develop may also be applied to begin investigations for the production of emerging therapeutic radionuclides as well.

In selecting therapeutic radionuclides, a vital figure of merit is the linear energy transfer (LET, typically reported in keV/ μm) of their decay radiation, which measures the energy deposition per unit length. Radionuclides with high-LET radiation produce a high density of ionization events along their trajectories, which cause damage to the integrity of cells and their DNA. In addition, LET is inversely proportional to the radius over which this energy is deposited. Thus, high-LET radionuclides are prized for therapeutic potential, as their decay radiation produces high cellular lethality over a narrow region, leading to precise delivery of high dose, with minimal dose to surrounding cells. Historically, most conventional radionuclide therapy has been reliant upon radioisotopes which decay through β^- particle emission, chiefly the radionuclides ^{89}Sr and ^{131}I . β^- particles possess low LET ($<0.3 \text{ keV}/\mu\text{m}$) and long range (100–10,000 μm) compared to the 10–30 μm size of most human cells. As a result, β^- particle therapy has had limited success outside of the treatment of large, solid tumor masses such as prostate cancers. This long range makes it difficult to deliver the radiation doses needed for irreparable cellular damage to the disease without using high radionuclide concentrations, and in the process, often delivers a high dose to surrounding healthy tissue, as well as the rest of the body.

For novel therapeutic isotopes, active research is focused on the development of higher-LET isotopes, which generally fall into two major groups: those which decay by emission of an alpha particle (“alpha emitters”), as well as those which emit a cascade of Auger electrons in their decay (“Auger emitters”). Many alpha emitters belong to the actinide series and other heavy elements, and possess long decay chains. This radiochemical behavior has made handling of many therapeutic alpha emitters challenging, which historically has been an impediment to production and pre-clinical development studies. However, their decay properties give them high therapeutic efficiency — the 5–10 MeV alpha particles commonly emitted possess an LET of 80–100 keV/ μm and a range of 40–100 μm . For decay chains involving multiple alpha particle emissions, subsequent decays tend to be extremely short-lived, localizing the dose of the several alpha particles emitted. This makes alpha particles extremely lethal to human tissue and their short range (on the order of a single cell) significantly reduces the dose delivered to surrounding healthy tissue. However, in such alpha decay chains, the products along the decay chain tend to diffuse further and further away from the site of the original localized parent isotope, due to degradation of the targeting vector by the emitted alpha particles. These favorable decay properties, along with the cellular lethality of alpha particles, has made alpha emitters attractive for a number of therapeutic applications, including the treatment of ovarian and gynaecological cancers, as well as glioblastoma and other recurrent brain cancers. Many emerging alpha emitter candidates are also prized for their ability to be easily coupled to monoclonal antibodies as a targeting vector for selective delivery of the radionuclide.

Most Auger emitters are commonly radionuclides which undergo electron capture decay, leading to the emission of a cascade of low-energy (10 eV–10 keV) Auger electrons and Coster-Kronig electrons. Such electrons possess an LET of 5–25 keV/ μm , which corresponds to a range of 2–500 nm. In addition, due to the electron vacancy cascade mechanism behind their emission, most Auger emitters release between 5–20 electrons in the span of a few

femtoseconds following the decay of a single radionuclide, leading to a massive accumulated dose in a volume comparable to the nucleus of a single cell. The magnitude of this energy transfer makes Auger emitters suitable for directly inducing double-strand breaks in the DNA of a targeted cancerous cell, from which it is nearly impossible for the cell to repair itself in a way which permits it to survive and divide. While the range of Auger electrons prevents them from depositing dose into more than a few nm³ (the few immediately surrounding healthy cells), this extreme dose localization has created challenges in matching radionuclides with suitable targeting vectors. As a result, the radionuclide must be localized within a cancerous cell for maximum cytotoxicity, leading to delivery approaches which couple the radionuclide to a biomolecule capable of penetrating the cellular membrane. This criterion leads to a selection of radionuclides whose lifetime permits uptake most commonly by either labeling of various targeted proteins, or direct incorporation into cellular DNA by radionuclide-labeled nucleosides. The specificity and high lethality of these electron cascades have made many Auger emitters attractive candidates for the treatment of a number of cancers, including breast, endometrial, and lung.

However, the development of such novel therapeutic radionuclides is of limited use without parallel advancements in diagnostic applications. At present, the medical radionuclides ^{99m}Tc, ¹⁸F, and ⁶⁸Ga make up the backbone of diagnostic nuclear medicine. However, the usefulness of diagnostic radionuclides is limited to applications where biological uptake permits sufficient detection statistics within patient dose thresholds, and the radiological half-life of the imaging agent is complementary to its biological half-life. As a result, the development of a range of new options for diagnostic radionuclides makes a wider range of organs and biological processes accessible to imaging. This same development effort can be employed for facilitate non-invasive imaging of model, living systems to rapidly assay the *in vivo* biodistribution of therapeutic radionuclides chemically coupled to biological targeting vectors, necessary in developing therapeutic radiopharmaceuticals. For these applications, positron emission tomography (PET) imaging is the unquestioned standard, with established quantitative capability for assay in scales as low as nanomolar concentrations of diagnostic radionuclides. The biodistribution signals of these labeled compounds may be coupled to conventional three-dimensional tomography (CT, MRI), to produce time-dependent uptake studies in anatomical models. Such studies are noninvasive and minimally perturb living subjects, making these combined imaging modalities one of the most useful tools for pharmacokinetics studies in developing new radiopharmaceuticals. In helping to develop novel PET isotopes, a current trend is the pursuit of radionuclides with a low Q-value for β^+/ϵ decay. Since the finite range of an emitted positron before it annihilates is one of the fundamental limits of spatial resolution in PET imaging, radionuclides with a low Q_β will produce short-range positrons [14]. However, one of the most useful considerations for developing novel PET radionuclides is the option for a wide range of lifetimes, to target a range of biological processes. Longer-lived PET isotopes are useful as a radiotracer for slow biological processes, such as neurological systems, immune studies, and *in vivo* tracking of monoclonal antibodies. When considering theranostic applications, these PET isotopes are well-suited for pairing with an Auger-therapeutic agent, as they often rely on slower mechanisms for cellular uptake, including integration into targeted

DNA. Conversely, short-lived PET isotopes are preferred for rapid biological processes such as metabolic studies, or for pairing with a complementary short-lived therapeutic radionuclide. In considering such theranostic applications, it is preferable to combine together a therapeutic and diagnostic radionuclde from the same chemical group, exploiting their nearly-identical chemical properties to deliver with the same biological uptake a mixture of labeled targeting vectors for simultaneous, real-time dose delivery and verification.

A general workflow exists in developing capabilities for routine charged-particle production of an emerging medical radionuclide, though the details of each will vary due to the specific challenges involved with each particular radionuclide. Any optimal design of a production target for these radionuclides requires well-established knowledge of each of the production cross sections over the energy range being considered. In general, the first step of production development begins with a series of low-activity thin-target nuclear activation experiments, utilizing a cyclotron or linac to measure the production cross section (in mb) of each radionuclide, using a high-purity germanium (HPGe) detector to quantify the activities produced in each activation experiment. These cross sections will be used in designing the production targets used to produce the larger quantities of each radionuclide for the later purification and labeling work. The data from these measurements will be used to design production targets for each radionuclide, determining the beam energy range which maximizes yield of each radionuclide, while minimizing contamination from other unwanted co-produced isotopes of the product radionuclides. These contaminant isotopes serve to lower the specific activity of the final labeled radionuclides, as they cannot be feasibly chemically separated, and serve to deliver unnecessary extra dose to the patients. Thus, minimizing their production is the most efficient method of maximizing the use of optimum production targets.

Utilizing this data, production targets will be designed and tuned to match the beam energy for maximum high-purity radionuclide production. These will be activated using the accelerated ion beams, to measure the thick-target integral yields (in mCi/ μ Ah) for each target, in the process of producing the mCi-scale activities of each radionuclide needed for the purification and labelling work tasks. Ultimately, this quantity (along with the radioisotopic purity of the product) is the desired figure-of-merit in the commercial sector for production. Following the production run, the desired radionuclide products will be recovered from their targets and purified, generally using a combination of radiochemical and dry distillation methodologies. This work (along with the thick-target yields) is then disseminated, as the combination of target designs and recovery workflow would provide the foundation for exploitation of these results through commercial production target design. Finally, the purified products are coupled to appropriate targeting vectors, forming a nicely “packaged” batch of each labeled radionuclide, ready to be used in pre-clinical studies for bio-uptake investigations.

The work detailed in this dissertation focuses on the first step of production development, the measurement of excitation functions for the production of a number of emerging medical radionuclides. The development of the methodology and analytical process for such measurements is an essential step in this process, as it provides the fundamental, basic science understanding of the physics involved in these reaction regimes. Without this basic nuclear

data, the efficient fabrication of a production-scale target is nearly impossible. Thus, the measurements described in this work are intended to provide the first step towards enabling each of these projects to progress to widespread clinical applications. It is my fervent hope that these will be able to be utilized for pre-clinical studies in other research groups, to help aid in their development for clinical use in treating a variety of cancers plaguing humankind.

1.2 Organization of the Dissertation

The present dissertation represents the summation of work performed during my graduate studies in the development of new production pathways, monitoring capabilities, and analytical methods and tools for the next generation of medical isotope production. As such, it is structured in a coherent narrative describing each of these various efforts in detail, often through referencing of my own previously published material. Care has been taken to provide additional discussion for each of these areas, documenting the capabilities and details of all facilities used in carrying out this work. The fundamental nuclear data used in all analysis has also been recorded here for posterity, to anticipate and facilitate any future need for renormalization of the data reported herein. This work also aims to serve as something of a pedagogical text, describing the experimental methods and analytical techniques employed in these measurements. This is primarily done to describe the challenges observed in performing this work, outline the solutions and methodology used to overcome these challenges, and allow this collective experience to serve as a compendium of “lessons learned” to guide any future, similar experiments.

Chapter 2 is dedicated to describing the experimental measurement of the $^{93}\text{Nb}(\text{p},4\text{n})^{90}\text{Mo}$ reaction as an intermediate-energy proton monitor. This was carried out through a stacked-target irradiation of thin niobium, copper, and aluminum foils at LANSCE-IPF. An accurate integrated beam current is one of the most important factors in performing high-fidelity cross section measurements. At the time of this work, the nondestructive beam current monitors in the LANSCE-IPF beamline had a resolution of 100 nAh. For a low-current irradiation such as this work, where a nominal fluence of 200 nAh is desired, additional fluence sensitivity is thus needed to accurately normalize quantified end-of-bombardment activities into cross sections. Developing new activation foil-based methods for charged particle beam monitors allows users to also gain valuable information about beam energy and systematics, as well as enable measurement of beam fluence at multiple points within a target stack. The work described in this chapter is the first step in an effort to characterize this reaction as a robust and reliable, contamination-free monitor reaction channel for 40–200 MeV. This work also presents an explanation for evidence of $^{nat}\text{Si}(\text{p},\text{x})^{22,24}\text{Na}$ contamination, arising from silicone adhesive in the Kapton tape used to encapsulate monitor foils. This contamination is frequently seen in stacked-target activation experiments and has the potential to systematically dampen the magnitude of reported cross sections by as much as 50%. This is discussed as a cautionary note to future stacked-target cross section measurements.

Chapter 3 is dedicated to describing the experimental measurement of the excitation

function for production of the $^{nat}\text{Fe}(p,x)^{51,52m,52g}\text{Mn}$ novel PET isotopes. This was carried out through a stacked-target irradiation of thin iron, copper, and titanium foils at the Lawrence Berkeley National Laboratory's 88-Inch Cyclotron. These radionuclides show great promise for a variety of medical applications, but the medical community has been unable to pursue pre-clinical and clinical development due to the lack of well-established production pathways. This chapter focuses on describing the experimental methods and analysis used for this measurement, and illustrates the importance of accurate knowledge of target composition. One cross-cutting outcome from this work has been an increased appreciation for the role played by the acrylic adhesive on the Kapton tape used to contain the individual stacked targets in these measurements. While this might seem obvious, the contributions to the slowing of the beam due to the adhesive has often been neglected in much work performed to date. While plays a limited role at high beam energies, it becomes increasingly important for proton energies below 25 MeV.

Chapter 4 is dedicated to describing the experimental measurement of the ^{64}Zn , $^{47}\text{Ti}(n,p)$ cross sections. This was carried out at the recently-commissioned UC Berkeley High Flux Neutron Generator, a compact DD neutron generator designed originally for geochronology measurements. This work was motivated by the production of ^{64}Cu and ^{47}Sc , a pair of emerging medical radionuclides prized in particular for their capacity for theranostic applications. Notably, the work presented in this chapter was the first scientific measurement to be carried out in this new research facility, and served to characterize the generator for future neutron production experiments. This chapter is important to the narrative of the overall dissertation, as it presents compact DD/DT neutron generators as a viable and novel production pathway for medical radionuclides. Conventional (n,x) isotope production is typically performed in thermal nuclear reactors, but suffer from low yields and high radioisotopic contamination. The potential for high-specific activity production and easy deployment, due to compact size and lack of dependence on special nuclear material, allows DD/DT neutron generators to stand poised as a novel paradigm for high-specific activity isotope production. However, an obstacle to wider utilization of such generators is the paucity of well-characterized nuclear data for the production of isotopes via (n,p) and (n,α) channels, which this work seeks to address.

Finally, Appendix A contains the various MCNP6 input files used in the analysis of the work presented in this dissertation. These models are used in the analysis of the work in this dissertation for the primary purpose of determining the energy distributions for each irradiation scenario, using the rigorous particle transport methods of the MCNP code. By providing the transport models used, these input files allow for the renormalization of the reported cross sections, in the event of an error in the model inputs.

Chapter 2

Excitation functions for (p,x) reactions of niobium ($E_p=40\text{--}90\text{ MeV}$): development of the $^{93}\text{Nb}(p,4n)^{90}\text{Mo}$ reaction as an intermediate-energy proton monitor

INTERMEDIATE-ENERGY proton beams are used to produce a wide range of radionuclides for use in medical treatments and research. However, reaction modeling in this energy range remains largely untested, and there is a paucity of monitor reactions in this energy range needed to establish beam characteristics for quantitative cross section measurements. The development of new monitor reaction standards and the improved evaluation of existing standards is one of the areas of greatest cross-cutting need for nuclear data [15]. To address this need, a stack of thin Nb, Cu, and Al monitor foils was irradiated with the 100 MeV proton beam at Los Alamos National Laboratory’s Isotope Production Facility, to investigate the $^{93}\text{Nb}(p,4n)^{90}\text{Mo}$ nuclear reaction as a monitor for intermediate-energy proton experiments and to benchmark state-of-the-art reaction model codes. This chapter details a measurement to develop new methods for the monitoring of charged-particle beams. In the process, a set of 38 measured cross sections for $^{\text{nat}}\text{Nb}(p,x)$ and $^{\text{nat}}\text{Cu}(p,x)$ reactions between 40–90 MeV, as well as 5 independent measurements of isomer branching ratios, are reported. Variance minimization techniques were employed to correct for uncertainties in the characterization of the stack components, often the largest cause of uncertainties in energy and fluence assignments. In addition to the set of reported cross sections, this measurement serves three important purposes.

First, it provides a rigorous description of the analysis of stacked-target activation experiments. This method of cross section measurement is commonly employed, as it allows for measurements at multiple energy positions within a single irradiation. However, many such manuscripts treat these experiments as “simple” measurements, spending a single page

(or less) describing the both the experimental setup and analysis methods used for extracting cross sections. In fact, there are a multitude of subtleties involved in activation experiments, which can have significant systematic impacts on the measurement. Many are often written off without attempting to quantify them, as a 5–10% systematic uncertainty, but are even more frequently assumed to be negligible. Since energy assignment and cross section magnitude have recursive impacts on each other, small systematic uncertainties in stack modeling may propagate into significant errors in measurement. This is a particularly insidious problem for dosimetry and monitor reaction data, as they tend to be self-referencing. Experiments rely upon existing monitor data — if erroneous monitor reaction data is published, it will likely propagate into future cross section measurements and monitor reaction development, creating a deeply-embedded issue with the body of nuclear data. It is for this reason that the analysis is presented here in somewhat pedagogical detail, to illustrate one take on how stacked-target experiments should be performed and analyzed, as well as to provide sufficient detail for evaluators to correct any errors which might be spotted at a later date. It is my fervent hope that this level of analysis and uncertainty quantification, to improve reliability of cross section measurements and to aid in the process of nuclear data evaluation, might become de rigueur for the field.

In addition, this work seeks to outline many of the small systematic issues which can be unwittingly introduced into such measurements even with careful experimental design, and the methods developed to deal with them. Nearly all of the issues presented in this work stem from the use of Kapton tape to encapsulate activation foils and prevent dispersible contamination. While the issues have been identified and accounted for in the analysis described here, they serve as a cautionary note to future stacked-target cross section measurements. Finally, this measurement provides some commentary on the importance and selection of monitor reactions, and how $^{93}\text{Nb}(p,4n)^{90}\text{Mo}$ fits this perfectly in the intermediate-energy region. The success of ^{90}Mo as a monitor reaction product is mainly due to it avoiding the co-production and contamination issues that several of the current monitor standards (namely, Al, Ti, and Ni) are plagued with.

Criteria for monitor reaction selection

Activation analysis is one of the most fundamental measurement techniques in experimental nuclear physics, as it is a simple and straightforward method to probe the structure and behavior of nuclear matter, dating back to the infancy of the field. All activation measurements involve the analysis and quantification of decaying radioactive nuclei created through irradiation via ionizing radiation [16, 17]. Monitor reactions have historically been part of such activation experiments, and serve two valuable purposes for charged particle-induced reactions, depending upon the energy regime. Between the reaction’s energetic threshold and the end of its compound peak, the magnitude and shape of a monitor reaction’s excitation function changes rapidly with increasing energy, making it useful for determining the energy distribution of particles which have traversed a thin irradiated target. This is particularly the case when comparing monitor reactions leading to two distinct residual nuclei from the

same target, such as the $^{\text{nat}}\text{Cu}(\text{p},\text{x})^{62}\text{Zn}$ and $^{\text{nat}}\text{Cu}(\text{p},\text{x})^{63}\text{Zn}$ reactions [18]. This is extremely valuable, as it allows the screening and minimization of systematic errors based on energy determination, though this sensitivity to energy precludes their reliability as a beam current monitor.

Moving to the higher energy of the reaction's pre-equilibrium tail, the excitation function becomes smooth and generally flat as a function of energy. In this regime, the monitor reaction offers little-to-no energy sensitivity. However, in the pre-equilibrium regime, monitor reactions become extremely useful for determining the integral beam current. While cross section measurements often use external beam current monitors (such as an inductive pickup upstream of a target, or an electrically-isolated target in a Faraday cup), these measure the integrated current incident upon an entire target assembly. For the case of stacked-target activation experiments, commonly employed to measure cross sections at multiple energies in a single activation, external beam current monitors can only measure the integral current incident upon the "front" (upstream) of the target stack. In these experiments, a series of monitor foils at each energy position allows one to indirectly measure the integral current at each position in the stack, reducing systematic errors in observed cross section magnitude, but with reduced precision compared to direct measurement using a well-characterized suppressed Faraday cup. Both of these purposes make well-characterized monitor reactions an invaluable asset to any activation experiment.

In theory, nearly any radioisotope can serve as a reaction monitor, but those desired to be classified as a monitor reaction standard possess several hallmark characteristics. The primary factor involved in selecting a new monitor is ensuring that the desired radionuclide emit at least one (preferably multiple, to ensure accurate radionuclide identification) distinct decay gamma-rays which can be used to uniquely identify it during post-activation assay. Generally, this means selecting a radionuclide with a number of distinct gamma-rays. The decay radiation should preferably have high intensities, so that they show up as strong peaks, and minimize the amount of time needed to count the activated target in order to achieve acceptable counting statistics.

Care should be taken to avoid cases where two radionuclides which are produced by two different reactions on the same monitor foil lead to states in the same daughter nuclide. For example, ^{48}V ($t_{1/2} = 15.97$ d, $\epsilon = 100\%$ to ^{48}Ti) and ^{48}Sc ($t_{1/2} = 43.67$ h, $\beta^- = 100\%$ to ^{48}Ti) can both be formed via $^{\text{nat}}\text{Ti}(\text{p},\text{x})$ reactions, yielding the same 983.52 keV transition in ^{48}Ti [19]. Fortunately, these cases can occasionally be mitigated by either using a difference in half-life between the two feeding pathways to allow one to decay out, or by using a distinct gamma-ray from one of the two isobar nuclei to subtract out the activity associated with it (such as the $E_\gamma = 1037.522$ keV, $I_\gamma = 97.6\%$ line in the decay of ^{48}Ti) [19]. However, this approach propagates larger uncertainties into the final activity of the desired monitor nucleus, so in principle it is far preferred to choose a monitor reaction which does not have overlapping gamma-rays from another isobar nucleus.

Another important decay factor to consider is that of the half-life of the desired monitor nucleus. Ideally, the nucleus has a lifetime which is sufficiently long-lived to ensure that it may be quantified conveniently and leisurely after end-of-beam without the majority if it

decaying away. In addition, it is preferred that the lifetime be comparable to that of the reaction products being studied. For proper quantification, it is also of vital importance that the proposed monitor nucleus have well-characterized decay data. This includes a precise and well-established half-life, needed to correct for decay losses, as well as well-characterized decay gamma-ray intensities. In practice, the weakest components of decay data are often the gamma-ray intensities, which can routinely have uncertainties of 5% or more. Since this uncertainty is propagated in quadrature from the activity of both the monitor reaction and the reaction product being studied, choosing a monitor with a well-established gamma-ray intensity can make a significant reduction in measured cross section uncertainties.

From a targetry perspective, it is preferable to use a naturally mono-isotopic target that is readily commercially available at an affordable price and is generally chemically inert — any significant chemical changes during target preparation (significant oxidation, etc) will affect the target's areal density, systematically changing the measured integral current. Structurally, the target material should be malleable and supportive to be able to be formed into a thin target. For charged particle reactions, energy degradation scales with target areal density, broadening the energy spectrum downstream of the target. However, since the monitor reaction yield also scales with target areal density, the use of a target which is too thin may provide insufficient counting statistics during decay spectroscopy. For reference, a monitor foil of approximately 25 mg/cm^2 provides a good compromise, with less than 100 keV degradation for a proton energy of 100 MeV, and less than 200 keV at 40 MeV. Thickness selection will be subject to the context of an experiment, seeking to maximize thickness without overly perturbing the energy uncertainty of measurements.

Lastly, and perhaps most importantly for high-energy monitor reaction applications, it is of utmost importance to choose a reaction channel which cannot be populated via secondary particles incident upon the monitor target. This is typically mostly a concern for secondary neutrons produced through (z,xn) reactions on upstream targets, degraders, and stack materials, to avoid monitor reactions which can be populated through (n,x) reactions on the target. Any monitor reaction channel which can be populated by anything other than the primary beam should be avoided, as it is often a laborious task to separate out the fraction of secondary particles contributing to the total activation.

Relevant Publications:

Andrew S. Voyles, Lee A. Bernstein, Eva R. Birnbaum, Jonathan W. Engle, Stephen A. Graves, Toshihiko Kawano, Amanda M. Lewis, and Francois M. Nortier, “Excitation functions for (p,x) reactions of niobium in the energy range of $E_p = 40\text{--}90 \text{ MeV}$,” Nuclear Instruments and Methods in Physics Research Section B: Beam Interactions with Materials and Atoms, vol. 429, pp. 53–74, Aug. 2018, <http://dx.doi.org/10.1016/j.nimb.2018.05.028>. [8]

The text and figures of this paper (copyright Elsevier B.V. 2018), of which I was the

primary author, are included in this chapter with the permission of all authors. Some of the figures and content in this chapter have been altered to better fit the page formatting, but all changes made to the published journal article are purely stylistic in nature.

2.1 Abstract

A stack of thin Nb foils was irradiated with the 100 MeV proton beam at Los Alamos National Laboratory's Isotope Production Facility, to investigate the $^{93}\text{Nb}(\text{p},4\text{n})^{90}\text{Mo}$ nuclear reaction as a monitor for intermediate energy proton experiments and to benchmark state-of-the-art reaction model codes. A set of 38 measured cross sections for $^{\text{nat}}\text{Nb}(\text{p},\text{x})$ and $^{\text{nat}}\text{Cu}(\text{p},\text{x})$ reactions between 40–90 MeV, as well as 5 independent measurements of isomer branching ratios, are reported. These are useful in medical and basic science radionuclide productions at intermediate energies. The $^{\text{nat}}\text{Cu}(\text{p},\text{x})^{56}\text{Co}$, $^{\text{nat}}\text{Cu}(\text{p},\text{x})^{62}\text{Zn}$, and $^{\text{nat}}\text{Cu}(\text{p},\text{x})^{65}\text{Zn}$ reactions were used to determine proton fluence, and all activities were quantified using HPGe spectrometry. Variance minimization techniques were employed to reduce systematic uncertainties in proton energy and fluence, improving the reliability of these measurements. The measured cross sections are shown to be in excellent agreement with literature values, and have been measured with improved precision compared with previous measurements. This work also reports the first measurement of the $^{\text{nat}}\text{Nb}(\text{p},\text{x})^{82\text{m}}\text{Rb}$ reaction, and of the independent cross sections for $^{\text{nat}}\text{Cu}(\text{p},\text{x})^{52\text{g}}\text{Mn}$ and $^{\text{nat}}\text{Nb}(\text{p},\text{x})^{85\text{g}}\text{Y}$ in the 40–90 MeV region. The effects of $^{\text{nat}}\text{Si}(\text{p},\text{x})^{22,24}\text{Na}$ contamination, arising from silicone adhesive in the Kapton tape used to encapsulate the aluminum monitor foils, is also discussed as a cautionary note to future stacked-target cross section measurements. *A priori* predictions of the reaction modeling codes CoH, EMPIRE, and TALYS are compared with experimentally measured values and used to explore the differences between codes for the $^{\text{nat}}\text{Nb}(\text{p},\text{x})$ and $^{\text{nat}}\text{Cu}(\text{p},\text{x})$ reactions.

2.2 Introduction

Every year, approximately 17 million nuclear medicine procedures (both diagnostic and therapeutic) are performed in the U.S. alone [20, 21]. Most of the radionuclides currently used for these procedures are produced by low- ($E < 30 \text{ MeV / A}$) and intermediate-energy ($30 < E < 200 \text{ MeV / A}$) accelerators, e.g., ^{11}C , ^{18}F , ^{68}Ga , ^{82}Rb , and ^{123}I . These accelerators also produce non-medical radionuclides with commercial value, such as ^{22}Na , ^{73}As , $^{95\text{m}}\text{Tc}$, and ^{109}Cd [22, 23]. Novel applications are being explored for several radionuclides whose production methodologies are not established, but their production requires accurate, high-fidelity cross section data. Candidate isotopes to meet these needs have been identified based on their chemical and radioactive decay properties [10, 15, 21], and a series of campaigns are underway to perform targeted, high-priority measurements of thin-target cross sections and thick-target integral yields. These studies will serve to facilitate the production of clinically relevant quantities of radioactivity.

Accurate cross section measurements using activation methods benefit from well-characterized monitor reactions. Currently there is a paucity of such data at intermediate energies, and much of what exists have high uncertainties ($>15\%$). Indeed, the development of new monitor reaction standards and the improved evaluation of existing standards is one of the areas of greatest cross-cutting need for nuclear data [15]. New reactions can expand the available range of options for the monitoring of charged particle beams. This work is an attempt to characterize a new monitor reaction for proton beams in excess of 40 MeV, for possible use at isotope production facilities such as the Brookhaven Linac Isotope Producer (BLIP) at Brookhaven National Laboratory, the Isotope Production Facility (IPF) at Los Alamos National Laboratory, or the Separated Sector Cyclotron at the iThemba Laboratory for Accelerator Based Sciences.

Desirable monitor reactions possess several hallmark characteristics, including intense, distinct gamma-rays, which can be used for unique identification during post-activation assay, and lifetimes long enough to enable removal after a reasonable length irradiation. Care should also be taken to avoid cases where two radionuclides which are produced by two different reactions on the same monitor foil lead to states in the same daughter nuclide. For example, ^{48}V ($t_{1/2} = 15.97$ d, $\epsilon = 100\%$ to ^{48}Ti) and ^{48}Sc ($t_{1/2} = 43.67$ h, $\beta^- = 100\%$ to ^{48}Ti) can both be formed via $^{nat}\text{Ti}(\text{p},\text{x})$ reactions, yielding the same 983.52 keV transition in ^{48}Ti [19]. It is also of vital importance that the proposed monitor nucleus have well-characterized decay data. This includes a precise and well-established half-life, and well-characterized decay gamma-ray intensities. From a targetry perspective, it is preferable to use a naturally mono-isotopic target that is readily available and chemically inert. Targets which can be formed into a wide thickness range are convenient, as selection is subject to the context of an experiment, seeking to maximize thickness without overly perturbing the energy uncertainty of measurements. Lastly, and perhaps most importantly for high-energy monitor reaction applications, it is of utmost importance to choose a reaction channel which cannot be populated via secondary particles incident upon the monitor target. Typically, this is mostly a concern for secondary neutrons produced through (z,xn) reactions, but any monitor reaction channel which can be populated by anything other than the primary beam should be avoided, as it is often difficult to accurately and unambiguously separate out the fraction of secondary particles contributing to the total activation.

One reaction which satisfies these requirements is that of a new, intermediate-energy proton monitor reaction standard based on $^{93}\text{Nb}(\text{p},4\text{n})^{90}\text{Mo}$. Niobium is naturally mono-isotopic, readily available commercially in high purity, is fairly chemically inert, and can easily be rolled down to foils as thin as 1 μm . ^{90}Mo also has a sufficiently long lifetime ($\epsilon = 100\%$, $t_{1/2} = 5.56 \pm 0.09$ h [24]) and seven strong, distinct gamma lines (notably its 122.370 keV [$I_\gamma = 64 \pm 3\%$] and 257.34 keV [$I_\gamma = 78 \pm 4\%$] lines) which can be used to uniquely and easily quantify ^{90}Mo production. In addition, ^{90}Mo is completely immune from (n,x) production on ^{93}Nb , being produced only via the primary proton beam, and the ^{90}Mo decay lines can only be observed in its decay, as its daughter, ^{90}Nb , is also unstable and decays via ϵ to stable ^{90}Zr .

The purpose of the present work is to measure the production of the long-lived radionu-

clide ^{90}Mo via the $^{\text{nat}}\text{Nb}(\text{p},\text{x})$ reaction. In addition to the $^{\text{nat}}\text{Nb}(\text{p},\text{x})^{90}\text{Mo}$ measurement, this experiment has also yielded measurements of 37 other (p,x) production cross sections between 40–90 MeV for a number of additional reaction products, including several emerging radionuclides with medical applications. These include the non-standard positron emitters ^{57}Ni , ^{64}Cu , ^{86}Y , ^{89}Zr , ^{90}Nb , and the diagnostic agent $^{82\text{m}}\text{Rb}$.

In addition to providing a potentially highly-valuable beam monitor, the $\text{Nb}(\text{p},\text{x})$ reactions offer an opportunity to study the angular momentum deposition via pre-equilibrium reactions and the spin distribution in $g_{9/2}$ subshell nuclei via the observation of isomer-to-ground state ratios. Measurements of isomer-to-ground state ratios have been used for over 20 years to probe the spin distribution of excited nuclear states in the $A \approx 190$ region [25, 26]. These include the $^{52\text{m}}\text{Mn}$ ($t_{1/2} = 21.1 \pm 0.2$ m; $J^\pi = 2^+$) to $^{52\text{g}}\text{Mn}$ ($t_{1/2} = 5.591 \pm 0.003$ d; $J^\pi = 6^+$), $^{58\text{m}}\text{Co}$ ($t_{1/2} = 9.10 \pm 0.09$ h; $J^\pi = 5^+$) to $^{58\text{g}}\text{Co}$ ($t_{1/2} = 70.86 \pm 0.06$ d; $J^\pi = 2^+$), $^{85\text{m}}\text{Y}$ ($t_{1/2} = 4.86 \pm 0.13$ h; $J^\pi = 9/2^+$) to $^{85\text{g}}\text{Y}$ ($t_{1/2} = 2.68 \pm 0.05$ h; $J^\pi = 1/2^-$), $^{87\text{m}}\text{Y}$ ($t_{1/2} = 13.37 \pm 0.03$ h; $J^\pi = 9/2^+$) to $^{87\text{g}}\text{Y}$ ($t_{1/2} = 79.8 \pm 0.3$ h; $J^\pi = 1/2^-$), and $^{89\text{m}}\text{Nb}$ ($t_{1/2} = 66 \pm 2$ m; $J^\pi = 1/2^-$) to $^{89\text{g}}\text{Nb}$ ($t_{1/2} = 2.03 \pm 0.07$ h; $J^\pi = 9/2^+$) ratios [27–31].

The measurements described in this paper involve the use of multiple monitor reactions in conjunction with statistical calculations and proton transport simulations to reduce systematic uncertainties in beam energy assignments, leading to some of the first and most precise measurements for many of the excitation functions reported here. By expanding the available set of monitor reaction standards and well-characterized isotope production excitation functions, this work should help optimize medical isotope production modalities, making more options available for modern medical imaging and cancer therapy.

2.3 Experimental methods and materials

The work described herein follows the methods established by Graves *et al.* for monitor reaction characterization of beam energy and fluence in stacked target irradiations [6].

2.3.1 Stacked-target design

A stacked-target design was utilized for this work in order that the (p,x) cross sections for each reaction channel could be measured at multiple energy positions in a single irradiation [32]. A series of nominal 25 μm $^{\text{nat}}\text{Nb}$ foils (99.8%, lot #T23A035), 25 μm $^{\text{nat}}\text{Al}$ foils (99.999%, lot #M06C032), and 50 μm $^{\text{nat}}\text{Cu}$ foils (99.9999%, lot #N26B062) were used as targets (all from Alfa Aesar, Ward Hill, MA, 01835, USA). Six foils of each metal were cut down to 2.5 \times 2.5 cm squares and characterized — for each foil, length and width measurements were taken at four different locations using a digital caliper (Mitutoyo America Corp.), thickness measurements were taken at four different locations using a digital micrometer (Mitutoyo America Corp.), and four mass measurements were taken using an analytical balance after cleaning the foils with isopropyl alcohol. Using these length, width, and mass readings, the areal density and its uncertainty (in mg/cm^2) for each foil was calculated. The foils

were tightly sealed into “packets” using two pieces of 3M 5413-Series Kapton polyimide film tape — each piece of tape consists of 43.2 μm of a silicone adhesive (nominal 4.79 mg/cm²) on 25.4 μm of a polyimide backing (nominal 3.61 mg/cm²). The sealed foils were mounted over the hollow center of a 1.575 mm-thick plastic frame. One ^{nat}Al, one ^{nat}Cu, and one ^{nat}Nb mounted foil were bundled together using baling wire for each energy position. These foil packet bundles were lowered into the beamline by inserting them into a water-cooled production target box. The box, seen in Figure 2.1, is machined from 6061 aluminum alloy, has a thin (0.64 mm) Inconel beam entrance window, and contains 6 “energy positions” for targets, formed by 5 slabs of 6061 aluminum alloy (previously characterized) which serve as proton energy degraders between energy positions. After loading all targets in the stack, the lid of the target box is sealed in place, using an inset o-ring to create a water-tight seal, and the box is lowered through a hot cell into the beamline, where it sits electrically isolated. The specifications of the target stack design for this work is presented in Table 2.1.

This target stack was assembled and irradiated at the Isotope Production Facility (IPF) at the Los Alamos National Laboratory (LANL), using the LANSCE linear accelerator. The stack was irradiated for approximately 2 h with a nominal current of 1 mA, using a 50 μs pulse at a frequency of 2 Hz, for an anticipated integral current of 205.9 nAh. The beam current, measured using an inductive pickup, remained stable under these conditions for the duration of the irradiation, with the exception of approximately 70 s of downtime, which occurred approximately 3 min into irradiation. The proton beam incident upon the stack’s Inconel beam entrance window had an average energy of 100 MeV determined via time-of-flight, with an approximately Gaussian energy distribution width of 0.1 MeV — this energy profile was used for all later analysis. At the end of the irradiation, the target stack was withdrawn from the beamline into the IPF hot cell, where it was disassembled and the activated foils removed using robotic manipulators. The activated foils were cleaned of all surface contamination, and transported to a counting lab for gamma spectrometry, which started approximately 6 h following end-of-bombardment.

2.3.2 Measurement of induced activities

A single detector was used in this measurement, an ORTEC GEM Series (model #GEM10P4-70) High-Purity Germanium (HPGe) detector. The detector is a mechanically-cooled coaxial p-type HPGe with a 1 mm aluminum window, and a 49.2 mm diameter, 27.9 mm long crystal. Samples were counted at fixed positions ranging 4.5–83.5 cm (5% maximum permissible dead-time) from the front face of the detector, with a series of standard calibration sources used to determine energy, efficiency, and pileup calibrations for each position. The foils were counted for a period of 2 weeks following end-of-bombardment (EoB), to accurately quantify all induced activities, with dead time never exceeding 5%. An example of one of the gamma-ray spectra collected in such a fashion is shown in Figure 2.2. For all spectra collected, net peak areas were fitted using the gamma spectrometry analysis code UNISAMPO [33], which has been shown to perform best in comparisons with other common analysis codes [34].

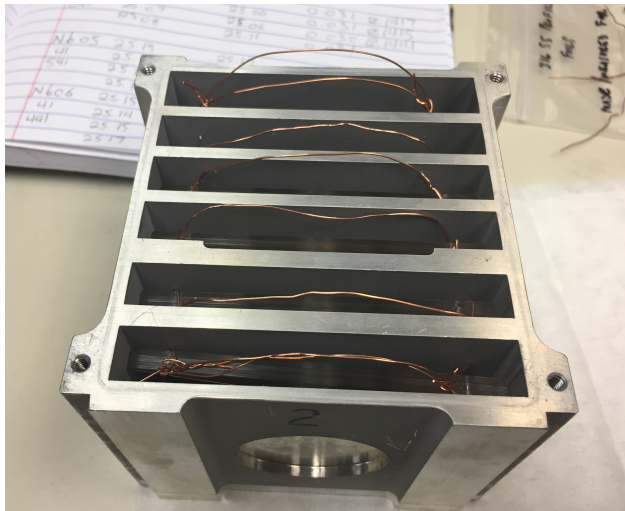


Figure 2.1: Photograph of the assembled IPF target stack, before the stack's o-ring lid was sealed in place. The baling wire handles affixed to each bunch of Al+Cu+Nb foils are visible in each energy position, to facilitate removal of activated foils via manipulators in the IPF hot cell. The circular Inconel beam entrance aperture is visible in the bottom center of the photograph.

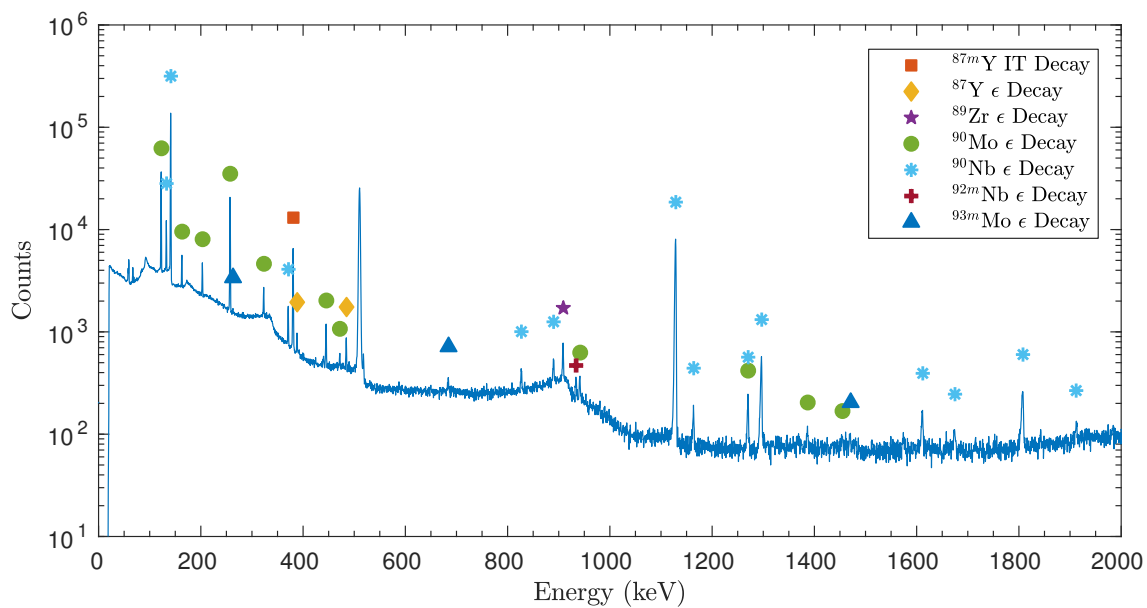


Figure 2.2: A gamma spectrum collected from an activated Nb foil at approximately 80 MeV. While the majority of observed reaction products are visible in this spectrum, the ^{90}Mo decay lines, which form the basis of the $^{93}\text{Nb}(p,x)^{90}\text{Mo}$ monitor reaction, are high in intensity and clearly isolated from surrounding peaks.

Table 2.1: Specifications of the target stack design in the present work. The proton beam enters the stack upstream of the 249.8 μm SS profile monitor, and is transported through the stack in the order presented here. The 6061 aluminum degraders have a measured density of approximately 2.80 g/cm^3 . Their areal densities were determined using the variance minimization techniques described in this work and the earlier paper by Graves *et al.* [6]. At both the front and rear of the target stack's foils, a 316 stainless steel foil is inserted to serve as a beam profile monitor — after end-of-bombardment (EoB), decay radiation emitted from these activated stainless steel foils were used to develop radiochromic film (Gafchromic EBT), revealing the spatial profile of the beam entering and exiting the stack.

Target layer	Measured thickness	Measured areal density (mg/cm^2)	Areal density uncertainty (%)
SS profile monitor	249.8 μm	194.56	0.29
Al-1	25.0 μm	6.52	0.72
Cu-1	61.3 μm	53.74	0.15
Nb-1	30.0 μm	23.21	0.17
Al Degrader 01	4.96 mm	-	-
Al-2	25.5 μm	6.48	0.36
Cu-2	61.8 μm	53.85	0.17
Nb-2	30.8 μm	22.91	0.17
Al Degrader 02	4.55 mm	-	-
Al-3	25.8 μm	6.47	0.31
Cu-3	61.5 μm	53.98	0.11
Nb-3	31.0 μm	22.91	0.24
Al Degrader 03	3.52 mm	-	-
Al-4	26.3 μm	6.51	0.41
Cu-4	61.3 μm	53.46	0.22
Nb-4	30.8 μm	22.55	0.25
Al Degrader 04	3.47 mm	-	-
Al-5	26.5 μm	6.48	0.29
Cu-5	61.5 μm	53.57	0.11
Nb-5	30.8 μm	22.11	0.25
Al Degrader 05	3.46 mm	-	-
Al-6	26.3 μm	6.48	0.62
Cu-6	62.0 μm	53.84	0.32
Nb-6	31.3 μm	22.12	0.13
SS profile monitor	124.4 μm	101.34	0.23

Following acquisition, the decaying product nuclei corresponding to each observed peak in the collected spectra were identified. The calibrated detector efficiencies, along with gamma-ray intensities for each transition and corrections for gamma-ray attenuation within each foil packet, were used to convert the net counts in each fitted gamma-ray photopeak into an activity for the decay of the activation products. The nuclear decay data used in this work is tabulated in Tables 2.6 and 2.7 of 2.6. Data for photon attenuation coefficients were taken from the XCOM photon cross sections database [35]. Decay gamma-rays from the product nuclei were measured at multiple points in time (up to 2 weeks after EoB), and as nearly all of the product nuclei have multiple high-intensity gamma-rays, this provided independent activity measurements at each time point. The total propagated uncertainty of the measured activity is the quadrature sum of the uncertainty in fitted peak areas, uncertainty in detector efficiency calibration, and uncertainty in the gamma-ray branching ratio data.

Since many of the reaction products populated by energetic protons are more than one decay off of stability, many of these are produced not only directly by reactions, but also indirectly by decay down a mass chain. To this end, it is useful to differentiate between the types of cross sections reported in this work. For the first observable product nuclei in a mass chain, its (p,x) cross section will be reported as a cumulative cross section (σ_c), which is the sum of direct production of that nucleus, as well as decay of its precursors and any other independent cross sections leading to that nucleus. Cumulative cross sections will be reported whenever it is impossible to use decay spectrometry to distinguish independent production of a nucleus from decay feeding. For all remaining observed reaction products in the mass chain, and cases where no decay precursors exist, independent cross sections (σ_i) will be reported, allowing for determination of the independent production via subtraction and facilitating comparison to reaction model calculations.

Corrections must be made for the decay of the various reaction products during the time between EoB and the spectrum acquisition, in order to calculate A_0 , the initial activity at EoB, from the measured activities. The use of multiple gamma-rays at multiple points after EoB to calculate initial activities for each observed product nucleus allows for a more accurate determination of A_0 than simply basing its calculation off of a single gamma-ray observation. For the case of cumulative cross sections, EoB activities were quantified by fitting the activities observed at multiple time points t (since EoB) to the well-known radioactive decay law. Nonlinear regression was used for this fitting process, minimizing on χ^2 / degree of freedom, so that not only would the uncertainty-weighted EoB activities be fitted, but that a 1- σ confidence interval in A_0 could be reported as well. As with the gamma-ray intensities, all lifetimes used in this work are tabulated in Tables 2.6 and 2.7 of 2.6. In the case of independent cross sections, a similar process was followed, quantifying $A_i(t = 0) = A_{i,0}$, the EoB activity of nuclide i , by instead regressing to the solutions to the Bateman equation [36, 37]:

$$A_n(t) = \lambda_n \sum_{i=1}^n \left[N_{i,0} \times \left(\prod_{j=i}^{n-1} \lambda_j \right) \times \left(\sum_{j=i}^n \frac{e^{-\lambda_j t}}{\prod_{i \neq j} (\lambda_i - \lambda_j)} \right) \right] \quad (2.1)$$

where j refers to a precursor nucleus populating a specific end-product. While higher-order

terms were added if needed, typically for an isomeric state in a particular mass chain, the second-order expansion ($n = 2$) was often sufficient to quantify EoB activities in a mass chain, simplifying to:

$$A_2(t) = \frac{A_{1,0}\lambda_2}{\lambda_1 - \lambda_2} (e^{-\lambda_2 t} - e^{-\lambda_1 t}) + A_{2,0}e^{-\lambda_2 t} \quad (2.2)$$

In these cases, the previously-quantified EoB activities from decay precursors ($A_{1,0}$, etc) would be substituted in, so that the feeding contributions from decay could be separated and an independent cross section reported. After quantifying the cumulative EoB activities at the top of a mass chain and all subsequent independent EoB activities, these will be later used to report the various cross sections for all observed reaction products and isomeric states.

2.3.3 Proton fluence determination

In addition to the LANSCE-IPF beamline's direct beam current measurements, thin $^{\text{nat}}\text{Al}$ and $^{\text{nat}}\text{Cu}$ foils were included along with the $^{\text{nat}}\text{Nb}$ targets at each energy position, to provide more sensitive beam current monitors. The IAEA-recommended $^{\text{nat}}\text{Al}(p,x)^{22}\text{Na}$, $^{\text{nat}}\text{Al}(p,x)^{24}\text{Na}$, $^{\text{nat}}\text{Cu}(p,x)^{56}\text{Co}$, $^{\text{nat}}\text{Cu}(p,x)^{62}\text{Zn}$, and $^{\text{nat}}\text{Cu}(p,x)^{65}\text{Zn}$ monitor reactions were used for proton fluence measurement [18]. Due to the large energy degradation between the front and back of the target stack, a non-trivial broadening of the proton energy distribution was expected for all monitor and target foils. As a result, the integral form of the well-known activation equation was used to accurately determine proton fluence ($I\Delta t$) in each monitor foil:

$$I\Delta t = \frac{A_0\Delta t}{\rho\Delta r (1 - e^{-\lambda\Delta t}) \int \sigma(E) \frac{d\phi}{dE} dE} \quad (2.3)$$

where A_0 is the EoB activity for the monitor reaction product, I is the proton current, $\rho\Delta r$ is the foil's areal density, λ is the monitor reaction product's decay constant, Δt is the length of irradiation, $\sigma(E)$ is the IAEA recommended cross section at energy E , and $\frac{d\phi}{dE}$ is the differential proton fluence. Using this formalism, the quantified EoB activities for each monitor reaction may be converted into a measured proton fluence at each energy position.

The propagated uncertainty in proton fluence is calculated as the quadrature sum of the uncertainty in quantified EoB activity, uncertainty in the duration of irradiation (conservatively estimated at 60 s, to account for any transient changes in beam current), uncertainty in foil areal density, uncertainty in monitor product half-life (included, but normally negligible), uncertainty in IAEA recommended cross section, and uncertainty in differential proton fluence. Of these, the first four contributions are all easily quantified in the preparation and execution of a stacked target irradiation; the last two contributions prove to be more nuanced, however. The uncertainty in proton fluence for irradiated monitor foils is derived from statistical uncertainty in the modeling of proton transport in the stack irradiation, discussed in subsection 2.3.4. The uncertainty in IAEA recommended cross section values

must be estimated indirectly, as no uncertainty in the recommended cross sections is provided in the current IAEA evaluation. Fortunately, the recommended cross section values for each monitor reaction tend to closely match one of the selected experimental source data sets used in their evaluation. Since these data sets have listed uncertainties in the original manuscripts, uncertainties in IAEA recommended cross section values have been estimated by the uncertainty in the data set most closely matching the IAEA recommended values. For the monitor reactions employed in this work, these data sets are G. Steyn (1990) for ${}^{\text{nat}}\text{Al}(p,x){}^{22}\text{Na}$ [38], M. Uddin (2004) for ${}^{\text{nat}}\text{Al}(p,x){}^{24}\text{Na}$ [39], and S. Mills (1992) for ${}^{\text{nat}}\text{Cu}(p,x){}^{56}\text{Co}$, ${}^{\text{nat}}\text{Cu}(p,x){}^{62}\text{Zn}$, and ${}^{\text{nat}}\text{Cu}(p,x){}^{65}\text{Zn}$ [40].

2.3.4 Proton transport calculations

Initial estimates of the proton beam energy in all foils were calculated using the Anderson & Ziegler (A&Z) stopping power formalism [41–43]. These estimates of average beam energy in each foil are useful for the preliminary stack design. However, for final energy and fluence determinations, a more rigorous method of proton transport modeling is needed. The Monte Carlo N-Particle transport code MCNP6.1 was used for simulation of the full 3-D target stack, including determination of the full proton energy distribution for each stack position [44]. MCNP6 provides a far more robust method of proton transport, as it is able to account for beam losses due to scattering and reactions, as well as production of secondary particles. As it is a Monte Carlo-based code, the uncertainty in energy distribution scales inversely with the number of source protons simulated. 10^8 source protons were used for all simulations, which places the statistical uncertainty in proton energy distributions at less than 0.01%.

The ability to model the full energy distribution in each target position is vital for stacked target irradiations, due to the progressively larger energy straggling towards the rear of the stack. The initial proton beam has a finite energy spread (an approximately 0.1 MeV Gaussian width at 100 MeV), and since stopping power for charged particles is inversely proportional to their energy, the low-energy tail of the energy distribution is degraded more in each stack element than the high-energy tail. This effect compounds towards the rear of the stack, creating a significantly broadened low-energy tail, and a progressively larger net shift of the centroid to a lower energy. To account for this increasing energy uncertainty, a suitably representative energy must be established for each foil in the target stack. In this work, the flux-weighted average proton energy in each foil, $\langle E \rangle$, represents the energy centroid for protons in a target stack component, calculated using the energy distributions $\frac{d\phi}{dE}$ from MCNP6 modeling of proton transport:

$$\langle E \rangle = \frac{\int E \frac{d\phi}{dE} dE}{\int \frac{d\phi}{dE} dE} \quad (2.4)$$

Likewise, to represent the energy uncertainty for each stack position, the full width at half maximum (FWHM) of the MCNP6-modeled energy distribution is chosen for each energy

position reported. While most experimental uncertainties are reported at the 1σ level, the 2.355σ FWHM is used here to ensure at the 98% confidence interval that this width includes the “true” energy centroid value.

The “variance minimization” techniques described by Graves *et al.* have been employed here to further reduce the uncertainty in proton energy assignments [6]. This method is based on the assumption that the independent measurements of proton fluence from the five monitor reactions used in this work should all be consistent at each energy position. If the monitor reaction cross sections and MCNP6-modeled energy distributions are both accurate, disagreement in the observed proton fluences is due to poorly characterized stopping power in simulations, or a systematic error in the areal densities of the stack components [6, 45]. This disagreement is minor at the front of the stack, and gets progressively worse as the beam is degraded, due to the compounded effect of systematic uncertainties in stack areal densities.

Due to the significantly greater areal density of the thick 6061 aluminum degraders as compared to the other stack elements (nominal 3–5 mg/cm², relative to nominal 1000–1400 mg/cm²), the areal density of each of the 6061 aluminum degraders were varied uniformly in MCNP6 simulations by a factor of up to $\pm 25\%$ of nominal values, to find the effective density which minimized variance in the measured proton fluence at the lowest energy position (Al-6, Cu-6). This lowest energy position was chosen as a minimization candidate, as it is most sensitive to systematic uncertainties in stack design. The results of this minimization technique, shown in Figure 2.3, indicate a clear minimum in proton fluence variance for flux-weighted average 41.34 MeV protons entering the last energy position. This is approximately 2 MeV lower than the nominal MCNP6 simulations, and approximately 3 MeV lower than nominal A&Z calculations, both of which used the nominal 2.80 g/cm³ measured density of the 6061 aluminum degraders. This energy corresponds to a 6061 aluminum areal density of 2.52% greater than nominal measurements, and serves as a lump correction for other minor systematic uncertainties in stack design, including stack areal densities and incident beam energy.

The impact of this variance minimization is clearly seen in Figure 2.4. As expected, the 2.52% increase in 6061 aluminum areal density has an almost negligible impact on the higher-energy positions, but causes a progressively larger downshift in proton energies at the later energy positions. In addition, as one moves to the rear positions, the disagreement in the independent proton fluence measurements is reduced. It is worth noting that the proton fluence measured by the $^{nat}\text{Al}(p,x)^{22}\text{Na}$ monitor reaction (threshold 21.0 MeV) is consistently higher in magnitude than all other monitor channels, with an increasing disparity at higher energies. This disparity is due to silicon in the Kapton tape (comprised of a silicone adhesive layer on a polyimide backing) used for sealing the foil packets, making up approximately 10% of the silicone on a stoichiometric basis. The ^{22}Na and ^{24}Na monitor channels can also be populated off of natural silicon (92.2% ^{28}Si), predominantly via $^{28}\text{Si}(p,\alpha 2pn)^{22}\text{Na}$ (threshold 35.3 MeV) and $^{28}\text{Si}(p,4pn)^{24}\text{Na}$ (threshold 44.6 MeV). ^{29}Si and ^{30}Si are also potential targets for $(p,x)^{22,24}\text{Na}$, albeit with higher energetic thresholds and smaller cross sections. The attribution of excess $^{nat}\text{Al}(p,x)^{22,24}\text{Na}$ activity to the silicone adhesive is supported by the observation of ^{22}Na and ^{24}Na activities in all Cu and Nb foil positions. $^{nat}\text{Si}(p,\alpha 2pn)$ is

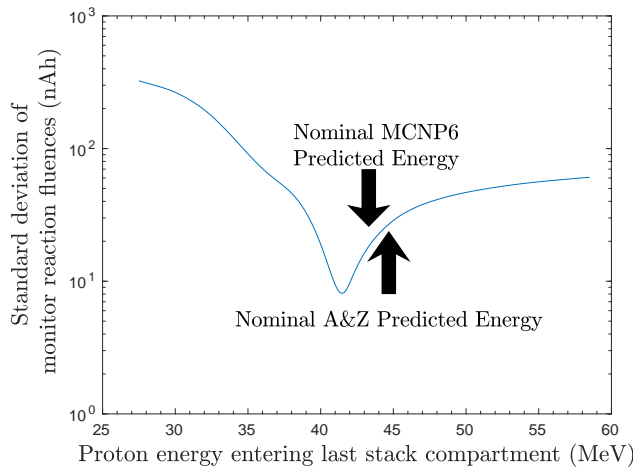


Figure 2.3: Result of the variance minimization performed by adjusting the degrader density in MCNP6 simulations of the target stack. A flux-weighted average proton energy of 41.34 MeV entering the last energy position creates a clear minimum in observed reaction fluence variance, corresponding to an areal density 2.52% greater than nominal. The variance minimum occurring at a lower incident energy than nominal MCNP6 and A&Z calculations indicates that there exists an additional systematic beam degradation not accounted for in modeling of proton transport in the stack design.

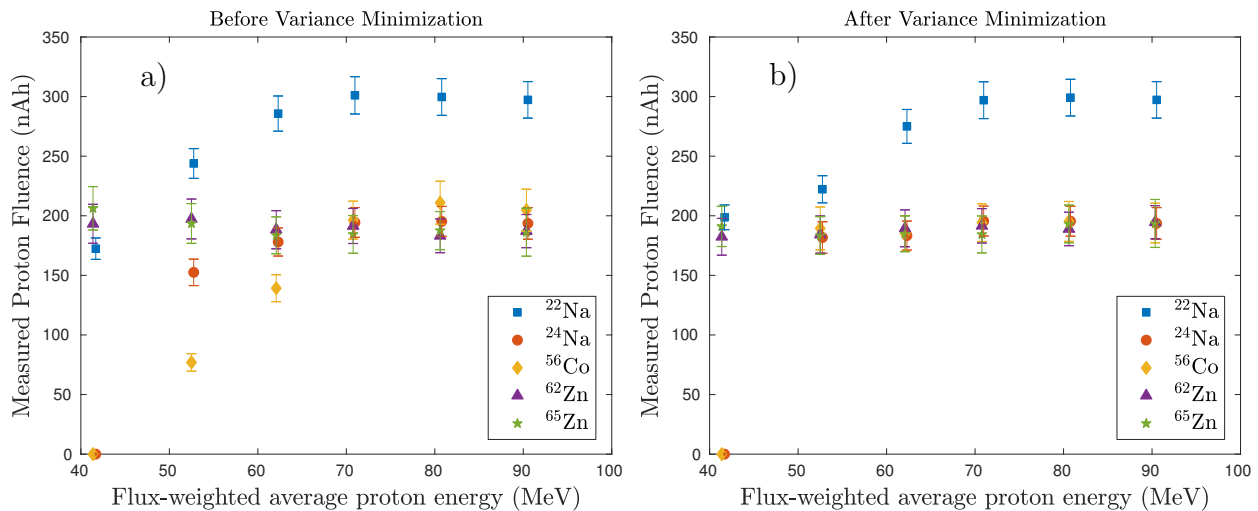


Figure 2.4: Results of variance minimization through enhancement of the effective areal density of the 6061 aluminum degraders by 2.52%. A noticeable reduction of variance in measured proton fluence is seen, particularly at the rear stack positions. Following minimization, additional apparent fluence is observed in the ${}^{\text{nat}}\text{Al}(p,x){}^{22}\text{Na}$ and ${}^{\text{nat}}\text{Al}(p,x){}^{24}\text{Na}$ monitor channels, due to contamination from ${}^{\text{nat}}\text{Si}(p,x){}^{22,24}\text{Na}$ on the silicone adhesive used for sealing foil packets.

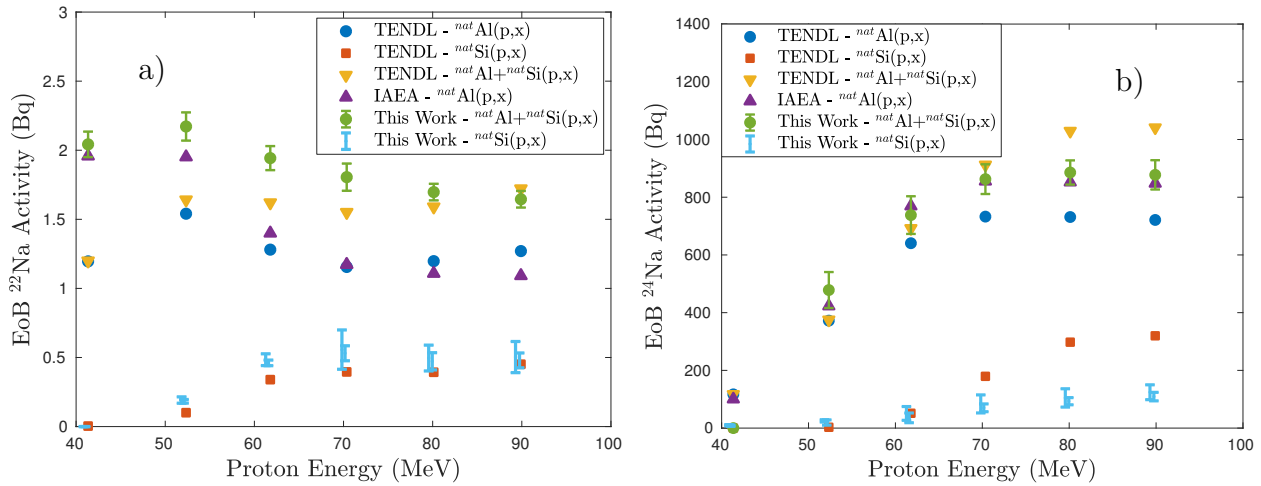


Figure 2.5: Estimates of EoB ${}^{\text{nat}}\text{Al}(\text{p},\text{x})^{22,24}\text{Na}$ and ${}^{\text{nat}}\text{Si}(\text{p},\text{x})^{22,24}\text{Na}$ activities using TENDL-2015 cross sections, in comparison with the IAEA recommended ${}^{\text{nat}}\text{Al}(\text{p},\text{x})^{22,24}\text{Na}$ cross sections. At low energies, experimentally observed apparent ${}^{22,24}\text{Na}$ activities in each Al foil packet are consistent with IAEA recommendations, but diverge at higher energies as the ${}^{\text{nat}}\text{Si}(\text{p},\text{x})^{22}\text{Na}$ exit channels begin to open up. ${}^{22,24}\text{Na}$ activities consistent with TENDL-2015 estimates are observed in each Nb and Cu foil packet as well, confirming that contamination may be attributed to activation of silicone adhesives.

competitive with the ${}^{\text{nat}}\text{Al}(\text{p},\text{x})$ production route, seen when comparing the total measured activities of ${}^{22,24}\text{Na}$ in each Al foil packet, relative to the expected EoB activities for each reaction channel (Figure 2.5). Since no evaluated cross section data exists in this energy region for ${}^{28}\text{Si}(\text{p},\text{x})^{22}\text{Na}$ (and only minimal ${}^{\text{nat}}\text{Si}$ data exists), the TENDL-2015 library is used to estimate the expected relative EoB activities for ${}^{\text{nat}}\text{Al}(\text{p},\text{x})^{22,24}\text{Na}$ and ${}^{\text{nat}}\text{Si}(\text{p},\text{x})^{22,24}\text{Na}$, relative to IAEA recommended ${}^{\text{nat}}\text{Al}(\text{p},\text{x})^{22,24}\text{Na}$ cross sections. Several observations are immediately obvious. At lower energies, the magnitude of ${}^{\text{nat}}\text{Al}(\text{p},\text{x})^{22}\text{Na}$ is large compared to ${}^{\text{nat}}\text{Si}(\text{p},\text{x})^{22}\text{Na}$, which is why the ${}^{\text{nat}}\text{Al}(\text{p},\text{x})^{22}\text{Na}$ monitor agrees in fluence at the 40 (and almost at the 50) MeV position. At higher energies, the apparent ${}^{\text{nat}}\text{Al}(\text{p},\text{x})^{22}\text{Na}$ activity begins to diverge from the IAEA expected activities as ${}^{\text{nat}}\text{Si}(\text{p},\text{x})^{22}\text{Na}$ production begins to open up, which accounts for the nearly 50% apparent excess fluence in ${}^{22}\text{Na}$ between 60–90 MeV. For ${}^{24}\text{Na}$ production, we see similar behavior, with only a minor increase in apparent ${}^{24}\text{Na}$ activity, since the observed ${}^{\text{nat}}\text{Si}(\text{p},\text{x})^{24}\text{Na}$ yield remains consistently low in magnitude. The observed ${}^{24}\text{Na}$ activities also follow the shape of the TENDL-2015 ${}^{\text{nat}}\text{Si}(\text{p},\text{x})^{24}\text{Na}$ yields, albeit smaller in magnitude at the higher energy positions.

There are several important conclusions to be drawn from this simple estimate using the TENDL ${}^{\text{nat}}\text{Si}(\text{p},\text{x})^{22,24}\text{Na}$ yields. The observation of the ${}^{22,24}\text{Na}$ activities in Cu and Nb foils represents an indirect measurement of the ${}^{\text{nat}}\text{Si}(\text{p},\text{x})^{22,24}\text{Na}$ cross sections, but will not be reported due to uncertainties in the areal density of the Si in the adhesive. However,

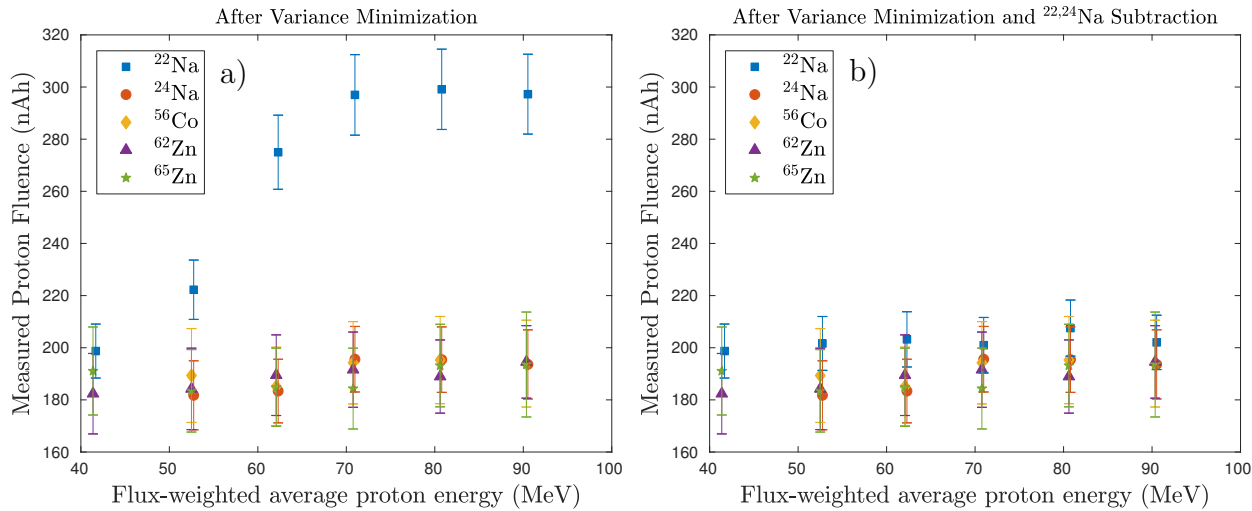


Figure 2.6: The “extra fluence” observed in the $^{\text{nat}}\text{Al}(p,x)^{22}\text{Na}$ and $^{\text{nat}}\text{Al}(p,x)^{24}\text{Na}$ monitor channels is caused by contamination from $^{\text{nat}}\text{Si}(p,x)^{22,24}\text{Na}$ on the silicone adhesive used for sealing foil packets. Following subtraction of $^{22,24}\text{Na}$ activities observed in the silicone adhesive of Nb and Cu foils in the same energy “compartment”, the consistency of the $^{\text{nat}}\text{Al}(p,x)^{22}\text{Na}$ monitor reaction improves dramatically. By excluding these contaminated channels, the remaining 3 independent monitor reactions serve to minimize uncertainty in stack energy assignments and incident fluence.

if we assume a 10% Si stoichiometric basis and an areal density of 4.79 mg/cm^2 (based on bulk density), we can subtract out the measured $^{22,24}\text{Na}$ activity at each Nb and Cu foil position (correcting for the minor difference in proton energy between adjacent foils) from the apparent $^{22,24}\text{Na}$ activities observed in each Al foil packet, in order to obtain the “true” or uncontaminated fluence via the Al monitor reactions, shown in Figure 2.6. Following subtraction, the $^{22,24}\text{Na}$ fluences become more consistent with other monitor reaction channels, though ^{22}Na fluence remains 3–6% higher than the weighted mean of the remaining monitor reaction channels. While the dramatic improvement in monitor reaction consistency builds confidence, in the interest of surety and because they are consistent, only the $^{\text{nat}}\text{Cu}(p,x)^{56}\text{Co}$, $^{\text{nat}}\text{Cu}(p,x)^{62}\text{Zn}$, and $^{\text{nat}}\text{Cu}(p,x)^{65}\text{Zn}$ monitor reaction channels will be used for fluence determination for the reported cross sections. This serves as a pointed example of the importance of selecting monitor reaction products inaccessible through channels aside from the primary reaction ($^{\text{nat}}\text{Al}(p,x)^{22,24}\text{Na}$, in this case), as noted previously.

Using this variance minimized degrader density, the final incident proton energy distributions $\frac{d\phi}{dE}$ from MCNP6 simulation are shown for the six irradiated Nb foils in Figure 2.7. As expected, the energy distribution becomes increasingly more broadened at the lower energy positions, as a result of the beam energy degradation. In addition, as the beam becomes more degraded, the magnitude of the peak of each energy distribution (as well as the integral of each distribution) is reduced, as beam fluence is lost due to scattering, and

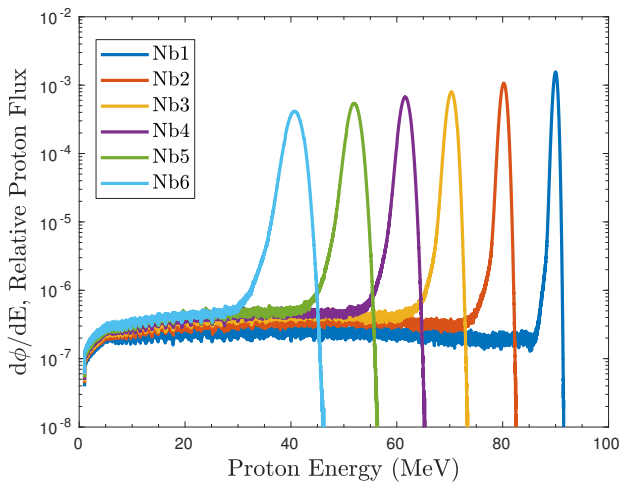


Figure 2.7: Final variance minimized incident proton energy distributions for the Nb foils, as simulated in MCNP6. The distribution tallies in each foil are all normalized to be per source proton, which was 10^8 in all simulations. As the beam is degraded, proton energy distributions become visibly broadened due to straggling, and drop in magnitude due to scattering losses.

the peak-to-low-energy-tail ratio increases as more secondary protons are produced upstream. As with the monitor foils, these distributions were used to calculate the energy centroid (as the flux-weighted average proton energy) and uncertainty (as the FWHM of the distribution) for the final proton energy assignment of each Nb foil.

An enhanced version of the final ${}^{\text{nat}}\text{Cu}(p,x){}^{56}\text{Co}$, ${}^{\text{nat}}\text{Cu}(p,x){}^{62}\text{Zn}$, and ${}^{\text{nat}}\text{Cu}(p,x){}^{65}\text{Zn}$ monitor reaction fluences is shown in Figure 2.8. Without the reliable use of the ${}^{\text{nat}}\text{Al}(p,x){}^{22}\text{Na}$ and ${}^{\text{nat}}\text{Al}(p,x){}^{24}\text{Na}$ monitor channels, local interpolation cannot be used for fluence assignment to the Nb foils, and global interpolation is reliant upon a validated model for fluence loss. The uncertainty-weighted mean for the three ${}^{\text{nat}}\text{Cu}(p,x)$ monitor channels was calculated at each energy position, to determine the final fluence assignments for the Nb and Cu foils. Uncertainty in proton fluence is likewise calculated by error propagation of the fluence values at each energy position. These weighted-mean fluences are plotted in Figure 2.8, along with the estimated fluence according to both MCNP6 transport and an uncertainty-weighted linear χ^2 fit to the individual monitor channel fluence measurements. Both models reproduce the observed fluence data consistently within uncertainty, with the MCNP6 model predicting a slightly greater fluence loss throughout the stack. These models are used purely to provide an extrapolation from the 90 MeV energy position back to the “front” of the stack at 100 MeV, to compare with the nominal fluence measured by IPF upstream current monitors.

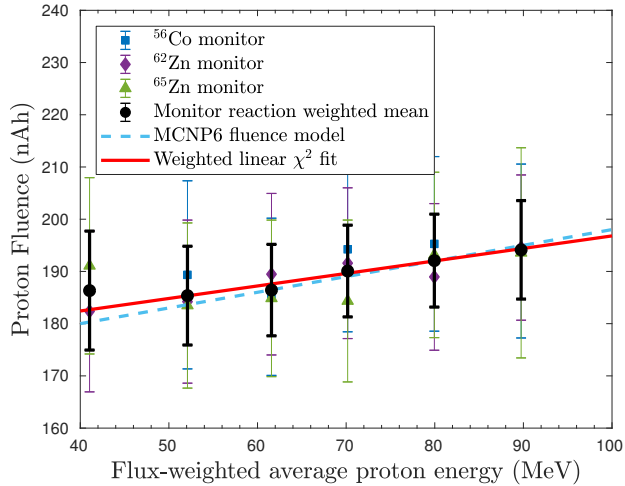


Figure 2.8: Final uncertainty-weighted mean proton fluences throughout the target stack, based on the variance-minimized observed fluence from the the ${}^{\text{nat}}\text{Cu}(\text{p},\text{x})^{56}\text{Co}$, ${}^{\text{nat}}\text{Cu}(\text{p},\text{x})^{62}\text{Zn}$, and ${}^{\text{nat}}\text{Cu}(\text{p},\text{x})^{65}\text{Zn}$ monitor reactions. The fluence drops by approximately 7.2–8.9% from the incident fluence of 196.9–198.8 nAh over the length of the target stack, based on fluence loss models from MCNP6 simulations and an empirical fit to fluence measurements.

2.3.5 Calculation of measured cross sections

Using the quantified EoB activities along with the variance-minimized proton fluence, it is possible to calculate the final cross sections for the various observed $\text{Nb}(\text{p},\text{x})$ reactions. While thin ($\approx 22 \text{ mg/cm}^2$) Nb foils were irradiated to minimize the energy width of these cross section measurements, it is important to note that all cross sections reported here are flux-averaged over the energy distribution subtended by each foil, as seen in Figure 2.7. For both the cumulative and independent activities quantified, cross sections were calculated as:

$$\sigma = \frac{A_0}{\rho \Delta r I (1 - e^{-\lambda \Delta t})} \quad (2.5)$$

where A_0 is the EoB activity for the monitor reaction product, I is the proton current, $\rho \Delta r$ is the foil's areal density, λ is the monitor reaction product's decay constant, and Δt is the length of irradiation. The beam current, measured using an inductive pickup, remained stable for the duration of the irradiation, with the exception of approximately 70 s of downtime, occurring approximately 3 min into irradiation. The propagated uncertainty in cross section is calculated as the quadrature sum of the uncertainty in quantified EoB activity (which includes uncertainty in detector efficiencies), uncertainty in the duration of irradiation (conservatively estimated at 60 s, to account for any transient changes in beam current), uncertainty in foil areal density, uncertainty in monitor product half-life (included, but normally negligible), and uncertainty in proton current (quantified by error propagation of the monitor reaction fluence values at each energy position, as seen in Figure 2.8).

2.4 Results

After irradiation, all foils were confirmed to still be sealed inside their Kapton packets, verifying that no activation products were lost due to packet failure and dispersal. In addition, each activated foil had a small “blister” under the Kapton tape layer, caused by a combination of thermal swelling and the formation of short-lived beta activities. This blister shows the location where the primary proton beam was incident upon the foil. The $^{\text{nat}}\text{Cu}(p,x)^{56}\text{Co}$, $^{\text{nat}}\text{Cu}(p,x)^{62}\text{Zn}$, and $^{\text{nat}}\text{Cu}(p,x)^{65}\text{Zn}$ monitor reactions were used to determine the uncertainty-weighted mean fluence at each energy position (seen in Figure 2.8). A fluence of $198.8 \pm 6.7 \text{ nAh}$ was calculated to be incident upon the target stack using the MCNP6 fluence model, and a fluence of $196.9 \pm 11.3 \text{ nAh}$ using the linear fit model, both of which are consistent with the nominal fluence of 205.9 nAh based on IPF upstream current monitors. As fluence loss in the target box’s entrance window scales with $\sigma_{\text{tot}}\rho\Delta r$, it is expected that an extrapolation back to the stack entrance will underestimate the nominal fluence incident upon the box. This incident fluence dropped by approximately 8.9% to $180.9 \pm 5.4 \text{ nAh}$ (and by 7.2% to $182.7 \pm 13.5 \text{ nAh}$ using the linear fit model) over the length of the target stack, which is consistent with similar measurements at IPF in the past [6]. This loss of fluence is due to a combination of (p,x) reactions throughout the target stack, as well as large-angle deflections (primarily in the aluminum degraders) from scattering of the beam.

Using the final proton fluence at each energy position, cross sections for ^{51}Cr , ^{52g}Mn , ^{52m}Mn , ^{54}Mn , ^{55}Co , ^{56}Ni , ^{57}Ni , ^{57}Co , ^{58g}Co , ^{58m}Co , ^{59}Fe , ^{60}Co , ^{61}Cu , and ^{64}Cu were extracted for (p,x) reactions on $^{\text{nat}}\text{Cu}$ foils in the 40–90 MeV region, as recorded in Table 2.2. For (p,x) reactions on $^{\text{nat}}\text{Nb}$ foils, the (p,x) cross sections for ^{82m}Rb , ^{83}Sr , ^{85g}Y , ^{85m}Y , ^{86}Zr , ^{86}Y , ^{87}Zr , ^{87g}Y , ^{87m}Y , ^{88}Zr , ^{88}Y , ^{89g}Nb , ^{89m}Nb , ^{89}Zr , ^{90}Mo , ^{90}Nb , ^{91m}Nb , ^{92m}Nb , and ^{93m}Mo were extracted, as recorded in Table 2.3. In addition, as there exist a number of isomers with radioactive ground states in these mass regions, independent measurements of isomer-to-ground-state branching ratios for $^{52m/g}\text{Mn}$, $^{58m/g}\text{Co}$, $^{85m/g}\text{Y}$, $^{87m/g}\text{Y}$, and $^{89m/g}\text{Nb}$ were extracted and are recorded in Table 2.4. Comparisons of the measured cross sections and isomer branching ratios with literature data (retrieved from EXFOR [46]) are seen in the figures of 2.7 and 2.8. The propagated uncertainty in these cross sections varies widely based on the reaction product in question, with the major components arising from uncertainty in EoB activity ($\pm 3\text{--}7\%$), proton fluence ($\pm 4\text{--}6\%$), and foil areal density ($\pm 0.1\text{--}0.6\%$).

These results have several notable features. The various $^{\text{nat}}\text{Cu}(p,x)$ cross sections measured here are in excellent agreement with the body of measurements in the literature, but have been measured nearly exclusively with the highest precision to date. Similarly, the various $^{\text{nat}}\text{Nb}(p,x)$ cross sections measured here are in excellent agreement with literature data, which is far more sparse in the 40–90 MeV region than for $^{\text{nat}}\text{Cu}(p,x)$ — fewer than three existing measurements have been performed for the majority of the reactions presented here. Indeed, the $^{\text{nat}}\text{Nb}(p,x)^{83}\text{Sr}$, $^{\text{nat}}\text{Nb}(p,x)^{85}\text{Y}$, $^{\text{nat}}\text{Nb}(p,x)^{89}\text{Nb}$, $^{\text{nat}}\text{Nb}(p,x)^{90}\text{Mo}$, $^{\text{nat}}\text{Nb}(p,x)^{91m}\text{Nb}$, and $^{\text{nat}}\text{Nb}(p,x)^{98m}\text{Mo}$ reactions each possess no more than a total of three data points in this energy region. Not only do the $^{\text{nat}}\text{Nb}(p,x)$ measurements in this work fill in the sparse data in this energy region, but they have been measured with the highest precision relative to

Table 2.2: Measured cross sections for the various $^{\text{nat}}\text{Cu}(p,x)$ reaction products observed in this work. Cumulative cross sections are designated as σ_c , independent cross sections are designated as σ_i .

E_p (MeV)	Production cross section (mb)					
	$89.74^{+0.48}_{-0.43}$	$79.95^{+0.67}_{-0.64}$	$70.17^{+0.91}_{-0.85}$	$61.58^{+1.03}_{-0.98}$	$52.10^{+1.25}_{-1.20}$	$41.05^{+1.62}_{-1.54}$
$^{51}\text{Cr}(\sigma_c)$	0.919 ± 0.079	0.373 ± 0.023	0.450 ± 0.028	0.303 ± 0.016	—	—
$^{52}\text{Mn}(\sigma_c)$	1.70 ± 0.11	0.570 ± 0.031	0.0407 ± 0.0022	0.00526 ± 0.00057	—	—
$^{52g}\text{Mn}(\sigma_i)$	0.673 ± 0.043	0.239 ± 0.018	0.0164 ± 0.0023	0.000986 ± 0.000053	—	—
$^{52m}\text{Mn}(\sigma_c)$	1.023 ± 0.091	0.331 ± 0.030	0.0244 ± 0.0036	0.00427 ± 0.00052	—	—
$^{54}\text{Mn}(\sigma_i)$	5.87 ± 0.37	3.77 ± 0.21	4.14 ± 0.22	4.84 ± 0.26	1.680 ± 0.091	—
$^{55}\text{Co}(\sigma_c)$	1.71 ± 0.11	1.015 ± 0.058	0.193 ± 0.012	0.0299 ± 0.0028	0.00235 ± 0.00022	—
$^{56}\text{Ni}(\sigma_c)$	0.0806 ± 0.0051	0.1005 ± 0.0055	0.0906 ± 0.0046	0.0304 ± 0.0016	—	—
$^{57}\text{Ni}(\sigma_c)$	1.465 ± 0.093	1.202 ± 0.065	1.400 ± 0.071	2.13 ± 0.11	1.565 ± 0.083	0.0262 ± 0.0015
$^{57}\text{Co}(\sigma_i)$	40.1 ± 2.5	35.6 ± 1.9	35.8 ± 1.8	48.5 ± 2.5	47.7 ± 2.5	3.21 ± 0.18
$^{58}\text{Co}(\sigma_c)$	57.7 ± 4.5	55.0 ± 4.7	42.7 ± 3.4	33.7 ± 2.8	39.0 ± 3.8	62.3 ± 4.6
$^{58g}\text{Co}(\sigma_i)$	14.0 ± 2.5	10.8 ± 2.1	6.1 ± 1.6	7.8 ± 1.4	7.1 ± 1.7	1.12 ± 0.32
$^{58m}\text{Co}(\sigma_i)$	43.6 ± 3.7	44.2 ± 4.3	36.6 ± 3.0	25.8 ± 2.5	31.9 ± 3.3	61.1 ± 4.6
$^{59}\text{Fe}(\sigma_c)$	0.865 ± 0.057	0.837 ± 0.046	0.749 ± 0.039	0.616 ± 0.034	0.209 ± 0.014	—
$^{60}\text{Co}(\sigma_c)$	13.23 ± 0.87	13.47 ± 0.78	11.14 ± 0.94	11.44 ± 0.80	9.30 ± 0.87	6.6 ± 1.1
$^{61}\text{Cu}(\sigma_c)$	50.5 ± 3.3	56.1 ± 3.2	65.1 ± 3.6	72.2 ± 4.0	80.6 ± 4.7	157.1 ± 8.6
$^{64}\text{Cu}(\sigma_i)$	38.7 ± 2.7	42.8 ± 2.4	45.5 ± 2.7	50.2 ± 2.8	55.7 ± 3.0	63.3 ± 3.6

existing literature data.

This work presents the first measurements of several observables in this mass region, including the $^{\text{nat}}\text{Nb}(p,x)^{82m}\text{Rb}$ reaction in the 40–90 MeV region, the independent cross section for $^{\text{nat}}\text{Cu}(p,x)^{52g}\text{Mn}$, and the ^{52m}Mn (2^+) / ^{52g}Mn (6^+) isomer branching ratio via $^{\text{nat}}\text{Cu}(p,x)$. The cumulative cross sections from these data are also consistent with existing measurements of the cumulative $^{\text{nat}}\text{Cu}(p,x)^{52}\text{Mn}$ cross section. Similarly, this work offers the first measurement of the independent cross sections for $^{\text{nat}}\text{Nb}(p,x)^{85g}\text{Y}$, as well as the first measurement of the ^{85m}Y ($9/2^+$) / ^{85g}Y ($1/2^-$) isomer branching ratio via $^{\text{nat}}\text{Nb}(p,x)$.

Notably, this work is the most well-characterized measurement of the $^{\text{nat}}\text{Nb}(p,x)^{90}\text{Mo}$ reaction below 100 MeV to date, with cross sections measured at the 4–6% uncertainty level. This is important, as it presents the first step towards characterizing this reaction for use as a proton monitor reaction standard below 100 MeV. $^{\text{nat}}\text{Nb}(p,x)^{90}\text{Mo}$ can only be populated through the (p,4n) reaction channel, so no corrections for (n,x) contamination channels or decay down the A=90 isobar are needed. ^{90}Mo possesses seven strong, distinct gamma lines which can easily be used for its identification and quantification. Finally, the production of ^{90}Mo in the 40–90 MeV region is quite strong, with a peak cross section of approximately 120 mb. Combining the reaction yield and gamma abundance, the use of approximately 23 mg/cm² Nb targets easily provided sufficient counting statistics for activity quantification in the 40–90 MeV region. This result presents the first step towards the use of ^{90}Mo as a clean and precise charged particle monitor reaction standard in irradiations up to approximately 24 h in duration.

In addition to the $^{\text{nat}}\text{Nb}(p,x)^{90}\text{Mo}$ measurement, this experiment has also yielded mea-

Table 2.3: Measured cross sections for the various $^{\text{nat}}\text{Nb}(p,x)$ reaction products observed in this work. Cumulative cross sections are designated as σ_c , independent cross sections are designated as σ_i .

E_p (MeV)	Production cross section (mb)					
	$89.37_{-0.45}^{+0.47}$	$79.55_{-0.64}^{+0.68}$	$69.70_{-0.85}^{+0.90}$	$61.07_{-0.98}^{+1.05}$	$51.51_{-1.21}^{+1.25}$	$40.34_{-1.55}^{+1.58}$
^{82m}Rb (σ_c)	2.48 ± 0.22	—	—	—	—	—
^{83}Sr (σ_c)	4.02 ± 0.61	4.78 ± 0.42	3.49 ± 0.36	—	—	—
^{85}Y (σ_c)	13.78 ± 0.55	7.52 ± 0.51	2.11 ± 0.14	—	—	—
^{85g}Y (σ_i)	2.37 ± 0.11	2.08 ± 0.17	0.557 ± 0.037	—	—	—
^{85m}Y (σ_i)	11.41 ± 0.54	5.44 ± 0.48	1.55 ± 0.13	—	—	—
^{86}Zr (σ_c)	12.68 ± 0.68	18.21 ± 0.93	19.28 ± 0.97	6.16 ± 0.32	—	—
^{86}Y (σ_i)	33.4 ± 1.8	41.6 ± 2.2	39.9 ± 2.1	13.56 ± 0.72	—	—
^{87}Zr (σ_c)	47.4 ± 7.3	28.0 ± 2.8	32.2 ± 2.9	49.8 ± 5.0	38.2 ± 3.7	1.12 ± 0.17
^{87}Y (σ_i)	110.0 ± 7.2	54.7 ± 2.8	61.0 ± 2.9	90.0 ± 4.9	67.2 ± 3.6	2.91 ± 0.17
^{87g}Y (σ_i)	28.0 ± 5.8	7.4 ± 1.3	6.55 ± 0.64	5.8 ± 2.2	2.63 ± 0.47	0.942 ± 0.073
^{87m}Y (σ_i)	82.0 ± 4.3	47.3 ± 2.5	54.4 ± 2.8	84.2 ± 4.4	64.6 ± 3.6	1.97 ± 0.15
^{88}Zr (σ_c)	159.1 ± 7.8	144.6 ± 6.8	62.4 ± 3.1	21.2 ± 1.0	33.6 ± 1.8	65.3 ± 4.0
^{88}Y (σ_i)	17.2 ± 1.1	13.27 ± 0.86	7.98 ± 0.72	2.91 ± 0.25	9.2 ± 1.4	9.88 ± 0.69
^{89}Nb (σ_c)	—	—	179 ± 14	214.4 ± 9.8	—	—
^{89g}Nb (σ_i)	—	—	145 ± 14	186.4 ± 9.6	—	—
^{89m}Nb (σ_i)	—	—	34.7 ± 2.6	28.0 ± 2.0	—	—
^{89}Zr (σ_i)	211 ± 11	243 ± 13	294 ± 15	257 ± 13	55.4 ± 3.0	15.5 ± 1.0
^{90}Mo (σ_i)	21.3 ± 1.1	26.4 ± 1.3	34.5 ± 1.6	61.9 ± 3.1	122.0 ± 6.1	24.2 ± 1.5
^{90}Nb (σ_i)	158.3 ± 8.1	174.9 ± 8.5	209.3 ± 9.9	272 ± 14	369 ± 19	163.9 ± 9.8
^{91m}Nb (σ_c)	—	—	—	—	—	66.5 ± 5.8
^{92m}Nb (σ_i)	43.7 ± 2.4	47.3 ± 2.4	49.8 ± 2.6	52.9 ± 2.8	55.3 ± 3.1	59.9 ± 3.9
^{93m}Mo (σ_i)	0.97 ± 0.20	1.29 ± 0.15	1.62 ± 0.24	1.85 ± 0.15	1.86 ± 0.14	2.00 ± 0.15

 Table 2.4: Measured isomer-to-ground-state branching ratios for the various $^{\text{nat}}\text{Nb}(p,x)$ and $^{\text{nat}}\text{Cu}(p,x)$ reaction products observed in this work.

E_p (MeV)	Isomer branching ratio					
	$89.74_{-0.43}^{+0.48}$	$79.95_{-0.64}^{+0.67}$	$70.17_{-0.85}^{+0.91}$	$61.58_{-0.98}^{+1.03}$	$52.10_{-1.20}^{+1.25}$	$41.05_{-1.54}^{+1.62}$
$^{\text{nat}}\text{Cu}(p,x)^{52}\text{Mn}$	0.603 ± 0.066	0.581 ± 0.062	0.598 ± 0.095	0.81 ± 0.13	—	—
$^{\text{nat}}\text{Cu}(p,x)^{58}\text{Co}$	0.757 ± 0.088	0.80 ± 0.10	0.858 ± 0.099	0.767 ± 0.097	0.82 ± 0.12	0.98 ± 0.10
E_p (MeV)	$89.37_{-0.45}^{+0.47}$	$79.55_{-0.64}^{+0.68}$	$69.70_{-0.85}^{+0.90}$	$61.07_{-0.98}^{+1.05}$	$51.51_{-1.21}^{+1.25}$	$40.34_{-1.55}^{+1.58}$
$^{\text{nat}}\text{Nb}(p,x)^{85}\text{Y}$	0.828 ± 0.051	0.724 ± 0.080	0.736 ± 0.080	—	—	—
$^{\text{nat}}\text{Nb}(p,x)^{87}\text{Y}$	0.746 ± 0.063	0.865 ± 0.063	0.893 ± 0.063	0.936 ± 0.070	0.961 ± 0.075	0.676 ± 0.065
$^{\text{nat}}\text{Nb}(p,x)^{89}\text{Nb}$	—	—	0.193 ± 0.021	0.130 ± 0.011	—	—

surements of a number of additional emerging radionuclides with medical applications. These include the non-standard positron emitters ^{57}Ni [6, 47–49], ^{64}Cu [50–57], ^{86}Y [30, 31, 58–66], ^{89}Zr [67–71], ^{90}Nb [72, 73], and the Auger-therapy agent $^{82\text{m}}\text{Rb}$ [74, 75]. Production of these radionuclides offers no major advantages over established pathways, with the generally lower yields and radioisotopic purities failing to justify the convenience of natural targets via $^{\text{nat}}\text{Cu}(\text{p},\text{x})$ and $^{\text{nat}}\text{Nb}(\text{p},\text{x})$. The one possible exception to this trend is the non-standard positron emitter ^{57}Ni ($t_{1/2} = 35.60 \pm 0.06$ h, $\epsilon=100\%$ to ^{57}Co [76]) — the $^{57}\text{Ni}/^{56}\text{Ni}$ ratio of production rates is approximately 290 at 61.58 MeV, and varies from 45–75 at the 70–90 MeV positions. This $^{\text{nat}}\text{Cu}(\text{p},\text{x})$ route offers both higher yield and higher radioisotopic purity over the established $^{\text{nat}}\text{Co}(\text{p},3\text{n})$ pathway, which suffers from approximately fivefold greater ^{56}Ni contamination [77, 78].

We wish to urge caution in future stacked-target activation experiments by avoiding the use of silicone adhesive-based tapes for foil containment, especially when paired with the use of Al monitor foils. Acrylic-based tape options are commercially available, and are immune from (p,x) production of $^{22,24}\text{Na}$ activities, due to being of too low-Z for these reaction channels to be possible. Even with subtraction of $^{22,24}\text{Na}$ activities though irradiating a Kapton tape “blank” or similar, we observe the Al monitor channels to measure consistently higher proton fluence than via Cu monitor channels, by 5–8%. If Al monitors are used in conjunction with silicone-based tapes, even with subtraction of excess ^{22}Na activities, a systematically enhanced fluence may be determined, leading to cross sections reported with inaccurately diminished magnitude. Furthermore, since data for monitor reactions are often self-referencing, the propagated impact of this systematic enhancement in fluence may have far-reaching consequences for both medical isotope production, as well as for the evaluated nuclear data libraries, which use these proton activation experiments as input.

As mentioned before, cumulative cross sections are reported here for the first observable product nuclei in a mass chain, or whenever it is impossible to use decay spectrometry to distinguish direct production of a nucleus from decay feeding. For all remaining observed reaction products in the mass chain, and cases where no decay precursors exist, independent cross sections are reported, allowing for determination of the direct production via subtraction. This, in turn, offers the opportunity to gauge the predictive capabilities of modern nuclear models used in the reaction evaluation process. The reaction channels with independent cross sections were compared to calculations with the reaction modeling codes EMPIRE, TALYS, and CoH, run with the default settings. The default optical models and E1 gamma strength function models for each code are presented in Table 2.5. The large energy range covered by many of the exit channels, which extends significantly beyond the range of pure compound nuclear/evaporation, allows the data to be used to study the differences between these modeling codes in the pre-equilibrium regime.

The default level density in both CoH and TALYS is the Gilbert-Cameron model, which uses a Constant Temperature model below a critical energy and Fermi Gas model above it. The default level density in EMPIRE is the Enhanced Generalized Superfluid Model (EGSM) which uses the Generalized Superfluid model below a critical energy, and Fermi Gas model above it [79]. The EGSM densities are normalized to D_0 and the discrete levels, but in such a

Table 2.5: Default settings for the reactions codes

<u>Code Version</u>	<u>Proton/Neutron Optical Model</u>	<u>Alpha Optical Model</u>	<u>E1 γSF Model</u>
EMPIRE-3.2.3[80]	Koning-Delaroche[81]	Avrigeanu(2009)[82]	Modified Lorentzian[83]
TALYS-1.8[84]	Koning-Delaroche	Specific folded potential[84]	Brink-Axel Lorentzian[84]
CoH-3.5.1[85, 86]	Koning-Delaroche	Avrigeanu(1994)[87]	Generalized Lorentzian[85, 86]

way that only the level density below the neutron separation energy is effected by the discrete levels chosen for the normalization. All three codes use a two-exciton phenomenological model to calculate the pre-equilibrium cross section, but the specific implementation differs between the codes.

Given the large number of exit channels in this data set, we will limit our discussion to cross sections for the production of a specific residual nucleus with experimental data through the full rise and fall of the peak, and at least 1% of the total reaction cross section. Exit channel cross sections that do not exhibit the full rise and fall of the peak, which is identified as being dominated by the formation of a compound nucleus, do not provide enough information to analyze the calculations. Residual nuclei like ^{88}Zr that can be produced by multiple reaction channels, such as $(\text{p},\alpha 2\text{n})$ and by $(\text{p},2\text{p}4\text{n})$ are also not discussed in depth. We exclude reactions with cross sections with peak values less than 1% of the total reaction cross section because their behavior is extremely sensitive to more dominant channels. The three residual nuclei that meet all of the above criteria for which there is an independent measurement of the residual production cross section are ^{86}Y , ^{90}Mo , and ^{90}Nb .

The $^{93}\text{Nb}(\text{p},\alpha\text{p}3\text{n})^{86}\text{Y}$ reaction channel, which peaks at approximately 70 MeV, is well within the compound regime for the entire energy region of this experiment (Figure 2.9). The data collected on this residual is consistent with the one other data set available, taken in 1997 by Michel *et al.* [77]. The $^{93}\text{Nb}(\text{p},4\text{n})^{90}\text{Mo}$ and $^{93}\text{Nb}(\text{p},\text{p}3\text{n})^{90}\text{Nb}$ channels both peak early in the energy region, around 50 MeV, and the data clearly show the full rise, peak, and fall of the compound cross section (Figure 2.10 & 2.11). In both of these channels, this data is consistent with the data by Titarenko *et al.* in 2011 [75].

The ^{90}Nb production cross section exhibits a persistent pre-equilibrium “tail” that keeps the channel open well after the compound cross section has fallen away. TALYS, TENDL, and CoH seem to have the correct shape for this pre-equilibrium cross section, with magnitudes that are just slightly too low. EMPIRE, however, does not level off as much as the data and the other codes are seen to, and misses the high-energy data points.

In all three channels, the TALYS, TENDL, and CoH calculations rise, peak, and fall at lower energies than the data, while EMPIRE calculates the peak to occur at higher energies. For ^{90}Mo , the EMPIRE peak is representative of the data. For ^{86}Y and ^{90}Nb , the peak is missed by all three of the codes.

The magnitudes of the TALYS and TENDL calculations are consistently too low in the three channels studied here. For ^{86}Y , CoH and EMPIRE also predict smaller cross sections than the data would suggest, which may be influenced by incorrect modeling of other, stronger, channels. The magnitude of the peak in the CoH calculation for ^{90}Mo is consistent with the

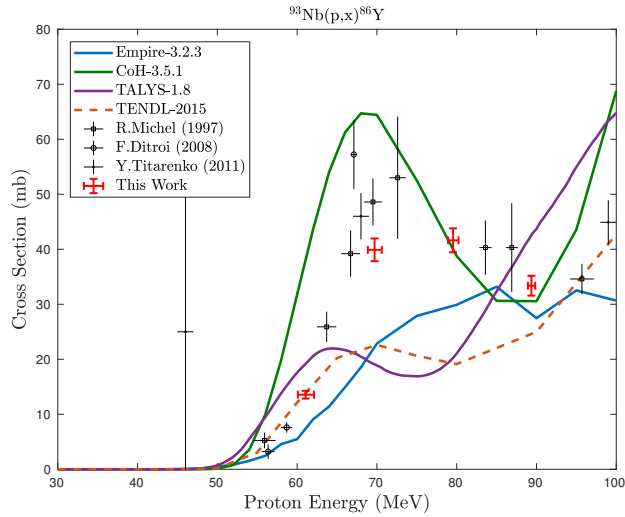


Figure 2.9: Measured $^{93}\text{Nb}(p,x)^{86}\text{Y}$ cross section, with the $^{93}\text{Nb}(p,\alpha p3n)^{86}\text{Y}$ reaction channel visibly peaking at approximately 70 MeV.

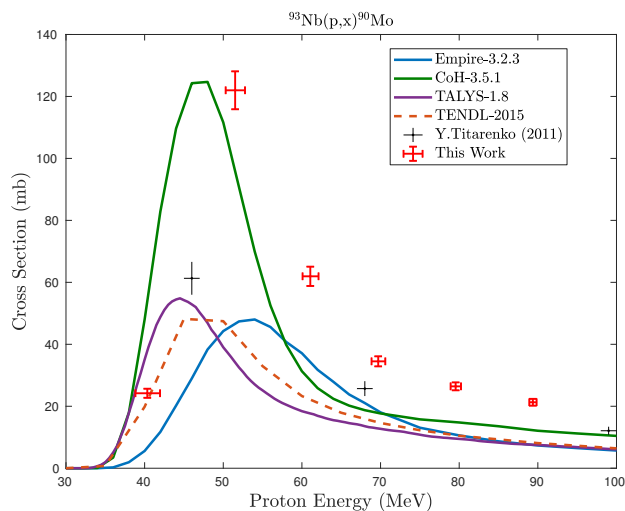


Figure 2.10: Measured $^{93}\text{Nb}(p,x)^{90}\text{Mo}$ cross section, with the $^{93}\text{Nb}(p,4n)^{90}\text{Mo}$ reaction channel visibly peaking at approximately 50 MeV.

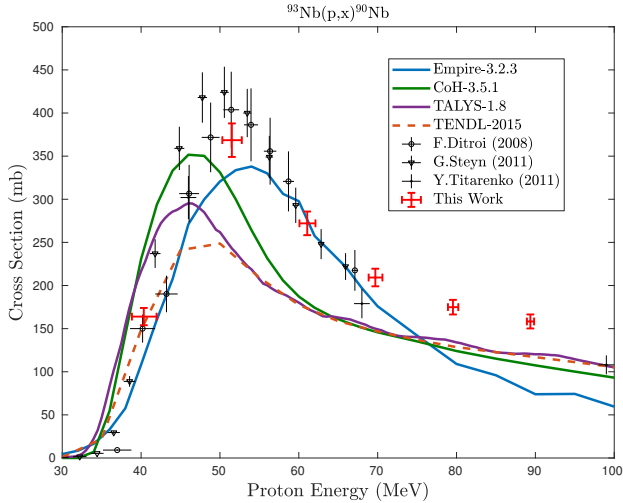


Figure 2.11: Measured $^{93}\text{Nb}(p,x)^{90}\text{Nb}$ cross section, with the $^{93}\text{Nb}(p,p3n)^{90}\text{Nb}$ reaction channel visibly peaking at approximately 50 MeV.

data, while EMPIRE predicts a cross section that is approximately the same magnitude as that of TALYS. ^{90}Nb is one of the strongest measured channels, approximately 10% of the total reaction cross section, and the values from the three codes are all consistent, but too small, in magnitude.

2.5 Conclusions

We present here a set of measurements of 38 cross sections for the $^{\text{nat}}\text{Nb}(p,x)$ and $^{\text{nat}}\text{Cu}(p,x)$ reactions between 40–90 MeV, as well as independent measurements of five isomer branching ratios. Nearly all cross sections have been reported with higher precision than previous measurements. We report the first measurements of the $^{\text{nat}}\text{Nb}(p,x)^{82\text{m}}\text{Rb}$ reaction, as well as the first measurement of the independent cross sections for $^{\text{nat}}\text{Cu}(p,x)^{52\text{m}}\text{Mn}$, $^{\text{nat}}\text{Cu}(p,x)^{52\text{g}}\text{Mn}$, and $^{\text{nat}}\text{Nb}(p,x)^{85\text{g}}\text{Y}$ in the 40–90 MeV region. We advise that future activation experiments avoid the use of silicone-based adhesives, particularly in conjunction with aluminum monitor foils, to avoid reporting an enhanced fluence due to $^{22,24}\text{Na}$ contamination. We also use these measurements to illustrate the deficiencies in the current state of reaction modeling for 40–90 MeV $^{\text{nat}}\text{Nb}(p,x)$ and $^{\text{nat}}\text{Cu}(p,x)$ reactions. Finally, this work provides another example of the usefulness of the recently-described variance minimization techniques for reducing energy uncertainties in stacked target charged particle irradiation experiments.

2.6 Decay data

The lifetimes and gamma-ray branching ratios listed in these tables were used for all calculations of measured cross sections reported in this work, and have been taken from the most recent edition of Nuclear Data Sheets for each mass chain [5, 24, 27–31, 76, 88–105].

Table 2.6: Decay data for gamma-rays observed in $^{\text{nat}}\text{Al}(\text{p},\text{x})$ and $^{\text{nat}}\text{Cu}(\text{p},\text{x})$.

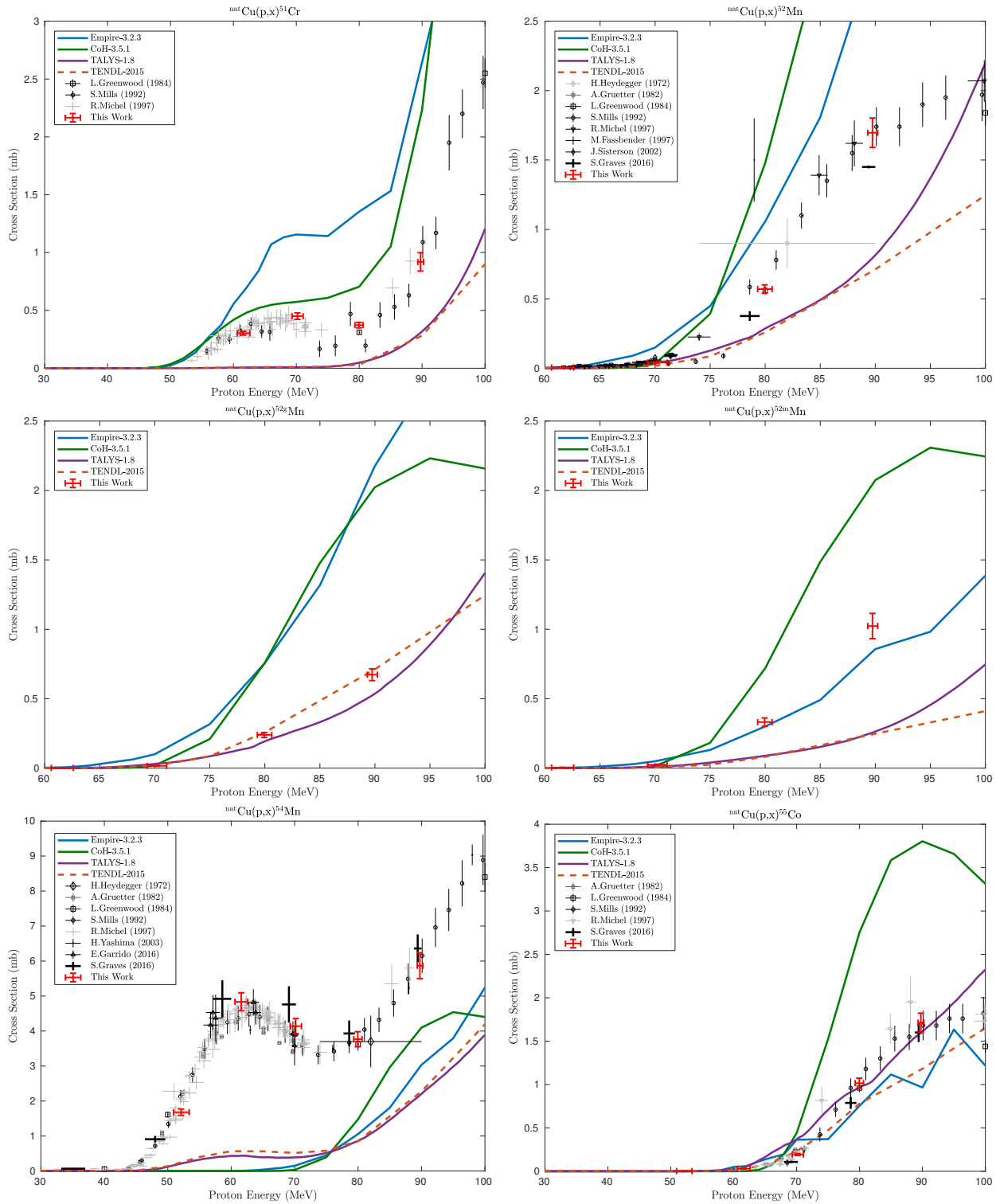
Nuclide	Half-life	E_{γ} (keV)	I_{γ} (%)
^{22}Na	2.6018(22) y	1274.537	99.940(14)
^{24}Na	14.997(12) h	1368.626	99.9936(15)
^{51}Cr	27.704(3) d	320.0824	9.910(10)
^{52m}Mn	21.1(2) m	1434.0600	98.2(5)
^{52}Mn	5.591(3) d	744.233	90.0(12)
	5.591(3) d	935.544	94.5(13)
	5.591(3) d	1246.278	4.21(7)
	5.591(3) d	1434.092	100.0(14)
^{54}Mn	312.20(20)	834.848	99.9760(10)
^{55}Co	17.53(3) h	477.2	20.2(17)
	17.53(3) h	931.1	75.0(35)
	17.53(3) h	1316.6	7.1(3)
	17.53(3) h	1408.5	16.9(8)
^{56}Ni	6.075(10) d	158.38	98.8(10)
	6.075(10) d	269.50	36.5(8)
	6.075(10) d	480.44	36.5(8)
	6.075(10) d	749.95	49.5(12)
	6.075(10) d	811.85	86.0(9)
	6.075(10) d	1561.80	14.0(6)
^{56}Co	77.236(26) d	846.770	99.9399(2)
	77.236(26) d	1037.843	14.05(4)
	77.236(26) d	1238.288	66.46(12)
	77.236(26) d	1360.212	4.283(12)
	77.236(26) d	1771.357	15.41(6)
^{57}Ni	35.60(6) h	127.164	16.7(5)
	35.60(6) h	1377.63	81.7(24)
	35.60(6) h	1757.55	5.75(20)
	35.60(6) h	1919.52	12.3(4)
^{57}Co	271.74(6) d	122.06065	85.60(17)
	271.74(6) d	136.47356	10.68(8)
^{58}Co	70.86(6) d	810.7593	99.450(10)
	70.86(6) d	863.951	0.686(10)
^{59}Fe	44.495(9) d	1099.245	56.5(18)
	44.495(9) d	1291.590	43.2(14)
^{60}Co	5.2714(5) y	1173.228	99.85(3)
	5.2714(5) y	1332.492	99.9826(6)
^{61}Cu	3.339(8) h	282.956	12.2(2.2)
	3.339(8) h	373.050	2.1(4)
	3.339(8) h	656.008	10.8(20)
	3.339(8) h	1185.234	3.7(7)
^{62}Zn	9.193(15) h	243.36	2.52(23)
	9.193(15) h	246.95	1.90(18)
	9.193(15) h	260.43	1.35(13)
	9.193(15) h	394.03	2.24(17)
	9.193(15) h	548.35	15.3(14)
	9.193(15) h	596.56	26.0(20)
^{64}Cu	12.701(2) h	1345.77	0.475(11)
^{65}Zn	243.93(9) d	1115.539	50.04(10)

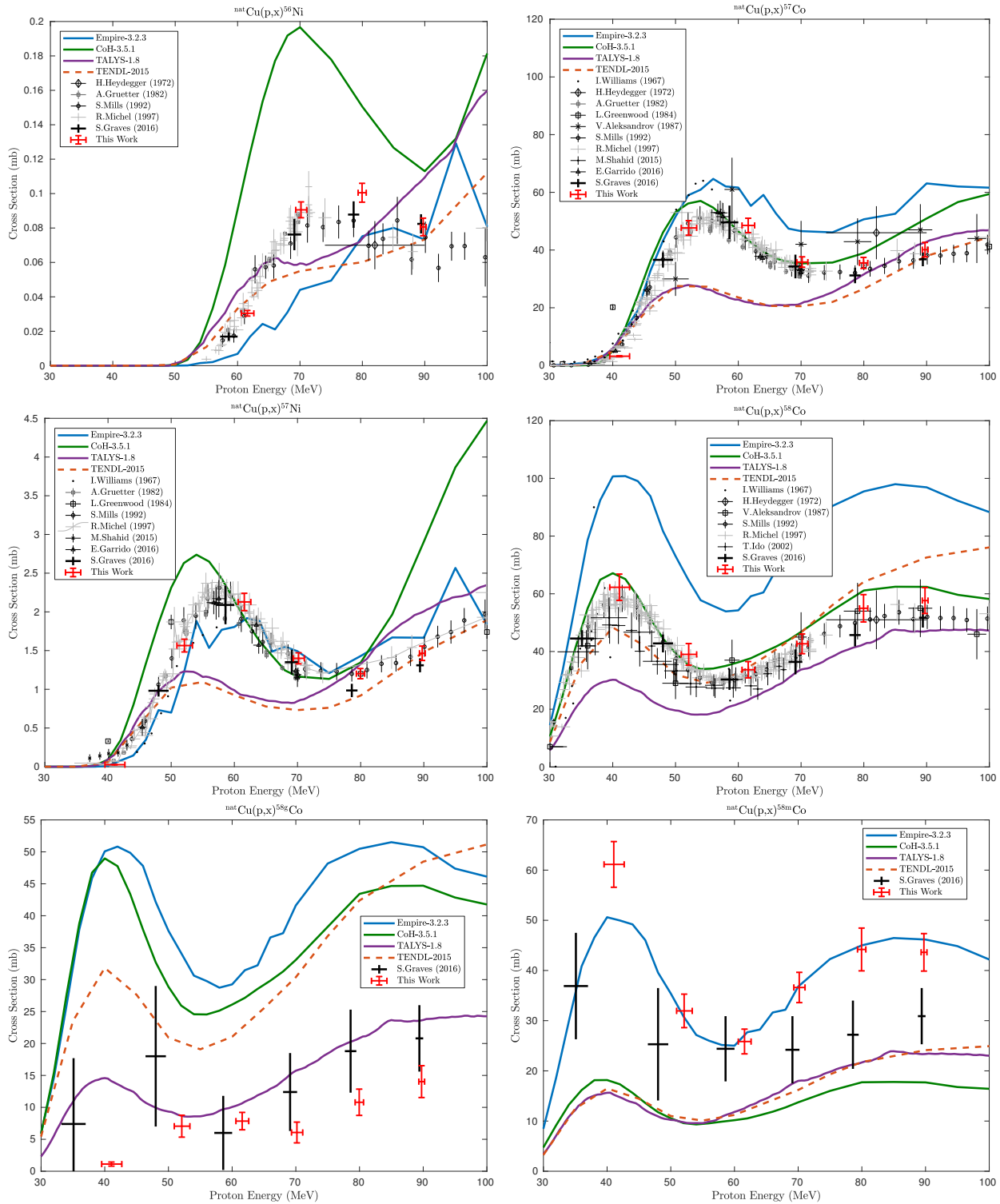
Table 2.7: Decay data for gamma-rays observed in $^{\text{nat}}\text{Nb}(p,x)$.

Nuclide	Half-life	E_{γ} (keV)	I_{γ} (%)
^{82m}Rb	6.472(6) h	554.35	62.4(9)
	6.472(6) h	619.11	37.98(9)
	6.472(6) h	776.52	84.39(21)
	6.472(6) h	1044.08	32.07(8)
	32.41(3) h	418.37	4.2(3)
^{83}Sr	32.41(3) h	762.65	26.7(22)
	32.41(3) h	231.7	22.8(22)
^{85m}Y	4.86(13) h	231.7	22.8(22)
	2.68(5) h	231.65	84(9)
^{85}Y	2.68(5) h	913.89	9.0(9)
	16.5(1) h	242.8	95.84(2)
^{86}Zr	16.5(1) h	612.0	5.8(3)
	14.74(2) h	443.13	16.9(5)
^{86}Y	14.74(2) h	627.72	32.6(1)
	14.74(2) h	1076.63	82.5(4)
	14.74(2) h	1153.05	30.5(9)
	14.74(2) h	1854.38	17.2(5)
	14.74(2) h	1920.72	20.8(7)
^{87}Zr	1.68(1) h	380.79	62.79(10)
	1.68(1) h	1227.0	2.80(4)
^{87m}Y	13.37(1) h	380.79	78.05(8)
	79.8(3) h	388.5276	82.2(7)
^{87}Y	79.8(3) h	484.805	89.8(9)
	83.4(3) d	392.87	97.29(14)
^{88}Y	106.627(21) d	898.042	93.7(3)
	106.627(21) d	1836.063	99.2(3)
^{89m}Nb	66(2) m	588.0	95.57(13)
	2.03(7) h	1511.4	1.9(4)
^{89}Nb	2.03(7) h	1627.2	3.5(7)
	2.03(7) h	1833.4	3.3(7)
^{89}Zr	78.41(12) h	909.15	99.04(3)
	78.41(12) h	1713.0	0.745(13)
^{90}Mo	5.56(9) h	122.370	64(3)
	5.56(9) h	162.93	6.0(6)
	5.56(9) h	203.13	6.4(6)
	5.56(9) h	257.34	78(4)
	5.56(9) h	323.20	6.3(6)
	5.56(9) h	472.2	1.42(16)
	5.56(9) h	941.5	5.5(7)
^{90}Nb	14.6(5) h	132.716	4.13(4)
	14.6(5) h	141.178	66.8(7)
	14.6(5) h	1611.76	2.38(7)
^{91m}Nb	60.86(22) d	104.62	0.574(1)
	60.86(22) d	1204.67	2.0(3)
^{92m}Nb	10.15(2) d	912.6	1.78(10)
	10.15(2) d	934.44	99.15(4)
^{93m}Mo	6.85(7) d	263.049	57.4(11)
	6.85(7) d	684.693	99.9(8)
	6.85(7) d	1477.138	99.1(11)

2.7 Measured excitation functions

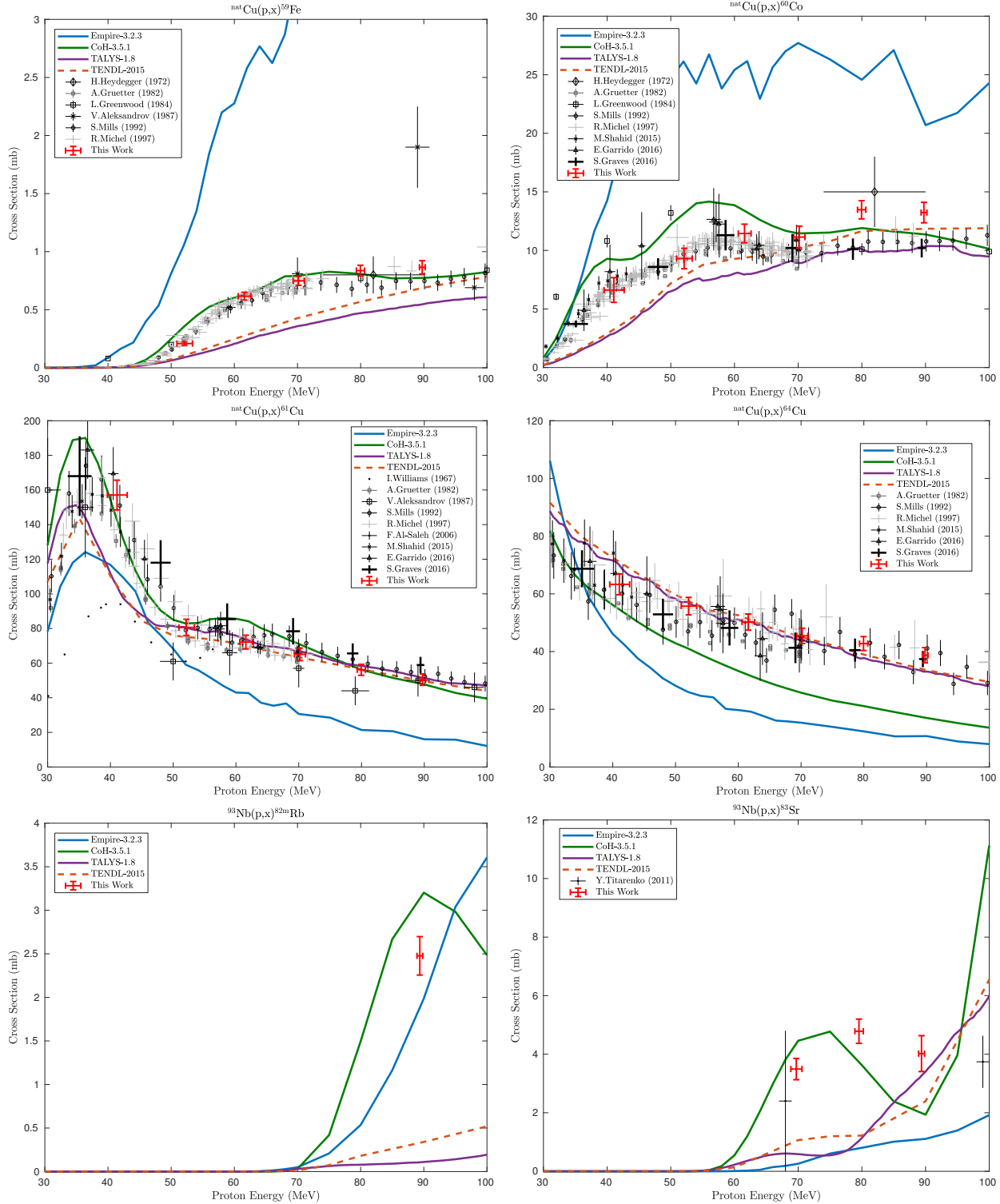
Figures of the cross sections measured in this work are presented here, in comparison with literature data [6, 40, 64, 75, 77, 106–121], the TENDL-2015 data library [84], and the reaction modeling codes CoH-3.5.1, EMPIRE-3.2.3, and TALYS-1.8 [80, 84, 86].

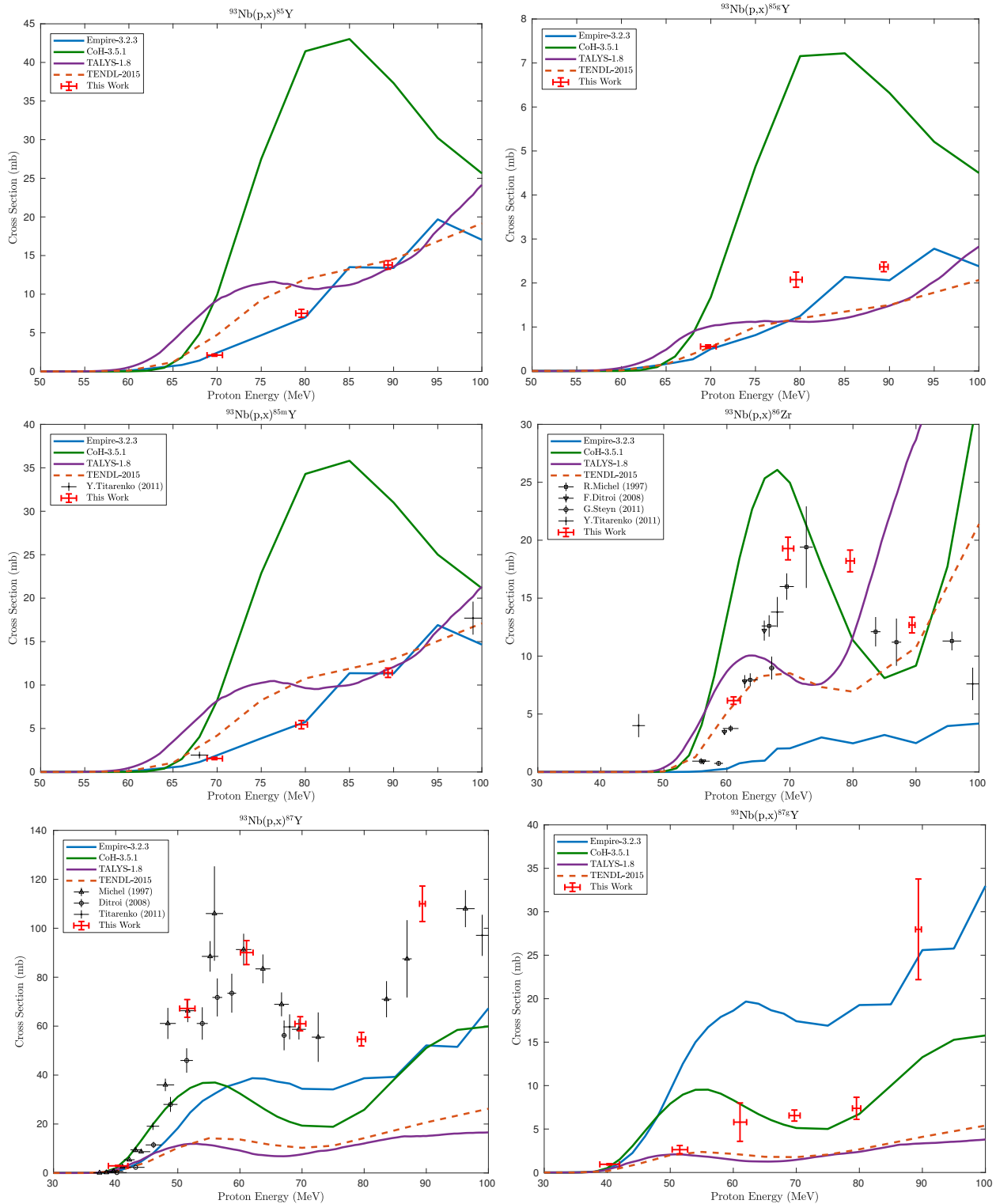


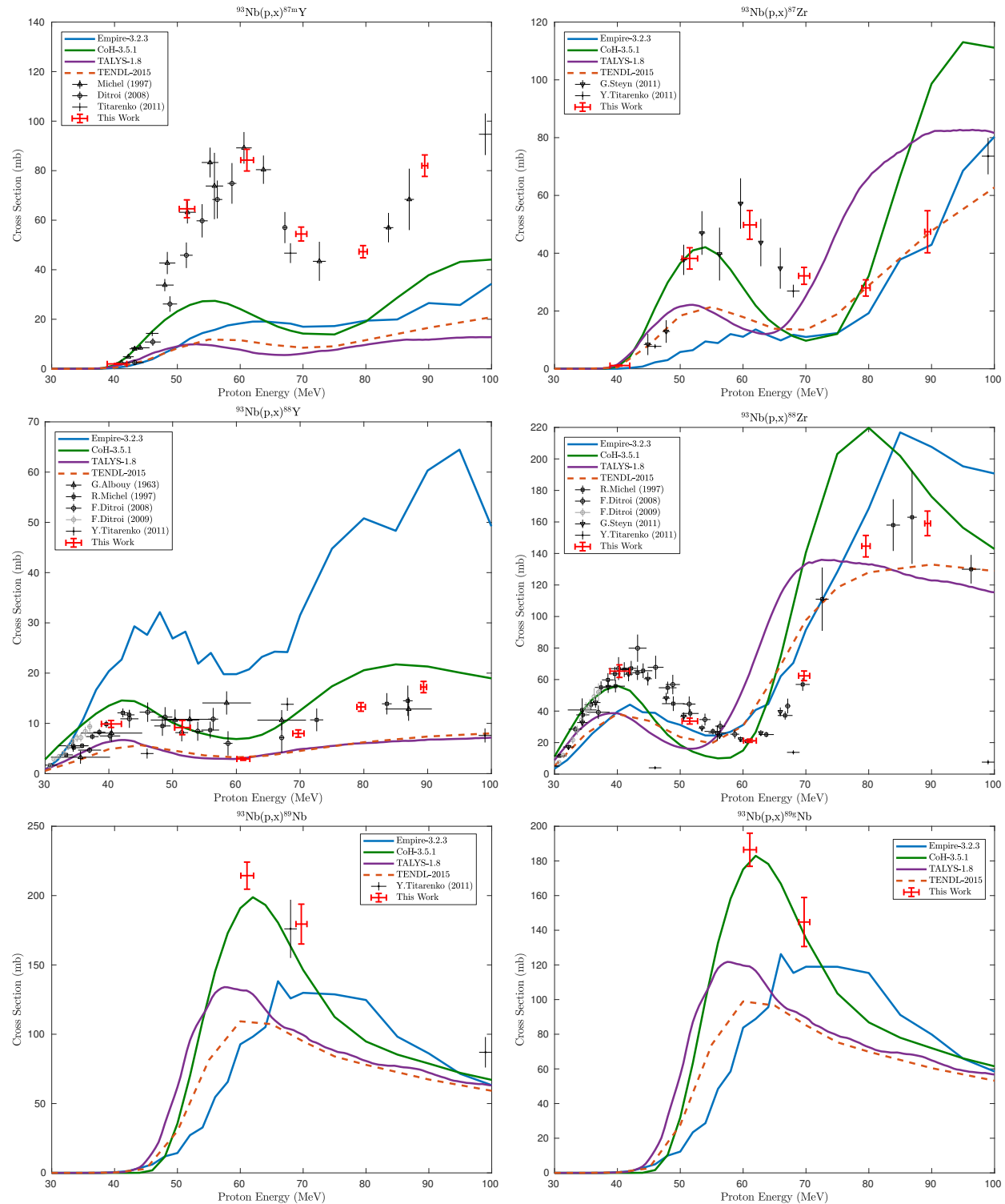


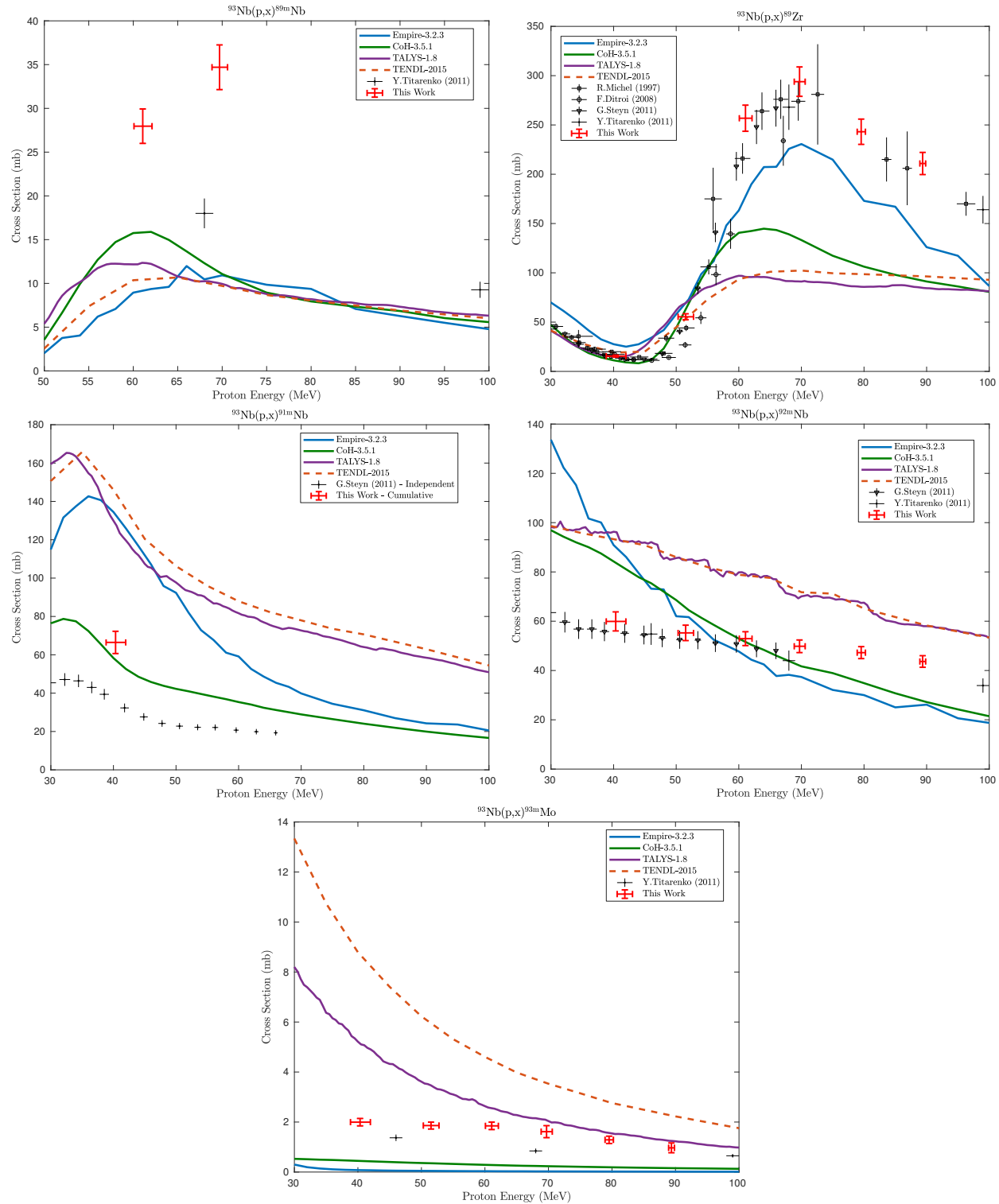
CHAPTER 2. DEVELOPMENT OF THE $^{93}\text{Nb}(P,4N)^{90}\text{Mo}$ REACTION AS AN
INTERMEDIATE-ENERGY PROTON MONITOR

40



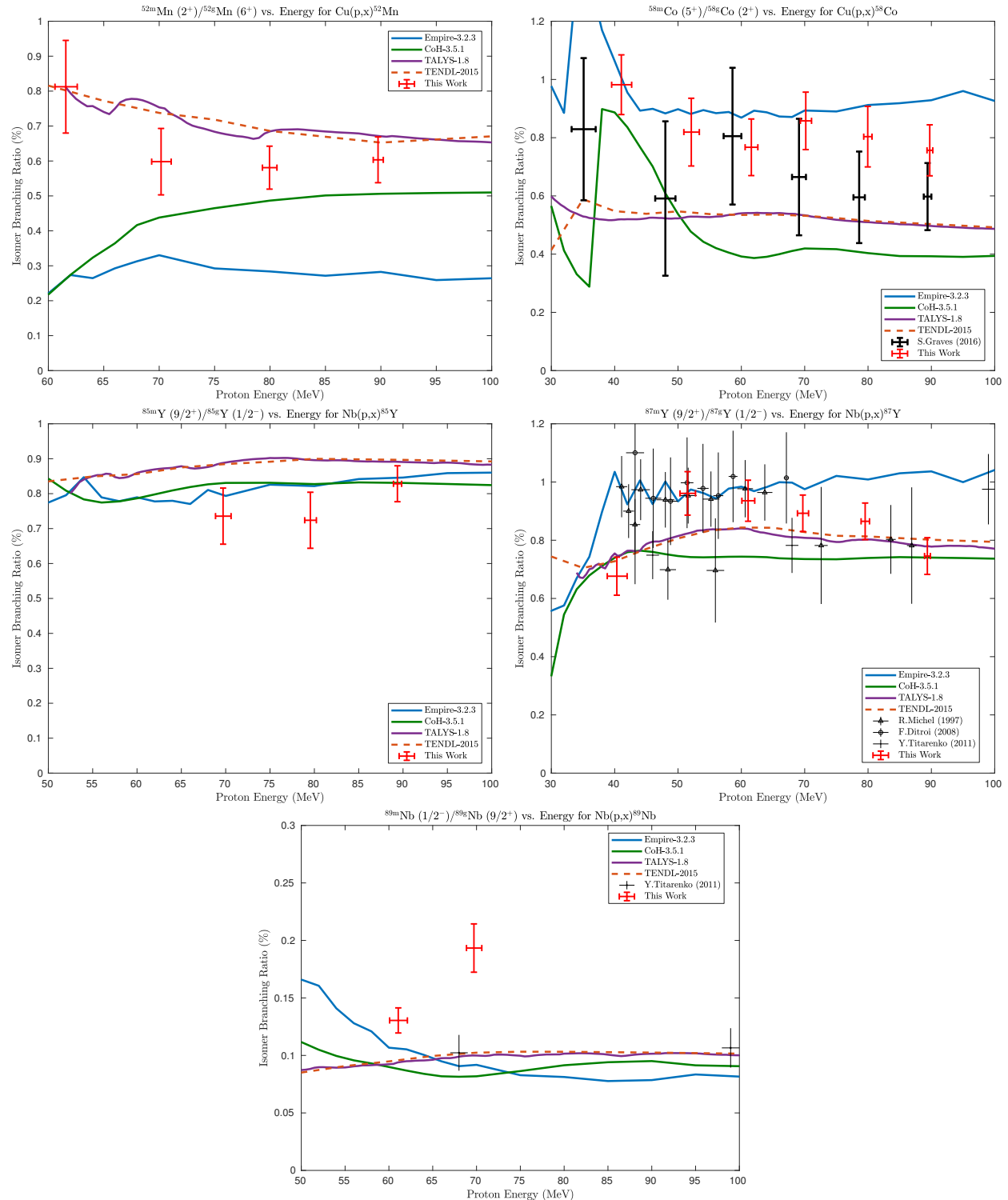






2.8 Measured isomer-to-ground state branching ratios

Plots of the isomer-to-ground state ratios measured in this work are presented here, in comparison with literature data and reaction modeling codes [6, 75, 77, 117].



2.9 Additional discussion

Additional discussion of the experimental and analytical details for this work, which were excluded from the published journal article to preserve its scope, are included here.

LANSCE overview

As discussed in section 2.3, the target stack for this work was assembled and irradiated at the Isotope Production Facility (IPF) at the Los Alamos National Laboratory (LANL), using the LANSCE linear accelerator. The LANSCE complex, constructed in 1972, is a large facility at the Los Alamos National Laboratory’s Technical Area 53, housing many basic and applied science facilities supported by the LANSCE-LINAC linear accelerator [122]. The accelerator has proton injector ion sources capable of supplying both positive- and negative-ion beams. The ions are accelerated up to 750 keV, where they are injected into a drift-tube linear accelerator. This accelerator, which operates as a standing-wave linear accelerator in the “zero mode” (or TM_{010}) electromagnetic field configuration, accelerates the ions up to 100 MeV. From here, the negative-ion beam is injected into the side-coupled cavity linear accelerator (800 m in length), which accelerates the ions up to the facility’s maximum 800 MeV. This beam is passed along to the various research centers at the LANSCE complex, which include the Lujan Center, Proton Radiography Center, Ultracold Neutron Source, and the Weapons Neutrons Research Facility. Alternatively, the 100 MeV positive-ion beam may be “peeled off” following acceleration in the drift-tube linac, where it is diverted to the Isotope Production Facility. At IPF, thick production targets and thin-target stacks may be lowered through a dedicated hot cell into the IPF beamline for irradiation. This facility serves to produce a variety of commercial isotopes for medical, industrial, basic science, and national security applications. A schematic of the LANSCE beamline is presented in Figure 2.12, and a photograph of the LANSCE complex is seen in Figure 2.13.

Radiation damage of materials

As charged particles traverse a material, they transfer energy primarily through scattering reactions, leaving a damage trail along their path [123, 124]. The average energy transfer in a collision by an incident particle of energy E and mass m , on a single atom with mass M , is

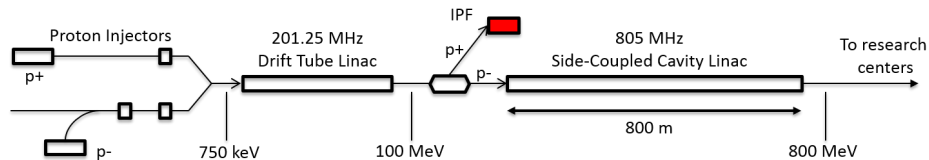


Figure 2.12: Schematic diagram of the LANSCE beamline at LANL. From the initial injectors, a proton beam is accelerated to 100 MeV in a drift-tube linear accelerator, where it is diverted away to the IPF beamline, highlighted in red.



Figure 2.13: Aerial photograph of the LANSCE beamline. Proton injectors are seen in the foreground building near the arrow’s tail. The IPF beamline and operations facility is seen to the left of the main LANSCE beamline, circled in red. The target box seen in Figure 2.1 is lowered into the beamline here, via a hot cell.

given by:

$$\langle T \rangle = \frac{1}{2} T_{max} = \frac{2mM}{(m + M)^2} E \quad (2.6)$$

For crystalline, metallic, and other ionic materials with a well-defined bulk lattice structure, if the energy transferred to an atom is large enough, the atoms can be knocked out of their lattice sites. This displacement energy, E_d , is typically about 25 eV for most solid materials [125]. This displaced atom is referred to as the primary knock-on atom (PKA), and is now mobile and capable moving throughout the material, with energy T . If $T \geq E_d$, the PKA is free to collide with another atom in the lattice, transferring:

$$\langle T_2 \rangle = \frac{1}{2} T_{max} = \frac{2mM}{(m + M)^2} \langle T \rangle \quad (2.7)$$

to the second atom. If $T_2 \geq E_d$, the PKA is free to collide with yet another atom, transferring:

$$\langle T_3 \rangle = \frac{1}{2} T_{max} = \frac{2mM}{(m + M)^2} \langle T_2 \rangle \quad (2.8)$$

This process keeps repeating, as long as $T_n \geq E_d$, producing a cascade of atoms knocked out of their lattice sites, all of which are heavy charged ions, and will rapidly scatter in the nearby material. Each time an atom is knocked out of its lattice site, it produces a Frenkel

Table 2.8: Displacement cascade approximate thresholds [7]

Incident Radiation Type	Single Displacements	Defect Clusters
Charged Particles	0.2 keV/A	8 keV/A
Neutrons	185 eV	5 keV
Gammas	1 MeV	Not observed

pair — the interstitial atom displaced from its lattice site, and a vacancy in its old lattice site [125, 126]. These are known as zero-dimensional defects in the material. During the cascade, all of the secondary interstitial displaced atoms may go on to knock out many other atoms themselves. The cascade will continue on for N_f total collisions, until the average energy of the cascade knock on particles is:

$$2E_d = \frac{T}{2^{N_f}} \quad (2.9)$$

for an original incident radiation particle with energy T . This cascade will thus produce a total number of displaced particles, ν , such that:

$$\nu = \frac{T}{2E_d} \quad (2.10)$$

For the example of an original incident 1 MeV proton, the proton may produce as many as

$$\nu = \frac{1 \text{ MeV}}{2(25 \text{ eV})} = 20,000 \text{ displacements} \quad (2.11)$$

All of the vacancy and interstitials formed by the cascade are extremely thermodynamically unstable, especially the interstitials, which are stuck in between lattice sites in the crystal lattice. To minimize the energy of the system, vacancies and interstitials diffuse from their primary site, and may recombine, annealing the damage caused by that pair [127]. However, vacancies and interstitials may also diffuse towards like defects instead, linking to form large three-dimensional void and precipitate cluster defects in the material, which also reduces the energy of the crystal system. These defect clusters may easily be as large as 150 Å across. In addition, if the energy transfer in a PKA cascade is $\langle T \rangle \approx 5 \text{ keV}$, cascades of such cluster defects may be formed nearly instantaneously, instead of single displacements [7, 128]. It is worth pointing out that, in addition to the primary beam, secondary ionizing radiation may also cause material damage. However, due to the different interaction mechanisms for the different types of ionizing radiation, observed displacement cascades may have different energy thresholds. Some typical threshold values for cascades are reported in Table 2.8 below.

While this gives a brief overview of radiation damage in ionic materials, for plastics and other amorphous polymer solids, a different damage mechanism exists. This is due to the fact that these types of material are dominated by covalent bonding. In such materials, when atoms are sufficiently excited following scattering by ionizing radiation, they are not

displaced from their lattice position, but instead may have their electron bond pairs broken up. This results in the original molecule disintegrating, and potentially re-forming into one or more new, different molecules. Thus, radiation damage in covalent materials results in chemical changes, as opposed to the physical changes seen in ionic materials. Plastics and other polymers exist as a massive single macromolecule, formed by repeating chains of smaller molecules called monomers. In the case of polymers, the extensive bond geometry in the overall molecule determines many of its properties and appearance, making such materials highly vulnerable to radiation damage [129].

When polymer bonds are broken, free radicals are formed in the severed chain segments. These free radicals are highly likely to propagate and terminate by reforming in new arrangements, which can be loosely lumped into three categories. Cross-linking is the formation of new bonds between previously-separate chains. This rearrangement produces a more rigid and brittle polymer with increased molecular mass, and is a common damage mechanism in softer polymers, such as silicones and polyethylenes. Fragmentation is the termination of segments with broken bonds, leading to the formation of many separate short-chain polymers. This rearrangement produces a softer, more fluid polymer with decreased molecular mass, and is a common damage mechanism in harder polymers, such as Lucite and synthetic rubbers. Both cross-linking and fragmentation affect the materials properties of a polymer — mechanical strength, solubility, and discoloration are commonly affected by these damage mechanisms. Finally, fragmented chain segments may polymerize to form completely new polymers than the original macromolecule, with a wide variety and chemical and physical properties [130].

Of these materials properties, discoloration is one of the most commonly encountered radiation damage effects seen in the context of activation experiments. Permanent discoloration occurs in polymers primarily due to heating effects from the beam. Temporary, annealable discoloration is more common in activation experiments. This variety is caused when residual free radicals become trapped in the polymer, and are unable to recombine and terminate. Moreover, they are able to be reversed through annealing, disappearing as oxygen diffuses into the polymer, helping to terminate the residual free radicals. This process will often occur at room temperature, but is greatly catalyzed when the polymer is heated [131, 132].

Beam profile measurements

Verify that we used polyethylene!!!

Following tuning of the 100 MeV proton beam into the IPF beamline, the current is measured immediately upstream of the target position using a pair of nondestructive inductive pickups. The final remaining step prior to loading the target box for irradiation is to tune the beam optics and spatial profile. This is performed by loading a sheet of polyethylene (approximately 3 mm thick) into the the IPF beamline, at the same location of the target box's beam entrance window. This sheet acts as a beam profile monitor, and is irradiated with 5 $\mu\text{A}\cdot\text{min}$ of the proton beam. Following exposure, the polyethylene monitor is withdrawn back into the IPF hot cell, where it is inspected to verify the shape and location of the beam profile. These beam profile irradiations leave an annealable discoloration of the beam

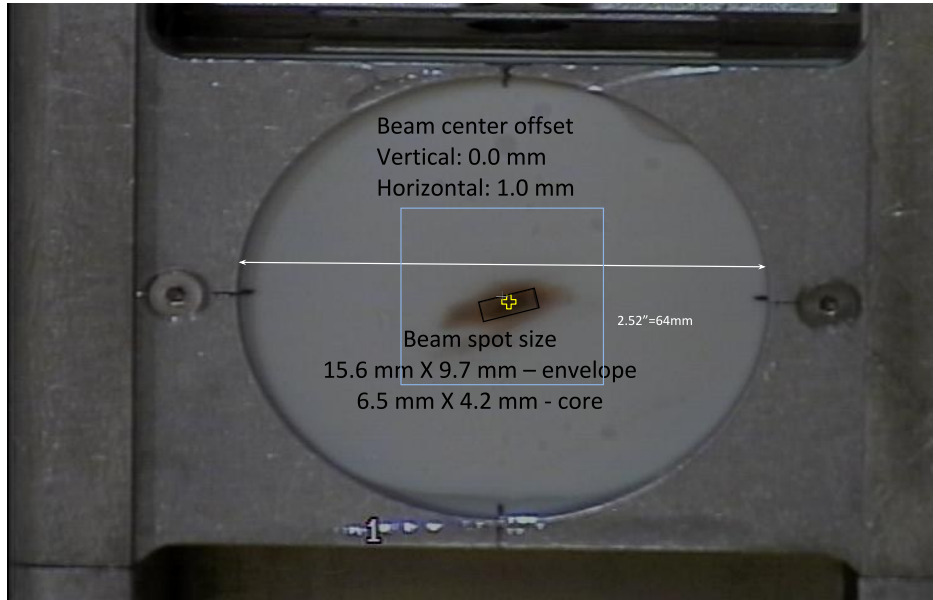


Figure 2.14: Final beam spot profile for the IPF Nb(p.x) measurement. The 100 MeV proton beam is confirmed to be centered on the target position, and is focused to underfill the 25×25 mm target foils.

profile, which resembles a “burn mark”, and are observed to passively revert within 1–2 weeks. The final pre-irradiation beam spot from the Nb(p.x) measurement is seen in Figure 2.14. LANSCE accelerator operations staff use this feedback to fine-tune the beam, centering the beam spot upon the target stack and focusing it to ensure that it underfills the target foils. This process of optics tuning via polyethylene profile monitors is repeated until an acceptable beam profile is attained. At this point, the target box is lowered into the beamline, and the irradiation commences.

This polyethylene beam profile monitor is useful for determining the beam profile incident upon the stack’s beam entrance window. However, the beam broadens as it traverses the target stack, with large-angle deflections (primarily in the aluminum degraders) from scattering of the beam. To image the actual beam profile incident upon the first foil in the stack (Al-1), a 316 stainless steel foil (SS-6) is inserted upstream of Al-1 to serve as a beam profile monitor for the activation foils. Likewise, another stainless steel profile monitor (SS-1) is inserted downstream of the last foil in the stack (Nb-6). These stainless steel monitors are cut to the same length and width as the plastic frames used for mounting foils, and are characterized in Table 2.1.

As described in subsection 2.3.1, decay radiation emitted from the activated stainless steel foils were used to develop radiochromic film (Gafchromic EBT), revealing the spatial profile of the beam entering and exiting the stack. Radiochromic films, such as Gafchromic EBT, come in multiple varieties, depending on the dose range and the type of ionizing radiation desired to provide sensitivity to. In general, such films are commonly self-developing, containing

a radiation-sensitive organic polymer dye as the active layer. This dye, much like the polyethylene beam profile monitors, is damaged by ionizing radiation, with multiple free radicals initiated in the process. These free radicals result in cross-linking, breaking of double bonds, and fragmentation of the dye polymer, which causes the damaged dye to undergo a large visible change in color. The intensity of this color change is often proportional to the dose received by the film, and is preferred to be energy-independent [133]. Many such films are sensitive to prolonged UV exposure, and will slowly develop if not kept in a cool, dark environment, leading to systematic errors in observed dose. The thin dye layer in most films is extremely sensitive, so care must be taken to avoid bending or deforming, which can make them insensitive to development when irradiated. For reference, the Gafchromic EBT film used in this work is comprised of a pair of 25 μm active layers containing the radiation-sensitive EBT emulsion dye, separated by a 3 μm surface layer and sandwiched in between a pair of 97 μm layers of clear polyester, acting as a supportive and protective backing.

The radiochromic films developed by the SS-6 and SS-1 stainless steel beam profile monitors are seen in Figure 2.15. In addition, extra aluminum monitor foils mounted on plastic frames are superimposed behind each film. It is clear from the upstream (SS-6) film that the proton beam profile was consistent with that seen in the final pre-irradiation beam spot check of Figure 2.14. The downstream (SS-1) film reveals that the beam was not completely attenuated, and clearly displays the broadening expected due to scattering in the target stack. More importantly, the beam profiles in both films appears to be completely contained within the 25 \times 25 mm activation foils, including the beam envelope. If the beam were to be misaligned on the foils, or were to have sufficiently broadened such that it greatly overfilled the foils, the activation foils would be exposed to only a fraction of the total beam current. If fluence measurements are purely taken from an external current monitor (such as an inductive pickup upstream of a target, or an electrically-isolated target in a Faraday cup), the fraction of current which misses the foils will not be detected. This leads to reporting a false, larger fluence, which will cause all cross sections to be erroneously reported with a reduced magnitude. Thus, it is for this reason that having monitor foils at each energy position builds confidence in reported cross sections, as they serve to screen for systematic errors such as this. However, profile monitors play a vital role in the detection of lost beam fluence when monitor foils are unavailable.

Since the color change developed by irradiation is proportional to the dose deposited in the film, the optical density of the film may be used to measure dose. In clinical external-beam radiation therapy, these films are commonly used in quality assurance to map and verify the dose contours for therapeutic gamma-ray fields. However, the dose sensitivity of these films is often greater than the ability to be visually distinguished beyond simple qualitative inspection. As a result, following exposure, the film may be digitized using any flatbed scanner. Image analysis may be thus used to measure the optical density profile as a surrogate for dose or beam intensity profiles. The optical density is often fit to a curve of the form

$$d_x(D) = a + \frac{b}{D - c} \quad (2.12)$$

where $d_x(D)$ is the optical density of exposed radiochromic film in scanner color channel x at dose D , and a , b , and c are calibration parameters. Using a standard irradiation source (commonly a collimated ^{60}Co source), a calibration curve can thus be measured to convert optical density into an absolute dose. This is most common in clinical and quality assurance applications. In addition, modern radiochromic films are often designed such that the characteristic exposure curve for the active layer dye differs between the red, green, and blue color channels, offering even further enhanced sensitivity to dose [14, 134, 135].

However, for cases where an absolute dose is not necessary, the optical density can still be used for a qualitative measure of relative beam intensity, or relative dose. Using the image analysis code ImageJ-2.0.0, profiles of the total optical density were extracted for both the SS-1 and SS-6 radiochromic films [136]. These are seen in Figure 2.16, as relative beam intensity profiles along the major and minor axis of each film. As seen visually, for both axes, the peak beam intensity drops from SS-6 to SS-1, as the proton fluence is clearly broadened by scattering reactions in the target stack. Along the major (“horizontal”) axis, the FWHM of the beam profile broadens from 0.679 cm to 1.039 cm, and along the minor (“vertical”) axis, the FWHM of the beam profile broadens from 0.453 cm to 0.902 cm. In addition, the centroid position of the minor axis appears to shift by approximately 0.19 cm between the front and rear of the stack. The measured beam profiles were fit using a Gaussian model with linear background, to aid in comparing the widths of each profile. The Gaussian model does well to fit the beam profiles overall, though it overestimates the peak height for a given Gaussian width. This is likely due to the fact that the beam itself has an intrinsic spatial width before any interactions with the target stack; this leads to more broadening of the beam envelope than of its core.

Target preparation

As described in subsection 2.3.1, all activation foils in this work were tightly sealed into “packets” using two pieces of 3M 5413-Series Kapton polyimide film tape. The sealed foils were then mounted over the hollow center of a 1.575 mm-thick plastic frame. This gives each foil a fixed, rigid, position, preventing it from shifting out of alignment as the target stack is lowered into the beamline. In addition, the hollow center is cut out such that the plastic frame does not degrade and scatter the beam at each foil position. One ^{nat}Al , one ^{nat}Cu , and one ^{nat}Nb mounted foil were bundled together using baling wire for each energy position. One such bundle is seen in Figure 2.17, illustrating how the three foils of each bundle are aligned with each other. This is primarily to maintain a comparable area of exposed foil at each energy position, in the case of significant beam spot broadening. These foil packet bundles were lowered into the beamline by inserting them into a water-cooled production target box. After sealing the target box, it is inserted into the IPF hot cell, seen in Figure 2.18. In the hot cell, robotic manipulators are used to attach a mounting frame to the top of the target box. The frame is used to mount the target box onto a motorized track, which extends below the hot cell, and is used to lower the target box by approximately 12 m into its position in the IPF beamline. Following irradiation, the track raises the target box back into the hot

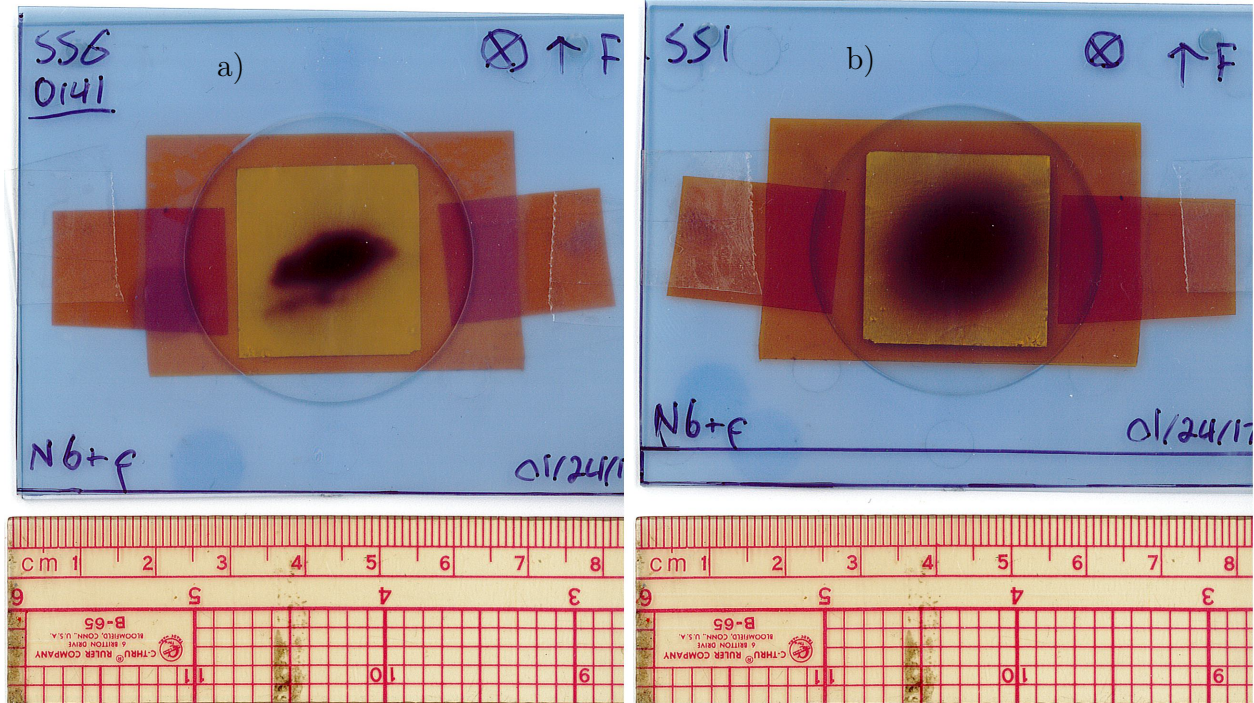


Figure 2.15: Radiochromic films for the IPF $\text{Nb}(p,x)$ measurement, developed by the stainless steel beam profile monitors in (a) the front of the stack (SS-6) and (b) the rear of the stack (SS-1). An unused Al monitor foils is aligned behind each film, confirming that both the beam core and envelope underfilled the activation foils.

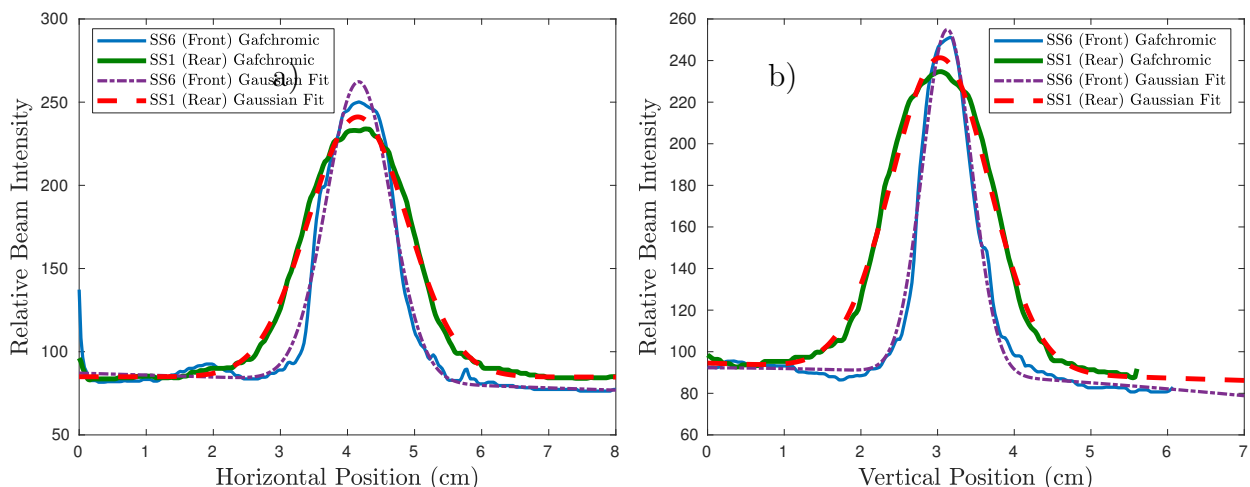


Figure 2.16: Relative beam intensity profiles for the radiochromic films seen in Figure 2.15. The intensity profiles were analyzed using ImageJ along (a) the major axis and (b) minor axis of each beam spot.

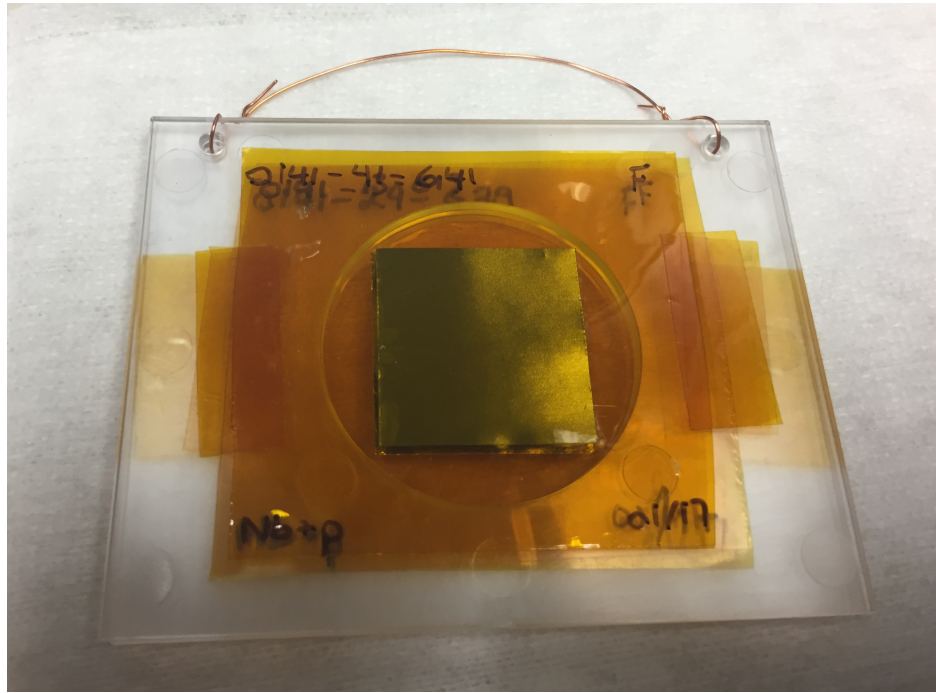


Figure 2.17: A stacked bundle of Nb (visible on top), Cu, and Al activation foils, for the 60 MeV position of the Nb(p,x) target stack. All foils are mounted over the aperture of a 1.575 mm-thick plastic frame and bundled together with baling wire.

cell, where it is detached and opened via manipulators. Foil removal is performed in the hot cell via the manipulators, as the target box becomes highly activated with short-lived Al activation products, which makes manual handling hazardous. The foil bundles are removed using the baling wire loop “handles”, and removed from the hot cell via a pass-through, for decontamination and transfer to the counting lab.

MCNP modeling

A rendering of the IPF Nb(p,x) target stack, as modeled in MCNP6, is seen in Figure 2.19. This model is the same described in subsection 2.3.4 for simulation of proton transport. The full input file for this MCNP model is included here for reference, in Appendix A.2. In this figure, the 100 MeV proton beam enters from the left of the figure, where it is incident (in the positive x direction) upon the Inconel beam entrance window (yellow). The other stack elements, described in Table 2.1 are illustrated here, as well. The green cell is the cooling water channel for the target box, the air filling the target box is shown in light blue, and the 6061 aluminum beam degraders are shown in dark blue. The thin black lines seen in between degraders are the Nb, Cu, and Al activation points at each energy position, sealed in Kapton tape. The detail of each foil sealed in the Kapton is not visible here, simply due to the size scale of the stack assembly.

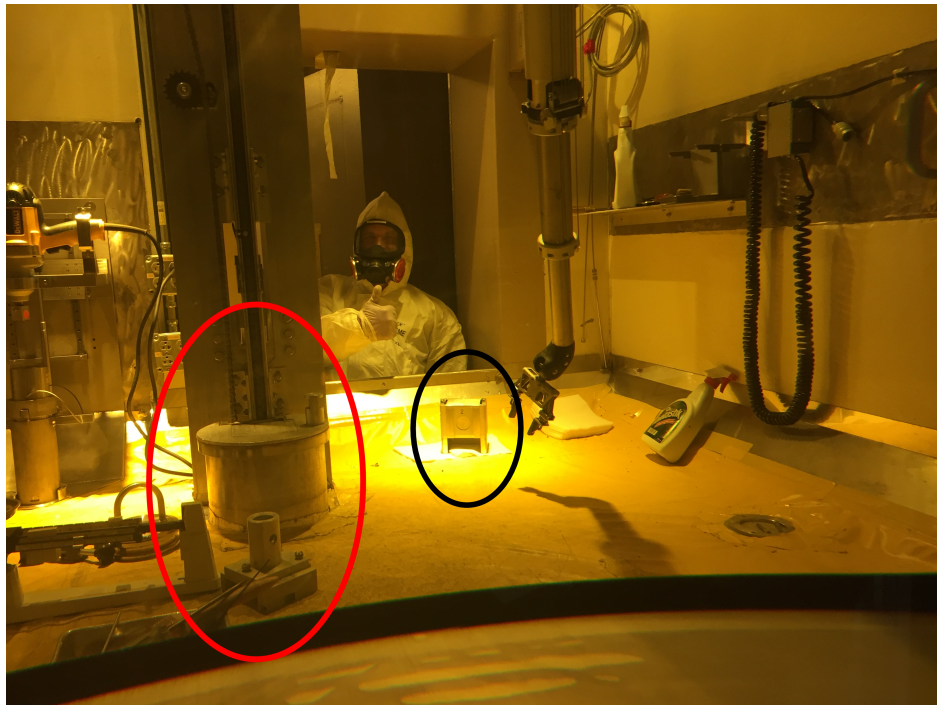


Figure 2.18: The IPF hot cell, used for lowering and retrieving the target stack (circled in black) and polyethylene beam profile monitors from the IPF beamline. Robotic manipulators are used for handling of all components in the hot cell, including mounting them onto a motorized track for insertion into the beamline. This track and mount are seen circled in red.

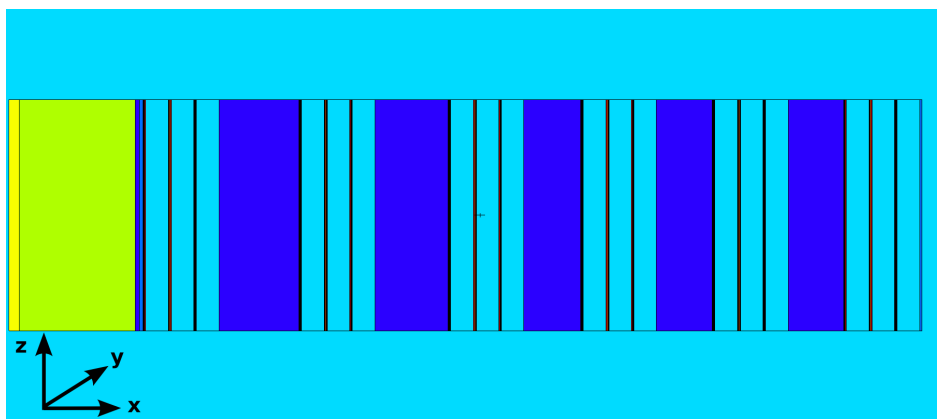


Figure 2.19: Simplified top-down MCNP6 model of the IPF Nb(p,x) target stack. The 100 MeV proton beam enters from the left of the figure, where it is incident upon the Inconel beam entrance window (yellow). The beam is transported down the length of the stack, towards the rear of the stack on the right side of the figure.

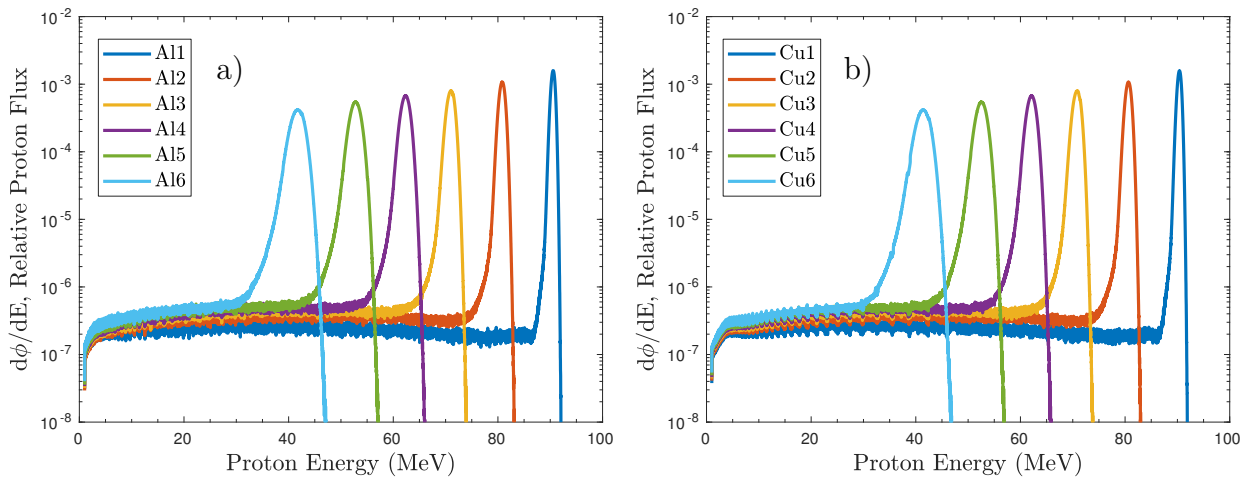


Figure 2.20: Final variance minimized incident proton energy distributions for the (a) Al and (b) Cu foils, as simulated in MCNP6. The distribution tallies in each foil are all normalized to be per source proton, which was 10^8 in all simulations. As the beam is degraded, proton energy distributions become visibly broadened due to straggling, and drop in magnitude due to scattering losses.

Using this MCNP6 model, the proton energy distribution is tallied in all volumes of the stack assembly. As seen in Figure 2.7 of subsection 2.3.4, the corresponding incident proton energy distributions $\frac{d\phi}{dE}$ from MCNP6 simulation (using the variance minimized degrader density) are shown for the six irradiated Cu and Al foils in Figure 2.20. In addition, the MCNP6 model tracks the production and transport of secondary neutrons produced through (p,xn) reactions on the target stack components. The proton energy distribution is tallied in all Al, Cu, and Nb foils, and is seen in Figure 2.21. The neutron flux is consistently 3–4 orders of magnitude smaller than the corresponding proton flux, and is seen to be visibly downscattered when moving down the stack.

Additionally, using this proton transport model, it is possible to plot the FWHM of the proton energy distribution in each of the Cu and Al monitor foils, as a function of its flux-weighted average proton energy. This is seen in Figure 2.22. As seen in the recent work of Graves *et al.*, this FWHM distribution can be fit via linear regression [6]. The results of this fit (with $R^2 = 0.9986$) would suggest that the broadening of proton energy distribution in the target stack is linearly proportional to energy degradation, which is overwhelmingly from the aluminum degraders between energy positions. This serves to build confidence, through consistency with the results from this similar measurement. In the event that the FWHM of a stack element could not be directly calculated using the MCNP model output, this linear model could be used to estimate the element’s FWHM through interpolation.

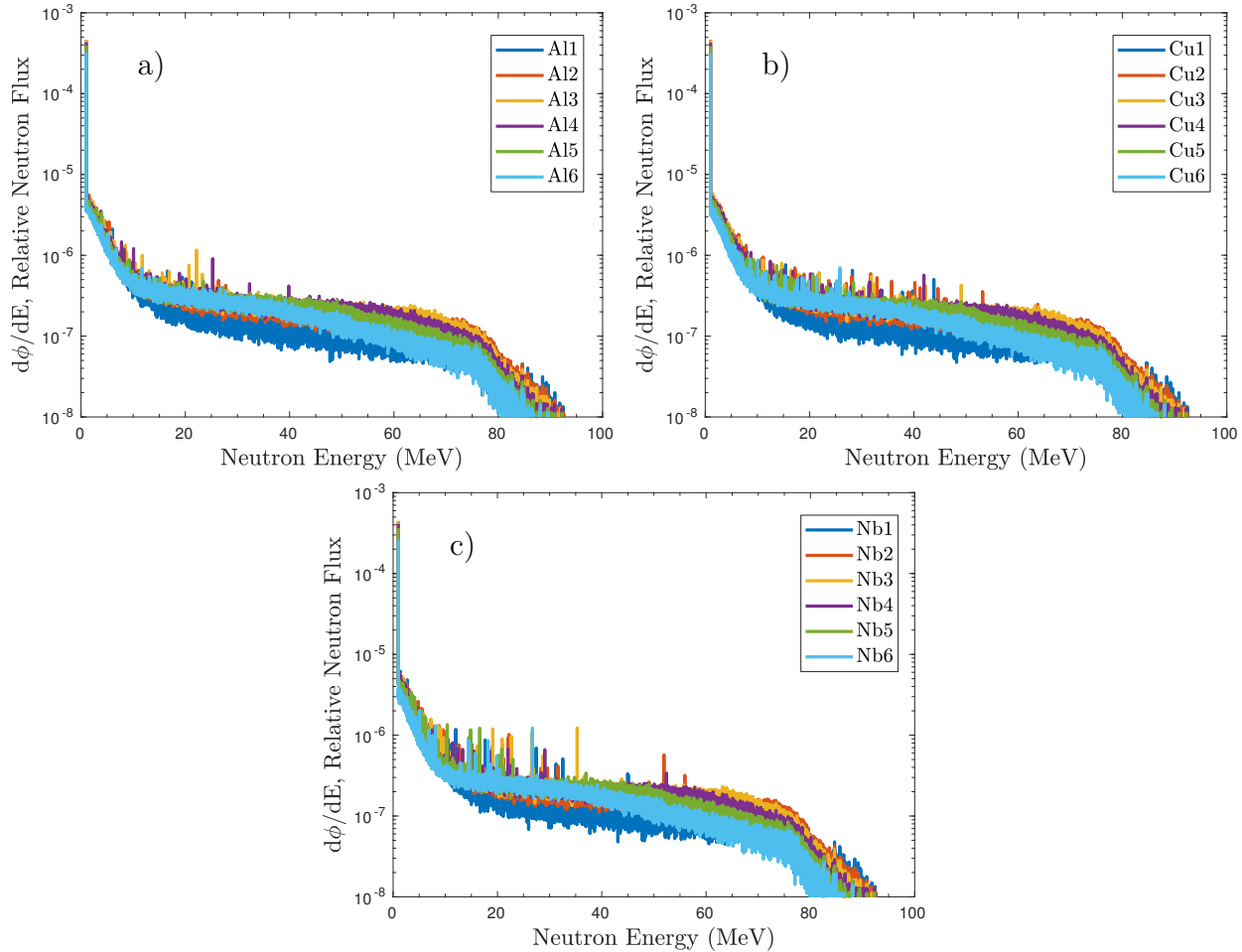


Figure 2.21: Final variance minimized incident neutron energy distributions for the (a) Al, (b) Cu, and (C) Nb foils, as simulated in MCNP6. The distribution tallies in each foil are all normalized to be per source proton, which was 10^8 in all simulations. As the beam is degraded, neutron energy distributions become visibly downscattered.

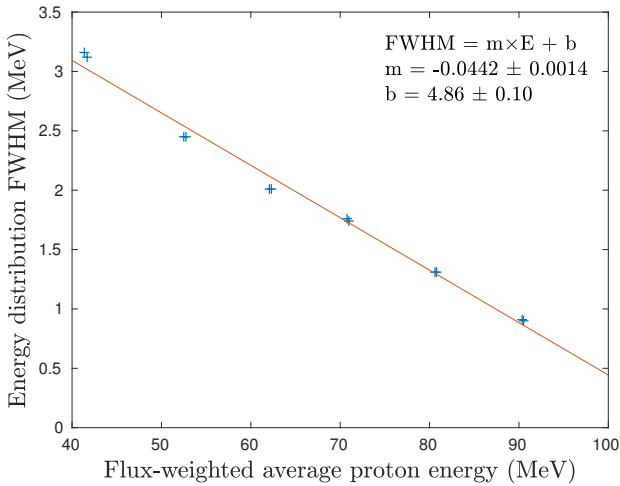


Figure 2.22: FWHM for the proton energy distributions of Cu and Al foils seen in Figure 2.20, as a function of the flux-weighted average proton energy.

$^{22,24}\text{Na}$ production

As discussed in subsection 2.3.4, the observation of the $^{22,24}\text{Na}$ activities in Cu and Nb foils represents an indirect measurement of the $^{\text{nat}}\text{Si}(p,x)^{22,24}\text{Na}$ cross sections, but was not reported in the journal article due to uncertainties in the areal density of the Si in the adhesive. The EoB $^{22,24}\text{Na}$ activities have been measured directly, but to convert these into absolute cross sections, accurate knowledge of the precise silicone composition and areal density are required. These have been taken as a 10% Si stoichiometric basis and an areal density of 4.79 mg/cm² (based on bulk density), respectively, for the purposes of transport calculations, but this level of confidence is insufficient for the reporting of a cross section. Using these assumptions, the apparent cumulative $^{\text{nat}}\text{Si}(p,x)^{22,24}\text{Na}$ cross sections are included here for the purpose of completeness, tabulated in Table 2.9 and plotted in Figure 2.23, in comparison with literature data [77, 137–141].

By subtracting out the measured $^{22,24}\text{Na}$ activity at each Nb and Cu foil position (correcting for the minor difference in proton energy between adjacent foils) from the apparent $^{22,24}\text{Na}$ activities observed in each Al foil packet, the “true” or uncontaminated fluence via the Al monitor reactions is obtained, shown in Figure 2.6. Following subtraction, the $^{22,24}\text{Na}$ fluences become more consistent with other monitor reaction channels, though ^{22}Na fluence remains 3–6% higher than the weighted mean of the remaining monitor reaction channels. While this would circumvent the assumptions needed for reporting $^{\text{nat}}\text{Si}(p,x)^{22,24}\text{Na}$ cross sections, subtraction of inaccurately quantified $^{22,24}\text{Na}$ activity in each Nb and Cu foil would propagate into the final fluence determination at each energy position, shifting the magnitude of all reported cross sections. While the dramatic improvement in monitor reaction consistency builds confidence, in the interest of surety and because they are consistent, only the $^{\text{nat}}\text{Cu}(p,x)^{56}\text{Co}$, $^{\text{nat}}\text{Cu}(p,x)^{62}\text{Zn}$, and $^{\text{nat}}\text{Cu}(p,x)^{65}\text{Zn}$ monitor reaction channels will be

Table 2.9: Apparent cumulative ${}^{\text{nat}}\text{Si}(\text{p},\text{x})^{22,24}\text{Na}$ cross section measurements, as observed in this work.

	Production cross section (mb)					
E_p (MeV)	$89.74^{+0.48}_{-0.43}$	$79.95^{+0.67}_{-0.64}$	$70.17^{+0.91}_{-0.85}$	$61.58^{+1.03}_{-0.98}$	$52.10^{+1.25}_{-1.20}$	$41.05^{+1.62}_{-1.54}$
${}^{\text{nat}}\text{Si}(\text{p},\text{x})^{22}\text{Na}$	20.4 ± 3.0	20.4 ± 3.8	22.9 ± 3.1	20.3 ± 5.5	8.1 ± 2.1	—
${}^{\text{nat}}\text{Si}(\text{p},\text{x})^{24}\text{Na}$	3.21 ± 0.43	2.77 ± 0.33	2.10 ± 0.25	1.08 ± 0.20	0.59 ± 0.11	0.254 ± 0.038
E_p (MeV)	$89.37^{+0.47}_{-0.45}$	$79.55^{+0.68}_{-0.64}$	$69.70^{+0.90}_{-0.85}$	$61.07^{+1.05}_{-0.98}$	$51.51^{+1.25}_{-1.21}$	$40.34^{+1.58}_{-1.55}$
${}^{\text{nat}}\text{Si}(\text{p},\text{x})^{22}\text{Na}$	22.1 ± 2.8	21.7 ± 3.6	26.0 ± 2.9	27.6 ± 5.2	9.9 ± 2.0	—
${}^{\text{nat}}\text{Si}(\text{p},\text{x})^{24}\text{Na}$	3.65 ± 0.50	3.11 ± 0.45	2.50 ± 0.96	1.54 ± 0.73	0.76 ± 0.15	0.303 ± 0.056

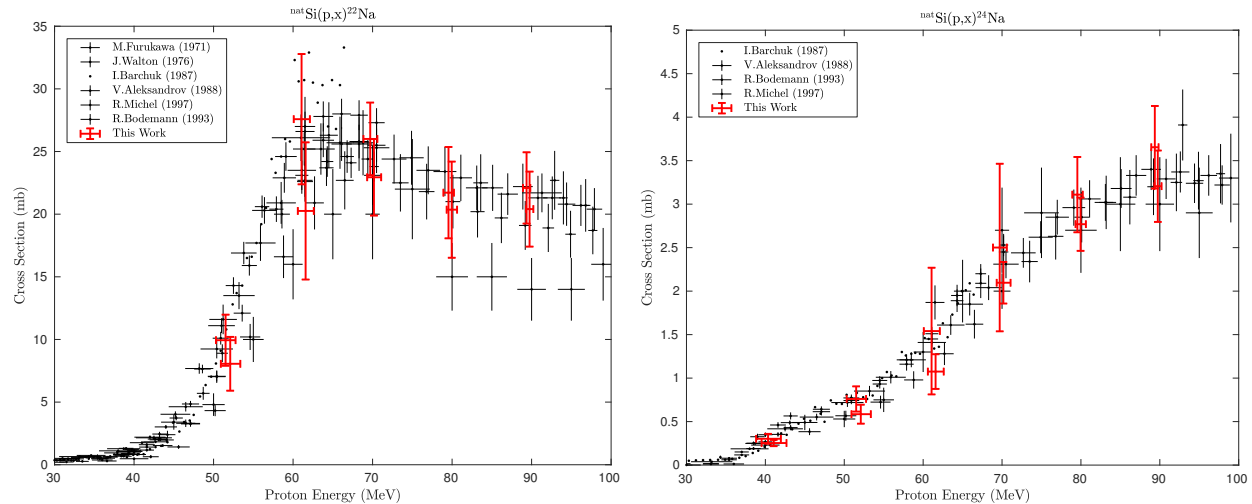


Figure 2.23: Apparent cumulative ${}^{\text{nat}}\text{Si}(\text{p},\text{x})^{22,24}\text{Na}$ cross section measurements, from production in the silicone adhesive of the Cu and Nb foils.

used for fluence determination for the reported cross sections. This serves as a pointed example of the importance of selecting monitor reaction products inaccessible through channels aside from the primary reaction (${}^{\text{nat}}\text{Al}(\text{p},\text{x})^{22,24}\text{Na}$, in this case), as noted previously.

Potential pathways for isotope production

In the published journal article, cross sections for ^{51}Cr , ^{52}gMn , $^{52\text{m}}\text{Mn}$, ^{54}Mn , ^{55}Co , ^{56}Ni , ^{57}Ni , ^{57}Co , $^{58\text{g}}\text{Co}$, $^{58\text{m}}\text{Co}$, ^{59}Fe , ^{60}Co , ^{61}Cu , and ^{64}Cu were extracted for (p,x) reactions on ${}^{\text{nat}}\text{Cu}$ foils in the 40–90 MeV region, as recorded in Table 2.2. For (p,x) reactions on ${}^{\text{nat}}\text{Nb}$ foils, the (p,x) cross sections for $^{82\text{m}}\text{Rb}$, ^{83}Sr , $^{85\text{g}}\text{Y}$, $^{85\text{m}}\text{Y}$, ^{86}Zr , ^{86}Y , ^{87}Zr , $^{87\text{g}}\text{Y}$, $^{87\text{m}}\text{Y}$, ^{88}Zr , ^{88}Y , $^{89\text{g}}\text{Nb}$, $^{89\text{m}}\text{Nb}$, ^{89}Zr , ^{90}Mo , ^{90}Nb , $^{91\text{m}}\text{Nb}$, $^{92\text{m}}\text{Nb}$, and $^{93\text{m}}\text{Mo}$ were extracted, as recorded in

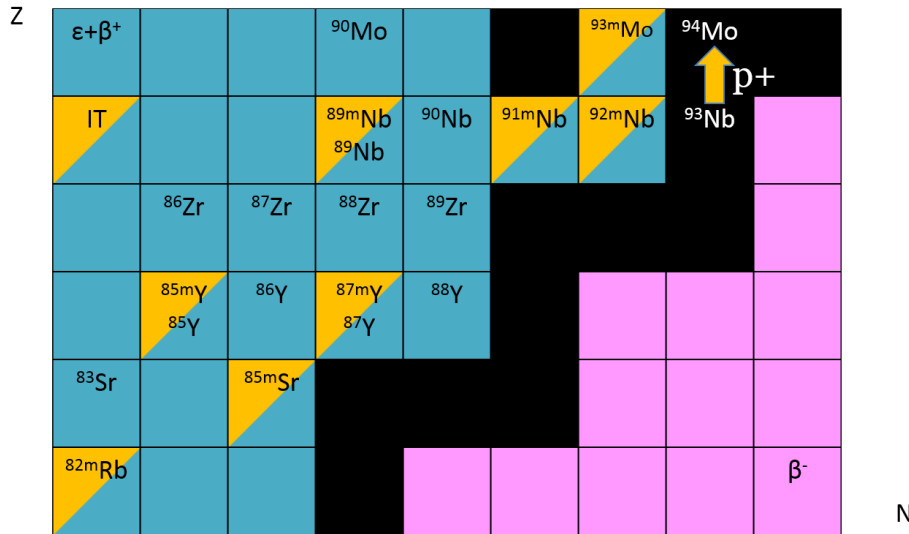


Figure 2.24: Reaction products observed in the $^{\text{nat}}\text{Nb}(p,x)$ measurement. **84Sr is stable - update plot!**



Figure 2.25: Reaction products observed in the $^{\text{nat}}\text{Cu}(p,x)$ measurement.

Table 2.3. As an alternative to a simple list of the various observed reaction products, these may be visualized in Figure 2.24 and Figure 2.25, in the style of excerpts from the Chart of Nuclides. These figures display the target and compound nuclei for both $^{\text{nat}}\text{Nb}(p,x)$ and $^{\text{nat}}\text{Cu}(p,x)$, along with all observed reaction products, to illustrate the mass range probed in this measurement.

In addition to the $^{\text{nat}}\text{Nb}(p,x)^{90}\text{Mo}$ monitor reaction measurement, this experiment has

also yielded measurements of a number of additional emerging radionuclides with medical applications. These include the non-standard positron emitters ^{57}Ni [6, 47–49], ^{64}Cu [50–57], ^{86}Y [30, 31, 58–66], ^{89}Zr [67–71], ^{90}Nb [72, 73], and the Auger-therapy agent $^{82\text{m}}\text{Rb}$ [74, 75]. Discussion of the suitability for $^{\text{nat}}\text{Nb}(\text{p},\text{x})$ and $^{\text{nat}}\text{Cu}(\text{p},\text{x})$ production pathways of these valuable medical radionuclides is included here.

^{57}Ni ($t_{1/2} = 35.60 \pm 0.06$ h, $\epsilon=100\%$ to ^{57}Co [76]), while useful on its own as a positron emitter, stands poised as a particularly promising candidate for theranostic pairing with the soft β^- emitter ^{66}Ni ($t_{1/2} = 54.6 \pm 0.3$ h, $\beta^- = 100\%$ to ^{66}Cu [142]) [6, 47–49]. $^{\text{nat}}\text{Cu}(\text{p},\text{x})^{57}\text{Ni}$ would seem to be an intriguing production pathway, due to the ready availability of Cu metal as target, combined with the fact that production in this pathway strongly favors ^{57}Ni over ^{56}Ni — indeed, the $^{57}\text{Ni}/^{56}\text{Ni}$ ratio of production rates is approximately 290 at 61.58 MeV, and varies from 45–75 at the 70–90 MeV positions. The traditional route for ^{57}Ni production is via $^{\text{nat}}\text{Co}(\text{p},3\text{n})^{57}\text{Ni}$, but at moderate energies, suffers from more ^{56}Ni contamination than $^{\text{nat}}\text{Cu}(\text{p},\text{x})$ ($\sigma_{^{57}\text{Ni}}/\sigma_{^{56}\text{Ni}} \approx 10$ at maximum). Lower-energy production via $^{\text{nat}}\text{Co}(\text{p},3\text{n})$ at 24–40 MeV is below threshold for ^{56}Ni , but has a peak cross section of approximately 10 mb, making $^{\text{nat}}\text{Cu}(\text{p},\text{x})$ the superior production route for moderate-energy accelerators [77, 78].

^{64}Cu ($t_{1/2} = 12.7$ h) undergoes β^+ decay (61.5% branching ratio) to ^{64}Ni or β^- decay (38.5% branching ratio) to ^{64}Zn [5], with the PET branch suited for imaging of prostate and colorectal cancers [50–52]. Several production routes currently exist: $^{64}\text{Ni}(\text{p},\text{n})$ uses 8–14 MeV protons on the expensive enriched target ^{64}Ni (0.9255% natural abundance), but offers a high radioisotopic purity assuming a highly enriched target [53, 54]. $^{68}\text{Zn}(\text{p},\alpha\text{n})$ requires more energetic 20–30 MeV protons, and necessitates an enriched target (18.45% natural abundance) to avoid the co-production of radio-copper impurities [55, 56]. More recently, the use of compact DD neutron generators for $^{\text{nat}}\text{Zn}(\text{n},\text{p})$ production has been proposed, with the promise of mCi-scale production with high specific activity [57].

^{86}Y ($t_{1/2} = 14.74 \pm 0.02$ h, $\epsilon=100\%$ to ^{86}Sr [101]) is another novel emerging PET isotope, whose longer half-life has poised it for applications as a tracer for slower metabolic processes, as well as in pharmacokinetics studies [58–61]. In particular, it is highly desired to form a theranostic pair with the widely-employed β^- therapy agent ^{90}Y ($t_{1/2} = 64.00 \pm 0.21$ h, $\beta^- = 100\%$ to ^{90}Zr [24]), which can be produced from a long-lived ^{90}Sr generator and emits no discrete observable gamma-rays or x-rays though decay [143]. Although a weak positron branch exists and bremsstrahlung scintigraphy is commonly used for clinical imaging of the ^{90}Y biodistribution, theranostics necessitate an imaging isotope to be paired for quantification of its uptake and biodistribution [144]. Conventional production of ^{86}Y proceeds through low-energy (7–14 MeV) irradiation via $^{86}\text{Sr}(\text{p},\text{n})$, which requires an enriched ^{86}Sr target (9.86% natural abundance), in order to eliminate contamination from (p,n) on the other stable $^{84,87,88}\text{Sr}$ isotopes [62]. Alternatively, production at 33–43 MeV via $^{88}\text{Sr}(\text{p},3\text{n})$ has been proposed — this pathway also requires an enriched target (82.58% natural abundance) for the same reason, but contamination with other Y co-activities will be even more pronounced than via (p,n), due to the opening of (p,n) and (p,2n) channels on all stable Sr isotopes [63, 64]. Minimizing activity from other isotopes of the element in question is essential for producing radionuclides in high specific activity, as these competing isotopes are often impractical to

separate out by radiochemical means. As a result, it would appear that $^{\text{nat}}\text{Nb}(\text{p},\text{x})$ is a poor route for ^{86}Y production in this respect, as it only reaches a maximum of approximately 35% radioisotopic purity. The dominant yttrium radioisotope produced by $^{\text{nat}}\text{Nb}(\text{p},\text{x})$ in the 40–90 MeV region is ^{87}Y ($t_{1/2} = 79.8 \pm 0.3$ h, $\epsilon^- = 100\%$ to ^{87m}Sr [30]). However, ^{87}Y itself has application as a generator for ^{87m}Sr ($t_{1/2} = 2.815 \pm 0.012$ h, IT=99.70% to ^{87}Sr [30]), which is used for imaging studies of metastatic bone cancers, especially when in a theranostic pair with the established therapy agent ^{89}Sr ($t_{1/2} = 50.563 \pm 0.0025$ d, $\beta^- = 100\%$ to ^{89}Y [31]) [65, 66].

^{89}Zr ($t_{1/2} = 78.41 \pm 0.12$ h, $\epsilon = 100\%$ to ^{89}Y [31]) is a long-lived positron emitter useful as a tracer for slow biological processes, immune studies, and imaging of liver and breast cancers [67–69]. Current production focuses on $^{89}\text{Y}(\text{p},\text{n})^{89}\text{Zr}$ between 9–14 MeV, which offers an extremely high-purity route on a mono-isotopic target and a strong population of ^{89}Zr , with a peak cross section of nearly 800 mb [70, 71]. Due to co-production of additional $^{86,87,88}\text{Zr}$ radio-zirconium, $^{\text{nat}}\text{Nb}(\text{p},\text{x})$ is clearly inferior to $^{89}\text{Y}(\text{p},\text{n})^{89}\text{Zr}$, as the Nb route has a smaller peak cross section of approximately 290 mb, and achieves only 10–20% radioisotopic purity in the 50–90 MeV region.

^{90}Nb ($t_{1/2} = 14.60 \pm 0.05$ h, $\epsilon = 100\%$ to ^{90}Zr [24]) is an emerging positron emitter with a moderate lifetime, making it suited for immune and tumor uptake studies [72, 73]. It is typically produced using 8–15 MeV protons via $^{90}\text{Zr}(\text{p},\text{n})^{90}\text{Nb}$, using an enriched target (51.45% natural abundance) for high radioisotopic purity, and produces a product with minimal contamination and a peak cross section of approximately 750 mb [72]. $^{\text{nat}}\text{Nb}(\text{p},\text{x})^{90}\text{Nb}$ offers a possible alternative pathway using a natural target, at the expense of a smaller peak cross section. ^{90}Nb may be produced directly with an approximately 370 mb peak cross section and 99% radioisotopic purity, or could be produced as a $^{90}\text{Mo}/^{90}\text{Nb}$ generator, which would have nearly 100% radioisotopic purity by using protons below the $^{\text{nat}}\text{Nb}(\text{p},5\text{n})$ threshold of 45.76 MeV. However, the greatest problem with using the $^{\text{nat}}\text{Nb}(\text{p},\text{x})$ reaction to produce ^{90}Nb is the inability to separate the radioisotope from the target itself, rendering the production of a high-specific activity product impossible.

Finally, ^{82m}Rb ($t_{1/2} = 6.472 \pm 0.006$ h, $\epsilon = 100\%$ to ^{82}Kr [99]) is a diagnostic and emerging Auger-therapy agent, typically seen as a contaminant in $^{82}\text{Sr}/^{82}\text{Rb}$ generators [74]. It is commonly produced via $^{82}\text{Kr}(\text{p},\text{n})$ at 10–15 MeV, using an enriched ^{82}Kr gaseous target, with a peak cross section of approximately 400 mb at 12 MeV [74]. Production via $^{\text{nat}}\text{Nb}(\text{p},\text{x})$ offers the use of metallic, natural abundance targetry, but requires significantly higher energy (>80 MeV) protons, peaking at approximately 20 mb near 600 MeV [75]. It is clear that this production route offers no advantage over existing $^{82}\text{Kr}(\text{p},\text{n})$ routes for in-house production.

Chapter 3

Measurement of nuclear excitation functions for proton induced reactions ($E_p = ??? - 55$ MeV) on natural Fe

LOW-ENERGY proton beams are used to produce a wide range of radionuclides for use in medical treatments and research. In particular, medical cyclotrons (most commonly in K=18 or K=30 configurations) are responsible for producing the overwhelming majority of routine clinical radionuclides. As of 2015, an international network of more than 1,200 medical cyclotrons are currently in operation, regularly extracting proton and deuteron beams [145]. As a result, in developing production pathways for novel radionuclides, being able to leverage this network of cyclotrons presents one of the greatest pathways to enable widespread utilization of next-generation, personalized medical radionuclides. Production routes using low-energy proton and deuteron beams can be easily exploited by this network of cyclotrons, without the need for investment in additional infrastructure beyond new production targets and radiochemical modules. This investment pales in comparison to the costs associated with commissioning a new medical cyclotron, and likely offers the fastest pathway to mass clinical applications of novel radionuclides.

It is for this reason that we chose to pursue the low-energy production of ^{51}Mn and $^{52\text{g}},^{52\text{m}}\text{Mn}$ as the first novel radionuclides in the nuclear data campaign within the Bay Area Nuclear Data Group. This was performed as the first science measurement in this campaign, following a successful fielding run in April 2016, to test our ability to measure cross sections in stacked-target experiments. The medical community's desire for $^{51,52}\text{Mn}$ production was first brought to my attention while attending the 16th International Workshop on Targetry and Target Chemistry (in Santa Fe, NM) in the Fall of 2016. Several talks were presented at this workshop, discussing the biological uptake, early imaging studies, and promise of new imaging applications based on ^{51}Mn and $^{52\text{g}},^{52\text{m}}\text{Mn}$ [6]. However, a common theme amongst these presentations was the lack of well-established production pathways for these radionuclides. Higher-energy production routes (using copper and cobalt targetry) offered decent yields, but

very low radiochemical purity. Lower-energy production routes were identified as one of the highest-priority interests for the community, but these were impeded by the paucity of cross section data using the desired cobalt and iron targetry routes. Following the workshop, our group decided to take on this task by performing a stacked-target experiment using natural iron foils, with titanium and copper monitor foils.

This chapter details a new measurement for the production cross sections of the $^{51,52}\text{Mn}$ PET isotopes, using low-energy proton beams. A series of stacked target thin-foil activation experiments have been conducted at the LBNL 88-Inch Cyclotron, as part of a larger campaign to address deficiencies in cross-cutting nuclear data needs. In the process, a set of 38 measured cross sections for $^{\text{nat}}\text{Fe(p,x)}$, $^{\text{nat}}\text{Cu(p,x)}$, and $^{\text{nat}}\text{Ti(p,x)}$ reactions between threshold and 55 MeV, as well as 5 independent measurements of isomer branching ratios, are reported. Variance minimization techniques were employed to correct for uncertainties in the characterization of the stack components, often the largest cause of uncertainties in energy and fluence assignments. From a development perspective, this measurement provided the first evidence of the significant impact played by the adhesives on the Kapton tape used to contain the individual stacked targets. While this may seem obvious, the compounding contributions to the slowing of the beam due to the adhesive has been neglected in similar work performed at LANL-IPF to date. While this is expected to play a limited role at high beam energies, it becomes increasingly important for proton energies below 25 MeV. In addition to the interest in the production of $^{51,52}\text{Mn}$ for PET research, this measurement offered an opportunity to study the distribution of angular momentum in compound nuclear and direct pre-equilibrium reactions, ia observation of the $^{52\text{m}}\text{Mn}$ ($t_{1/2} = 21.1 \pm 0.2$ min; $J^\pi = 2^+$) to $^{52\text{g}}\text{Mn}$ ($t_{1/2} = 5.591 \pm 0.003$ d; $J^\pi = 6^+$) ratio [27, 90].

3.1 Abstract

A stack of thin Fe foils was irradiated with 55 MeV and 25 MeV proton beams at Lawrence Berkeley National Laboratory's 88-Inch Cyclotron, to investigate the $^{\text{nat}}\text{Fe(p,x)}$ nuclear reaction channels as a pathway for low-energy production of the emerging non-standard PET radionuclides ^{51}Mn and $^{52\text{m,g}}\text{Mn}$. A set of 38 measured cross sections for $^{\text{nat}}\text{Fe(p,x)}$, $^{\text{nat}}\text{Cu(p,x)}$, and $^{\text{nat}}\text{Ti(p,x)}$ reactions between threshold and 55 MeV, as well as 5 independent measurements of isomer branching ratios, are reported. These are useful in medical and basic science radionuclide productions at low energies. The $^{\text{nat}}\text{Cu(p,x)}^{56}\text{Co}$, $^{\text{nat}}\text{Cu(p,x)}^{62}\text{Zn}$, and $^{\text{nat}}\text{Cu(p,x)}^{65}\text{Zn}$ monitor reactions were used to determine proton fluence, with all activities quantified via HPGe spectrometry. Variance minimization techniques were employed to reduce systematic uncertainties in proton energy and fluence, improving the reliability of these measurements. The measured cross sections are shown to be in excellent agreement with literature values, and have been measured with improved precision compared with previous measurements. This work also reports the first measurement of the $^{\text{nat}}\text{Nb(p,x)}^{82\text{m}}\text{Rb}$

reaction, and of the independent cross sections for ${}^{nat}\text{Cu}(p,x){}^{52g}\text{Mn}$ and ${}^{nat}\text{Nb}(p,x){}^{85g}\text{Y}$ in the 40–90 MeV region. *A priori* predictions of the reaction modeling codes CoH, EMPIRE, and TALYS are compared with experimentally measured values and used to explore the differences between codes for the ${}^{nat}\text{Fe}(p,x)$, ${}^{nat}\text{Cu}(p,x)$, and ${}^{nat}\text{Ti}(p,x)$ reactions, illustrating that these codes fail to reproduce the deposition of angular momentum at both compound and pre-compound energies.

3.2 Introduction

The next generation of nuclear medicine would appear to be based upon the production of novel, emerging radionuclides [10]. The targeted and personalized nature of therapy and imaging applications using these novel radionuclides makes possible an improvement in clinical practice, offering many patients the possibility for better survival rates and quality lives [9, 11]. While the chemical and radioactive decay properties of many of these radionuclides are well-established, their broad-scale clinical applications are reliant upon well-characterized nuclear data to facilitate large-scale production. One particular group of emerging radionuclides are the various positron-emitting isotopes of manganese, which have been identified as having potential for a range of diagnostic applications [146–151]. In particular, a significant interest has been expressed in producing the emerging radionuclides ${}^{51}\text{Mn}$ for clinical use in metabolic PET studies, as well as ${}^{52g}\text{Mn}$ for pre-clinical imaging of neural and immune processes via PET [6]. As part of a larger campaign to address deficiencies in cross-cutting nuclear data needs, our group has performed a measurement of the nuclear excitation functions of the radionuclides ${}^{51}\text{Mn}$, ${}^{52m}\text{Mn}$, and ${}^{52g}\text{Mn}$. This was carried out in a thin-foil stacked-target experiment, using proton irradiation of natural iron foils with titanium and copper monitor foils. While recent work has been performed in the 40–100 MeV energy region, this work seeks to complement these measurements and extend them down to reaction thresholds, to investigate the feasibility of production using the international network of low-energy medical cyclotrons [6].

Manganese radionuclides are desirable for radiopharmaceutical applications, as manganese is a chemically versatile element, biologically relevant, and essential in trace quantities. Manganese possesses well-established biochemistry, and has been proven to be chelated well by DOTA for tracking monoclonal antibodies, with high biostability at neutral pH [147]. ${}^{52}\text{Mn}$ ($t_{1/2} = 5.591 \pm 0.003$ d, $I_{\beta^+} = 29.4\%$, $E_{\beta^+, avg} = 0.242$ MeV) has been shown to be useful for immunoPET applications, with its rapid blood clearance offering the possibility for imaging within minutes of injection [27]. Its lifetime allows for immunoPET imaging up to 2–3 weeks after administration, giving ${}^{52}\text{Mn}$ a longer duration for useful imaging than the more established immunoPET agents ${}^{89}\text{Zr}$ or ${}^{64}\text{Cu}$ [147]. ${}^{52}\text{Mn}$ has high uptake in the heart, liver, kidneys, and pancreas, making it a useful diagnostic agent for pancreatic β -cell, insulinoma, and porphysome imaging. However, its long lifetime and unfavorable decay gamma-rays (notably, its 744.233 keV [$I_\gamma = 90.0 \pm 1.2\%$], 935.544 keV [$I_\gamma = 94.5 \pm 1.3\%$], and 1434.092 keV [$I_\gamma = 100.0 \pm 1.4\%$] lines) make it undesirable for clinical applications, but easily

shipped worldwide and highly suitable for pre-clinical imaging [27]. The 52m Mn isomer ($t_{1/2} = 21.1 \pm 0.2$ min, $I_{\beta^+} = 96.6\%$, $E_{\beta, \text{avg}} = 1.172$ MeV) offers a much stronger positron emission branch than 52g Mn, but its short lifetime makes production and handling difficult, and its high-intensity gamma emission (1434.06 keV [$I_\gamma = 98.2 \pm 0.5\%$]) contributes significantly to patient dose [27]. Another emerging manganese radionuclide is 51 Mn ($t_{1/2} = 46.2 \pm 0.1$ min, $I_{\beta^+} = 97.09\%$, $E_{\beta, \text{avg}} = 0.973$ MeV), whose short lifetime makes it clinically suited for rapid metabolic studies [90]. 51 Mn has a comparable positron branch and energy to 52m Mn, more suitable for clinical use than the soft positron emissions of 52g Mn. In addition, 51 Mn lacks any strong decay gamma-rays (its longer-lived daughter 51 Cr [$t_{1/2} = 27.704 \pm 0.003$ d] has only a single 320.0284 keV [$I_\gamma = 9.910 \pm 0.010\%$] line), making it the best choice of these radionuclides for clinical imaging applications [90].

While these efforts have been motivated by the production cross section of the 51,52g,52m Mn radionuclides for PET studies, this experiment offers an opportunity to study the distribution of angular momentum in compound nuclear and direct pre-equilibrium reactions via observation of the 52m Mn ($t_{1/2} = 21.1 \pm 0.2$ min; $J^\pi = 2^+$) to 52g Mn ($t_{1/2} = 5.591 \pm 0.003$ d; $J^\pi = 6^+$) ratio [27, 90]. Measurements of isomer-to-ground state ratios have been used for over 20 years to probe the spin distribution of excited nuclear states in the $A \approx 190$ region [25, 26]. These measurements provide a range of cross section data invaluable to not only the medical isotope production community, but also serve to measure the spin distribution in $f_{7/2}$ subshell nuclei via the observation of isomer-to-ground state ratios, and as new data to improve the predictive capabilities of reaction modeling codes. In addition, these experiments provide valuable insight into the challenges involved in precision cross section data measurements.

3.3 Experimental Methods and Materials

The work described herein follows the methods utilized in our recent work and established by Graves *et al.* for monitor reaction characterization of beam energy and fluence in stacked target irradiations [6, 8].

3.3.1 Stacked-target design

Update these energies after finalizing the analysis...

A pair of target stacks were constructed for this work, due to the large energy range desired to be spanned. One stack covers the 55–20 MeV range and the other covers 25–5 MeV, to minimize the systematic uncertainties associated with significant degradation of beam energy. In addition, the complementary energy of the stacks helps build confidence through multiple overlapping measurements between 20–25 MeV. A series of nominal 25 μm nat Fe foils (99.5%), 25 μm nat Ti foils (99.6%), and 25 μm nat Cu foils (99.95%) were used (all from Goodfellow Corporation, Coraopolis, PA 15108, USA) targets were used. In each stack, seven foils of each metal were cut down to 2.5×2.5 cm squares and characterized — for each foil, length and width measurements were taken at four different locations using a digital caliper

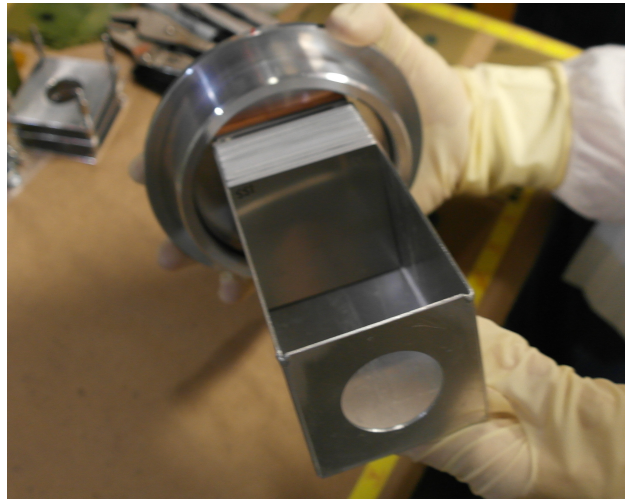


Figure 3.1: Photograph of the assembled 25 MeV target stack, before it was mounted in the beamline. The proton beam enters through the circular entrance in the foreground, and the upstream stainless steel profile monitor (SS-5) is visible at the front of the stack.

(Mitutoyo America Corp.), thickness measurements were taken at four different locations using a digital micrometer (Mitutoyo America Corp.), and four mass measurements were taken using an analytical balance after cleaning the foils with isopropyl alcohol. Using these length, width, and mass readings, the areal density and its uncertainty (in mg/cm^2) for each foil was calculated. The foils were tightly sealed into “packets” using two pieces of 3M 1205-Series Kapton polyimide film tape — each piece of tape consists of 38.1 μm of an acrylic adhesive (nominal 4.49 mg/cm^2) on 25.4 μm of a polyimide backing (nominal 3.61 mg/cm^2). The sealed foils were mounted over the hollow center of a 1.5875 mm-thick aluminum frame. Targets of 6061 aluminum alloy serve as proton energy degraders between energy positions. The target box, seen in Figure 3.1, is machined from 6061 aluminum alloy, and mounts on the end of an electrically-isolated beamline. The specifications of both target stack designs for this work are presented in Table 3.1.

Both target stacks were assembled and separately irradiated at the Lawrence Berkeley National Laboratory (LBNL), using the 88-Inch Cyclotron, a K=140 sector-focused cyclotron. The 25 MeV stack was irradiated for approximately 20 minutes with a nominal current of 100 nA, for an anticipated integral current of 31.61 nAh. The 55 MeV stack was irradiated for approximately 10 minutes with a nominal current of 120 nA, for an anticipated integral current of 20.78 nAh. The beam current, measured using a current integrator on the electrically-isolated beamline, remained stable under these conditions for the duration of each irradiation. The proton beam incident upon each stack’s upstream stainless steel profile monitor had a maximum energy of either 25 or 55 MeV, with an approximately 2% energy width due to multi-turn extraction — these energy profiles were used for all later analysis. Following end-of-bombardment (EoB), each stack was removed from the beamline and disassembled. All activated foils were transported to a counting lab for gamma spectrometry, which started

Table 3.1: Specifications of the 25 MeV and 55 MeV target stack designs in the present work. The proton beam enters the stack upstream of the SS-5 and SS-3 profile monitors, respectively, and is transported through the stack in the order presented here. The 6061 aluminum degraders have a measured density of approximately 2.69 g/cm³. Their areal densities were determined using the variance minimization techniques described in this work and our earlier paper [8]. A 316 stainless steel foil is inserted at both the front and rear of each target stack as a monitor of the beam's spatial profile, by developing radiochromic film (Gafchromic EBT3) after end-of-bombardment (EoB).

25 MeV Target layer	Measured thickness	Measured areal density (mg/cm ²)	Uncertainty in areal density (%)	55 MeV Target layer	Measured thickness	Measured areal density (mg/cm ²)	Uncertainty in areal density (%)
SS profile monitor SS-5	130.94 μm	100.57	0.17	SS profile monitor SS-3	130.9 μm	100.48	0.17
Fe-08	26.25 μm	19.69	0.17	Fe-01	25.75 μm	20.22	0.21
Ti-14	25.01 μm	10.87	0.36	Ti-01	25.88 μm	11.09	0.16
Cu-14	24.01 μm	17.49	0.40	Cu-01	28.81 μm	22.40	0.11
Al Degrader E-09	256.5 μm	—	—	Al Degrader A-1	2.24 mm	—	—
Fe-09	26.5 μm	19.90	0.09	Fe-02	25.5 μm	19.91	0.13
Ti-15	23.81 μm	10.97	0.11	Ti-02	25.74 μm	10.94	0.24
Cu-15	21.81 μm	17.63	0.46	Cu-02	28.75 μm	22.32	0.40
Al Degrader H-01	127.09 μm	—	—	Al Degrader A-2	2.24 mm	—	—
Fe-10	26.5 μm	19.84	0.11	Fe-03	25.25 μm	20.00	0.27
Ti-16	24.6 μm	10.96	0.32	Ti-03	25.91 μm	11.25	0.15
Cu-16	22.01 μm	17.22	0.25	Cu-03	28.86 μm	22.49	0.20
Fe-11	27.26 μm	19.96	0.17	Al Degrader C-1	0.97 mm	—	—
Ti-17	25.01 μm	10.88	0.25	Fe-04	25.25 μm	19.93	0.33
Cu-17	29 μm	21.91	0.33	Ti-04	25.84 μm	10.91	0.18
Fe-12	27.01 μm	20.03	0.12	Cu-04	28.78 μm	22.38	0.29
Ti-18	25.01 μm	11.00	0.87	Al Degrader C-2	0.97 mm	—	—
Cu-18	28.75 μm	22.33	0.14	Fe-05	25.64 μm	20.02	0.24
Fe-13	26.25 μm	20.05	0.16	Ti-05	25.86 μm	10.99	0.30
Ti-19	26.6 μm	11.01	0.22	Cu-05	28.77 μm	22.35	0.12
Cu-19	28.75 μm	22.32	0.19	Al Degrader C-3	0.97 mm	—	—
Fe-14	25.75 μm	20.11	0.19	Fe-06	25.75 μm	20.21	0.26
Ti-20	27.01 μm	11.06	0.35	Ti-06	25.5 μm	11.15	0.23
Cu-20	28.26 μm	22.34	0.28	Cu-06	28.83 μm	22.43	0.10
SS profile monitor SS-6	131.5 μm	100.99	0.17	Al Degrader C-4	0.97 mm	—	—
				Fe-07	25.76 μm	19.93	0.19
				Ti-07	25.75 μm	11.17	0.33
				Cu-07	28.76 μm	22.34	0.24
				Al Degrader H-02	127.04 μm	—	—
				SS profile monitor SS-4	131.21 μm	101.25	0.16

approximately 30 minutes following the end of each irradiation.

3.3.2 Quantification of induced activities

A single detector was used in this measurement, an ORTEC GMX Series (model #GMX-50220-S) High-Purity Germanium (HPGe) detector. The detector is a nitrogen-cooled coaxial n-type HPGe with a 0.5 mm beryllium window, and a 64.9 mm diameter, 57.8 mm long crystal. Samples were counted at fixed positions ranging 5–60 cm (5% maximum permissible dead-time) from the front face of the detector, with a series of standard calibration sources used to determine energy and efficiency for each position. The foils were counted for a period of 4 weeks following end-of-bombardment (EoB), to accurately quantify all induced activities. An example of one of the gamma-ray spectra collected in such a fashion is shown in Figure 3.2. For all spectra collected, net peak areas were fitted using the gamma spectrometry analysis code FitzPeaks [152], which utilizes the SAMPO fitting algorithms for gamma ray spectra [33].

The net counts in each fitted gamma-ray photopeak were converted into activities for the decaying activation products, using calibrated detector efficiencies and gamma-ray intensities for each transition. The nuclear decay data used in this work is tabulated, for reference, in Table 3.7 and Table 3.8 of Appendix 3.6. Corrections for gamma-ray attenuation within each foil packet were made, using photon attenuation coefficients from the XCOM photon cross sections database [35]. The total propagated uncertainty in activity is the quadrature sum of the uncertainty in fitted peak areas, uncertainty in detector efficiency calibration, and uncertainty in the gamma-ray branching ratio data.

As in our previous work, these activities used to calculate cross sections, and are differentiated between cumulative and independent [8]. For the first observable product nuclei in a mass chain, its (p,x) cross section will be reported as a cumulative cross section (σ_c), which is the sum of direct production of that nucleus, as well as decay of its precursors and any other independent cross sections leading to that nucleus. Cumulative cross sections will be reported whenever it is impossible to use decay spectrometry to distinguish independent production of a nucleus from decay feeding. For all remaining observed reaction products in the mass chain, and cases where no decay precursors exist, independent cross sections (σ_i) will be reported, allowing for determination of the independent production via subtraction and facilitating comparison to reaction model calculations. Solutions to the first- and higher-order Bateman equations are used for separation of feeding contributions from decay precursors, that independent cross sections may be reported [36, 37].

3.3.3 Proton fluence determination

In addition to the stack's overall beam current measurements using beamline current integrators, thin nat Ti and nat Cu foils were included along with the nat Fe targets at each energy position, to monitor beam current at each position within the stack. The IAEA-recommended nat Ti(p,x) 46 Sc, nat Ti(p,x) 48 V, nat Cu(p,x) 62 Zn, and nat Cu(p,x) 63 Zn monitor reactions were

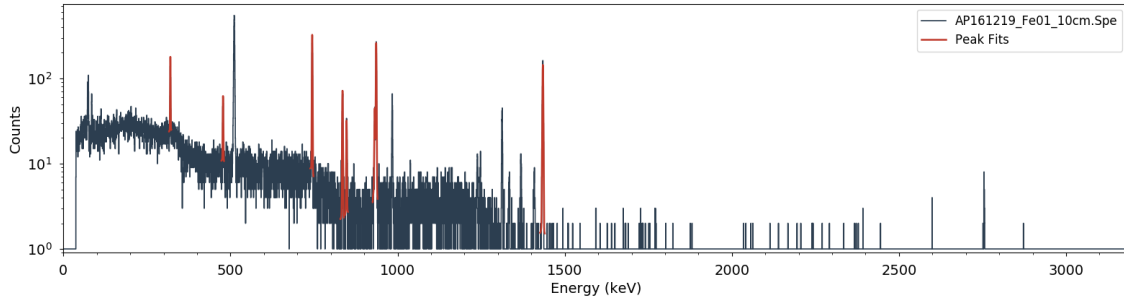


Figure 3.2: Replace this figure!!! A gamma spectrum collected from an activated Fe foil at approximately 80 MeV. While the majority of observed reaction products are visible in this spectrum, the ^{51}Cr , $^{52\text{m}}\text{Mn}$, and $^{52\text{g}}\text{Mn}$ decay lines, which form the primary reaction channels of interest, are clearly isolated from surrounding peaks.

used for proton fluence measurement [153]. As in our previous work, the integral form of the well-known activation equation was used to determine proton fluence ($I\Delta t$), in order to account for energy loss across each monitor foil:

$$I\Delta t = \frac{A_0\Delta t}{\rho\Delta r (1 - e^{-\lambda\Delta t}) \int \sigma(E) \frac{d\phi}{dE} dE} \quad (3.1)$$

The propagated uncertainty in proton fluence is calculated as the quadrature sum of (1) the uncertainty in quantified EoB activity, (2) uncertainty in the duration of irradiation (conservatively estimated at 60 s, to account for any transient changes in beam current), (3) uncertainty in foil areal density, (4) uncertainty in monitor product half-life (included, but normally negligible), (5) uncertainty in IAEA recommended cross section (using values from the 2017 IAEA re-evaluation [153]), and (6) uncertainty in differential proton fluence (from transport simulations).

3.3.4 Proton transport calculations

Estimates of the proton beam energy for preliminary stack designs were calculated using the Anderson & Ziegler (A&Z) stopping power formalism [41–43]. However, the more rigorous Monte Carlo N-Particle transport code MCNP6.1 was used for simulation of the full 3-D target stack, to determine the full proton energy and fluence distribution for each foil [44]. 10^8 source protons were used for all MCNP simulations, which places the statistical uncertainty in proton energy distributions at less than 0.01%. As with the determination of proton fluence in monitor foils, the progressively increasing energy straggles towards the rear of each stack is accounted for using the differential proton fluence from MCNP simulation of proton transport. These energy distributions $\frac{d\phi}{dE}$ are used to calculate a flux-weighted average proton energy $\langle E \rangle$, which accounts for the slowing-down of protons within a foil (particularly in the

low-energy stack) and reports the effective energy centroid for each foil:

$$\langle E \rangle = \frac{\int E \frac{d\phi}{dE} dE}{\int \frac{d\phi}{dE} dE} \quad (3.2)$$

To report a complete description of the representative energy for each foil, a bin width is provided through the energy uncertainty, calculated as the full width at half maximum (FWHM) of the MCNP6-modeled energy distribution for each foil.

To correct for a spread in the apparent proton fluence, seen most strongly in rear stack positions, the “variance minimization” techniques utilized in our recent work and established by Graves *et al.* have been used to reduce uncertainty in proton fluence assignments [6, 8]. This method is based on the assumption that the independent measurements of proton fluence from the different monitor reactions used in this work should all be consistent at each energy position. Assuming that the recommended monitor reaction cross sections and MCNP6-modeled energy distributions are both accurate, residual disagreement in the observed proton fluences is thus primarily due to poorly characterized stopping power in simulations, or a systematic error in the areal densities of the stack components. This disagreement is minor at the front of the stack, and gets progressively worse as the beam is degraded, due to the compounded effect of systematic uncertainties in stack areal densities.

When performing a variance minimization, it is important to apply this variation of effective areal density to the stack components which have the most significant impact on beam degradation, as any systematic error in the areal densities used for these components will cause a disagreement in the observed fluences. For the 55 MeV stack, the aluminum degraders are used for variance minimization, as they make up more than 80% of the areal density of the stack, and this play the largest role in beam degradation.

Update this post-results! For the 25 MeV stack, the Kapton tape was chosen for variance minimization, as the foil packets themselves are responsible for the majority of beam degradation. While it only makes up approximately 20% of the low-energy stack’s areal density, the Kapton surrounding each foil packet has a greater areal density than the foil itself. In addition, it is far easier to directly characterize the areal density of the metallic foils than it is for the Kapton, resulting in only an approximate value for the latter. This is of relatively minor consequence for higher-energy irradiations (especially relative to any beam degraders), but the stopping power of the Kapton at this energy range may cause as much as a loss of 0.5 MeV by the rear of this stack, making the precise areal density a source of significant uncertainty.

In performing the minimization, the areal density of each of the aluminum degraders (for the 55 MeV stack) were varied uniformly in MCNP6 simulations by a factor of up to $\pm 25\%$ of nominal values, to find the effective density which minimized variance in the measured proton fluence at the lowest energy position (Ti-07, Cu-07). For the 25 MeV stack, the areal density of the E-09 and H-01 aluminum degraders was taken from that reached in the minimization of the 55 MeV stack. Using this value, the areal density of each of the Kapton tape layers were

likewise varied uniformly by a factor of up to $\pm 25\%$ of nominal values, to find the effective density which minimized variance in the measured proton fluence at the next-to-lowest energy position (Ti-19, Cu-19). These lowest energy positions were chosen as minimization candidates, as they are the most sensitive to systematic uncertainties in stack design, due to the compounded effect of proton stopping powers. In the 25 MeV stack, activity was not seen in gamma spectrometry for the lowest-energy (Ti-20, Cu-20) monitor foils, implying that the beam was stopped at some point in between Fe-14 and Ti-20. This observation is conclusive proof that the true areal densities of the stack components differs from nominally measured values (primarily for the difficult-to-characterize Kapton tape), as transport calculations using nominal areal densities predict that the beam should exit the stack (at the SS-6 profile monitor) with an energy of approximately 7 MeV. As a result, this position was not used for minimization, with the Ti-19 and Cu-19 position being the lowest-energy reliable monitor foils in the stack. The results of the minimization technique indicate a clear minimum in proton fluence variance for flux-weighted average **41.34 MeV** protons entering the last energy position of the 55 MeV stack. This is approximately **2 MeV** lower than the nominal MCNP6 simulations, and approximately **3 MeV** lower than nominal A&Z calculations, both of which used the nominal 2.80 g/cm^3 measured density of the aluminum degraders. This energy corresponds to an aluminum areal density of **2.52%** greater than nominal measurements, and serves as a lump correction for other minor systematic uncertainties in stack design, including stack areal densities and incident beam energy. Similarly, for the 25 MeV stack, variance minimization converges on flux-weighted average **41.34 MeV** protons entering the Fe-13/Ti-19/Cu-19 energy position, which is approximately **2 MeV** lower than the nominal MCNP6 simulations, and approximately **3 MeV** lower than nominal A&Z calculations. This energy corresponds to a Kapton tape areal density of **2.52%** greater than nominal measurements. The impact of this variance minimization for improving disagreement in proton fluence is clearly seen in Figure 3.3.

An enhanced version of the final ${}^{nat}\text{Ti}(p,x){}^{46}\text{Sc}$, ${}^{nat}\text{Ti}(p,x){}^{48}\text{V}$, ${}^{nat}\text{Cu}(p,x){}^{62}\text{Zn}$, and ${}^{nat}\text{Cu}(p,x){}^{63}\text{Zn}$ monitor reaction fluences is shown in Figure 3.4. The uncertainty-weighted mean for the two ${}^{nat}\text{Cu}(p,x)$ and two ${}^{nat}\text{Ti}(p,x)$ monitor channels was calculated at each energy position, to determine the final fluence assignments for the Cu and Ti foils, respectively, and the uncertainty-weighted mean for all four monitor channels was used to determine the final fluence assignments for the Fe foils. Uncertainty in proton fluence is calculated by error propagation of the fluence values at each energy position. These weighted-mean fluences are plotted in Figure 3.4, along with the estimated fluence according to both MCNP6 transport and an uncertainty-weighted linear χ^2 fit to the individual monitor channel fluence measurements. **Both models reproduce the observed fluence data consistently within uncertainty, with the MCNP6 model predicting a slightly greater fluence loss throughout the stack.** These models are used purely to provide an extrapolation from the highest-energy position back to the “front” of each stack, to compare with the nominal fluence measured by the beamline current integrators.

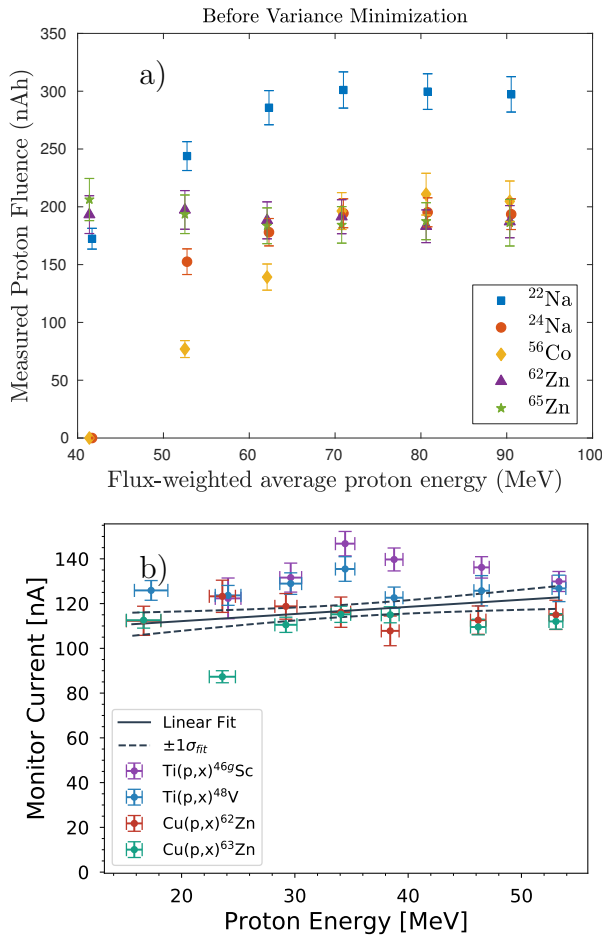


Figure 3.3: **Update this figure!!!** Results of variance minimization through enhancement of the effective areal density of the aluminum degraders by **2.52%** (55 MeV stack) and Kapton tape by **2.52%** (25 MeV stack). A noticeable reduction of variance in measured proton fluence is seen, particularly at the rear stack positions.

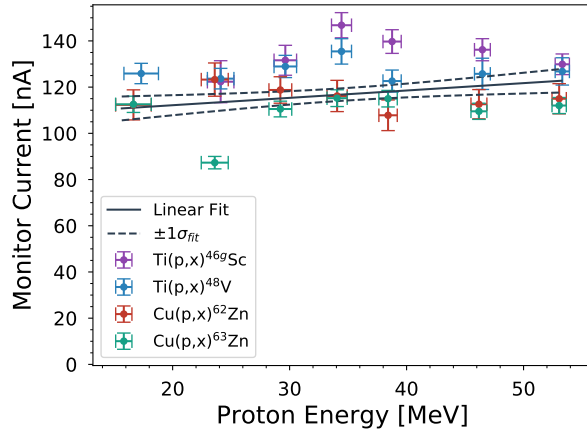


Figure 3.4: **Update this figure!!!** Final uncertainty-weighted mean proton fluences throughout the target stack, based on the variance-minimized observed fluence from the the ${}^{\text{nat}}\text{Ti}(\text{p},\text{x}){}^{46}\text{Sc}$, ${}^{\text{nat}}\text{Ti}(\text{p},\text{x}){}^{48}\text{V}$, ${}^{\text{nat}}\text{Cu}(\text{p},\text{x}){}^{62}\text{Zn}$, and ${}^{\text{nat}}\text{Cu}(\text{p},\text{x}){}^{63}\text{Zn}$ monitor reactions. The fluence drops by approximately **7.2–8.9%** from the incident fluence of **196.9–198.8 nAh** over the length of the target stack, based on fluence loss models from MCNP6 simulations and an empirical fit to fluence measurements.

3.3.5 Calculation of measured cross sections

Using the quantified EoB activities along with the variance-minimized proton fluence, it is possible to calculate the final cross sections for the various observed (p,x) reactions. While thin (≈ 10 – 20 mg/cm^2) foils were irradiated to minimize the energy bins of these cross section measurements, it is important to note that all cross sections reported here are flux-averaged over the energy distribution subtended by each foil, as seen in Figure 3.5. For both the cumulative and independent activities quantified, cross sections were calculated as:

$$\sigma = \frac{A_0}{\rho \Delta r I (1 - e^{-\lambda \Delta t})} \quad (3.3)$$

where A_0 is the EoB activity for the monitor reaction product, I is the proton current, $\rho \Delta r$ is the foil's areal density, λ is the monitor reaction product's decay constant, and Δt is the length of irradiation. The beam current, measured using a current integrator connected to the electrically-isolated target box, remained stable for the duration of the irradiation. The propagated uncertainty in cross section is calculated as the quadrature sum of the uncertainty in quantified EoB activity (which includes uncertainty in detector efficiencies), uncertainty in the duration of irradiation (conservatively estimated at 30 s, to account for any minor transient changes in beam current), uncertainty in foil areal density, uncertainty in monitor product half-life (included, but normally negligible), and uncertainty in proton current (quantified by error propagation of the monitor reaction fluence values at each energy position, as seen in Figure 3.4).

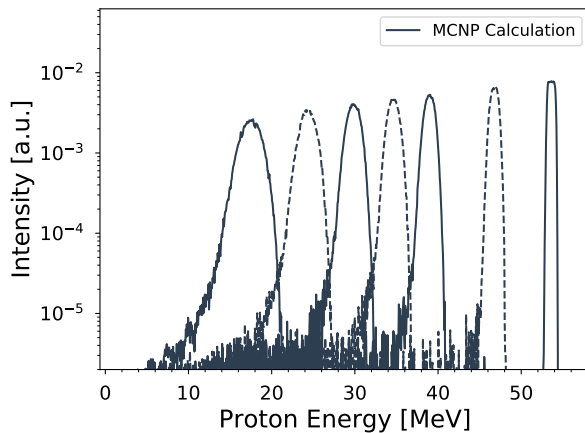


Figure 3.5: Add 25 MeV stack tallies here! Final variance minimized incident proton energy distributions for the Fe foils, as simulated in MCNP6. The distribution tallies in each foil are all normalized to be per source proton, which was 10^8 in all simulations. As the beam is degraded, proton energy distributions become visibly broadened due to straggling, and drop in magnitude due to scattering losses.

3.4 Results and Discussion

3.4.1 Measurement of nuclear excitation functions

After irradiation, all foils were confirmed to still be sealed inside their Kapton packets, verifying that no activation products were lost due to packet failure and dispersal. With the exception of two foils (Cu-20 and Ti-20), each activated foil had a small “blister” under the Kapton tape layer, caused by a combination of thermal swelling and the formation of short-lived beta activities. This blister verifies that the primary proton beam was incident upon the foil, and provided the first evidence (before gamma-ray spectrometry) that the beam was stopped in the stack between Fe-14 and Ti-20. Using the $^{nat}\text{Cu}(p,x)^{56}\text{Co}$, $^{nat}\text{Cu}(p,x)^{62}\text{Zn}$, and $^{nat}\text{Cu}(p,x)^{65}\text{Zn}$ monitor reactions, as discussed in subsection 3.3.4, a fluence of $198.8 \pm 6.7 \text{ nAh}$ was calculated to be incident upon the 55 MeV target stack using the MCNP6 fluence model, and a fluence of $196.9 \pm 11.3 \text{ nAh}$ using the linear fit model. Similarly, for the 25 MeV stack, a fluence of $198.8 \pm 6.7 \text{ nAh}$ was calculated to be incident upon the 55 MeV target stack using the MCNP6 fluence model, and a fluence of $196.9 \pm 11.3 \text{ nAh}$ using the linear fit model. All of these are consistent with the nominal fluence of 20.78 nAh (for the 55 MeV stack) and 31.61 nAh (for the 25 MeV stack) measured using the beamline current integrators. As fluence loss scales with $\sigma_{tot}\rho\Delta r$, it is expected that an extrapolation back to the stack entrance (through the SS-3/SS-5 profile monitors) will underestimate the nominal fluence incident upon the box. This incident fluence dropped by approximately 8.9% to $180.9 \pm 5.4 \text{ nAh}$ (and by 7.2% to $182.7 \pm 13.5 \text{ nAh}$ using the linear fit model) over the length of the target stack, which is consistent with similar measurements at IPF in the past [6, 8]. This loss of fluence

Table 3.2: Measured cross sections for the various $^{nat}\text{Fe}(p,x)$ reaction products observed in this work. Cumulative cross sections are designated as σ_c , independent cross sections are designated as σ_i .

	Production cross section (mb)					
E_p (MeV)	$89.74^{+0.48}_{-0.43}$	$79.95^{+0.67}_{-0.64}$	$70.17^{+0.91}_{-0.85}$	$61.58^{+1.03}_{-0.98}$	$52.10^{+1.25}_{-1.20}$	$41.05^{+1.62}_{-1.54}$
$^{64}\text{Cu}(\sigma_i)$	38.7 ± 2.7	42.8 ± 2.4	45.5 ± 2.7	50.2 ± 2.8	55.7 ± 3.0	63.3 ± 3.6

Table 3.3: Measured cross sections for the various $^{nat}\text{Cu}(p,x)$ reaction products observed in this work. Cumulative cross sections are designated as σ_c , independent cross sections are designated as σ_i .

	Production cross section (mb)					
E_p (MeV)	$89.74^{+0.48}_{-0.43}$	$79.95^{+0.67}_{-0.64}$	$70.17^{+0.91}_{-0.85}$	$61.58^{+1.03}_{-0.98}$	$52.10^{+1.25}_{-1.20}$	$41.05^{+1.62}_{-1.54}$
$^{64}\text{Cu}(\sigma_i)$	38.7 ± 2.7	42.8 ± 2.4	45.5 ± 2.7	50.2 ± 2.8	55.7 ± 3.0	63.3 ± 3.6

Table 3.4: Measured cross sections for the various $^{nat}\text{Ti}(p,x)$ reaction products observed in this work. Cumulative cross sections are designated as σ_c , independent cross sections are designated as σ_i .

	Production cross section (mb)					
E_p (MeV)	$89.37^{+0.47}_{-0.45}$	$79.55^{+0.68}_{-0.64}$	$69.70^{+0.90}_{-0.85}$	$61.07^{+1.05}_{-0.98}$	$51.51^{+1.25}_{-1.21}$	$40.34^{+1.58}_{-1.55}$
$^{93m}\text{Mo}(\sigma_i)$	0.97 ± 0.20	1.29 ± 0.15	1.62 ± 0.24	1.85 ± 0.15	1.86 ± 0.14	2.00 ± 0.15

is due to a combination of (p,x) reactions throughout the target stack, as well as large-angle deflections (primarily in the aluminum degraders) from scattering of the beam.

Using the final proton fluence at each energy position, cross sections for (list of residual products) were extracted for (p,x) reactions on ^{nat}Fe foils in the 0–55 MeV region, as recorded in Table 3.2. For (p,x) reactions on ^{nat}Cu foils, the (p,x) cross sections for (list of residual products) were extracted, as recorded in Table 3.3. For (p,x) reactions on ^{nat}Ti foils, the (p,x) cross sections for (list of residual products) were extracted, as recorded in Table 3.4. In addition, as there exist a number of isomers with radioactive ground states in these mass regions, independent measurements of isomer-to-ground-state branching ratios for $^{52m/g}\text{Mn}$, $^{58m/g}\text{Co}$, $^{85m/g}\text{Y}$, $^{87m/g}\text{Y}$, and $^{89m/g}\text{Nb}$ were extracted and are recorded in Table 3.5. Comparisons of the measured cross sections and isomer branching ratios with literature data (retrieved from EXFOR [46]) are seen in the figures of Appendices 3.7 and 3.8. The propagated uncertainty in these cross sections varies widely based on the reaction product in question, with the major components arising from uncertainty in EoB activity (± 3 –7%), proton fluence (± 4 –6%), and foil areal density (± 0.1 –0.6%).

Table 3.5: Measured isomer-to-ground-state branching ratios for the various $^{nat}Fe(p,x)$, $^{nat}Cu(p,x)$, and $^{nat}Ti(p,x)$ reaction products observed in this work.

E_p (MeV)	Isomer branching ratio					
	$89.74^{+0.48}_{-0.43}$	$79.95^{+0.67}_{-0.64}$	$70.17^{+0.91}_{-0.85}$	$61.58^{+1.03}_{-0.98}$	$52.10^{+1.25}_{-1.20}$	$41.05^{+1.62}_{-1.54}$
$^{nat}Cu(p,x)^{52}Mn$	0.603 ± 0.066	0.581 ± 0.062	0.598 ± 0.095	0.81 ± 0.13	–	–
$^{nat}Cu(p,x)^{58}Co$	0.757 ± 0.088	0.80 ± 0.10	0.858 ± 0.099	0.767 ± 0.097	0.82 ± 0.12	0.98 ± 0.10
E_p (MeV)	$89.37^{+0.47}_{-0.45}$	$79.55^{+0.68}_{-0.64}$	$69.70^{+0.90}_{-0.85}$	$61.07^{+1.05}_{-0.98}$	$51.51^{+1.25}_{-1.21}$	$40.34^{+1.58}_{-1.55}$
$^{nat}Nb(p,x)^{85}Y$	0.828 ± 0.051	0.724 ± 0.080	0.736 ± 0.080	–	–	–
$^{nat}Nb(p,x)^{87}Y$	0.746 ± 0.063	0.865 ± 0.063	0.893 ± 0.063	0.936 ± 0.070	0.961 ± 0.075	0.676 ± 0.065
$^{nat}Nb(p,x)^{89}Nb$	–	–	0.193 ± 0.021	0.130 ± 0.011	–	–

Placeholder text follows...fill in actual discussion of results...

These results have several notable features. The various $^{nat}Cu(p,x)$ cross sections measured here are in excellent agreement with the body of measurements in the literature, but have been measured nearly exclusively with the highest precision to date. Similarly, the various $^{nat}Nb(p,x)$ cross sections measured here are in excellent agreement with literature data, which is far more sparse in the 40–90 MeV region than for $^{nat}Cu(p,x)$ — fewer than three existing measurements have been performed for the majority of the reactions presented here. Indeed, the $^{nat}Nb(p,x)^{83}Sr$, $^{nat}Nb(p,x)^{85}Y$, $^{nat}Nb(p,x)^{89}Nb$, $^{nat}Nb(p,x)^{90}Mo$, $^{nat}Nb(p,x)^{91m}Nb$, and $^{nat}Nb(p,x)^{98m}Mo$ reactions each possess no more than a total of three data points in this energy region. Not only do the $^{nat}Nb(p,x)$ measurements in this work fill in the sparse data in this energy region, but they have been measured with the highest precision relative to existing literature data.

This work presents the first measurements of several observables in this mass region, including the $^{nat}Nb(p,x)^{82m}Rb$ reaction in the 40–90 MeV region, the independent cross section for $^{nat}Cu(p,x)^{52g}Mn$, and the ^{52m}Mn (2^+) / ^{52g}Mn (6^+) isomer branching ratio via $^{nat}Cu(p,x)$. The cumulative cross sections from these data are also consistent with existing measurements of the cumulative $^{nat}Cu(p,x)^{52}Mn$ cross section. Similarly, this work offers the first measurement of the independent cross sections for $^{nat}Nb(p,x)^{85g}Y$, as well as the first measurement of the ^{85m}Y ($9/2^+$) / ^{85g}Y ($1/2^-$) isomer branching ratio via $^{nat}Nb(p,x)$.

Comment on details of 51/52Mn production here...

Notably, this work is the most well-characterized measurement of the $^{nat}Nb(p,x)^{90}Mo$ reaction below 100 MeV to date, with cross sections measured at the 4–6% uncertainty level. This is important, as it presents the first step towards characterizing this reaction for use as a proton monitor reaction standard below 100 MeV. $^{nat}Nb(p,x)^{90}Mo$ can only be populated through the (p,4n) reaction channel, so no corrections for (n,x) contamination channels or decay down the A=90 isobar are needed. ^{90}Mo possesses seven strong, distinct gamma lines which can easily be used for its identification and quantification. Finally, the production of ^{90}Mo in the 40–90 MeV region is quite strong, with a peak cross section of approximately 120 mb. Combining the reaction yield and gamma abundance, the use of approximately

23 mg/cm² Nb targets easily provided sufficient counting statistics for activity quantification in the 40–90 MeV region. This result presents the first step towards the use of ⁹⁰Mo as a clean and precise charged particle monitor reaction standard in irradiations up to approximately 24 h in duration.

Placeholder text follows...Comment on production pathways of medical radionuclides...

In addition to the ^{nat}Nb(p,x)⁹⁰Mo measurement, this experiment has also yielded measurements of a number of additional emerging radionuclides with medical applications. These include the non-standard positron emitters ⁵⁷Ni [6, 47–49], ⁶⁴Cu [50–57], ⁸⁶Y [30, 31, 58–66], ⁸⁹Zr [67–71], ⁹⁰Nb [72, 73], and the Auger-therapy agent ^{82m}Rb [74, 75]. Production of these radionuclides offers no major advantages over established pathways, with the generally lower yields and radioisotopic purities failing to justify the convenience of natural targets via ^{nat}Cu(p,x) and ^{nat}Nb(p,x). The one possible exception to this trend is the non-standard positron emitter ⁵⁷Ni ($t_{1/2} = 35.60 \pm 0.06$ h, $\epsilon=100\%$ to ⁵⁷Co [76]) — the ⁵⁷Ni/⁵⁶Ni ratio of production rates is approximately 290 at 61.58 MeV, and varies from 45–75 at the 70–90 MeV positions. This ^{nat}Cu(p,x) route offers both higher yield and higher radioisotopic purity over the established ^{nat}Co(p,3n) pathway, which suffers from approximately fivefold greater ⁵⁶Ni contamination [77, 78].

3.4.2 Comparison of reaction modeling with experimental results

As mentioned before, cumulative cross sections are reported here for the first observable product nuclei in a mass chain, or whenever it is impossible to use decay spectrometry to distinguish direct production of a nucleus from decay feeding. For all remaining observed reaction products in the mass chain, and cases where no decay precursors exist, independent cross sections are reported, allowing for determination of the direct production via subtraction. This, in turn, offers the opportunity to gauge the predictive capabilities of modern nuclear models used in the reaction evaluation process. The reaction channels with independent cross sections were compared to calculations with the reaction modeling codes EMPIRE, TALYS, and CoH, run with the default settings. The default optical models and E1 gamma strength function models for each code are presented in Table 3.6. The large energy range covered by many of the exit channels, which extends significantly beyond the range of pure compound nuclear/evaporation, allows the data to be used to study the differences between these modeling codes in the pre-equilibrium regime.

The default level density in both CoH and TALYS is the Gilbert-Cameron model, which uses a Constant Temperature model below a critical energy and Fermi Gas model above it. The default level density in EMPIRE is the Enhanced Generalized Superfluid Model (EGSM) which uses the Generalized Superfluid model below a critical energy, and Fermi Gas model above it [79]. The EGSM densities are normalized to D_0 and the discrete levels, but in such a way that only the level density below the neutron separation energy is effected by the discrete levels chosen for the normalization. All three codes use a two-exciton phenomenological model to calculate the pre-equilibrium cross section, but the specific implementation differs between the codes.

Table 3.6: Default settings for the reactions codes

<u>Code Version</u>	<u>Proton/Neutron Optical Model</u>	<u>Alpha Optical Model</u>	<u>E1 γSF Model</u>
EMPIRE-3.2.3[80]	Koning-Delaroche[81]	Avrigeanu(2009)[82]	Modified Lorentzian[83]
TALYS-1.8[84]	Koning-Delaroche	Specific folded potential[84]	Brink-Axel Lorentzian[84]
CoH-3.5.1[85, 86]	Koning-Delaroche	Avrigeanu(1994)[87]	Generalized Lorentzian[85, 86]

Given the large number of exit channels in this data set, we will limit our discussion to cross sections for the production of a specific residual nucleus with experimental data through the full rise and fall of the peak, and at least 1% of the total reaction cross section. Exit channel cross sections that do not exhibit the full rise and fall of the peak, which is identified as being dominated by the formation of a compound nucleus, do not provide enough information to analyze the calculations. Residual nuclei like ^{88}Zr that can be produced by multiple reaction channels, such as $(\text{p},\alpha 2\text{n})$ and by $(\text{p},2\text{p}4\text{n})$ are also not discussed in depth. We exclude reactions with cross sections with peak values less than 1% of the total reaction cross section because their behavior is extremely sensitive to more dominant channels. The three residual nuclei that meet all of the above criteria for which there is an independent measurement of the residual production cross section are ^{86}Y , ^{90}Mo , and ^{90}Nb .

The $^{93}\text{Nb}(\text{p},\alpha\text{p}3\text{n})^{86}\text{Y}$ reaction channel, which peaks at approximately 70 MeV, is well within the compound regime for the entire energy region of this experiment (Figure 2.9). The data collected on this residual is consistent with the one other data set available, taken in 1997 by Michel *et al.* [77]. The $^{93}\text{Nb}(\text{p},4\text{n})^{90}\text{Mo}$ and $^{93}\text{Nb}(\text{p},\text{p}3\text{n})^{90}\text{Nb}$ channels both peak early in the energy region, around 50 MeV, and the data clearly show the full rise, peak, and fall of the compound cross section (Figure 2.10 & 2.11). In both of these channels, this data is consistent with the data by Titarenko *et al.* in 2011 [75].

The ^{90}Nb production cross section exhibits a persistent pre-equilibrium “tail” that keeps the channel open well after the compound cross section has fallen away. TALYS, TENDL, and CoH seem to have the correct shape for this pre-equilibrium cross section, with magnitudes that are just slightly too low. EMPIRE, however, does not level off as much as the data and the other codes are seen to, and misses the high-energy data points.

In all three channels, the TALYS, TENDL, and CoH calculations rise, peak, and fall at lower energies than the data, while EMPIRE calculates the peak to occur at higher energies. For ^{90}Mo , the EMPIRE peak is representative of the data. For ^{86}Y and ^{90}Nb , the peak is missed by all three of the codes.

The magnitudes of the TALYS and TENDL calculations are consistently too low in the three channels studied here. For ^{86}Y , CoH and EMPIRE also predict smaller cross sections than the data would suggest, which may be influenced by incorrect modeling of other, stronger, channels. The magnitude of the peak in the CoH calculation for ^{90}Mo is consistent with the data, while EMPIRE predicts a cross section that is approximately the same magnitude as that of TALYS. ^{90}Nb is one of the strongest measured channels, approximately 10% of the total reaction cross section, and the values from the three codes are all consistent, but too small, in magnitude.

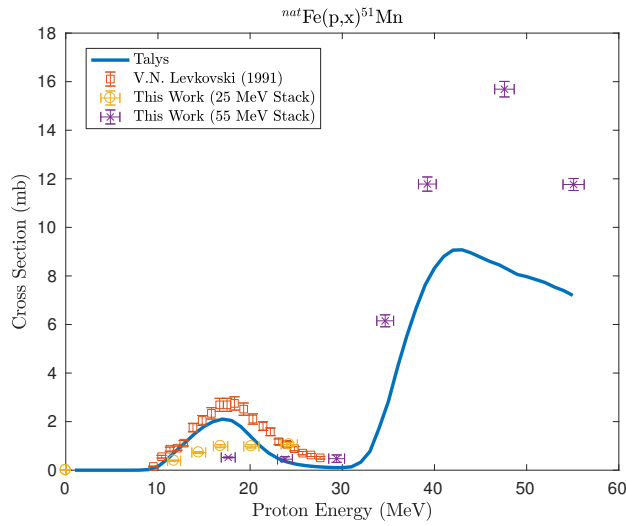


Figure 3.6: Measured $^{93}\text{Nb}(\text{p},\text{x})^{86}\text{Y}$ cross section, with the $^{93}\text{Nb}(\text{p},\alpha\text{p}3\text{n})^{86}\text{Y}$ reaction channel visibly peaking at approximately 70 MeV.

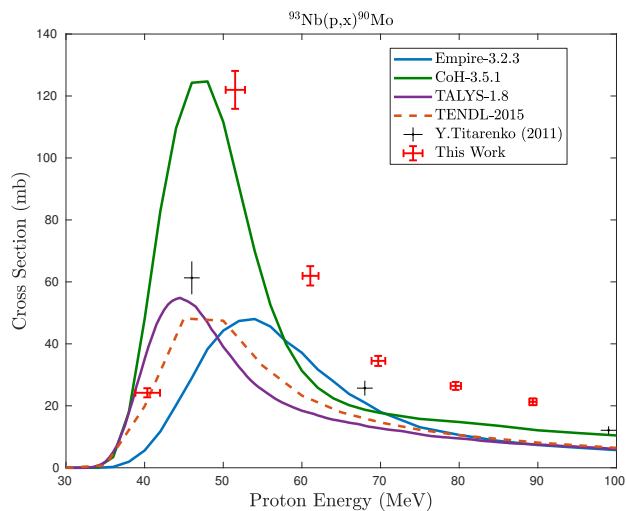


Figure 3.7: Measured $^{93}\text{Nb}(\text{p},\text{x})^{90}\text{Mo}$ cross section, with the $^{93}\text{Nb}(\text{p},4\text{n})^{90}\text{Mo}$ reaction channel visibly peaking at approximately 50 MeV.

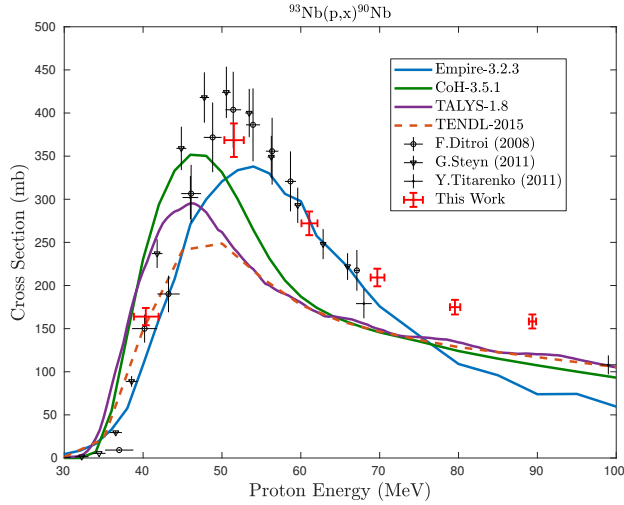


Figure 3.8: Measured $^{93}\text{Nb}(\text{p},\text{x})^{90}\text{Nb}$ cross section, with the $^{93}\text{Nb}(\text{p},\text{p}3\text{n})^{90}\text{Nb}$ reaction channel visibly peaking at approximately 50 MeV.

3.5 Conclusions

We present here a set of measurements of 38 cross sections for the $^{\text{nat}}\text{Fe}(\text{p},\text{x})$, $^{\text{nat}}\text{Cu}(\text{p},\text{x})$, and $^{\text{nat}}\text{Ti}(\text{p},\text{x})$ reactions up to 55 MeV, as well as independent measurements of five isomer branching ratios. Nearly all cross sections have been reported with higher precision than previous measurements. We report the first measurements of the $^{\text{nat}}\text{Nb}(\text{p},\text{x})^{82\text{m}}\text{Rb}$ reaction, as well as the first measurement of the independent cross sections for $^{\text{nat}}\text{Cu}(\text{p},\text{x})^{52\text{m}}\text{Mn}$, $^{\text{nat}}\text{Cu}(\text{p},\text{x})^{52\text{g}}\text{Mn}$, and $^{\text{nat}}\text{Nb}(\text{p},\text{x})^{85\text{g}}\text{Y}$ in the 40–90 MeV region. We also use these measurements to illustrate the deficiencies in the current state of reaction modeling up to 55 MeV for V $^{\text{nat}}\text{Fe}(\text{p},\text{x})$, $^{\text{nat}}\text{Cu}(\text{p},\text{x})$, and $^{\text{nat}}\text{Ti}(\text{p},\text{x})$ reactions. Finally, this work provides another example of the usefulness of the recently-described variance minimization techniques for reducing energy uncertainties in stacked target charged particle irradiation experiments.

3.6 Decay data

The lifetimes and gamma-ray branching ratios listed in these tables were used for all calculations of measured cross sections reported in this work, and have been taken from the most recent edition of Nuclear Data Sheets for each mass chain

Table 3.7: Decay data for gamma-rays observed in $^{\text{nat}}\text{Ti}(\text{p},\text{x})$ and $^{\text{nat}}\text{Cu}(\text{p},\text{x})$.

Nuclide	Half-life	E_γ (keV)	I_γ (%)
^{22}Na	2.6018(22) y	1274.537	99.940(14)

Table 3.8: Decay data for gamma-rays observed in ${}^{nat}\text{Fe}(\text{p},\text{x})$.

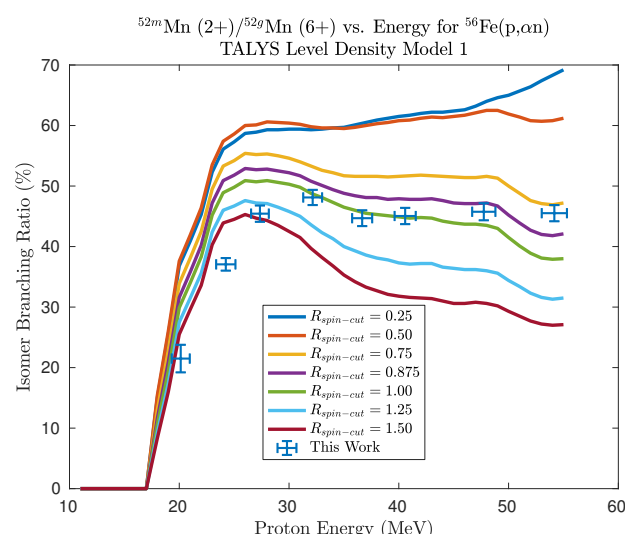
Nuclide	Half-life	E_γ (keV)	I_γ (%)
${}^{82m}\text{Rb}$	6.472(6) h	554.35	62.4(9)
	6.472(6) h	619.11	37.98(9)

3.7 Measured excitation functions

Figures of the cross sections measured in this work are presented here, in comparison with literature data

3.8 Measured isomer-to-ground state branching ratios

Plots of the isomer-to-ground state ratios measured in this work are presented here, in comparison with literature data and reaction modeling codes



3.9 Additional discussion

Additional discussion of the experimental and analytical details for this work, which will be excluded from the published journal article to preserve its scope, are included here.

88-Inch Cyclotron overview

As discussed in section 2.3, the target stacks for this work were assembled and irradiated at the 88-Inch Cyclotron at the Lawrence Berkeley National Laboratory (LBNL). The 88-Inch Cyclotron is part of the Nuclear Science Division at LBNL, and currently supports ongoing research campaigns in nuclear structure, astrophysics, heavy element studies, and accelerator and detector technology R&D. Major instrumentation at the 88-Inch Cyclotron include the Berkeley Gas-filled Separator (BGS), and the superconducting VENUS ion source, one of the most powerful Electron Cyclotron Resonance (ECR) ion sources in the world. Commissioned in 1961, the 88-Inch Cyclotron continues to operate programs of research in both basic and applied science. The machine is a iron-yoked, 300-ton, K=140 sector-focused isochronous cyclotron with both light- and heavy-ion capabilities. The machine is supported by a series of three generations of ECR ion sources designed and commissioned in-house, giving the cyclotron the capacity to extract any stable beam (with a variety of possible charge states) between protons and fully-stripped uranium beams. Protons and other light-ions are routinely available at high intensities (10–20 pμA), and most heavy-ion beams (through uranium) can be accelerated to maximum energies and currents that vary with the mass and charge state. While current administrative policy restricts operation to stable beams, the 88-Inch Cyclotron has previously run radioactive ion beams of ^{76}Kr , produced through batch mode irradiations via $^{74}\text{Se}(\alpha,2n)^{76}\text{Kr}$, which was then re-accelerated [154]. While the cyclotron has a main magnetic field capable of supporting acceleration up to K=140, at the time of writing, it routinely operates in a regime closer to an approximate K=60, due to RF power injection limitations.

A cyclotron uses a static magnetic field (typically, in the z -direction) to bend charged particles into a circular orbit, so that they can be repeatedly accelerated by a perpendicular and oscillating electric field. Injected particles are initially “kicked” into the acceleration field (at the 88-Inch Cyclotron, by a spiral inflector) and are attracted towards the negative electrode. While the particles traverse their $E \times B$ drift orbit, the polarity of the electrodes reverses, oscillating at the cyclotron frequency:

$$\omega_z(r) = \frac{qB_z(r)}{m} \quad (3.4)$$

This oscillation is synchronized such that when the particles reach the acceleration gap between the “dee” electrodes, the electric field accelerates particles forwards. As particles complete each half-orbit, and are accelerated across the gap, they continue to gain more and more kinetic energy:

$$E_k(r) = \frac{m}{2}r^2\omega_z^2(r) \quad (3.5)$$

It is important to note that in this design (the isochronous cyclotron), the magnetic field strength must increase radially, in order to maintain a constant cyclotron frequency. For convenience and easy translation between different tunes, the energy of a particular beam is often alternatively reported in terms of its energy per nucleon:

$$\frac{E_k}{A} = \frac{r^2 B_z^2(r)}{2m} \frac{q^2}{A} = K \left(\frac{Q}{A} \right)^2 \quad (3.6)$$

This gives rise to the so-called “K-factor”, which acts as a simple scaling parameter to compare the maximum acceleration energy between machines. It is important to note that this formulation neglects relativistic effects — for acceleration beyond $K \gtrsim 35$, relativistic mass corrections must be made, typically implemented through adjustments to the main field through so-called “trim coils” and “valley coils”.

One important consequence for isochronous cyclotrons is that, for a given tune (fixed K), any particles with the same charge-to-mass ratio will follow the same orbit. This is valuable to operation of the 88-Inch Cyclotron, as the ECR ion sources allow selection of ions with a particular charge state. This is exploited to produce “cocktail beams”, mixtures of ions of near-identical charge-to-mass ratio, without the need for re-tuning the cyclotron. The 88-Inch Cyclotron is home to the Berkeley Accelerator Space Effects (BASE) Facility, which uses these cocktails to provide well-characterized beams of protons, heavy ions, and other medium energy particles that simulate the space environment.

The 88-Inch Cyclotron offers a number of experimental “caves”, each dedicated to the various research programs carried out at the facility. The primary charged particle beams are extracted from the machine through the use of electrostatic deflectors, and are transported to one of several experimental caves through the use of dipole switching magnets to steer the beam, and quadrupole magnets to focus/defocus the beam’s optical profile. For all of the work described in this chapter, the irradiations were carried out in Cave 0, a cave dedicated to high-current beams, scintillator characterization, and isotope production. The target stacks described in this chapter (and seen in Figure 3.1) mount onto the end of the beamline which extends in this cave. A partial map of the 88-Inch Cyclotron facility and beamlines, highlighting the beam path to Cave 0, is presented in Figure 3.9.

Beam profile measurements

Following tuning of the 25 and 55 MeV proton beams into Cave 0, the final remaining step prior to loading the target box for irradiation is to tune the beam optics and spatial profile. In the prior fielding run from April 2016, this was performed by loading 3 pieces of the EBT3 Gafchromic film (the same as used for imaging the beam with stainless steel profile monitors) into the empty target stack holder, with one at the front end, one at the rear, and one in the middle. At this point, the target stack would be mounted into the beamline, which would be pumped down to the **200 mtorr** beamline pressure for a run. Following pumpdown, the “stack” of films would be exposed to an extremely short, low-current pulse of the tuned proton beam (approximately 0.1 nAh for 1 s), to directly expose the films and image the beam profile and

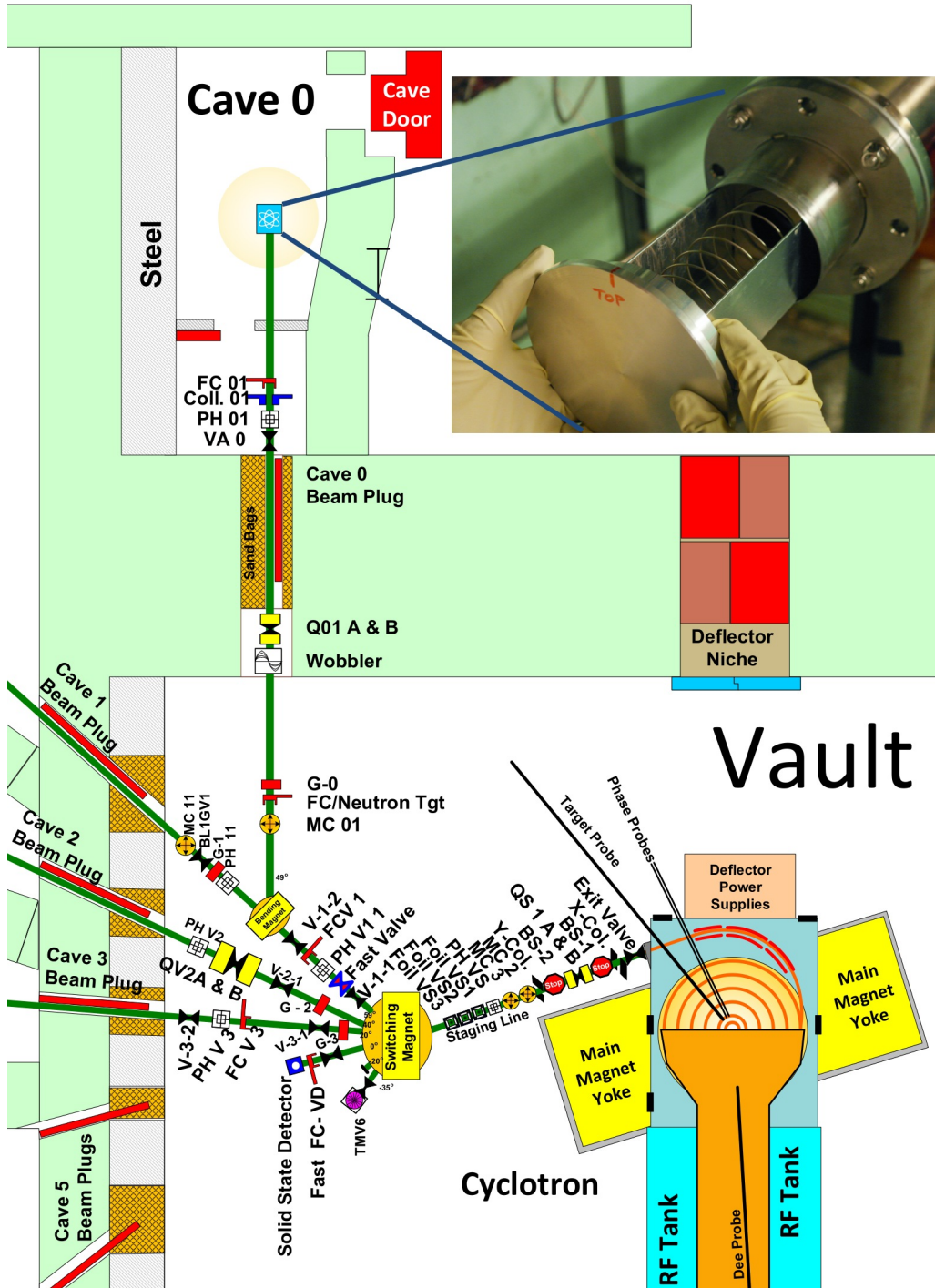


Figure 3.9: Schematic diagram of the 88-Inch Cyclotron facility and beamlines at LBNL, highlighting the beam path to Cave 0. A rear view of the target stack holder used in this work is seen here, where it mounts onto the end of the Cave 0 beamline.

optics. Running any more beam fluence than this would cause the entire film to be massively overexposed, nullifying its usefulness. At this point, the beamline would be brought up to atmosphere, and the films removed for interpretation. The cyclotron operator would then use the films to adjust the beam's horizontal and vertical position, and tune the beam optics to produce a "pencil-beam" spatial profile. This is to ensure that the beam spot will be centered on the mounted target foils, and fully constrained within the foils, under-filling them. After tuning the beam's optics, more films would be loaded, and this process would be repeated multiple times, confirming any adjustments made to improve the optics, until an acceptable beam spot was achieved. Each cycle of loading and unloading a set of films would take approximately 45 min, followed by approximately another 30 min to make any beam adjustments, followed by the 1 s film exposure. As a result, during this fielding run, optical tuning took nearly an entire day of beam time, which would be infeasible for future experiments.

To improve this process, I designed a phosphor target to mount into the end of the beamline during optics tuning, sealing onto the beamline during pumpdown via an inset o-ring. This design was based off of designs for the beam stop component of the target stack holder, but instead of featuring a solid aluminum end cap, it has a circular opening, designed to hold a glass puck. This puck forms a vacuum seal through an inset o-ring, and is held against the rear of the target by an aluminum frame. The blueprints for this phosphor are seen in Figure 3.10. On the inside (beamline-facing) side of the glass puck, a thin layer of vacuum greased was painted on, and mixed with a powdered phosphorescent paint, to create a thin phosphorescent layer. This target is mounted onto the end of the beamline during optics tuning, and has been used in all experiments since. When exposed to a low-current (approximately 0.1 nAh) beam, the phosphor glows brightly, outlining the beam profile. A low current is used, to ensure that the phosphor layer does not get overly heated and burn or flake off during tuning. By patching in a camera to the cave, the operators may tune the beam optics in real time, moving the beam spot and improving its spatial profile, while watching on a video feed from the remote camera. This has drastically shorted the optics tuning process down to less than a single hour, and has made all subsequent experiments far easier in the process. A remote view of this phosphor target during tuning is seen in Figure 3.11.

However, this phosphor target offers a fairly low-resolution image of the beam profile, mostly useful as a qualitative guide for tuning. As a result, a final film exposure is done after beam, optics appear satisfactory on the phosphor, to confirm the optics tune. After verifying that the beam spot is centered upon the target stack and focusing it to ensure that it underfills the target foils, the foils are loaded into the stack target holder, mounted in the beamline, and the irradiation commences.

These films are useful for determining the beam profile incident upon the front of each stack. However, the beam broadens as it traverses the target stack, with large-angle deflections (primarily in the aluminum degraders) from scattering of the beam. To image the actual beam profile incident upon the first foil in the stack (Fe-01 and Fe-08), a 316 stainless steel foil (SS-3 and SS-5) is inserted upstream of Fe-01 and Fe-08, for the 55 and 25 MeV stacks,

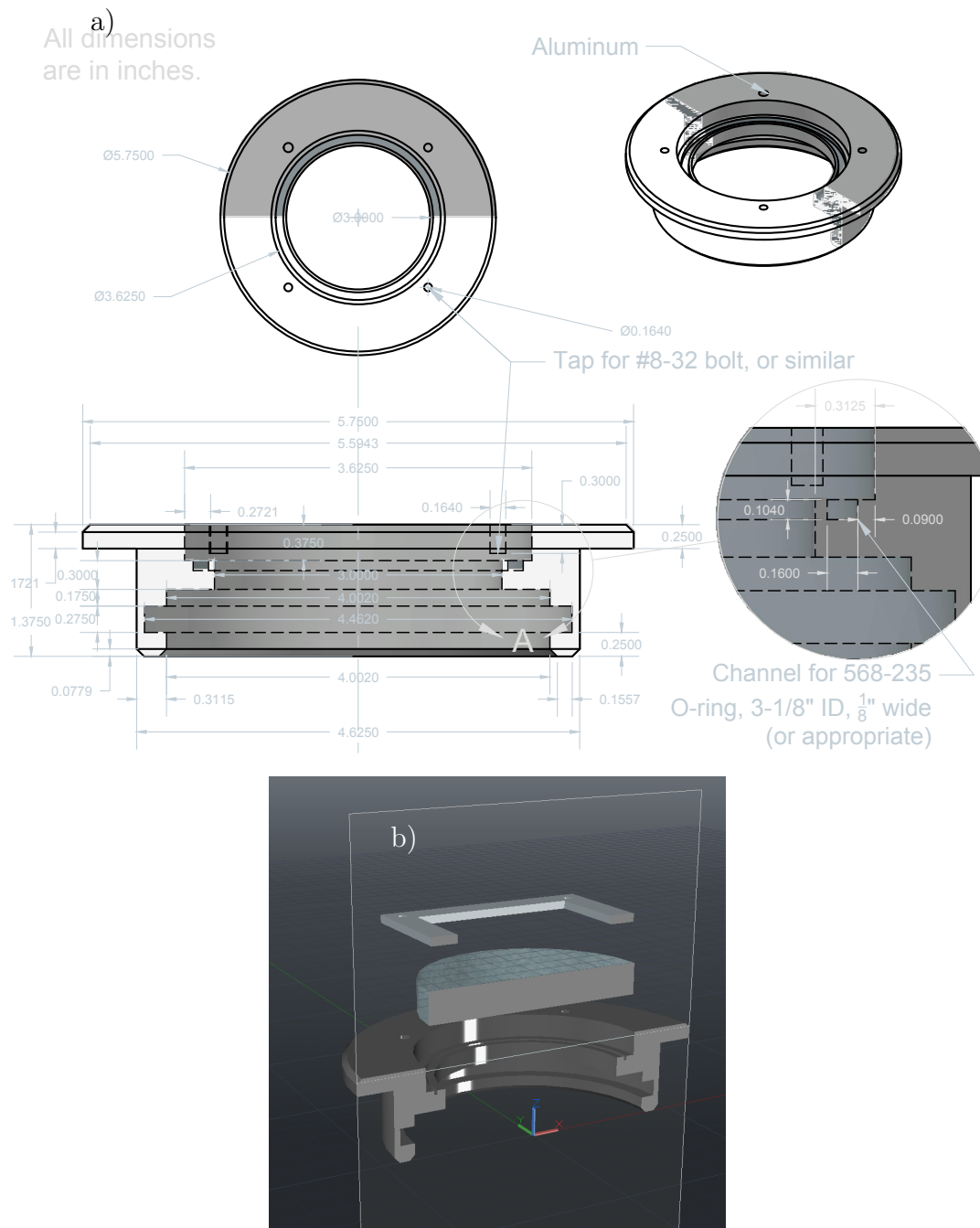


Figure 3.10: Blueprints (a) and 3D cutaway rendering (b) of the phosphor target used for real-time beam optics tuning at the 88-Inch Cyclotron.

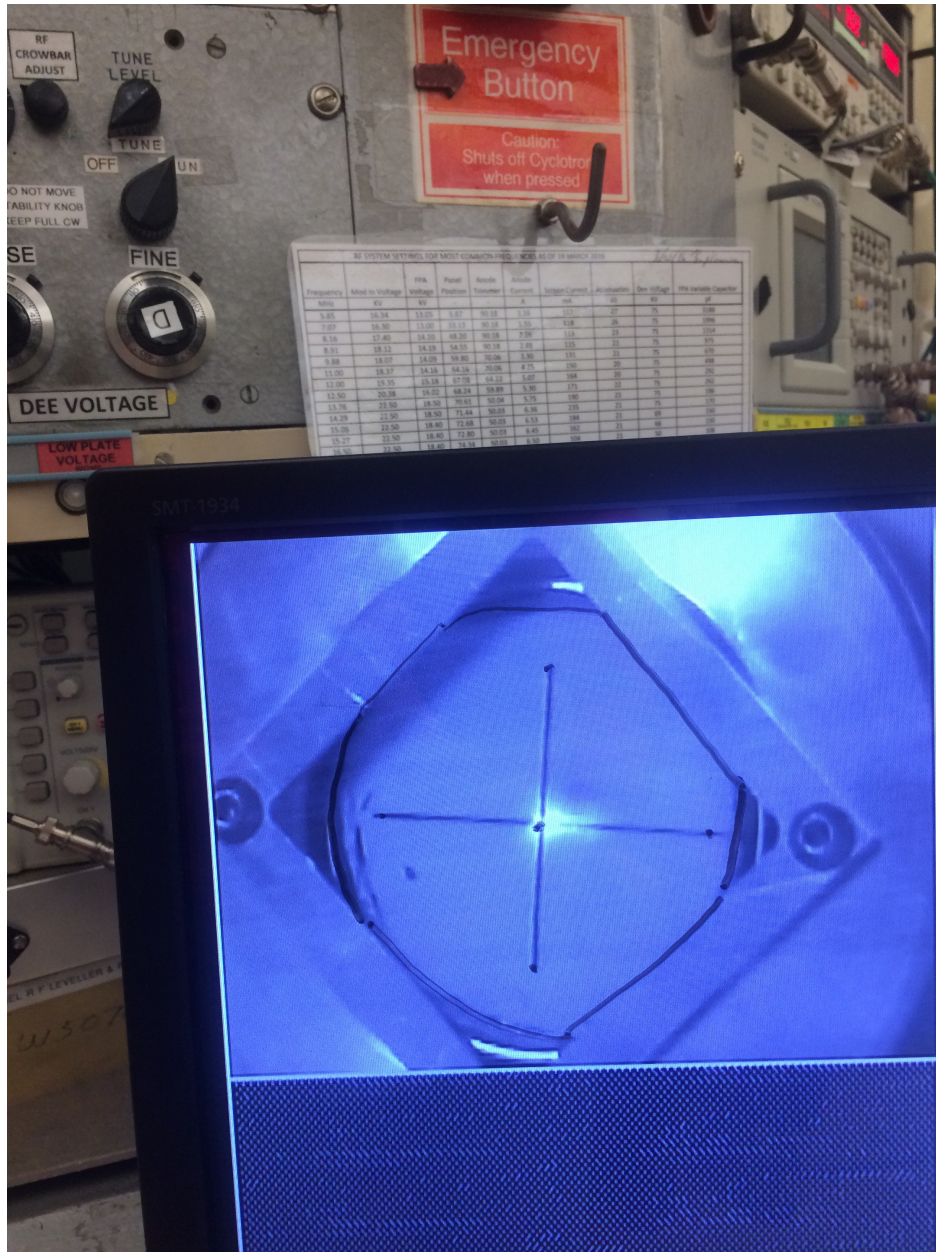


Figure 3.11: View of the remote feed of the phosphor target during beam optics tuning. The low-current proton beam used for tuning is visible as the bright glow around the reference crosshairs.

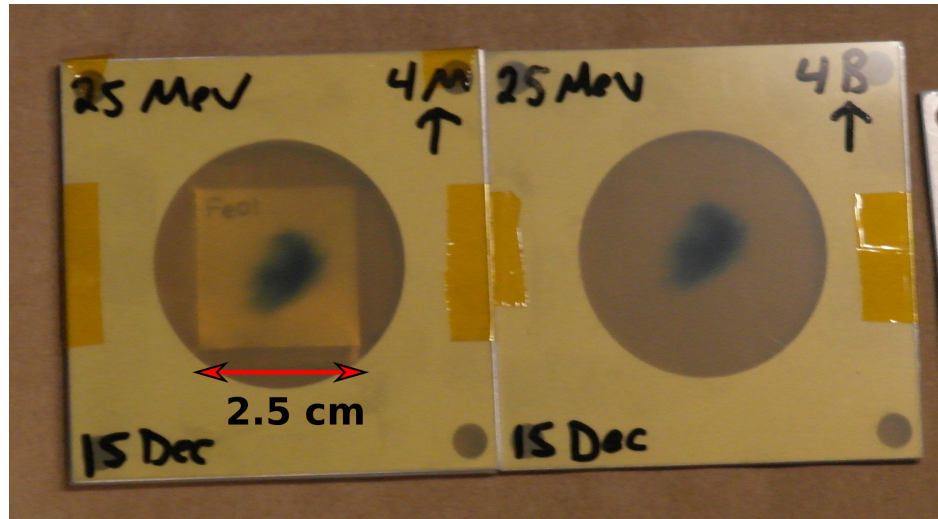


Figure 3.12: Final beam spot profile for the 25 MeV LBNL Fe(p,x) measurement. The proton beam is confirmed to be centered on the target position, and is focused to underfill the 25×25 mm target foils.

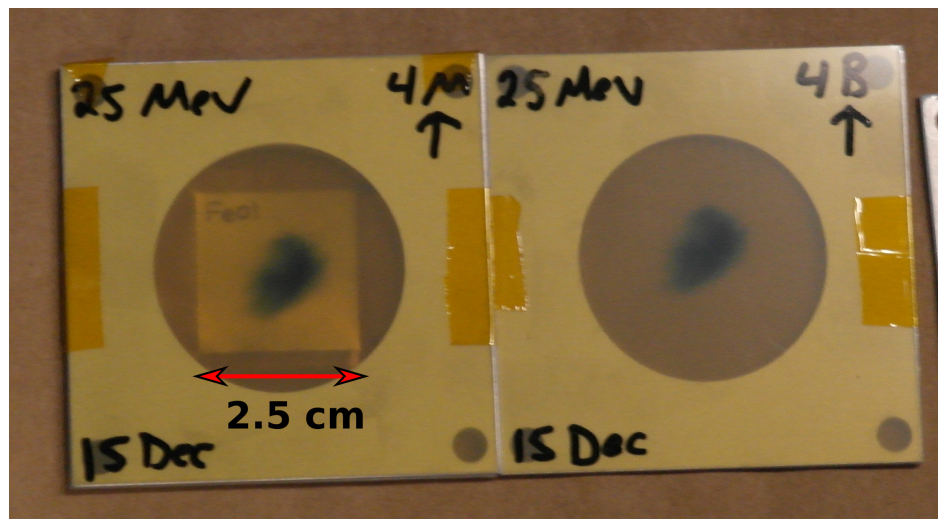


Figure 3.13: **Update this figure!!!** Final beam spot profile for the 55 MeV LBNL Fe(p,x) measurement. The proton beam is confirmed to be centered on the target position, and is focused to underfill the 25×25 mm target foils.

respectively, to serve as a beam profile monitor for the activation foils. Likewise, another stainless steel profile monitor (SS-4 and SS-6) is inserted downstream of the last foil in the stack (H-02 and Cu-20). These stainless steel monitors are cut to the same length and width as the aluminum frames used for mounting foils, and are characterized in Table 3.1.

As described in subsection 3.3.1, decay radiation emitted from the activated stainless steel foils were used to develop radiochromic film (Gafchromic EBT3), revealing the spatial profile of the beam entering and exiting the stack. The radiochromic films developed by the 55 MeV stack's SS-3 and SS-4 stainless steel beam profile monitors are seen in Figure 3.14. In addition, extra **aluminum** monitor foils mounted on aluminum frames are superimposed behind each film. It is clear from the upstream (SS-3) film that the proton beam profile was consistent with that seen in the final pre-irradiation beam spot check of Figure 3.13. The downstream (SS-4) film reveals that the beam was not completely attenuated, and clearly displays the broadening expected due to scattering in the target stack. More importantly, the beam profiles in both films appears to be completely contained within the 25×25 mm activation foils, including the beam envelope. As discussed previously in section 2.9, this confirms that the activation foils were exposed to the total beam current.

Using the image analysis code ImageJ-2.0.0, profiles of the total optical density were extracted for both the SS-3 and SS-4 radiochromic films [136]. These are seen in Figure 3.15, as relative beam intensity profiles along the major and minor axis of each film. As seen visually, for both axes, the peak beam intensity drops from SS-3 to SS-4, as the proton fluence is clearly broadened by scattering reactions in the target stack. Along the major ("horizontal") axis, the FWHM of the beam profile broadens from **0.679 cm to 1.039 cm**, and along the minor ("vertical") axis, the FWHM of the beam profile broadens from **0.453 cm to 0.902 cm**. In addition, the centroid position of the minor axis appears to shift by approximately **0.19 cm** between the front and rear of the stack. The measured beam profiles were fit using a Gaussian model with linear background, to aid in comparing the widths of each profile. The Gaussian model does well to fit the beam profiles overall, though it overestimates the peak height for a given Gaussian width. This is likely due to the fact that the beam itself has an intrinsic spatial width before any interactions with the target stack; this leads to more broadening of the beam envelope than of its core.

Similar profile measurement results are presented here for the 25 MeV stack as well. The radiochromic films developed by the 25 MeV stack's SS-5 and SS-6 stainless steel beam profile monitors are seen in Figure 3.16. In addition, extra **aluminum** monitor foils mounted on aluminum frames are superimposed behind each film. It is clear from the upstream (SS-5) film that the proton beam profile was consistent with that seen in the final pre-irradiation beam spot check of Figure 3.12. However, in a significant departure from the 55 MeV stack, no exposure is seen in the downstream (SS-6) film. This confirms the observation (based on a lack of HPGe-observed activity in the Ti-20 and Cu-20 monitor foils) that the beam was completely attenuated before the end of target stack. As discussed in subsection 3.3.4, this is primarily due to the actual target stack having a greater areal density than estimated during the stack design phase. The majority of this additional unaccounted areal density arises from the acrylic adhesive in the multiple Kapton tape layers. However, the beam profile

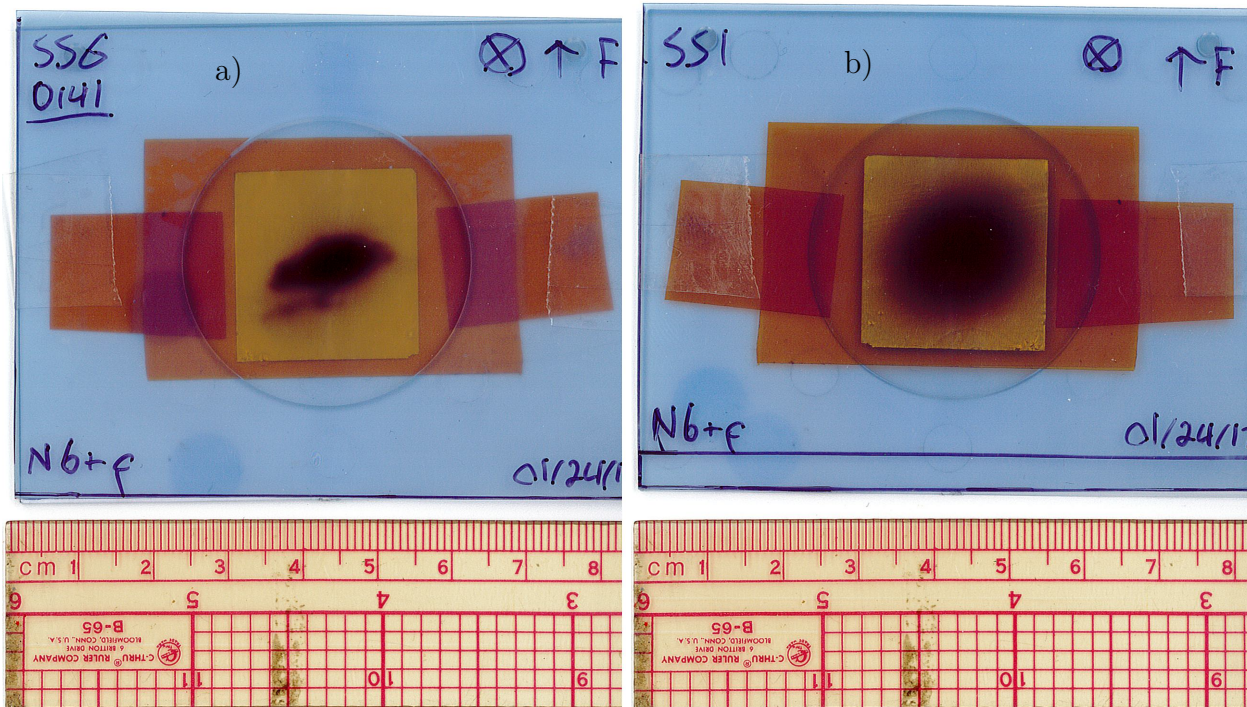


Figure 3.14: **Update this figure!!!** Radiochromic films for the 55 MeV LBNL Fe(p,x) measurement, developed by the stainless steel beam profile monitors in (a) the front of the stack (SS-3) and (b) the rear of the stack (SS-4). An unused Al monitor foils is aligned behind each film, confirming that both the beam core and envelope underfilled the activation foils.

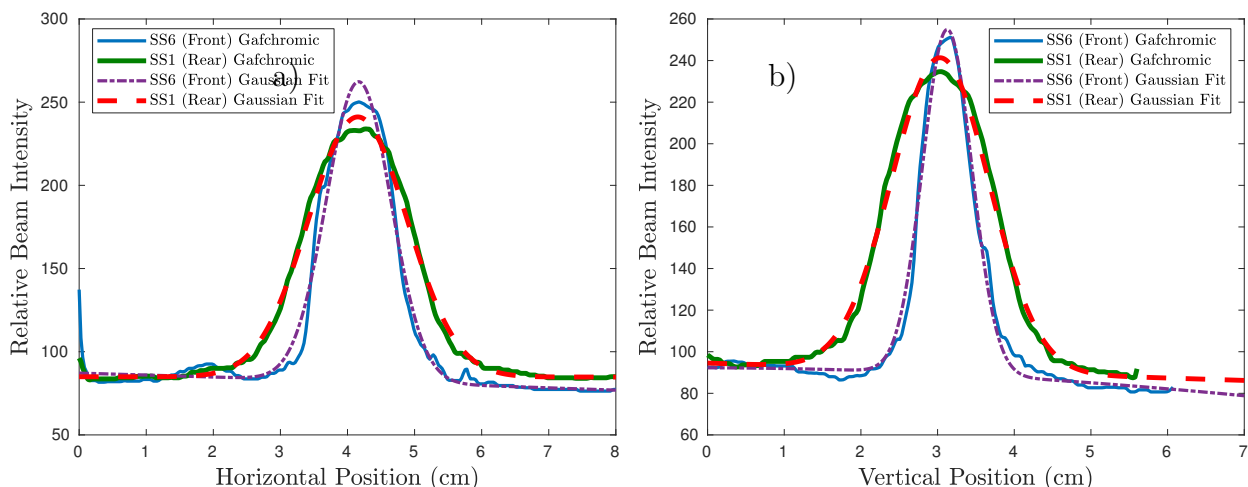


Figure 3.15: **Update this figure!!!** Relative beam intensity profiles for the radiochromic films seen in Figure 3.14. The intensity profiles were analyzed using ImageJ along (a) the major axis and (b) minor axis of each beam spot.

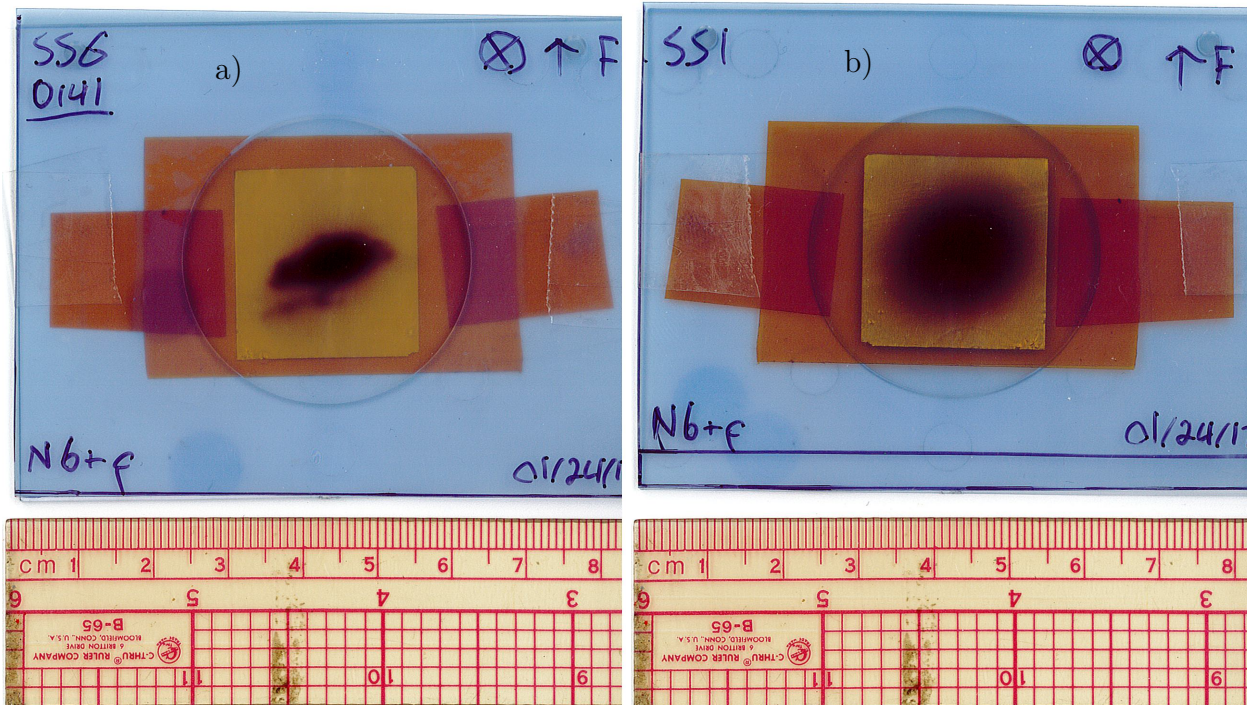


Figure 3.16: **Update this figure!!!** Radiochromic films for the 25 MeV LBNL Fe(p,x) measurement, developed by the stainless steel beam profile monitors in (a) the front of the stack (SS-5) and (b) the rear of the stack (SS-6). An unused Al monitor foils is aligned behind each film, confirming that both the beam core and envelope underfilled the activation foils. No exposure is seen in the SS-6 film, as the beam was stopped upstream within the target stack, between Fe-14 and Ti-20.

in the upstream film appears to be completely contained within the 25×25 mm activation foils, including the beam envelope. This small consolation confirms that the stack received the full entrance fluence, so the validity of the cross sections extracted from this stack still holds. Profiles of the total optical density were extracted for the SS-5 radiochromic film, seen in Figure 3.17, as relative beam intensity profiles along the major and minor axis of the film. While no commentary on the peak intensity and broadening can be provided due to the attenuation of the beam within the stack, the entrance profile may at least be reported. Along the major (“horizontal”) axis, the FWHM of the beam is **0.679 cm**, and along the minor (“vertical”) axis, the FWHM of the beam profile is **0.453 cm**.

Target preparation

As described in subsection 3.3.1, all activation foils in this work were tightly sealed into “packets” using two pieces of 3M 1205-Series Kapton polyimide film tape. The sealed foils were then mounted over the hollow center of a 1.5875 mm-thick aluminum frame. This gives

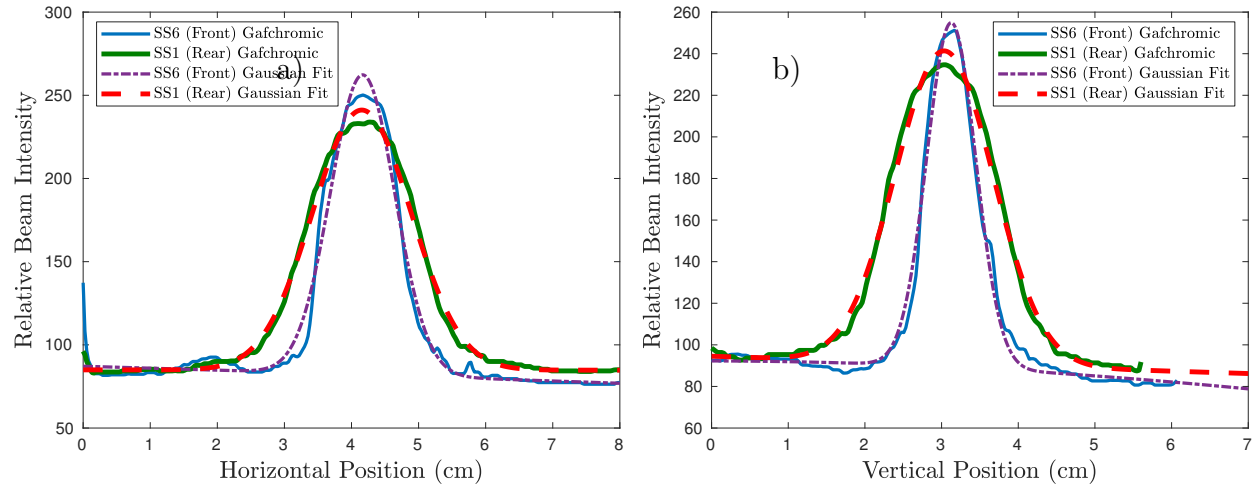


Figure 3.17: **Update this figure!!!** Relative beam intensity profiles for the radiochromic films seen in Figure 3.16. The intensity profiles were analyzed using ImageJ along (a) the major axis and (b) minor axis of each beam spot.

each foil a fixed, rigid, position, preventing it from shifting out of alignment during the mounting of the target stack holder. In addition, the hollow center is cut out such that the frame does not degrade and scatter the beam at each foil position. A number of such foils, ready to be loaded into the target holder, are seen in Figure 3.18. The width of the target stack holder is sized to match (within an approximately 1 mm tolerance) the width of the aluminum mounting frames, such that the frames are unable to slide or rotate once they are loaded. This is primarily to maintain a comparable area of exposed foil at each energy position, in the case of significant beam spot broadening, as well as to prevent movement of the frames. However, as an added precaution, a spring is inserted into the empty space between the stacked frames and the front of the target holder. The diameter of the spring is sized to be wider than the diameter of the hollow center cut out of the aluminum frames, to ensure that it is fully out of the beam's path. This spring is placed in the stack purely to provide additional compression on the stacked target frames, preventing them from sliding or rotating out of their intended position during irradiation. After loading all frames into the stack holder and securing them with the spring, the holder is mounted into the beamline, which is pumped down to **200 mtorr** for irradiation. Following irradiation, the beamline is raised back to atmospheric pressure, and the target holder is removed to a nearby work area. Foil removal is performed in this area, working quickly to separate the activated foils from the aluminum degraders and the stack holder's beam stop, which become highly activated with short-lived Al activation products. Foils are bagged up, and prepared for transfer to the counting lab.

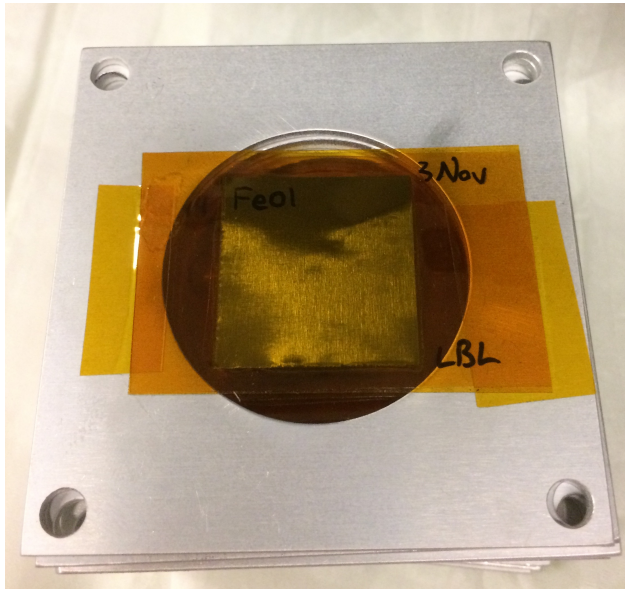


Figure 3.18: A stack of Fe, Cu, and Ti foils mounted on aluminum frames (Fe-01 visible on top), for the 55 MeV Fe(p,x) target stack. All foils are mounted over the aperture of a 1.5875 mm-thick aluminum frame.

MCNP modeling

A rendering of the 55 MeV Fe(p,x) target stack, as modeled in MCNP6, is seen in Figure 3.20. This model is the same described in subsection 3.3.4 for simulation of proton transport. The full input file for this MCNP model is included here for reference, in Appendix A.3. In this figure, the 55 MeV proton beam enters from the left of the figure, where it is incident (in the positive x direction) upon the **Inconel beam entrance window (yellow)**. The other stack elements, described in Table 3.1 are illustrated here, as well. **The green cell is the cooling water channel for the target box, the air filling the target box is shown in light blue, and the 6061 aluminum beam degraders are shown in dark blue.** The thin black lines seen in between degraders are the Nb, Cu, and Al activation points at each energy position, sealed in **Kapton tape**. The detail of each foil sealed in the Kapton is not visible here, simply due to the size scale of the stack assembly. Similarly, a rendering of the 25 MeV Fe(p,x) target stack, as modeled in MCNP6, is seen in Figure 3.21. The full input file for this MCNP model is included here for reference, in Appendix A.4.

Using this MCNP6 model, the proton energy distribution is tallied in all volumes of the stack assembly. As seen in Figure 3.5 of subsection 3.3.4, the corresponding incident proton energy distributions $\frac{d\phi}{dE}$ from MCNP6 simulation (using the variance minimized degrader density) are shown for the six irradiated Cu and Ti foils in Figure 3.22. In addition, the MCNP6 model tracks the production and transport of secondary neutrons produced through (p,xn) reactions on the target stack components. The proton energy distribution is tallied in all Ti, Cu, and Fe foils, and is seen in Figure 3.23. The neutron flux is consistently 3-4

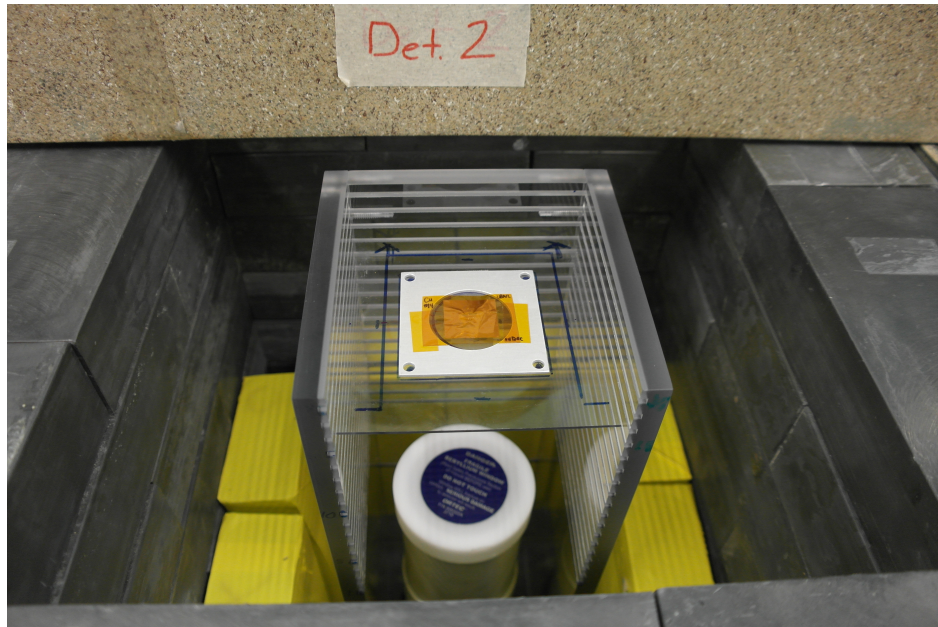


Figure 3.19: The ORTEC GMX Series (model #GMX-50220-S) High-Purity Germanium detector used for gamma spectroscopy of the activated foils, as described in subsection 3.3.2. The detector, counting foil Cu-14 in this figure, has a “ladder” permitting counting at various fixed distances (in 1 cm intervals) from the front face of the detector. With the lead shielding lid closed (for reduced background), the ladder permits counting up to 18 cm, and up to 75 cm with the lid open.

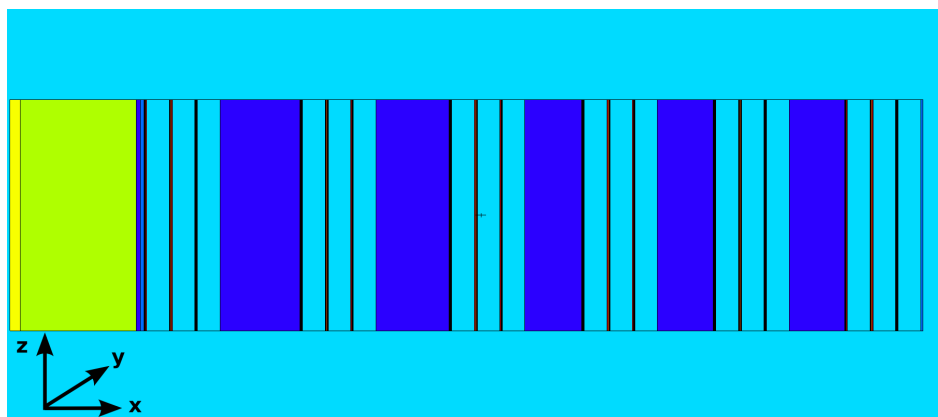


Figure 3.20: **Update this figure!!!** Simplified top-down MCNP6 model of the 55 MeV $\text{Fe}(p,x)$ target stack. The proton beam enters from the left of the figure, where it is incident upon the **Inconel beam entrance window (yellow)**. The beam is transported down the length of the stack, towards the rear of the stack on the right side of the figure.

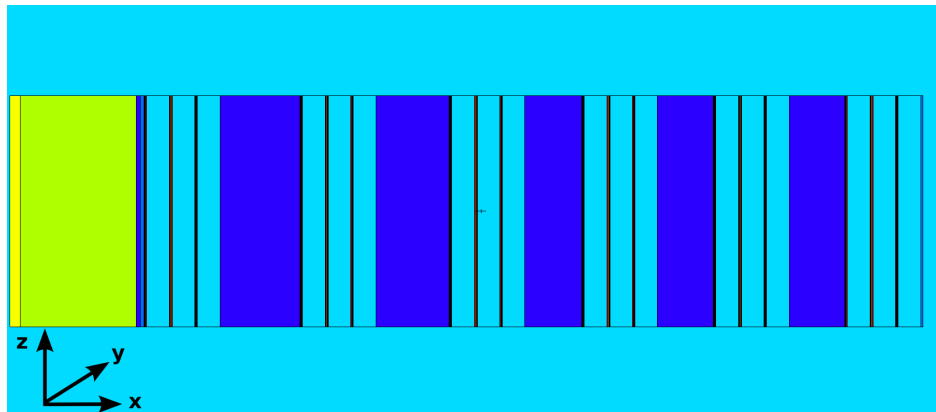


Figure 3.21: **Update this figure!!!** Simplified top-down MCNP6 model of the 25 MeV Fe(p,x) target stack. The proton beam enters from the left of the figure, where it is incident upon the Inconel beam entrance window (yellow). The beam is transported down the length of the stack, towards the rear of the stack on the right side of the figure.

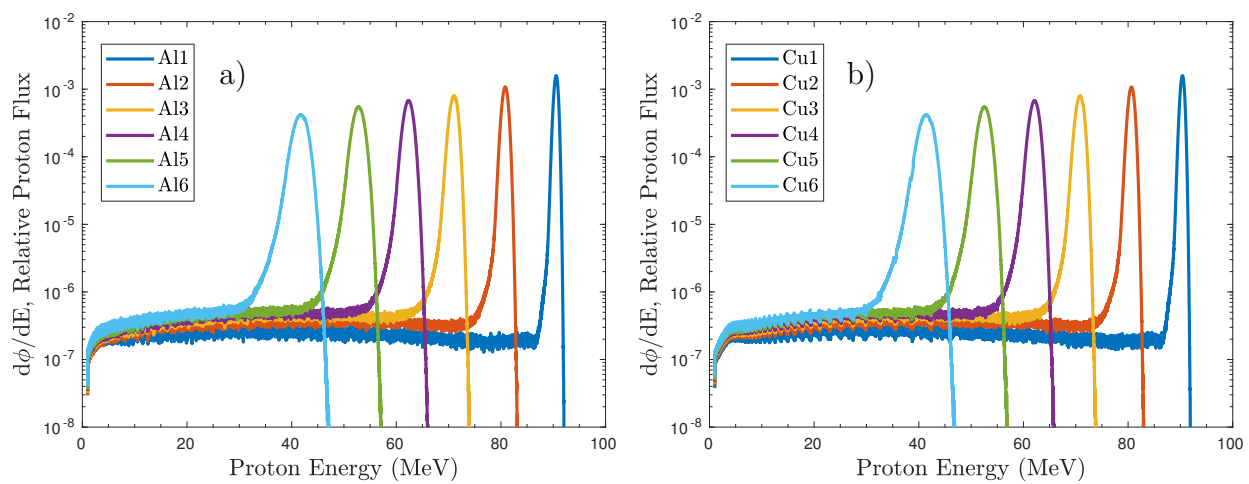


Figure 3.22: **Update this figure!!!** Final variance minimized incident proton energy distributions for the (a) Cu and (b) Ti foils, as simulated in MCNP6. The distribution tallies in each foil are all normalized to be per source proton, which was 10^8 in all simulations. As the beam is degraded, proton energy distributions become visibly broadened due to straggling, and drop in magnitude due to scattering losses.

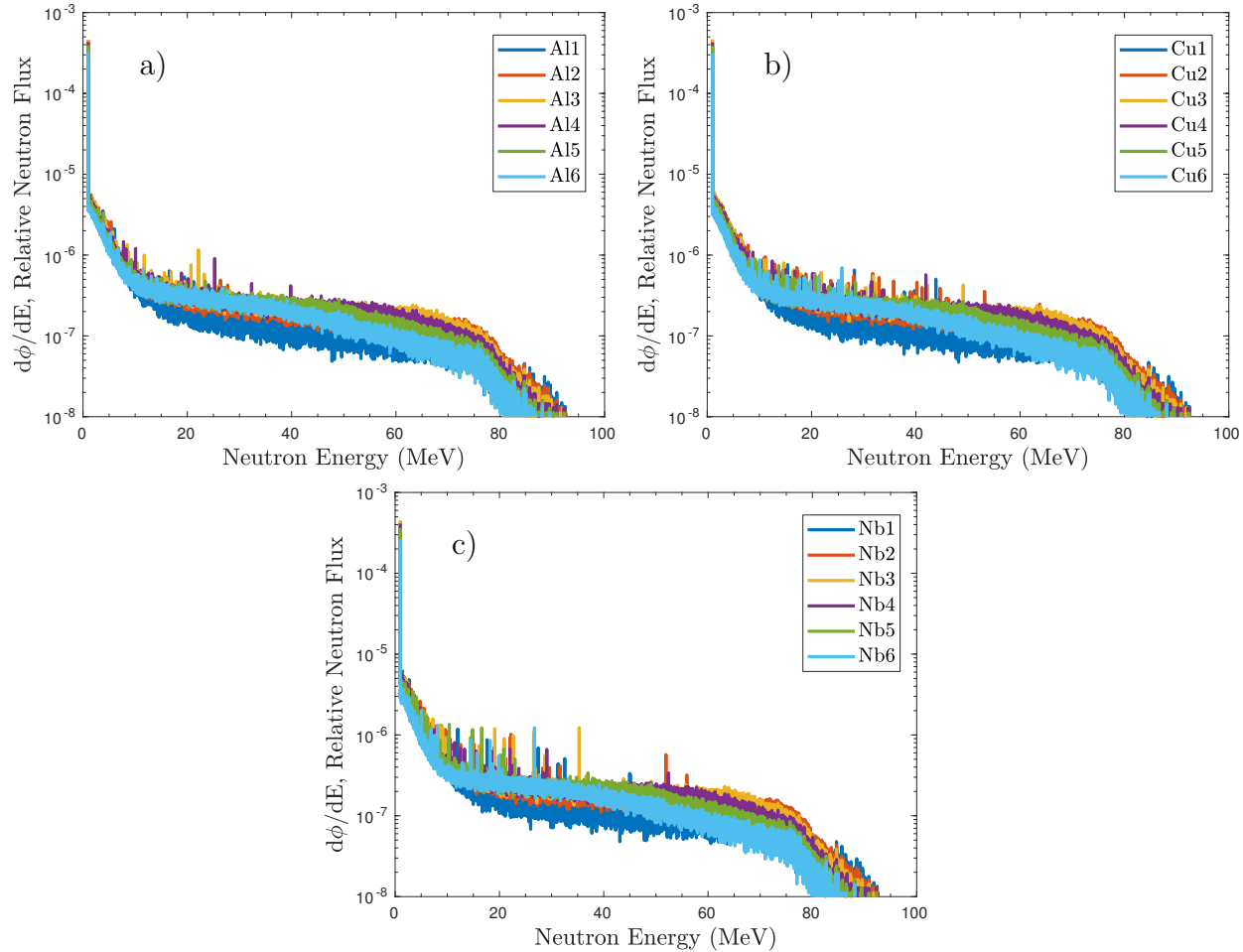


Figure 3.23: **Update this figure!!!** Final variance minimized incident neutron energy distributions for the (a) Cu, (b) Ti, and (C) Fe foils, as simulated in MCNP6. The distribution tallies in each foil are all normalized to be per source proton, which was 10^8 in all simulations. As the beam is degraded, neutron energy distributions become visibly downscattered.

orders of magnitude smaller than the corresponding proton flux, and is seen to be visibly downscattered when moving down the stack.

Additionally, using this proton transport model, it is possible to plot the FWHM of the proton energy distribution in each of the Cu and Al monitor foils, as a function of its flux-weighted average proton energy. This is seen in Figure 3.24. As seen in the recent work of Graves *et al.*, this FWHM distribution can be fit via linear regression [6]. The results of this fit (with $R^2 = 0.9986$) would suggest that the broadening of proton energy distribution in the target stack is linearly proportional to energy degradation, which is overwhelmingly from the aluminum degraders between energy positions. This serves to build confidence, through consistency with the results from this similar measurement. In the event that the

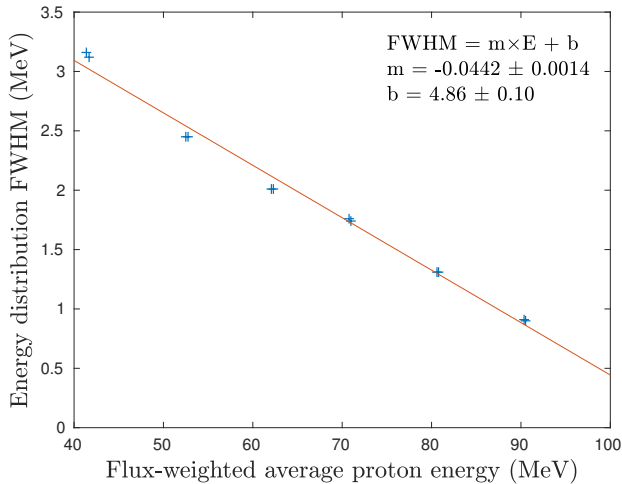


Figure 3.24: **Update this figure!!!** FWHM for the proton energy distributions of Cu and Ti foils seen in Figure 3.22, as a function of the flux-weighted average proton energy.

FWHM of a stack element could not be directly calculated using the MCNP model output, this linear model could be used to estimate the element's FWHM through interpolation.

Potential pathways for isotope production

Make sure to provide plenty of commentary here...

In the published journal article, cross sections for ^{51}Cr , ^{52g}Mn , ^{52m}Mn , ^{54}Mn , ^{55}Co , ^{56}Ni , ^{57}Ni , ^{57}Co , ^{58g}Co , ^{58m}Co , ^{59}Fe , ^{60}Co , ^{61}Cu , and ^{64}Cu were extracted for (p,x) reactions on $^{\text{nat}}\text{Cu}$ foils in the 40–90 MeV region, as recorded in Table 2.2. For (p,x) reactions on $^{\text{nat}}\text{Nb}$ foils, the (p,x) cross sections for ^{82m}Rb , ^{83}Sr , ^{85g}Y , ^{85m}Y , ^{86}Zr , ^{86}Y , ^{87}Zr , ^{87g}Y , ^{87m}Y , ^{88}Zr , ^{88}Y , ^{89g}Nb , ^{89m}Nb , ^{89}Zr , ^{90}Mo , ^{90}Nb , ^{91m}Nb , ^{92m}Nb , and ^{93m}Mo were extracted, as recorded in Table 2.3. As an alternative to a simple list of the various observed reaction products, these may be visualized in Figure 3.25, Figure 3.26, and Figure 3.27, in the style of excerpts from the Chart of Nuclides. These figures display the target and compound nuclei for both $^{\text{nat}}\text{Fe(p,x)}$, $^{\text{nat}}\text{Cu(p,x)}$, and $^{\text{nat}}\text{Ti(p,x)}$, along with all observed reaction products, to illustrate the mass range probed in this measurement.

In addition to the $^{\text{nat}}\text{Nb(p,x)}^{90}\text{Mo}$ monitor reaction measurement, this experiment has also yielded measurements of a number of additional emerging radionuclides with medical applications. These include the non-standard positron emitters ^{57}Ni [6, 47–49], ^{64}Cu [50–57], ^{86}Y [30, 31, 58–66], ^{89}Zr [67–71], ^{90}Nb [72, 73], and the Auger-therapy agent ^{82m}Rb [74, 75]. Discussion of the suitability for $^{\text{nat}}\text{Nb(p,x)}$ and $^{\text{nat}}\text{Cu(p,x)}$ production pathways of these valuable medical radionuclides is included here.

^{57}Ni ($t_{1/2} = 35.60 \pm 0.06$ h, $\epsilon=100\%$ to ^{57}Co [76]), while useful on its own as a positron emitter, stands poised as a particularly promising candidate for theranostic pairing with the soft β^- emitter ^{66}Ni ($t_{1/2} = 54.6 \pm 0.3$ h, $\beta^- = 100\%$ to ^{66}Cu [142]) [6, 47–49]. $^{\text{nat}}\text{Cu(p,x)}^{57}\text{Ni}$

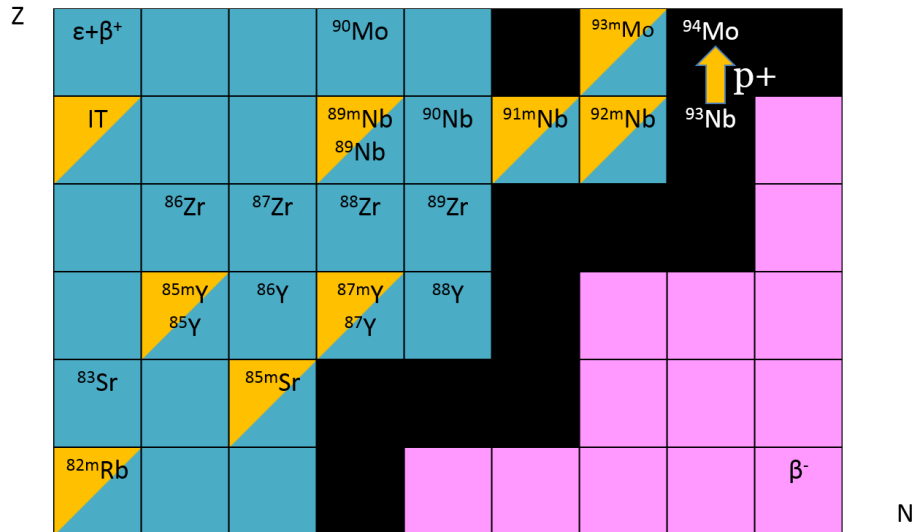


Figure 3.25: **Update this figure!!!** Reaction products observed in the ${}^{nat}\text{Fe}(p,x)$ measurement.

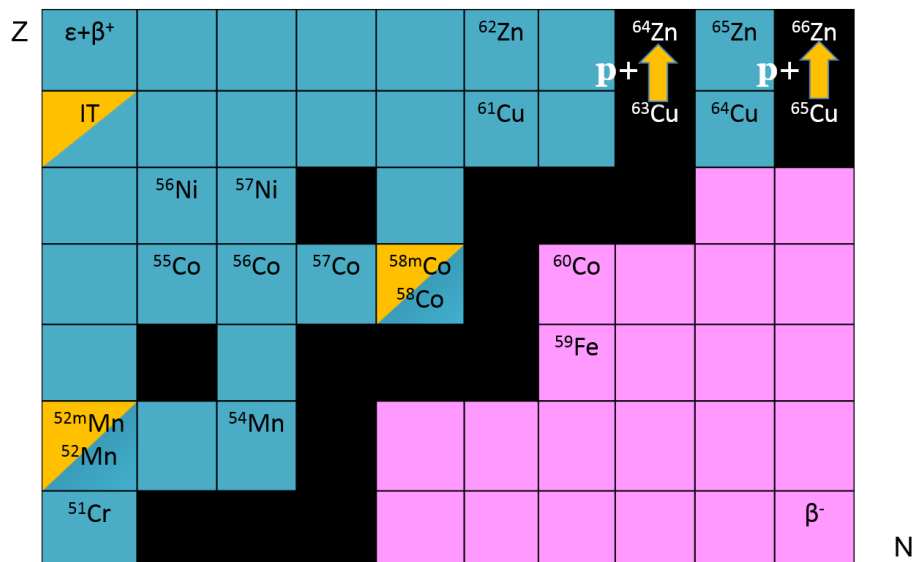


Figure 3.26: **Update this figure!!!** Reaction products observed in the ${}^{nat}\text{Cu}(p,x)$ measurement.

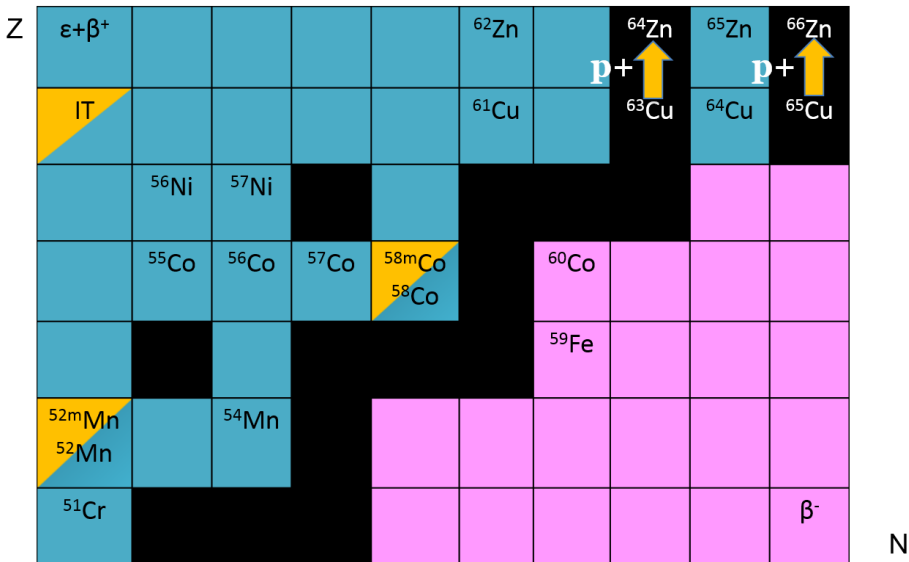


Figure 3.27: **Update this figure!!!** Reaction products observed in the ${}^{\text{nat}}\text{Ti}(\text{p},\text{x})$ measurement.

would seem to be an intriguing production pathway, due to the ready availability of Cu metal as target, combined with the fact that production in this pathway strongly favors ${}^{57}\text{Ni}$ over ${}^{56}\text{Ni}$ — indeed, the ${}^{57}\text{Ni}/{}^{56}\text{Ni}$ ratio of production rates is approximately 290 at 61.58 MeV, and varies from 45–75 at the 70–90 MeV positions. The traditional route for ${}^{57}\text{Ni}$ production is via ${}^{\text{nat}}\text{Co}(\text{p},3\text{n}){}^{57}\text{Ni}$, but at moderate energies, suffers from more ${}^{56}\text{Ni}$ contamination than ${}^{\text{nat}}\text{Cu}(\text{p},\text{x})$ ($\sigma_{57\text{Ni}}/\sigma_{56\text{Ni}} \approx 10$ at maximum). Lower-energy production via ${}^{\text{nat}}\text{Co}(\text{p},3\text{n})$ at 24–40 MeV is below threshold for ${}^{56}\text{Ni}$, but has a peak cross section of approximately 10 mb, making ${}^{\text{nat}}\text{Cu}(\text{p},\text{x})$ the superior production route for moderate-energy accelerators [77, 78].

${}^{64}\text{Cu}$ ($t_{1/2} = 12.7$ h) undergoes β^+ decay (61.5% branching ratio) to ${}^{64}\text{Ni}$ or β^- decay (38.5% branching ratio) to ${}^{64}\text{Zn}$ [5], with the PET branch suited for imaging of prostate and colorectal cancers [50–52]. Several production routes currently exist: ${}^{64}\text{Ni}(\text{p},\text{n})$ uses 8–14 MeV protons on the expensive enriched target ${}^{64}\text{Ni}$ (0.9255% natural abundance), but offers a high radioisotopic purity assuming a highly enriched target [53, 54]. ${}^{68}\text{Zn}(\text{p},\alpha\text{n})$ requires more energetic 20–30 MeV protons, and necessitates an enriched target (18.45% natural abundance) to avoid the co-production of radio-copper impurities [55, 56]. More recently, the use of compact DD neutron generators for ${}^{\text{nat}}\text{Zn}(\text{n},\text{p})$ production has been proposed, with the promise of mCi-scale production with high specific activity [57].

${}^{86}\text{Y}$ ($t_{1/2} = 14.74 \pm 0.02$ h, $\epsilon=100\%$ to ${}^{86}\text{Sr}$ [101]) is another novel emerging PET isotope, whose longer half-life has poised it for applications as a tracer for slower metabolic processes, as well as in pharmacokinetics studies [58–61]. In particular, it is highly desired to form a theranostic pair with the widely-employed β^- therapy agent ${}^{90}\text{Y}$ ($t_{1/2} = 64.00 \pm 0.21$ h, $\beta^-=100\%$ to ${}^{90}\text{Zr}$ [24]), which can be produced from a long-lived ${}^{90}\text{Sr}$ generator and emits no discrete observable gamma-rays or x-rays through decay [143]. Although a weak positron branch exists and bremsstrahlung scintigraphy is commonly used for clinical imaging of the

^{90}Y biodistribution, theranostics necessitate an imaging isotope to be paired for quantification of its uptake and biodistribution [144]. Conventional production of ^{86}Y proceeds through low-energy (7–14 MeV) irradiation via $^{86}\text{Sr}(\text{p},\text{n})$, which requires an enriched ^{86}Sr target (9.86% natural abundance), in order to eliminate contamination from (p,n) on the other stable $^{84,87,88}\text{Sr}$ isotopes [62]. Alternatively, production at 33–43 MeV via $^{88}\text{Sr}(\text{p},3\text{n})$ has been proposed — this pathway also requires an enriched target (82.58% natural abundance) for the same reason, but contamination with other Y co-activities will be even more pronounced than via (p,n) , due to the opening of (p,n) and $(\text{p},2\text{n})$ channels on all stable Sr isotopes [63, 64]. Minimizing activity from other isotopes of the element in question is essential for producing radionuclides in high specific activity, as these competing isotopes are often impractical to separate out by radiochemical means. As a result, it would appear that $^{\text{nat}}\text{Nb}(\text{p},\text{x})$ is a poor route for ^{86}Y production in this respect, as it only reaches a maximum of approximately 35% radioisotopic purity. The dominant yttrium radioisotope produced by $^{\text{nat}}\text{Nb}(\text{p},\text{x})$ in the 40–90 MeV region is ^{87}Y ($t_{1/2} = 79.8 \pm 0.3$ h, $\epsilon^- = 100\%$ to ^{87m}Sr [30]). However, ^{87}Y itself has application as a generator for ^{87m}Sr ($t_{1/2} = 2.815 \pm 0.012$ h, IT=99.70% to ^{87}Sr [30]), which is used for imaging studies of metastatic bone cancers, especially when in a theranostic pair with the established therapy agent ^{89}Sr ($t_{1/2} = 50.563 \pm 0.0025$ d, $\beta^- = 100\%$ to ^{89}Y [31]) [65, 66].

^{89}Zr ($t_{1/2} = 78.41 \pm 0.12$ h, $\epsilon = 100\%$ to ^{89}Y [31]) is a long-lived positron emitter useful as a tracer for slow biological processes, immune studies, and imaging of liver and breast cancers [67–69]. Current production focuses on $^{89}\text{Y}(\text{p},\text{n})^{89}\text{Zr}$ between 9–14 MeV, which offers an extremely high-purity route on a mono-isotopic target and a strong population of ^{89}Zr , with a peak cross section of nearly 800 mb [70, 71]. Due to co-production of additional $^{86,87,88}\text{Zr}$ radio-zirconium, $^{\text{nat}}\text{Nb}(\text{p},\text{x})$ is clearly inferior to $^{89}\text{Y}(\text{p},\text{n})^{89}\text{Zr}$, as the Nb route has a smaller peak cross section of approximately 290 mb, and achieves only 10–20% radioisotopic purity in the 50–90 MeV region.

^{90}Nb ($t_{1/2} = 14.60 \pm 0.05$ h, $\epsilon = 100\%$ to ^{90}Zr [24]) is an emerging positron emitter with a moderate lifetime, making it suited for immune and tumor uptake studies [72, 73]. It is typically produced using 8–15 MeV protons via $^{90}\text{Zr}(\text{p},\text{n})^{90}\text{Nb}$, using an enriched target (51.45% natural abundance) for high radioisotopic purity, and produces a product with minimal contamination and a peak cross section of approximately 750 mb [72]. $^{\text{nat}}\text{Nb}(\text{p},\text{x})^{90}\text{Nb}$ offers a possible alternative pathway using a natural target, at the expense of a smaller peak cross section. ^{90}Nb may be produced directly with an approximately 370 mb peak cross section and 99% radioisotopic purity, or could be produced as a $^{90}\text{Mo}/^{90}\text{Nb}$ generator, which would have nearly 100% radioisotopic purity by using protons below the $^{\text{nat}}\text{Nb}(\text{p},5\text{n})$ threshold of 45.76 MeV. However, the greatest problem with using the $^{\text{nat}}\text{Nb}(\text{p},\text{x})$ reaction to produce ^{90}Nb is the inability to separate the radioisotope from the target itself, rendering the production of a high-specific activity product impossible.

Finally, ^{82m}Rb ($t_{1/2} = 6.472 \pm 0.006$ h, $\epsilon = 100\%$ to ^{82}Kr [99]) is a diagnostic and emerging Auger-therapy agent, typically seen as a contaminant in $^{82}\text{Sr}/^{82}\text{Rb}$ generators [74]. It is commonly produced via $^{82}\text{Kr}(\text{p},\text{n})$ at 10–15 MeV, using an enriched ^{82}Kr gaseous target, with a peak cross section of approximately 400 mb at 12 MeV [74]. Production via $^{\text{nat}}\text{Nb}(\text{p},\text{x})$

offers the use of metallic, natural abundance targetry, but requires significantly higher energy (>80 MeV) protons, peaking at approximately 20 mb near 600 MeV [75]. It is clear that this production route offers no advantage over existing $^{82}\text{Kr}(\text{p},\text{n})$ routes for in-house production.

Chapter 4

Measurement of the ^{64}Zn , $^{47}\text{Ti}(\text{n},\text{p})$ cross sections using a DD neutron generator for medical isotope studies

THIS chapter details a measurement of the $^{64}\text{Zn}(\text{n},\text{p})^{64}\text{Cu}$ and $^{47}\text{Ti}(\text{n},\text{p})^{47}\text{Sc}$ cross sections. The measurement was performed using the UC Berkeley High Flux Neutron Generator (HFNG), a compact generator which produces a neutron flux through the DD fusion reaction. This generator, commissioned in 2015, was originally designed for radiometric dating applications in geochronology, with an emphasis on the $^{40}\text{Ar}/^{39}\text{Ar}$ dating technique. While other experiments have been carried out at the HFNG since this work was published, the work presented in this chapter was the first scientific measurement to be carried out in this new research facility. In addition to the pivotal role played in the early development of the HFNG, this work is notable for several aspects related to the development of alternative production pathways for medical radionuclides.

Production via (n,p) , using neutrons in the 2–3 MeV DD spectrum, provides an almost ideal pathway for production of isotopes accessible through this channel. This is due to the fact that the DD neutron spectrum is too slow for production of unwanted activities via (n,pxn) and $(\text{n},\alpha\text{xn})$ reactions, which cannot easily be separated from the desired radionuclides. DT generators offer higher production rates through increased neutron flux, but their more-energetic neutron spectra suffer from this opening of production channels for many unwanted radionuclide contaminants. In addition, especially in a generator with a low thermal neutron population such as the HFNG, the DD spectrum is too energetic for neutron capture to be competitive with (n,p) reaction rates. Production of multiple unwanted co-activities via (n,γ) is one of the largest issues faced by thermal reactor isotope production. This is primarily due to the separation of a single radionuclide product from this “sea” of contaminant co-products being impractical by radiochemical means, and often impossible by affordable means. As a result, reactor production suffers from low radioisotopic purity, as well as yields of low specific activity. In addition, production reactors suffer from difficulties with large-scale deployment due to their reliance on highly-enriched uranium, and a global trend currently

exists for the curtailment of such reactors.

These factors combine to make alternative pathways to reactor production a highly-sought goal for the field of nuclear medicine. The potential for high-specific activity production and easy deployment, due to compact size and lack of dependence on special nuclear material, allows a DD neutron generator to stand poised as a novel paradigm for isotope production. A challenge to wider utilization of such generators is the paucity of well-characterized nuclear data for the production of isotopes via (n,p) and (n,α) channels. This motivated the work described here, as a feasibility study for the use of compact DD neutron generators for nuclear data measurements, as well as the potential for serving as local medical isotope production capabilities. The design, commissioning, and operation of the HFNG has been the product of the time and efforts of numerous individuals, including three generations of PhD students at the UC Berkeley Department of Nuclear Engineering. These efforts culminated in the work presented in this chapter, the result of the first characterization experiments at the HFNG. Part of this characterization includes the description of a new figure of merit for isotope production in a neutron generator, η , the *neutron utilization factor*. This figure characterizes the effectiveness of a neutron generator for the production of a specific isotope, based on target configuration and reaction selectivity.

Relevant Publications:

A.S. Voyles, M.S. Basunia, J.C. Batchelder, J.D. Bauer, T.A. Becker, L.A. Bernstein, E.F. Matthews, P.R. Renne, D. Rutte, M.A. Unzueta, and K.A. van Bibber, “Measurement of the ^{64}Zn , $^{47}\text{Ti}(\text{n},\text{p})$ cross sections using a DD neutron generator for medical isotope studies,” Nuclear Instruments and Methods in Physics Research Section B: Beam Interactions with Materials and Atoms, vol. 410, pp. 230–239, Nov. 2017, <http://dx.doi.org/10.1016/j.nimb.2017.08.021>. [57]

The text and figures of this paper (copyright Elsevier B.V. 2017), of which I was the primary author, are included in this chapter with the permission of all authors. Some of the figures and content in this chapter have been altered to better fit the page formatting, but all changes made to the published journal article are purely stylistic in nature.

4.1 Abstract

Cross sections for the $^{47}\text{Ti}(\text{n},\text{p})^{47}\text{Sc}$ and $^{64}\text{Zn}(\text{n},\text{p})^{64}\text{Cu}$ reactions have been measured for quasi-monoenergetic DD neutrons produced by the UC Berkeley High Flux Neutron Generator (HFNG). The HFNG is a compact neutron generator designed as a “flux-trap” that maximizes the probability that a neutron will interact with a sample loaded into a specific, central location. The study was motivated by interest in the production of ^{47}Sc and ^{64}Cu as emerging medical isotopes. The cross sections were measured in ratio to the

$^{113}\text{In}(\text{n},\text{n}')^{113\text{m}}\text{In}$ and $^{115}\text{In}(\text{n},\text{n}')^{115\text{m}}\text{In}$ inelastic scattering reactions on co-irradiated indium samples. Post-irradiation counting using an HPGe and LEPS detectors allowed for cross section determination to within 5% uncertainty. The $^{64}\text{Zn}(\text{n},\text{p})^{64}\text{Cu}$ cross section for $2.76_{-0.02}^{+0.01}$ MeV neutrons is reported as 49.3 ± 2.6 mb (relative to ^{113}In) or 46.4 ± 1.7 mb (relative to ^{115}In), and the $^{47}\text{Ti}(\text{n},\text{p})^{47}\text{Sc}$ cross section is reported as 26.26 ± 0.82 mb. The measured cross sections are found to be in good agreement with existing measured values but with lower uncertainty (<5%), and also in agreement with theoretical values. This work highlights the utility of compact, flux-trap DD-based neutron sources for nuclear data measurements and potentially the production of radionuclides for medical applications.

4.2 Introduction

There has been significant interest in the past several years in exploring the use of neutron-induced reactions to create radionuclides for a wide range of applications. This interest is due to the volumetric absorption of neutrons as compared to charged particle beams (ranges of s/cm^2 as compared to $10\text{'s of mg}/\text{cm}^2$), together with the fact that isotope production facilities often produce large secondary neutron fields. Particular interest has been paid to (n,p) and (n,α) charge-exchange reactions since these reactions produce high-specific activity radionuclide samples without the use of chemical carriers in the separation process.

Two other potential neutron sources for (n,x) reactions exist in addition to the secondary neutron fields generated at existing isotope production facilities: reactors and neutron generators that utilize the $\text{D}(\text{T},\text{n})\alpha$ (“DT”) and $\text{D}(\text{D},\text{n})^3\text{He}$ (“DD”) reactions. While reactors produce copious quantities of neutrons, their energy spectra are often not well-suited to the preparation of high-purity samples due to the co-production of unwanted activities via neutron capture, in addition to the significant start-up costs and proliferation concerns involved in their commissioning [155]. Similarly, while the higher energy 14–15 MeV neutrons produced at DT generators are capable of initiating (n,p) and (n,α) reactions, their higher energy opens the possibility of creating unwanted activities via (n,pxn) and $(\text{n},\alpha\text{xn})$ reactions that cannot easily be separated from the desired radionuclides. DT generators may also often be limited by the restricted use of tritium at many institutions.

In contrast, the neutron spectrum from a DD reaction, which ranges from approximately 2–3 MeV, is ideally suited to (n,p) radionuclide production. However, the lower achievable flux from these generators limits their production capabilities. An additional complication is the relative paucity of high-quality, consistent cross section data for neutrons in the 2–3 MeV DD energy range.

The purpose of the present work is to explore the potential to use high-flux neutron generators to produce high-specific activity samples of radionuclides at the mCi level for local use in the application community. The research group at UC Berkeley has developed a High Flux Neutron Generator (HFNG) that features an internal target where samples can be placed just several millimeters from the neutron producing surface in order to maximize the utilization of the neutron yield for the production of a desired radionuclide [156–158].

The HFNG uses the $\text{D}(\text{D},\text{n})^3\text{He}$ reaction to produce neutrons with energies near 2.45 MeV together with a self-loading target design to maintain continuous operation without target replacement. In addition to the generator itself, efforts are underway to design neutron reflection capabilities to allow scattered neutrons multiple opportunities to interact with an internally mounted target. While these design efforts are underway, the HFNG can be used to better characterize production cross sections at the appropriate neutron energy.

The present work features a pair of cross section measurements for the production of two emerging non-standard medical radionuclides: the positron emitter $^{64}\text{Zn}(\text{n},\text{p})^{64}\text{Cu}$ and the single-photon emission computed tomography (SPECT) tracer $^{47}\text{Ti}(\text{n},\text{p})^{47}\text{Sc}$. ^{64}Cu ($t_{1/2} = 12.7$ h) undergoes β^+ decay (61.5% branching ratio) to ^{64}Ni or β^- decay (38.5% branching ratio) to ^{64}Zn [5]. The emitted short-range 190-keV β^- particle makes this an attractive therapeutic radionuclide, which also has the possibility for simultaneous positron emission tomography (PET) imaging for real-time dose monitoring and verification. This makes ^{64}Cu particularly desirable for emerging radiation therapy protocols [21, 50–52]. In addition, copper radiochemistry is well developed, and many existing ligands and carriers may be used for selective delivery of the radionuclide to different sites in patients. The second radionuclide studied, ^{47}Sc ($t_{1/2} = 3.35$ d), undergoes β^- decay to ^{47}Ti , emitting a high-intensity (63.8%) 159-keV gamma ray in the process [159]. This radionuclide is attractive as an emerging diagnostic isotope, due to the similarity of the emitted gamma ray to that of the well-established $^{99\text{m}}\text{Tc}$ [10, 160–162]. Due to the short half-life ($t_{1/2} = 6.0$ h) of and dwindling supplies of $^{99\text{m}}\text{Tc}$, ^{47}Sc stands poised as a potential solution to this shortage, due to its longer half-life and multiple production pathways without the need for highly enriched uranium [163]. In addition, when paired with ^{44}Sc , ^{47}Sc forms a promising “theranostic” pair for use in simultaneous therapeutic and diagnostic applications [11, 164].

Current methodology in radiochemistry has shown recovery of upwards of 95% of produced ^{64}Cu [165, 166] and ^{47}Sc [167–169] from solid target designs, without the need for additional carrier. By expanding the base of efficient reaction pathways, great advances are possible in making production of medical radionuclides more efficient and affordable for those in need. It is this desire to improve the options available for modern medical imaging and cancer therapy which has motivated the campaign of nuclear data measurements for isotope production at the UC Berkeley HFNG.

4.3 Experiment

4.3.1 Neutron source

Neutron activation was carried out via irradiation in the High-Flux Neutron Generator (HFNG), a DD neutron generator at the University of California, Berkeley. This generator extracts deuterium ions from an RF-heated deuterium plasma (using ion sources similar to designs from the Lawrence Berkeley National Laboratory [158]) through a nozzle, whose shape was designed to form a flat-profile beam, 5 mm in diameter. This deuterium beam is

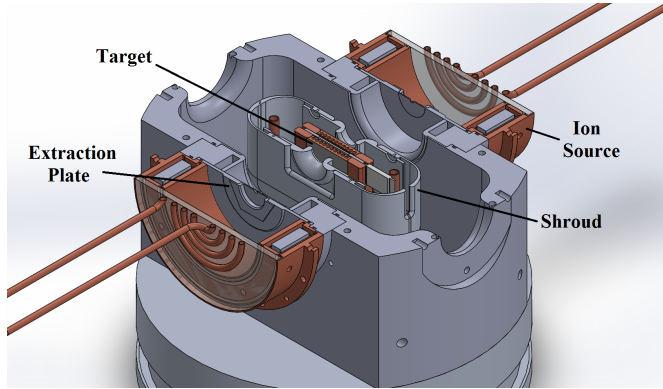


Figure 4.1: Cut-away schematic of the HFNG. The ion source is approximately 20 cm in diameter.

incident upon a water-cooled, self-loading titanium-coated copper target [156, 157], where the titanium layer acts as a reaction surface for DD fusion, producing neutrons with a well-known energy distribution as a function of emission angle [1]. While the machine's design features two deuterium ion sources impinging from both sides of the target, only a single source was used in the present work. Irradiation targets are inserted in the center of the titanium layer deuteron target, approximately 8 mm from the DD reaction surface, prior to startup. Figure 4.1 displays a cut-away schematic of the HFNG. A 100 keV deuterium beam was extracted at 1.3 mA, creating a flux of approximately $1.3 \cdot 10^7$ neutrons/cm²s on the target.

4.3.2 Cross section determination by relative activation

The approach used in both measurements was to irradiate foils of zinc or titanium, which were co-loaded with indium foils in order to determine their (n,p) cross sections relative to the well-established $^{113}\text{In}(\text{n},\text{n}')^{113m}\text{In}$ and $^{115}\text{In}(\text{n},\text{n}')^{115m}\text{In}$ neutron dosimetry standards [170, 171]. Table 4.1 lists physical characteristics of each foil for the various irradiations. In each experiment, the co-loaded foils were irradiated for 3 h at nominal operating conditions of 1.3 mA and 100 kV. After irradiation, the foils were removed and placed in front of an appropriate High-Purity Germanium (HPGe) gamma-ray detector and time-dependent decay gamma-ray spectra were collected.

One cm diameter, 1-mm thick natural abundance zinc and titanium targets were employed for the measurement. Each of these was co-loaded with a natural abundance Indium foil of 1 cm diameter and 0.5 mm thickness in a recess cut into a 2-mm thick polyethylene holder, as seen in Figure 4.2, which was mounted in the HFNG target center. Prior to loading, each foil was washed with isopropanol and dried, to remove any trace oils or residue that could become activated during irradiation.

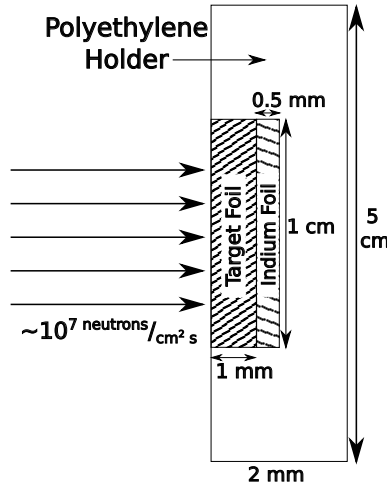


Figure 4.2: Schematic (not drawn to scale) of the sample holder used for the Berkeley HFNG.

Table 4.1: Foil characteristics for each of the three $(\text{Zn}/\text{In})^*$ experiments and the two $(\text{Ti}/\text{In})^\dagger$ experiments.

Foils Used	Metal Purity	Abundance (at. %)	Foil Density (mg/cm ²)	Thickness (mm)	Diameter (mm)	Mass (g)
^{nat} Zn	>99.99%	^{64}Zn (49.17%)	698.9	1.03 ± 0.01	9.93 ± 0.14	0.538 ± 0.005
				1.03 ± 0.01	9.76 ± 0.17	0.521 ± 0.005
				1.02 ± 0.01	9.89 ± 0.15	0.542 ± 0.005
^{nat} Ti	99.999%	^{47}Ti (7.44%)	434.7	1.16 ± 0.02	9.93 ± 0.04	0.337 ± 0.005
^{nat} In	>99.999%	^{113}In (4.29%), ^{115}In (95.71%)	317.6	1.15 ± 0.02	9.94 ± 0.03	0.337 ± 0.005
				0.49 ± 0.02*	9.75 ± 0.09*	0.248 ± 0.005*
				0.50 ± 0.03*	9.98 ± 0.15*	0.248 ± 0.005*
				0.49 ± 0.03*	9.96 ± 0.10*	0.241 ± 0.005*
				0.53 ± 0.06†	10.01 ± 0.11†	0.247 ± 0.005†
				0.50 ± 0.02†	10.00 ± 0.09†	0.248 ± 0.005†

4.3.3 Determination of effective neutron energy

The D(D,n)³He reaction at 100 keV lab energy produces neutrons with energies ranging from 2.18 to 2.78 MeV, over an angular range of 0–180° in the lab frame-of-reference with respect to the incident deuteron beam. This distribution has been well documented [1] and is shown in Figure 4.3 for 100 keV incident deuteron energy.

Since the samples are separated by only 8 mm from the DD reaction surface they subtend a fairly significant (~17° angular range in a region of high (approximately $1.3 \cdot 10^7$ neutrons/cm²s) neutron flux. This stands in contrast to other measurements which feature collimated beams and significantly lower total neutron flux.

The Monte Carlo N-Particle transport code MCNP6 [172] was used to model the neutron

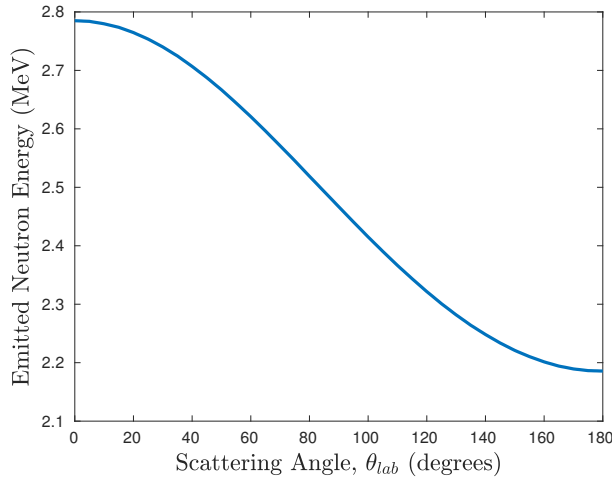


Figure 4.3: Energy-angle distribution for neutrons emitted following DD fusion, for 100 keV incident deuterons [1].

energy spectrum incident upon target foils co-loaded into the HFNG (see Figure 4.4). The neutron spectral distribution is also broadened by the temperature of the target. This gives rise to a slight difference in the neutron energy at the target location [157], which has been included in our stated energy window. This spectrum, peaked around 2.777 MeV, illustrates the forward-focused kinematics of the DD reaction subtended by the co-loaded sample foils. As expected, the production target is the dominant source of scatter — approximately 0.78% of the neutrons incident on the foils can be attributed to scatter in the neutron production target.

While this shows that the sample foils experience a very narrow energy distribution of incident neutrons, an effective neutron energy window must be determined. The MCNP6 simulation shows an identical flux-weighted average neutron energy of 2.765 MeV for both the Indium and target foils to the 1 keV level. Due to geometry and the kinematics of DD neutron emission, E_{max} , the maximum energy of a neutron subtending the target foils in this geometry is 2.783 MeV [1]. For this maximum energy, the number of reactions induced in a foil (containing N_T target nuclei) is given by:

$$R = N_T \int_0^{E_{max}} \sigma(E) \frac{d\phi}{dE} dE \quad (4.1)$$

From this definition, it is possible to calculate $F(E')$, the fraction of total reactions induced by neutrons up to some energy $E' < E_{max}$:

$$F(E') = \frac{\int_0^{E'} \sigma(E) \frac{d\phi}{dE} dE}{\int_0^{E_{max}} \sigma(E) \frac{d\phi}{dE} dE} \quad (4.2)$$

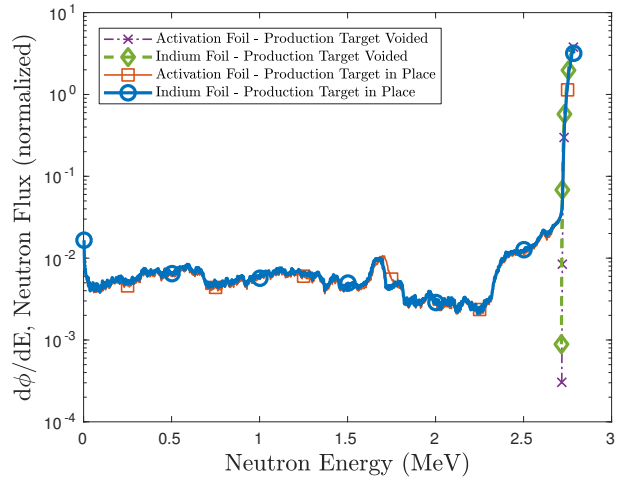


Figure 4.4: MCNP6-modeled neutron energy spectrum for the HFNG. The solid lines show the spectrum at the location of the indium and the activation foil. The dotted and dashed lines show the same with the neutron production target itself “voided” to remove scattering contributions.

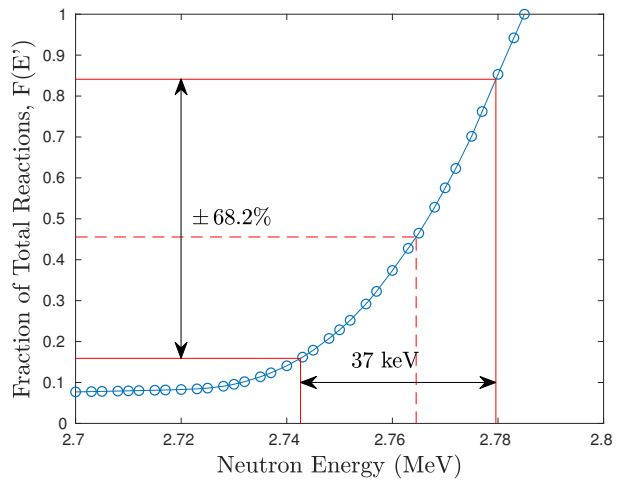


Figure 4.5: Fraction of total reactions induced in the Indium foil between the energies $[0, E']$. The solid red boundaries indicate the energy region that corresponds to 68.2% of the total activation.

Table 4.2: Gamma-ray properties for the decay lines measured in the present work.

Nuclide	Gamma-Ray Energy (keV)	Intensity (%)	$t_{1/2}$
^{64}Cu [5]	511.0	35.2 ± 0.4	12.701 h
^{47}Sc [159]	159.381	68.3 ± 0.4	3.3492 d
$^{113\text{m}}\text{In}$ [3]	391.698	64.94 ± 0.17	99.476 m
$^{115\text{m}}\text{In}$ [2]	336.241	45.9 ± 0.1	4.486 h
$^{116\text{m}}\text{In}$ [4]	416.90	27.2 ± 0.4	54.29 m

This quantity $F(E')$ is plotted in Figure 4.5. The fraction of total reactions in the indium foil can be used to characterize the effective neutron energy bin. Our approach, in analogy to the Gaussian quantity σ , will be to use a horizontal “error bar” to represent the energy range responsible for 68.2% of the reactions taking place. Using this approach, we report the effective energy bin as being $E_n = 2.765^{+0.014}_{-0.022}$ MeV. This 37-keV full-energy spread verifies that, at such close distances to the DD reaction surface, loaded target foils receive a quasi-monoenergetic neutron flux.

4.3.4 Measurement of induced activities

After irradiation, the co-loaded targets were removed from the HFNG and transferred to a counting lab, where their induced activities could be measured via gamma ray spectroscopy. Two detectors were used in this measurement. An Ortec 80% High-Purity Germanium (HPGe) detector was used for the detection of the positron annihilation radiation from the ^{64}Cu decay [5], the 391 keV gamma-ray from the $^{113\text{m}}\text{In}$ isomer [3], and the 336 keV gamma-ray from the decay of the $^{115\text{m}}\text{In}$ isomer [173]. An Ortec planar Low-Energy Photon Spectrometer (LEPS) was used for the detection of the lower-energy 159 keV gamma-ray from ^{47}Sc [159] as well as the two indium isomers mentioned above. Both detectors were calibrated for energy and efficiency, using ^{133}Ba , ^{137}Cs , and ^{152}Eu sources at various distances from the front face of each detector. These efficiencies, along with gamma ray intensities for each transition, were used to convert the integrated counts in each gamma ray photopeak into an activity for the activated isotopes and isomeric states.

The irradiated foils were counted in their polyethylene holder, 10 cm from the front face of the 80% HPGe and 1 cm from the front face of the LEPS, with the target foil (zinc or titanium) facing towards the front face of the detector when both target and monitor foils were counted simultaneously. All data collection was performed using the Ortec MAESTRO software. For each experiment the detector dead time was verified to be less than 5%. No summing corrections needed to be made since all of the gammas are either non-coincident or formed in a back-to-back annihilation event.

For the ^{47}Sc production experiments, the foils were counted simultaneously using a planar LEPS detector. For the ^{64}Cu production experiments, the Indium foil was first counted

separately using an 80% HPGe detector, to capture the short-lived Indium activities. This is due to the fact that the contaminant $^{115}\text{In}(\text{n},\gamma)$ reaction results in the production of ^{116m}In which has a 54 min half-life and results in the production of 1097 keV (58.5% branching), 1293 keV (84.8% branching) and 2112 keV (15.09% branching) gamma-rays that in turn produce a significant number of 511 keV gammas from pair-production followed by annihilation [4]. The foils were counted together again after approximately 4 h of separate collection, to allow for nearly all of the produced ^{116}In to decay. Example spectra for each production pathway can be seen in Figures Figure 4.6a and Figure 4.6b.

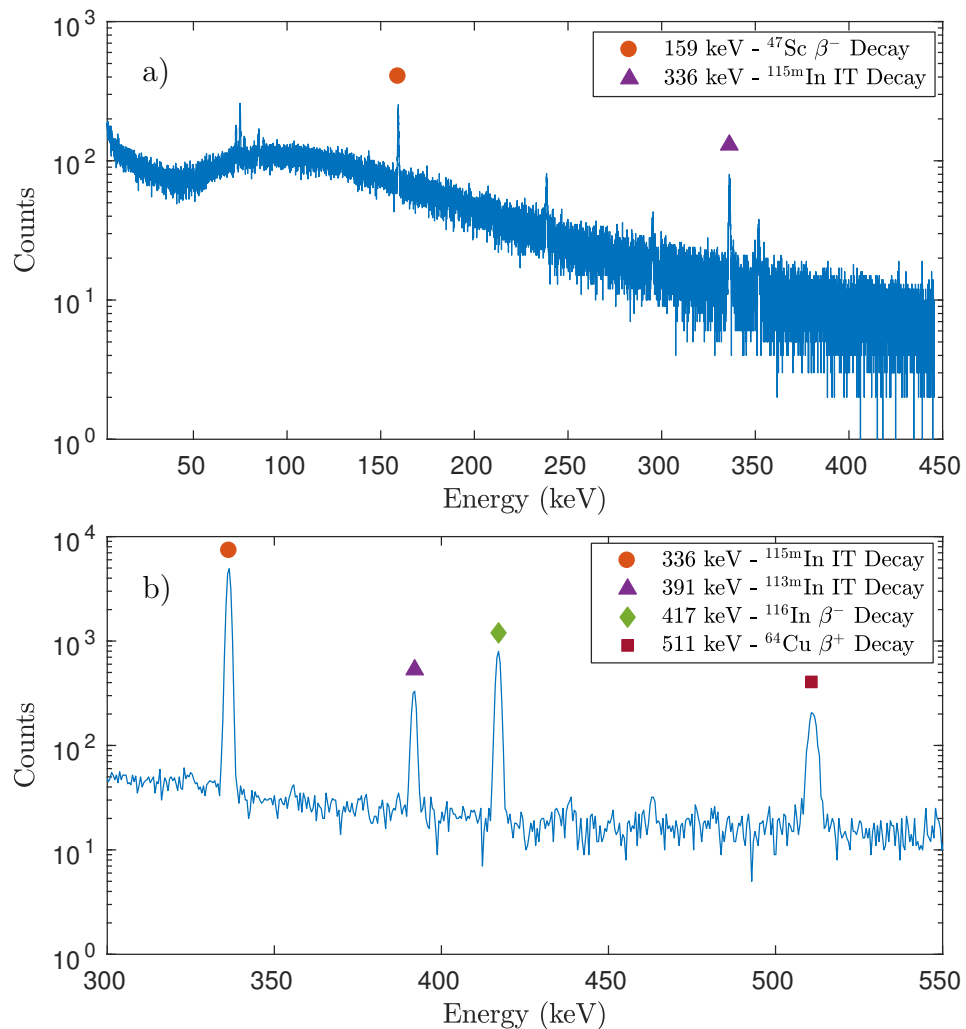


Figure 4.6: Example gamma spectra collected to monitor radioisotope production. (a) Gamma spectrum for the $^{47}\text{Ti}(\text{n},\text{p})^{47}\text{Sc}$ production pathway foils, counted using a LEPS detector and (b) gamma spectrum for the $^{64}\text{Zn}(\text{n},\text{p})^{64}\text{Cu}$ production pathway foils, counted using an 80% HPGe detector.

To verify that each peak corresponds to the assigned decay product, spectra were acquired

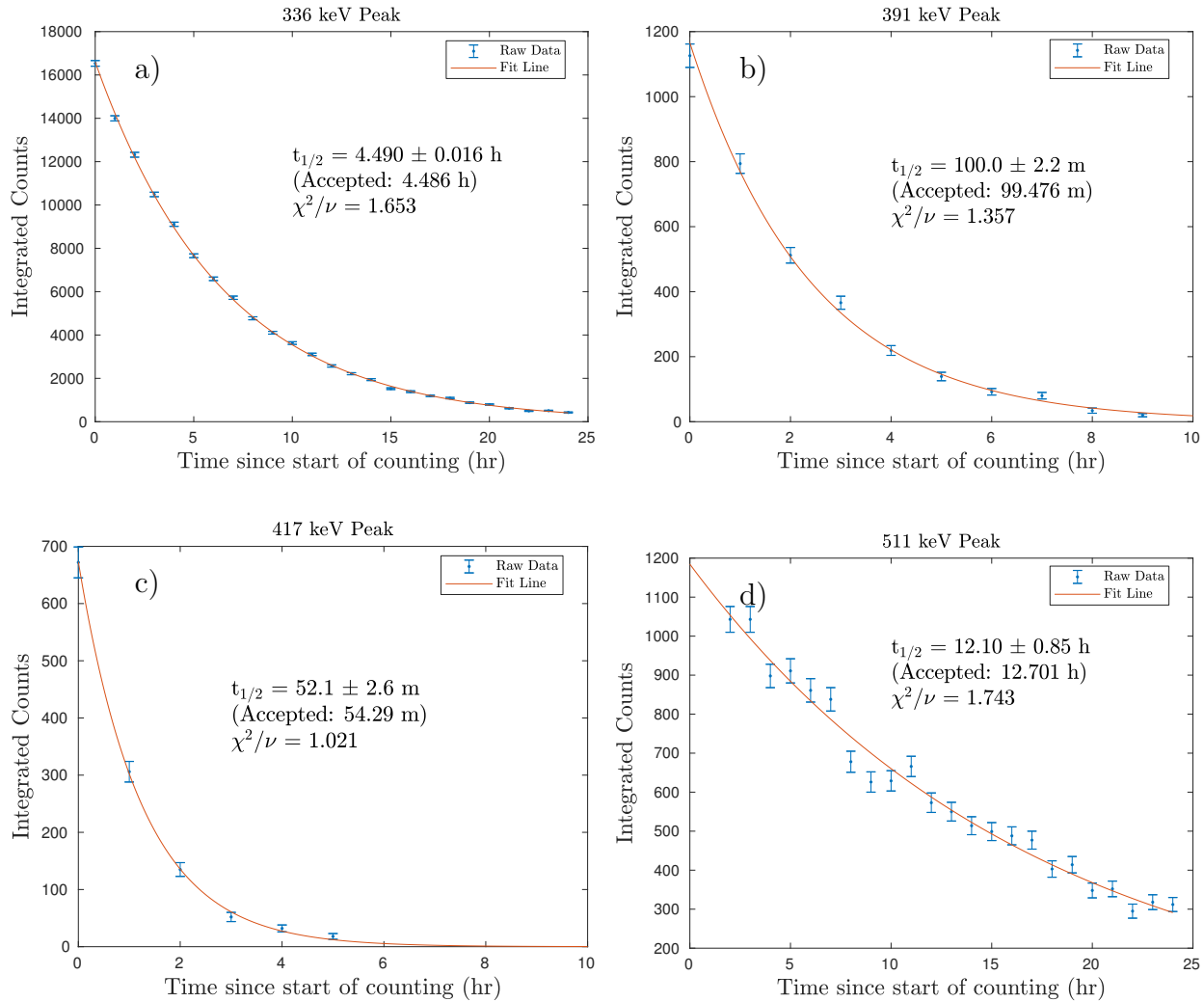


Figure 4.7: Decay curves used to verify photopeak transition assignment. (a) Decay curve for the isomeric transition of $^{115\text{m}}\text{In}$ [2], (b) decay curve for the isomeric transition of $^{113\text{m}}\text{In}$ [3], (c) decay curve for the β^- decay of ^{116}In [4], and (d) decay curve for the β^+ decay of ^{64}Cu [5].

in a sequence of 15–30 min intervals. The resulting time series displayed in Figures 4.7a – 4.7d allow the fitting of exponential decay functions for each nuclide and comparison of the measured half-life with literature values. The fitted functions for each transition agree (at the 1σ confidence level) with accepted half-lives [3–5, 159, 173], confirming the respective peak assignments.

The spectra for each sample were summed and the net peak areas were fitted using gf3, part of the RadWare analysis package from Oak Ridge National Laboratory [174, 175]. The background-subtracted integrated counts in each photopeak, as well as the counting duration

Table 4.3: Counting times and photopeak counts for each of the (Zn/In) and (Ti/In) experiments. The uncertainties in photopeak counts are a combination of the fit error and counting statistics.

Reference Foil	^{nat}In	^{nat}In	^{nat}In	^{nat}In	^{nat}In
Reference Foil Mass (g)	0.248	0.248	0.241	0.247	0.248
Target Foil	^{nat}Zn	^{nat}Zn	^{nat}Zn	^{nat}Ti	^{nat}Ti
Target Foil Mass (g)	0.538	0.521	0.542	0.337	0.337
Irradiation Time, t_i (s)	10800	10800	12629	11837	14254
Delay Time, t_d (s)	1785	16185	2290	89408	2390
Counting Time, t_c (s)	91188	54008	54002	86424	93631
Photopeak Counts, 336 keV (^{115m}In)	113665 ± 1490	76321 ± 275	39895 ± 201	2122 ± 55	55102 ± 268
Photopeak Counts, 391 keV (^{113m}In)	3382 ± 171	890 ± 40	3505 ± 54	_____	_____
Photopeak Counts, 511 keV (^{64}Cu)	16055 ± 643	12852 ± 118	27164 ± 159	_____	_____
Photopeak Counts, 159 keV (^{47}Sc)	_____	_____	_____	3877 ± 83	5544 ± 257

for each experiment, are tabulated in Table 4.3.

4.3.5 Experimental verification of incident neutron energy

As shown in subsection 4.3.2 above, the effective neutron energy depends on the angle range subtended by the sample with respect to the incident deuteron beam. In order to determine this angle it is necessary to measure the lateral location of the beam with respect to the sample location. This centroid position of the beam was measured using a 3×3 array of 0.5 cm diameter indium foils. The relative activity of these foils was then determined via post-irradiation counting of the ^{115m}In isomer ($t_{1/2} = 4.486$ h) [173]. Figure 4.8 shows the measured activities for these 9 indium foils. Based on these values we are able to verify that the beam was indeed vertically centered on the middle of the zinc and titanium samples, with a slight asymmetry of the neutron flux in the horizontal direction, accounted for in MCNP6 modeling of the energy-differential neutron flux. This small asymmetry likely contributes to the effective energy bin being lower than the 2.78 MeV expected for 0° neutron emission angle in Figure 4.3.

4.3.6 Calculation of measured cross sections

For a thin target consisting of N_T target nuclei (with a reaction cross section $\sigma(\bar{E})$), subjected to a constant neutron flux $\phi(\bar{E})$, the rate of production (R) of the product nucleus will be:

$$R = N_T \sigma(\bar{E}) \phi(\bar{E}) \quad (4.3)$$

If the target is subjected to this flux for an irradiation time t_i and decays for a delay time t_d (after end-of-beam) before gamma ray spectrum acquisition occurs for a counting time t_c ,

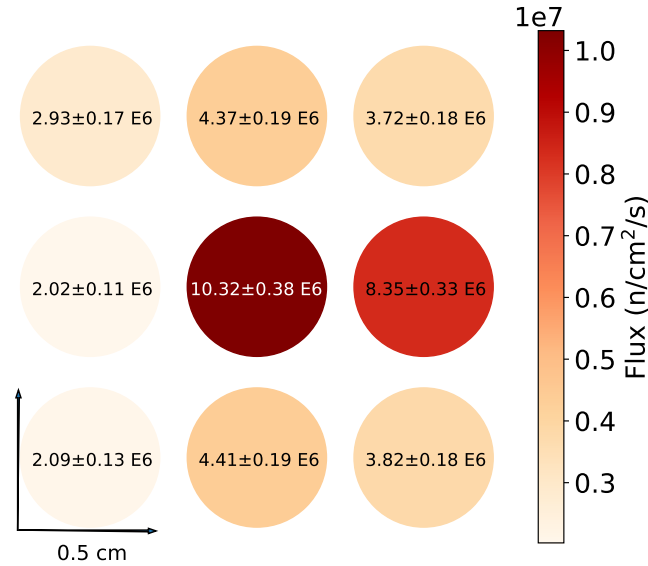


Figure 4.8: Relative fluxes as seen by a 3×3 array of indium foils. The central foil corresponds to the location in which target and monitor foils were mounted during the cross section measurements, verifying that the beam is centered on the middle of mounted foils.

then the number of product decays (N_D ; with decay constant λ) during the acquisition will be:

$$\begin{aligned} N_D &= \frac{R}{\lambda} \left(1 - e^{-\lambda t_i}\right) e^{-\lambda t_d} \left(1 - e^{-\lambda t_c}\right) \\ &= \frac{N_T \sigma(\bar{E}) \phi(\bar{E})}{\lambda} \left(1 - e^{-\lambda t_i}\right) e^{-\lambda t_d} \left(1 - e^{-\lambda t_c}\right) \end{aligned} \quad (4.4)$$

If this decay emits a gamma ray with absolute intensity I_γ (photons emitted per decay), and is detected with an absolute efficiency of ϵ_γ (photons detected / photons emitted), then the number of observed gamma rays during the acquisition will be:

$$\begin{aligned} N_\gamma &= N_D \epsilon_\gamma I_\gamma \\ &= \epsilon_\gamma I_\gamma \frac{N_T \sigma(\bar{E}) \phi(\bar{E})}{\lambda} \left(1 - e^{-\lambda t_i}\right) e^{-\lambda t_d} \left(1 - e^{-\lambda t_c}\right) \end{aligned} \quad (4.5)$$

Solving this equation for the cross section results in:

$$\sigma(\bar{E}) = \frac{N_\gamma \lambda}{N_T \epsilon_\gamma I_\gamma \phi(\bar{E}) (1 - e^{-\lambda t_i}) e^{-\lambda t_d} (1 - e^{-\lambda t_c})} \quad (4.6)$$

Equation 4.6 can be used to determine the unknown (n,p) cross sections relative to the well-known $^{115}\text{In}(\text{n},\text{n}')^{115\text{m}}\text{In}$ and $^{113}\text{In}(\text{n},\text{n}')^{113\text{m}}\text{In}$ inelastic scattering cross sections since the Zn and Ti samples were co-irradiated with indium foils. This approach has a number of advantages since the result is independent of neutron flux and only depends on the relative detector efficiencies at each gamma-ray energy. Equation 4.7 shows the ratio of the cross sections determined using this approach, in which subscript P indicates a quantity for either ^{64}Cu or ^{47}Sc , and subscript In indicates a quantity for either the $^{113\text{m}}\text{In}$ or $^{115\text{m}}\text{In}$ isomer. A minor term was added to correct for the small self-attenuation of the gamma rays emitted by the activated foils:

$$\frac{\sigma_P}{\sigma_{In}} = \frac{N_{\gamma,P}}{N_{\gamma,In}} \frac{N_{T,In}}{N_{T,P}} \frac{\lambda_P}{\lambda_{In}} \left(\frac{1 - e^{-\lambda_{In}t_i}}{1 - e^{-\lambda_P t_i}} \right) \frac{e^{-\lambda_{In}t_d}}{e^{-\lambda_P t_d}} \times \\ \times \left(\frac{1 - e^{-\lambda_{In}t_c}}{1 - e^{-\lambda_P t_c}} \right) \frac{\epsilon_{In}}{\epsilon_P} \frac{I_{\gamma,In}}{I_{\gamma,P}} \frac{e^{-\mu_{In}x_{In}/2}}{e^{-\mu_P x_P/2}} \quad (4.7)$$

where:

- N_γ is the integrated counts under a photopeak,
- σ is the cross section for either the production of a product or isomer [mb],
- N_T is the initial number of target nuclei,
- λ is the decay constant [s^{-1}],
- t_i is the irradiation time [s],
- t_d is the delay time (between the end-of-beam and the start of counting) [s],
- t_c is the counting time [s],
- ϵ is the detector efficiency for a particular photopeak,
- I_γ is the decay gamma ray absolute intensity [%],
- μ is the photon attenuation coefficient for a particular decay gamma ray in a foil [cm^{-1}],
- and x is the thickness of foil traversed by a particular decay gamma ray [cm]

In addition to the $^{115}\text{In}(\text{n},\text{n}')^{115\text{m}}\text{In}$ reference cross section, the $^{115}\text{In}(\text{n},\gamma)^{116\text{m}}\text{In}$ ($t_{1/2} = 54.29$ min [4]) activity can be used to determine the $^{64}\text{Zn}(\text{n},\text{p})$ and $^{47}\text{Ti}(\text{n},\text{p})$ cross section. The capture activity is potentially subject to contamination from lower energy, especially thermal, “room return” neutrons since the (n,γ) cross section at 25 meV is approximately 2000 times greater than at 2.7 MeV [170, 171].

With the exception of decay constants and time measurement, which have negligible uncertainty compared to other sources of uncertainties in this work, each of the parameters in this model carries an uncertainty. Based on the assumption that these uncertainties are uncorrelated, the total relative statistical uncertainty δ_σ is calculated by taking the quadrature sum of the relative uncertainties of each parameter δ_i :

$$\delta_\sigma = \|\vec{\delta}\|_2 = \sqrt{\sum_{i=1}^N \delta_i^2} \quad (4.8)$$

This total uncertainty is plotted as the cross section uncertainty in Figure 4.9 and Figure 4.10.

4.3.7 Systematic uncertainties

The largest source of systematic uncertainty in the cross section determined via the “ratio approach” is the 2.586% uncertainty in the $^{115}\text{In}(\text{n},\text{n}')$ $^{115\text{m}}\text{In}$ cross section and the 1.447% uncertainty in the $^{113}\text{In}(\text{n},\text{n}')$ $^{113\text{m}}\text{In}$ cross section [170, 171]. An additional uncertainty arises from the fact that the Zn/Ti samples are not located at exactly the same location as the indium monitor foils, and are therefore not subject to precisely the same neutron flux. However, the MCNP6 simulations shown in Figure 4.4 indicate that the difference in the flux that the two foils are subjected to is less than 1%, negligible compared to other sources of systematic uncertainty. Other monitor foils could be used instead of indium, with $^{58}\text{Ni}(\text{n},\text{p})^{58}\text{Co}$ (^{58}Co $t_{1/2} = 70.86$ d [28]) being one possible candidate, but the 4.486 h and 99.476 min half-lives of the $^{115\text{m}}\text{In}$ and $^{113\text{m}}\text{In}$ isomers [3, 173], respectively, make indium a better candidate for measuring the production of radionuclides with lifetimes much less than 71 days. The largest source of uncertainty in energy window arises from uncertainties in the actual dimension of the deuteron beam on the production target. We believe, based on “burn marks” on the neutron production target, that the beam was approximately circular, with a flat intensity profile and a 5 mm diameter. However, every 1 mm change in the beam radius would cause a 0.028 MeV shift in the centroid and a 0.053 MeV increase in the effective energy bin width, which places a natural limit on the reported effective neutron energy.

A much smaller systematic uncertainty arises from the fact that the two (n,p) cross sections and the reference In(n,n') cross sections have slightly different thresholds. The total activity in the In produced by the low energy neutrons (below the “knee” near 2.25 MeV in Figure 4.4) is 2.17%. The corresponding values from TALYS for the ^{64}Cu and ^{47}Sc activity are 0.24% and 0.85%, respectively. If we assume an uncertainty of $\pm 25\%$ in the TALYS calculations in this energy region it would introduce an additional systematic uncertainty in the $^{+10}_{-20}$ keV effective energy bin of ± 1.6 keV for ^{64}Cu and ± 5.7 keV for ^{47}Sc . As these are smaller than the precision of the existing effective energy bin, they can be considered negligible.

Table 4.4: Results of cross section measurement. Note that the last data point for the ^{47}Sc measurement (marked with *) was performed at a slightly different beam spot location, leading to a difference in effective neutron energy.

Reaction	$\sigma(E_n = 2.76_{-0.02}^{+0.01} \text{ MeV})$ (mb)
$^{64}\text{Zn}(n,p)^{64}\text{Cu}$ (relative to ^{113}In)	49.9 ± 3.2
	49.2 ± 2.7
	49.0 ± 2.5
$^{64}\text{Zn}(n,p)^{64}\text{Cu}$ (relative to ^{115}In)	45.9 ± 2.6
	46.5 ± 1.7
	46.8 ± 3.2
$^{47}\text{Ti}(n,p)^{47}\text{Sc}$ (relative to ^{115}In)	25.9 ± 1.2
	$26.7 \pm 1.4^*$

4.4 Results

Using the ratio method described, the cross sections for the $^{47}\text{Ti}(n,p)^{47}\text{Sc}$ and $^{64}\text{Zn}(n,p)^{64}\text{Cu}$ reactions have been calculated for an incident neutron energy of $E_n = 2.76_{-0.02}^{+0.01} \text{ MeV}$. These values are recorded in Table 4.4.

Figures 4.9 and 4.10 present the determined cross sections for production of $^{47}\text{Ti}(n,p)^{47}\text{Sc}$ and $^{64}\text{Zn}(n,p)^{64}\text{Cu}$ relative to literature data retrieved from EXFOR [46, 176–189]. The weighted average of the measurements give 49.3 ± 2.6 mb (relative to ^{113}In) and 46.4 ± 1.7 mb (relative to ^{115}In) for $^{64}\text{Zn}(n,p)^{64}\text{Cu}$, and 26.26 ± 0.82 mb for $^{47}\text{Ti}(n,p)^{47}\text{Sc}$. The $^{64}\text{Zn}(n,p)^{64}\text{Cu}$ cross section measured in this work is consistent with other literature results, but with a smaller uncertainty (<5%). However, in the case of the $^{47}\text{Ti}(n,p)^{47}\text{Sc}$ cross section, our results are consistent with the results from the Smith (1975), Armitage (1967), and Ikeda (1990) groups [180, 186, 187] and both the ENDF/B-VII.1 [190] and TALYS [84] values, but significantly below the results from the Hussain (1983), Gonzalez (1962), and Shimizu (2004) groups [182, 185, 189].

As mentioned above, the cross section can be obtained relative to both the inelastic scattering cross sections on ^{113}In and ^{115}In , and the capture of fast, unmoderated neutrons on ^{115}In . The result for the production of ^{116}In via the $^{115}\text{In}(n,\gamma)$ reaction was shown to be consistent with activation predominantly from the capture of fast neutrons, rather than from “room return” thermal neutrons. The MCNP neutron spectrum in Figure 4.4 confirms this - thermal and epithermal neutrons make up only 0.0771% of the total neutron population. This will be discussed in greater detail in the conclusion section below.

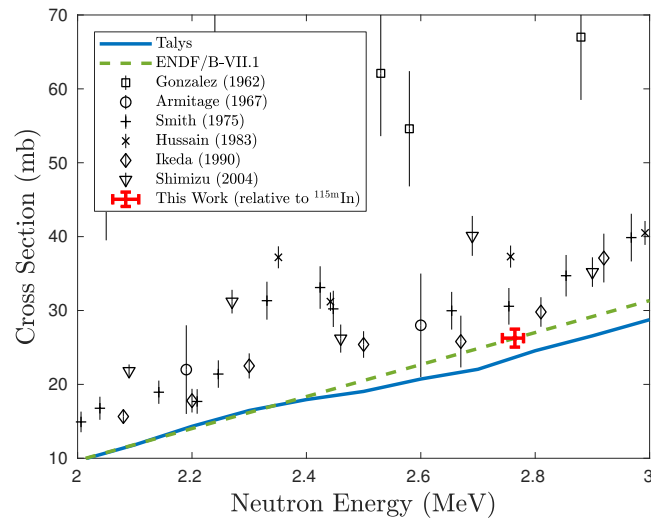


Figure 4.9: Measured $^{47}\text{Ti}(\text{n},\text{p})^{47}\text{Sc}$ cross section relative to indium activation.

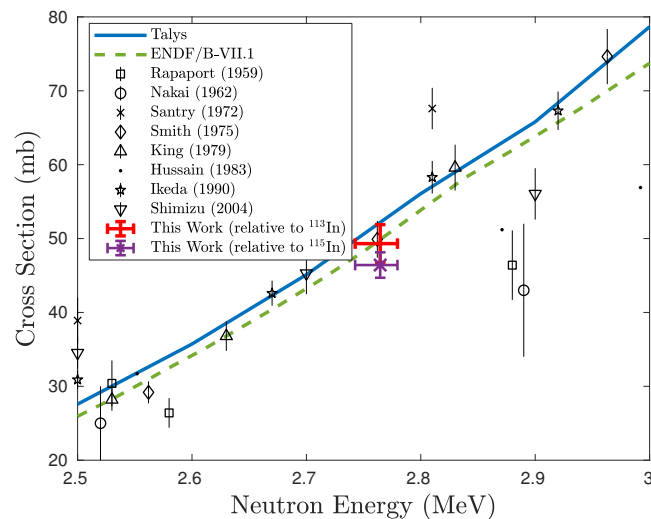


Figure 4.10: Measured $^{64}\text{Zn}(\text{n},\text{p})^{64}\text{Cu}$ cross section relative to indium activation.

4.5 Discussion

The proximity of the target to the neutron production surface opens the possibility of performing a measurement of the cross section over a limited energy range via mounting the samples slightly off-axis with respect to the beam. This could be accomplished using the 9-foil sample holder described in subsection 4.3.5 above. Mounting samples at each of these positions would subject the samples to neutrons with energies ranging from 2.765 MeV at the central location to 2.616 MeV at the four corners, with the other locations having intermediate energy values. These sorts of multi-sample measurements could be used to determine the “rising edge” of the cross sections, aiding in the development of optical models for the reactants.

These measurements also highlight the possibility of using fast neutrons from DD and/or DT generators to produce meaningful quantities of radioisotopes for a wide range of applications via charge exchange reactions, such as (n,p) and (n, α). Many applications, including diagnostic and therapeutic medical use, require mCi activity levels. For the production of a radionuclide sample, the saturation activity ($A_{saturation}$) is achieved at secular equilibrium:

$$R_{production} = R_{decay} = \lambda N_{product} \quad (4.9)$$

While the saturation activity represents the maximum activity that can be made at a generator with a given total neutron output, there may be situations where either a smaller activity is needed, or a shorter irradiation is desired. In this case, it is useful to introduce a neutron utilization factor (η_x). η_x is the constant of proportionality between R_n , the neutron source output (in neutrons/s), and the saturation activity:

$$A_{saturation} = \eta_x R_n \quad (4.10)$$

η_x represents the likelihood that a neutron produced in the generator will create x , the isotope of interest. It includes the overlap between the production target and the locus where the neutrons are being created, and the fraction of nuclear reactions which generate the desired activity x :

$$\eta_x = \frac{1}{R_n} \int_{\text{production target}} \phi(\mathbf{r}) \bar{\sigma}_x \rho_{target}(\mathbf{r}) d\mathbf{V},$$

$$d\mathbf{V} = r^2 dr \sin \theta d\theta d\varphi \quad (4.11)$$

where $\bar{\sigma}_x$ is the average cross section producing the radionuclide of interest, $\rho_{target}(\mathbf{r})$ is the density of the target as a function of position, and $\phi(\mathbf{r})$ is the neutron flux (in n/cm²/s) as a function of position. η_x allows us to cast the activity produced in a given irradiation time t_i as:

$$A(t_i) = \eta_x R_n (1 - e^{-\lambda t_i}) \quad (4.12)$$

Maximizing η_x would be the goal of any engineering design to produce a desired activity using a neutron generator at a minimum of cost and radiological impact.

An optimal design for the neutron generator would also allow for the possibility of reflecting fast neutrons back onto the target to maximize their utilization for radionuclide production. This sort of “flux trap” has been used for the production of radionuclides in reactors, but has not to date been optimized for use with fast neutrons at DD and/or DT neutron sources. The HFNG, with its self-loading target and “flux trap” geometry, has many features that make it well-suited for such isotope production purpose. Switching to DT operation would dramatically increase the flux as well as the production cross section, since (n,p) tends to be significantly larger at 14 MeV. However, the higher neutron energy would also open the (n,pn) channels. In the case of ^{47}Sc , this would lead to the presence of ^{46}Sc ($t_{1/2} = 83.79$ d [191]) in the sample, which might pose some concerns for medical applications. However, this is not an issue for ^{64}Cu since the (n,pn) channel leads to the production of stable ^{63}Cu .

Assuming a neutron flux of $1.3 \cdot 10^7$ neutrons/cm²s on the target, masses of 0.533 g of natural zinc and 0.337 g of natural titanium, and cross sections of 47.5 mb for $^{64}\text{Zn}(\text{n},\text{p})^{64}\text{Cu}$ and 26.26 mb for $^{47}\text{Ti}(\text{n},\text{p})^{47}\text{Sc}$, theoretical saturation activities for current operation at the time of this work are estimated to be 1.5 kBq of ^{64}Cu and 0.11 kBq of ^{47}Sc . This falls short of the mCi (37 MBq) level required for commercial application by a factor of 3-4 orders of magnitude, but with the operation of the second deuterium ion source, increased current, and fast neutron reflection, this goal may well be within reach. By increasing the activation target thickness to 1 cm (a factor of 10), switching to DT operation (a factor of 80), increasing current and running the second ion source (a factor of 60), and relying upon the higher (n,p) cross section at DT energies (a factor of approximately 3), we believe saturation activities of approximately 6 mCi of ^{64}Cu and 0.5 mCi of ^{47}Sc can be achieved. The activities produced at the end of irradiation averaged 453.8 Bq of ^{64}Cu , and 31.6 Bq of ^{47}Sc . Assuming a conservative neutron source output of 10^8 neutrons / second, we can estimate that, in present operation, the HFNG has an average $\eta_{64\text{Cu}} \approx 3.0 \cdot 10^{-5}$ for ^{64}Cu and $\eta_{47\text{Sc}} \approx 1.1 \cdot 10^{-5}$ for ^{47}Sc . This falls approximately 4 orders of magnitude short of the $\eta_x \approx 0.37$ needed for mCi-scale production. A factor of 10 in η_x could easily be gained through use of targets 1-cm in thickness without worry of contaminating reaction channels opening up, but η_x gains beyond this will require modification of operation conditions.

4.6 Conclusion and future work

Using activation methods on thin foils, the $^{47}\text{Ti}(\text{n},\text{p})^{47}\text{Sc}$ and $^{64}\text{Zn}(\text{n},\text{p})^{64}\text{Cu}$ production cross sections were measured for $2.76^{+0.01}_{-0.02}$ MeV neutrons produced using the High Flux Neutron Generator (HFNG) at UC Berkeley. The cross sections were measured with less than 5% uncertainty relative to the well-known $^{115}\text{In}(\text{n},\text{n}')^{115\text{m}}\text{In}$ and $^{113}\text{In}(\text{n},\text{n}')^{113\text{m}}\text{In}$ fast neutron cross sections [170, 171]. The measured values of 26.26 ± 0.82 mb and 49.3 ± 2.6 mb (relative to ^{113}In) or 46.4 ± 1.7 mb (relative to ^{115}In), respectively, are consistent with earlier experimental data and theoretical models, but have smaller uncertainties than previous

measurements.

In addition, the production of the ^{116}In via the $^{115}\text{In}(\text{n},\gamma)$ reaction was close to the value one would expect given an effective incident neutron energy of 2.45 MeV. While this is not consistent with the average neutron energy at the target location ($2.76_{-0.02}^{+0.01}$ MeV), the fact that it was close indicates the paucity of thermal neutrons in this central location. This in turn highlights the usefulness of such compact DD-neutron sources for producing “clean” activities via the (n,p) channel. The use of DD neutron generators can be an efficient method for the measurement of low-energy (n,p) reaction channels, as well as a relative method used to normalize measurements at higher neutron energies. In addition to improving the value of these measurements for nuclear reaction evaluation, our results highlight the potential use of compact neutron generators for the production of radionuclides locally for medical applications.

It is worth noting that at the time of publication, the HFNG is now operating at close to 10^9 n/s, with a clear path towards 10^{10} . Future work will involve the continued measurement of the (n,p) production cross sections for various other emerging therapeutic and diagnostic radioisotopes, to expand the toolset of options available for modern medical imaging and cancer therapy. This will focus on radionuclides which permit more customized and precise dose deposition, as well as patient-specific treatments.

4.7 Additional discussion

Additional discussion of the experimental and analytical details for this work, which were excluded from the published journal article to preserve its scope, are included here.

The basic design characteristics and operation of the HFNG have been described in this chapter, but a more detailed discussion of the generator may be found in the recent work of Ayllon *et al.* [192]. The HFNG is seen in Figure 4.12, illustrating the compact nature of the generator. A photograph of the actual sample holder used for the HFNG irradiations in this chapter is seen in Figure 4.11, for the case of a $^{64}\text{Zn}(\text{n},\text{p})^{64}\text{Cu}$ measurement.



Figure 4.11: Sample holder used for the Berkeley HFNG. The zinc (visible) foil is co-loaded on top of reference indium foil, ready for irradiation.



Figure 4.12: The UC Berkeley High-Flux Neutron Generator, along with UC Berkeley Nuclear Engineering PhD student Jon Morrell, who currently leads operation of the HFNG.

A rendering of the HFNG target chamber, as modeled in MCNP6, is seen in Figure 4.13. This figure presents a small subset of the full MCNP6 model of the HFNG, to better illustrate the geometry of the target chamber. This model is the same described in subsection 4.3.1 for simulation of neutron transport in the HFNG. The full input file for this MCNP model is included here for reference, in Appendix A.1.

As described in subsection 4.3.4, the activities produced in the HFNG irradiations were quantified via gamma-ray spectrometry. Two detectors were used in this measurement. An Ortec 80% High-Purity Germanium (HPGe) detector was used for the detection of the positron annihilation radiation from the ^{64}Cu decay [5], the 391 keV gamma-ray from the ^{113m}In isomer [3], and the 336 keV gamma-ray from the decay of the ^{115m}In isomer [173]. An Ortec planar Low-Energy Photon Spectrometer (LEPS) was used for the detection of the lower-energy 159 keV gamma-ray from ^{47}Sc [159] as well as the two indium isomers mentioned above. Both of these detectors are seen in Figure 4.14.

It is worth mentioning that, since natural zinc has five stable isotopes ($^{64,66-68,70}\text{Zn}$ [193]), one would expect to see reaction channels on all five isotopes. Indeed, $^{66}\text{Zn}(\text{n},\text{p})^{66}\text{Cu}$ has an energetic threshold of 1.886 MeV, but was not seen in the work described here, due to the reaction having a very weak cross section at these energies (approximately 0.2 mb [194]), and a short-lived product ($t_{1/2} = 5.120 \pm 0.014$ m [142]). Operating protocol requires a 30 minute delay between shutdown and entrance to the HFNG vault, to allow for short-lived

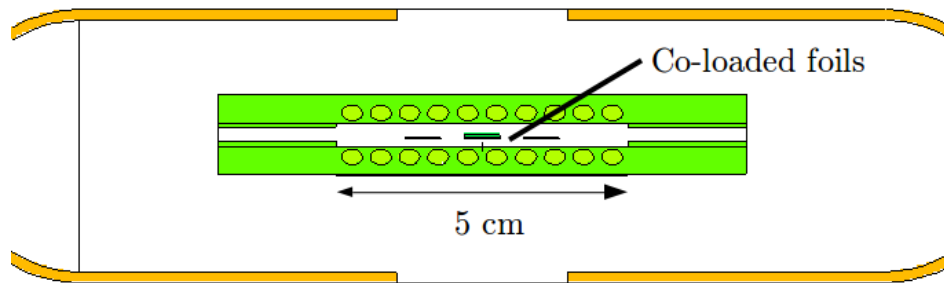


Figure 4.13: MCNP6 model of the HFNG target chamber, with reference scale. The co-loaded foils can be seen in the target chamber center. The ovals indicate the location of water cooling channels.

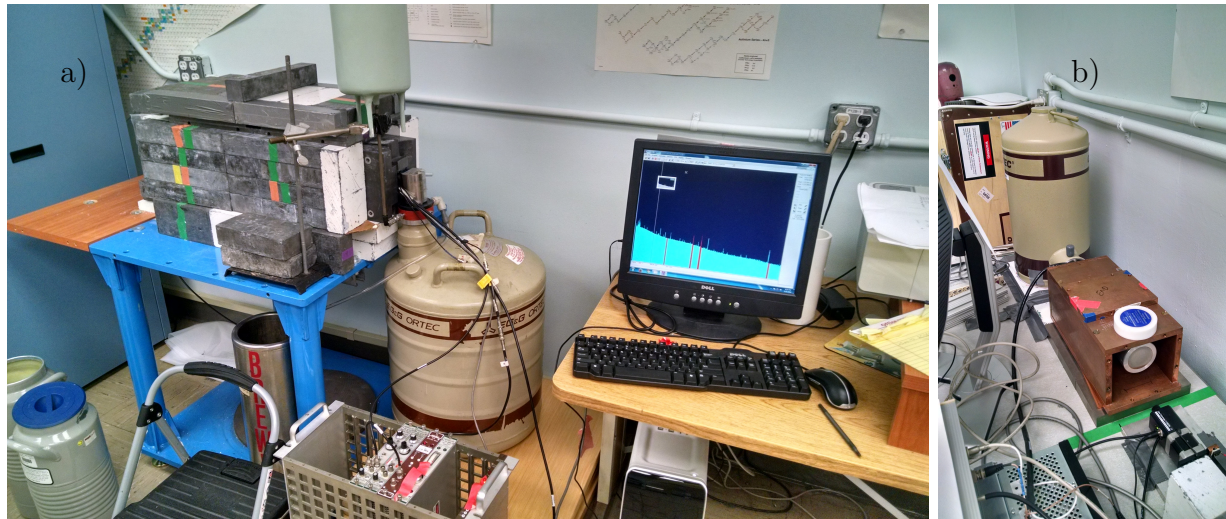


Figure 4.14: High-Purity Germanium Detectors used for gamma spectroscopy of the activated foils, as described in subsection 4.3.4. (a) Ortec 80% HPGe detector, (b) Ortec planar LEPS detector.

and airborne reaction products to decay out, and reduce prompt dose rates. However, this makes quantification difficult for any reaction products with lifetimes less than approximately 15 minutes. $^{68}\text{Zn}(\text{n},\text{p})^{68}\text{Cu}$ ($t_{1/2} = 30.9 \pm 0.6$ s [195]) is not observed due to the DD spectrum being below the energetic threshold of 3.712 MeV. A similar argument holds for $^{70}\text{Zn}(\text{n},\text{p})^{70}\text{Cu}$ ($t_{1/2} = 44.5 \pm 0.2$ s [196], threshold 5.889 MeV) — though both of these products would have decayed back into Zn long before the samples were removed from the HFNG.

However, none of these arguments apply to the case of $^{67}\text{Zn}(\text{n},\text{p})^{67}\text{Cu}$ ($t_{1/2} = 61.83 \pm 0.12$ h [197]), which is not short-lived, and has a positive reaction Q-value of 221.55 keV. Weak ^{67}Cu activities were indeed seen in the gamma spectrometry of the activated zinc targets, but no $^{67}\text{Zn}(\text{n},\text{p})^{67}\text{Cu}$ cross sections were reported. ^{67}Cu activity could not be quantified with sufficient confidence for the reporting of a cross section, especially one with significant medical applications. This is due to the low natural abundance (4.04%) of ^{67}Zn , combined with its weak cross section of approximately 1.5 mb at this energy [189]. In addition, at the time of the published work, HFNG operation was limited to irradiations with maximum durations of approximately three hours. ^{67}Cu is highly desired as part of a theranostic pair with ^{64}Cu , but no satisfactory production routes currently are available. Indeed, $^{67}\text{Zn}(\text{n},\text{p})^{67}\text{Cu}$ via fission neutrons has discrepant production data and extremely low radiochemical purity, and $^{68}\text{Zn}(\gamma,\text{p})^{67}\text{Cu}$, $^{70}\text{Zn}(\text{p},\alpha)^{67}\text{Cu}$, and $^{68}\text{Zn}(\text{p},2\text{p})^{67}\text{Cu}$ all suffer from low yields, and require enriched targets for radioisotopic purity [10]. $^{67}\text{Zn}(\text{n},\text{p})^{67}\text{Cu}$ data is extremely sparse in the 1–5 MeV region, with only 7 measured data points [189, 198–200]. It is clear that a repeated measurement of the $^{67}\text{Zn}(\text{n},\text{p})^{67}\text{Cu}$ cross section at the HFNG would be a useful endeavor, especially irradiating a target enriched in ^{67}Zn . With recent generator upgrades, it is capable of sustaining irradiations up to a few days in length — such an irradiation would be able to drive a zinc target much closer to the ^{67}Cu saturation activity, permitting this valuable measurement.

A similar argument can be made for the other $^{\text{nat}}\text{Ti}(\text{n},\text{p})$ channels. $^{46}\text{Ti}(\text{n},\text{p})^{46}\text{Sc}$ is energetically permitted, but was not observed — indeed, this cross section has not been observed below 3.6 MeV [180]. Much like ^{67}Cu , this measurement could easily be re-attempted using a longer irradiation ($t_{1/2} = 83.79 \pm 0.04$ d [191]) and an enriched target (8.25% natural ^{46}Ti abundance). $^{48}\text{Ti}(\text{n},\text{p})^{48}\text{Sc}$ and $^{50}\text{Ti}(\text{n},\text{p})^{50}\text{Sc}$ are inaccessible, as the DD spectrum falls below their energetic threshold of 3.273 MeV and 6.225 MeV, respectively. $^{49}\text{Ti}(\text{n},\text{p})^{49}\text{Sc}$ would be difficult to measure due to a lack of strong decay gamma-rays, but could be quantified via its 824.1 keV β^- emission ($I_\beta = 99.940\%$) using liquid scintillation spectrometry [201].

Recent and future HFNG experiments

The characterization described in this chapter has served as the basis for more recent measurements at the HFNG. The characterized energy spectrum and MCNP neutron transport model described here, along with experience gained in these measurements, have provided guidance for suitable experiments accessible at the HFNG facility. Two such recent experiments are described here.

Many proposed designs for molten salt reactors use chlorine-based salts as coolant. Unfortunately, the $^{35}\text{Cl}(\text{n},\text{p})$ reaction is a significant neutron “poison”, consuming fast spectrum neutrons needed to achieve criticality and producing the long-lived ^{35}S ($t_{1/2} = 87.37 \pm 0.04$ d [202]). In addition to the $^{35}\text{Cl}(\text{n},\text{p})$ reaction, $^{35}\text{Cl}(\text{n},\alpha)$ produces ^{32}P ($t_{1/2} = 14.268 \pm 0.005$ d [203]) which is used as a radiochemical tracer for metabolic studies. Unfortunately, no measurements of this important cross section exist between 100 keV and 14.1 MeV incident neutron energy. To this end, we performed an activation experiment using reagent-grade NaCl together with a ^{nat}In monitor. Preliminary results from this experiment have indicated a value far lower than in evaluated libraries, prompting a second series of measurements at a range of angles to determine the energy dependence of the cross section near 2.7 MeV. This result will not only inform future ^{35}Cl cross section evaluations, but will also provide a probe of transition between the Resolved and Unresolved Resonance energy regions and the energies where statistical models are expected to be more appropriate.

^{99m}Tc is one of the most well-known medical radionuclides, used as a diagnostic isotope in cardiac, renal, lung function, and tumor imaging studies. Collected in a $^{99}\text{Mo}/^{99m}\text{Tc}$ generator system, the ^{99}Mo parent has traditionally been produced as a fission product in thermal reactors. However, an aging reactor fleet and proliferation concerns associated with ^{99}Mo recovery have recently made the identification of alternative production pathways one of the highest priorities in the nuclear data community [15]. DD neutron generators stand poised as one such possible alternative, through production via the $^{98}\text{Mo}(\text{n},\gamma)^{99}\text{Mo}$ reaction. A recent measurement was performed at the HFNG to measure the energy dependence of this cross section at four energy locations near 2.7 MeV. The custom holder designed for this measurement is seen in Figure 4.15. This cross section has not been measured since 1967 [204] and re-measurement in the 1–10 MeV region has been listed as a vital nuclear data need for ^{99}Mo production.

With the capability established for precise (n,x) cross section measurements at the HFNG, a targeted experimental campaign is underway to address the needs of the nuclear data and applications communities. Current and future experiments focus on the measurement of cross sections for a number of emerging medical radionuclides, as well as novel production pathways for established radionuclides. These include the $^{32}\text{S}(\text{n},\text{p})^{32}\text{P}$, $^{67}\text{Zn}(\text{n},\text{p})^{67}\text{Cu}$, $^{89}\text{Y}(\text{n},\text{p})^{89}\text{Sr}$, $^{105}\text{Pd}(\text{n},\text{p})^{105}\text{Rh}$, $^{149}\text{Sm}(\text{n},\text{p})^{149}\text{Pm}$, $^{153}\text{Eu}(\text{n},\text{p})^{153}\text{Sm}$, $^{159}\text{Tb}(\text{n},\text{p})^{159}\text{Gd}$, $^{161}\text{Dy}(\text{n},\text{p})^{161}\text{Tb}$, $^{166}\text{Er}(\text{n},\text{p})^{166}\text{Ho}$, $^{169}\text{Tm}(\text{n},\text{p})^{169}\text{Er}$, $^{175}\text{Lu}(\text{n},\text{p})^{175}\text{Yb}$, and $^{177}\text{Hf}(\text{n},\text{p})^{177}\text{Lu}$ reactions.



Figure 4.15: Custom target holder for the measurement of the $^{98}\text{Mo}(n,\gamma)^{99}\text{Mo}$ cross section at four energy locations near 2.7 MeV.

Chapter 5

Conclusions and Outlook

IN THIS work, we have explored a variety of pathways for detailed measurements of the excitation functions of medical radionuclides. These have all been selected to provide basic science advances in enabling production through existing pathways for medical isotope production, as well for promising potential future pathways:

- Characterization of the $^{93}\text{Nb}(\text{p},4\text{n})^{90}\text{Mo}$ reaction as an intermediate-energy proton monitor;
- Production of the $^{51,52\text{m},52\text{g}}\text{Mn}$ novel PET isotopes through low-energy $^{\text{nat}}\text{Fe}(\text{p},\text{x})$ reactions;
- Production of ^{64}Cu and ^{47}Sc via $^{64}\text{Zn},^{47}\text{Ti}(\text{n},\text{p})$ reactions using a compact DD generator.

In addition, this work seeks to outline many of the small systematic issues which can be unwittingly introduced into such measurements even with careful experimental design, and the methods developed to deal with them. Nearly all of the issues presented in this work stem from the use of Kapton tape to encapsulate activation foils and prevent dispersible contamination. One cross-cutting outcome from this work has an increased appreciation for the role played by the silicone adhesive on this tape used to contain the individual stacked targets in these measurements. While this might seem obvious, the contributions to the slowing of the beam due to the adhesive has often been neglected in much work performed to date. While this plays a limited role at high beam energies, it becomes increasingly important for proton energies below 25 MeV. This work also presents an explanation for evidence of $^{\text{nat}}\text{Si}(\text{p},\text{x})^{22,24}\text{Na}$ contamination, arising from silicone adhesive in the Kapton tape used to encapsulate monitor foils. This contamination is frequently seen in stacked-target activation experiments and has the potential to systematically dampen the magnitude of reported cross sections by as much as 50%. This is a poignant reminder of the importance and selection of monitor reactions, and how $^{93}\text{Nb}(\text{p},4\text{n})^{90}\text{Mo}$ fits this perfectly in the intermediate-energy region. While these issues have been identified and accounted for in the analysis described here, they serve as a cautionary note to future stacked-target cross section measurements. In

addition to the novelty of advancing basic science, the measurement of these reactions provides an example of the poor current state of modeling for proton-induced nuclear reactions in the pre-equilibrium region. The nuclear data measured here provides a novel contribution in the fact that it may be able to be used as input parameters to tune and improve reaction modeling in this mass region by providing insight into the pre-equilibrium reaction mechanisms that play such an important role in this energy region.

This project has been focused almost completely on the basic nuclear physics thin-target measurements for each production reaction. The next step in continuing this work will be to repeat these measurements, extending the energy range explored in each of these experiments, and filling in the energy points in between those measured here for each excitation function. With a more well-characterized excitation function, these data will be used in designing production targets for large-scale (mCi-scale) activity production. Following production using these targets, radiochemical workup will purify the desired reaction products, and then couple the purified radionuclides to appropriate targeting vectors. Thus, the project will cover a scope leading from basic physics measurements, all the way up to delivering routine quantities of labelled radionuclides, ready to be used in early pre-clinical studies. The synthesis of the chemistry, nuclear physics, and novel target design skills necessary to complete this bench-to-preclinical production is a requirement for developing and bringing a new medical radionuclide to market. Without targeted collaboration or integrated campaigns for complete production development, many novel radionuclides remain stuck in this development pipeline.

Due to the breadth of chemistry, physics, and biomedical science which this development process requires, it is clear that this project is inherently interdisciplinary. Part of doing the itinerant work of science is often leaving good work behind undone, as a retained connection to a former institution, and helping those that follow to improve upon the work you've done. Moving beyond the work in the present dissertation would likely have excessively broadened its scope. However, the work described here may help to enable exciting new campaigns of investigation in basic science, disease biology research, and nuclear medicine. I hope to continue down this pipeline in my next activities, developing the radiochemical skills and expertise necessary for enabling me to help lead a complete, bench-to-pre-clinical campaign of novel medical radionuclide development. The production pathways described in this work will hopefully result in the development of capabilities for routine production for the labeled medical radionuclides $^{51,52m,52g}\text{Mn}$, ^{64}Cu , and ^{47}Sc . It is thus my fervent hope that these will be able to be utilized for preclinical studies in other academic and research laboratories, to help aid in their development for clinical use in treating a variety of diseases plaguing humankind.

Bibliography

- [1] H. Liskien and A. Paulsen, “Neutron production cross sections and energies for the reactions T(p,n)3He, D(d,n)3He, and T(d,n)4He,” *Atomic Data and Nuclear Data Tables*, vol. 11, no. 7, pp. 569–619, 1973.
- [2] H. H. Hansen, E. de Roost, W. van der Eijk, and R. Vaninbroukx, “The decay of ^{115}mIn ,” *Zeitschrift für Physik*, vol. 269, no. 2, pp. 155–161, 1974.
- [3] J. Blachot, “Nuclear Data Sheets for $A = 113$,” *Nuclear Data Sheets*, vol. 111, pp. 1471–1618, jun 2010.
- [4] J. Blachot, “Nuclear Data Sheets for $A = 116$,” *Nuclear Data Sheets*, vol. 111, pp. 717–895, mar 2010.
- [5] B. Singh, “Nuclear Data Sheets for $A = 64$,” *Nuclear Data Sheets*, vol. 108, pp. 197–364, feb 2007.
- [6] S. A. Graves, P. A. Ellison, T. E. Barnhart, H. F. Valdovinos, E. R. Birnbaum, F. M. Nortier, R. J. Nickles, and J. W. Engle, “Nuclear excitation functions of proton-induced reactions ($E_p=35\text{--}90$ MeV) from Fe, Cu, and Al,” *Nuclear Instruments and Methods in Physics Research, Section B: Beam Interactions with Materials and Atoms*, vol. 386, pp. 44–53, nov 2016.
- [7] M. Moll, “Radiation Damage in Silicon Particle Detectors - microscopic defects and macroscopic properties,” in *ROSE Collaboration (CERN RD48) - Research and Development on Silicon Detectors for Future Experiments*, no. April, Radiation effects on electronic components and systems for LHC - CERN Technical Training, 2000.
- [8] A. S. Voyles, L. A. Bernstein, E. R. Birnbaum, J. W. Engle, S. A. Graves, T. Kawano, A. M. Lewis, and F. M. Nortier, “Excitation functions for (p,x) reactions of niobium in the energy range of $E_p = 40\text{--}90$ MeV,” *Nuclear Instruments and Methods in Physics Research Section B: Beam Interactions with Materials and Atoms*, vol. 429, pp. 53–74, aug 2018.
- [9] D. A. Mulford, D. A. Scheinberg, and J. G. Jurcic, “The Promise of Targeted α -Particle Therapy,” *Journal of Nuclear Medicine*, vol. 46, pp. 199S–204S, jan 2005.

- [10] S. M. Qaim, "Nuclear data for production and medical application of radionuclides: Present status and future needs," *Nuclear Medicine and Biology*, vol. 44, pp. 31–49, 2016.
- [11] C. Müller, M. Bunka, S. Haller, U. Köster, V. Groehn, P. Bernhardt, N. van der Meulen, A. Türler, and R. Schibli, "Promising Prospects for ^{44}Sc -/ ^{47}Sc -Based Theragnostics: Application of ^{47}Sc for Radionuclide Tumor Therapy in Mice," *Journal of Nuclear Medicine*, vol. 55, pp. 1658–1664, oct 2014.
- [12] S. M. Bentzen, "Theragnostic imaging for radiation oncology: dose-painting by numbers," *The Lancet Oncology*, vol. 6, no. 2, pp. 112–117, 2005.
- [13] S. C. Srivastava, "Paving the Way to Personalized Medicine: Production of Some Promising Theragnostic Radionuclides at Brookhaven National Laboratory," *Seminars in Nuclear Medicine*, vol. 42, no. 3, pp. 151–163, 2012.
- [14] J. T. Bushberg, J. A. Seibert, E. M. Leidholdt, and J. M. Boone, *The Essential Physics of Medical Imaging*. Wolters Kluwer Health, 2011.
- [15] L. A. Bernstein, D. Brown, A. M. Hurst, J. H. Kelley, F. G. Kondev, E. A. McCutchan, C. D. Nesaraja, R. Slaybaugh, and A. Sonzogni, "Nuclear Data Needs and Capabilities for Applications Whitepaper," tech. rep., Lawrence Livermore National Laboratory (LLNL), Livermore, 2015.
- [16] W. D. Ehmann and D. E. Vance, *Radiochemistry and Nuclear Methods of Analysis*. Chemical Analysis: A Series of Monographs on Analytical Chemistry and Its Applications, Wiley, 1993.
- [17] P. Krüger, *Principles of activation analysis*. Wiley-Interscience, 1971.
- [18] S. Qaim, F. Tárkányi, P. Oblozinsky, K. Gul, A. Hermanne, M. Mustafa, F. Nortier, B. Scholten, Y. Shubin, S. Takács, and Y. Zhuang, "Charged particle cross-section database for medical radioisotope production: diagnostic radioisotopes and monitor reactions," *IAEA-TECDOC-1211*, 2001.
- [19] T. W. Burrows, "Nuclear Data Sheets for $A = 48$," *Nuclear Data Sheets*, vol. 107, no. 7, pp. 1747–1922, 2006.
- [20] D. Delbeke and G. M. Segall, "Status of and Trends in Nuclear Medicine in the United States," *Journal of Nuclear Medicine*, vol. 52, pp. 24S–28S, dec 2011.
- [21] NSAC Isotopes Subcommittee, "Meeting Isotope Needs and Capturing Opportunities for the Future: The 2015 Long Range Plan for the DOE-NP Isotope Program," tech. rep., 2015.

- [22] International Atomic Energy Agency, *Cyclotron Produced Radionuclides: Physical Characteristics and Production Methods*. No. 468 in Technical Reports Series, Vienna: International Atomic Energy Agency, 2009.
- [23] D. J. Schlyer, P. den Winkel, T. J. Ruth, M. M. Vora, M. Pillai, and M. Haji-Saeid, “Cyclotron produced radionuclides: Principles and practice,” Tech. Rep. 465, Technical Reports Series, 2008.
- [24] E. Browne, “Nuclear Data Sheets for A = 90,” *Nuclear Data Sheets*, vol. 82, pp. 379–546, nov 1997.
- [25] S. Sudár and S. M. Qaim, “Cross sections for the formation of $^{195}\text{Hg}^{m,g}$, $^{197}\text{Hg}^{m,g}$, and $^{196}\text{Au}^{m,g}$ in α and ^3He -particle induced reactions on Pt: Effect of level density parameters on the calculated isomeric cross-section ratio,” *Phys. Rev. C*, vol. 73, p. 34613, mar 2006.
- [26] N. Chakravarty, P. K. Sarkar, and S. Ghosh, “Pre-equilibrium emission effects in the measured isomeric yield ratios in alpha-induced reactions on ^{197}Au ,” *Phys. Rev. C*, vol. 45, pp. 1171–1188, mar 1992.
- [27] Y. Dong and H. Junde, “Nuclear Data Sheets for A = 52,” *Nuclear Data Sheets*, vol. 128, pp. 185–314, sep 2015.
- [28] C. D. Nesaraja, S. D. Geraedts, and B. Singh, “Nuclear Data Sheets for A = 58,” *Nuclear Data Sheets*, vol. 111, pp. 897–1092, apr 2010.
- [29] B. Singh and J. Chen, “Nuclear Data Sheets for A = 85,” *Nuclear Data Sheets*, vol. 116, no. Supplement C, pp. 1–162, 2014.
- [30] T. D. Johnson and W. D. Kulp, “Nuclear Data Sheets for A = 87,” *Nuclear Data Sheets*, vol. 129, pp. 1–190, nov 2015.
- [31] B. Singh, “Nuclear Data Sheets for A = 89,” *Nuclear Data Sheets*, vol. 114, pp. 1–208, jan 2013.
- [32] J. B. Cumming, “Monitor Reactions for High Energy Proton Beams,” *Annual Review of Nuclear Science*, vol. 13, pp. 261–286, dec 1963.
- [33] P. A. Aarnio, M. T. Nikkinen, and J. T. Routti, “UNISAMPO, comprehensive software for gamma-spectrum processing,” *Journal of Radioanalytical and Nuclear Chemistry*, vol. 248, pp. 371–375, may 2001.
- [34] K. R. Jackman, J. W. Engle, F. M. Nortier, K. D. John, E. R. Birnbaum, and D. E. Norman, “Synthetic spectra for radioactive strontium production QA/QC,” *Journal of Radioanalytical and Nuclear Chemistry*, vol. 302, no. 1, pp. 347–352, 2014.

- [35] M. J. Berger, J. H. Hubbell, S. M. Seltzer, J. Chang, J. S. Coursey, R. Sukumar, D. S. Zucker, and K. Olsen, “XCOM: Photon cross section database (version 1.5),” 2010.
- [36] H. Bateman, “The solution of a system of differential equations occurring in the theory of radioactive transformations,” in *Proc. Cambridge Philos. Soc.*, vol. 15, pp. 423–427, 1910.
- [37] J. Cetnar, “General solution of Bateman equations for nuclear transmutations,” *Annals of Nuclear Energy*, vol. 33, pp. 640–645, may 2006.
- [38] G. Steyn, S. Mills, F. Nortier, B. Simpson, and B. Meyer, “Production of ^{52}Fe via proton-induced reactions on manganese and nickel,” *International Journal of Radiation Applications and Instrumentation. Part A. Applied Radiation and Isotopes*, vol. 41, pp. 315–325, jan 1990.
- [39] M. Uddin, M. Hagiwara, F. Tarkanyi, F. Ditroi, and M. Baba, “Experimental studies on the proton-induced activation reactions of molybdenum in the energy range 22–67 MeV,” *Applied Radiation and Isotopes*, vol. 60, pp. 911–920, jun 2004.
- [40] S. J. Mills, G. F. Steyn, and F. M. Nortier, “Experimental and theoretical excitation functions of radionuclides produced in proton bombardment of copper up to 200 MeV,” *International Journal of Radiation Applications and Instrumentation Part A. Applied Radiation and Isotopes*, vol. 43, pp. 1019–1030, aug 1992.
- [41] H. H. Andersen and J. F. Ziegler, *Hydrogen stopping powers and ranges in all elements*. Pergamon Press, New York, jan 1977.
- [42] J. F. Ziegler and J. P. Biersack, *The Stopping and Range of Ions in Matter*, pp. 93–129. Boston, MA: Springer US, 1985.
- [43] J. F. Ziegler, “Stopping of energetic light ions in elemental matter,” *Journal of Applied Physics*, vol. 85, pp. 1249–1272, jan 1999.
- [44] T. Goorley, M. James, T. Booth, F. Brown, J. Bull, L. J. Cox, J. Durkee, J. Elson, M. Fensin, R. A. Forster, J. Hendricks, H. G. Hughes, R. Johns, B. Kiedrowski, R. Martz, S. Mashnik, G. McKinney, D. Pelowitz, R. Prael, J. Sweezy, L. Waters, T. Wilcox, and T. Zukaitis, “Initial MCNP6 Release Overview,” *Nuclear Technology*, vol. 180, pp. 298–315, dec 2012.
- [45] L. Marus, J. Engle, K. John, E. Birnbaum, and F. Nortier, “Experimental and computational techniques for the analysis of proton beam propagation through a target stack,” *Nuclear Instruments and Methods in Physics Research Section B: Beam Interactions with Materials and Atoms*, vol. 345, pp. 48–52, feb 2015.

- [46] N. Otuka, E. Dupont, V. Semkova, B. Pritychenko, A. I. Blokhin, M. Aikawa, S. Babykina, M. Bossant, G. Chen, S. Dunaeva, R. A. Forrest, T. Fukahori, N. Furutachi, S. Ganesan, Z. Ge, O. O. Gritzay, M. Herman, S. Hlavač, K. Kato, B. Lalremrata, Y. O. Lee, A. Makinaga, K. Matsumoto, M. Mikhaylyukova, G. Pikulina, V. G. Pronyaev, A. Saxena, O. Schwerer, S. P. Simakov, N. Soppera, R. Suzuki, S. Takács, X. Tao, S. Taova, F. Tárkányi, V. V. Varlamov, J. Wang, S. C. Yang, V. Zerkin, and Y. Zhuang, "Towards a More Complete and Accurate Experimental Nuclear Reaction Data Library (EXFOR): International Collaboration Between Nuclear Reaction Data Centres (NRDC)," *Nuclear Data Sheets*, vol. 120, pp. 272–276, 2014.
- [47] J. Zweit, P. Carnochan, R. Goodall, and R. Ott, "Nickel-57-doxorubicin, a potential radiotracer for pharmacokinetic studies using PET: production and radiolabelling," *Journal of nuclear biology and medicine (Turin, Italy : 1991)*, vol. 38, pp. 18–21, dec 1994.
- [48] J. Zweit, "Medium half-life inorganic radionuclides for PET imaging," *Current directions in radiopharmaceutical research and development*, pp. 47–61, 1996.
- [49] F. Rösch and R. P. Baum, "Generator-Based Radiopharmaceuticals for PET Dosimetry Before, During, and After Endoradiotherapy BT - Therapeutic Nuclear Medicine," pp. 83–94, Berlin, Heidelberg: Springer Berlin Heidelberg, 2014.
- [50] M. R. Lewis, M. Wang, D. B. Axworthy, L. J. Theodore, R. W. Mallet, A. R. Fritzberg, M. J. Welch, and C. J. Anderson, "In Vivo Evaluation of Pretargeted ^{64}Cu for Tumor Imaging and Therapy," *Journal of Nuclear Medicine*, vol. 44, pp. 1284–1292, aug 2003.
- [51] R. P. Bandari, Z. Jiang, T. S. Reynolds, N. E. Bernskoetter, A. F. Szczodroski, K. J. Bassuner, D. L. Kirkpatrick, T. L. Rold, G. L. Sieckman, T. J. Hoffman, J. P. Connors, and C. J. Smith, "Synthesis and biological evaluation of copper-64 radiolabeled [DUPA-6-Ahx-(NODAGA)-5-Ava-BBN(7-14)NH₂], a novel bivalent targeting vector having affinity for two distinct biomarkers (GRPr/PSMA) of prostate cancer," *Nuclear Medicine and Biology*, vol. 41, no. 4, pp. 355–363, 2014.
- [52] E. Gourni, L. Del Pozzo, E. Kheirallah, C. Smerling, B. Waser, J.-C. Reubi, B. M. Patterson, P. S. Donnelly, P. T. Meyer, and H. R. Maecke, "Copper-64 Labeled Macroyclic Sarcophagine Coupled to a GRP Receptor Antagonist Shows Great Promise for PET Imaging of Prostate Cancer," *Molecular Pharmaceutics*, vol. 12, no. 8, pp. 2781–2790, 2015.
- [53] F. Szelecsényi, G. Blessing, and S. Qaim, "Excitation functions of proton induced nuclear reactions on enriched ^{61}Ni and ^{64}Ni : Possibility of production of no-carrier-added ^{61}Cu and ^{64}Cu at a small cyclotron," *Applied Radiation and Isotopes*, vol. 44, pp. 575–580, mar 1993.

- [54] M. Aslam, S. Sudár, M. Hussain, A. A. Malik, H. A. Shah, and S. M. Qaim, "Charged particle induced reaction cross section data for production of the emerging medically important positron emitter ^{64}Cu : A comprehensive evaluation," *Radiochimica Acta*, vol. 97, p. 669, jan 2009.
- [55] K. Hilgers, T. Stoll, Y. Skakun, H. Coenen, and S. Qaim, "Cross-section measurements of the nuclear reactions $\text{natZn}(\text{d},\text{x})^{64}\text{Cu}$, $^{66}\text{Zn}(\text{d},\alpha)^{64}\text{Cu}$ and $^{68}\text{Zn}(\text{p},\alpha\text{n})^{64}\text{Cu}$ for production of ^{64}Cu and technical developments for small-scale production of ^{67}Cu via the $^{70}\text{Zn}(\text{p},\alpha)^{67}\text{Cu}$ process," *Applied Radiation and Isotopes*, vol. 59, pp. 343–351, nov 2003.
- [56] F. Szelecsényi, G. Steyn, Z. Kovács, C. Vermeulen, N. van der Meulen, S. Dolley, T. van der Walt, K. Suzuki, and K. Mukai, "Investigation of the $^{66}\text{Zn}(\text{p},2\text{pn})^{64}\text{Cu}$ and $^{68}\text{Zn}(\text{p},\text{x})^{64}\text{Cu}$ nuclear processes up to 100 MeV: Production of ^{64}Cu ," *Nuclear Instruments and Methods in Physics Research Section B: Beam Interactions with Materials and Atoms*, vol. 240, pp. 625–637, nov 2005.
- [57] A. Voyles, M. Basunia, J. Batchelder, J. Bauer, T. Becker, L. Bernstein, E. Matthews, P. Renne, D. Rutte, M. Unzueta, and K. van Bibber, "Measurement of the ^{64}Zn , $^{47}\text{Ti}(\text{n},\text{p})$ cross sections using a DD neutron generator for medical isotope studies," *Nuclear Instruments and Methods in Physics Research Section B: Beam Interactions with Materials and Atoms*, vol. 410, pp. 230–239, nov 2017.
- [58] H. F. Valdovinos, S. Graves, T. Barnhart, and R. J. Nickles, "Simplified and reproducible radiochemical separations for the production of high specific activity ^{61}Cu , ^{64}Cu , ^{86}Y and ^{55}Co ," *AIP Conference Proceedings*, vol. 1845, p. 20021, may 2017.
- [59] R. J. Nickles, "The production of a broader palette of PET tracers," *Journal of Labelled Compounds and Radiopharmaceuticals*, vol. 46, pp. 1–27, jan 2003.
- [60] S. M. Qaim, "Decay data and production yields of some non-standard positron emitters used in PET.," *The quarterly journal of nuclear medicine and molecular imaging*, vol. 52, no. 2, pp. 111–120, 2008.
- [61] S. M. Qaim, "Development of novel positron emitters for medical applications: nuclear and radiochemical aspects," *Radiochimica Acta*, vol. 99, pp. 611–625, oct 2011.
- [62] F. Rösch, S. Qaim, and G. Stöcklin, "Production of the positron emitting radioisotope ^{86}Y for nuclear medical application," *Applied Radiation and Isotopes*, vol. 44, pp. 677–681, apr 1993.
- [63] D. R. Sachdev, N. T. Porile, and L. Yaffe, "Reactions of ^{88}Sr with protons of energies 7–85 MeV," *Canadian Journal of Chemistry*, vol. 45, pp. 1149–1160, may 1967.
- [64] V. N. Levkovski, "Cross Sections of Medium Mass Nuclide Activation ($A=40\text{--}100$) by Medium Energy Protons and Alpha Particles ($E=10\text{--}50$ MeV)," 1991.

- [65] B. Kiselev and N. Faizrakhmanova, "Reaction cross sections of (p,n), (p,pn) and (p, α +n) on 93-Nb," in *Program and abstracts of 24th Conference on Nuclear Spectroscopy and Nuclear Structure*, (Kharkov), pp. 356–357, Gosudarstvennyj Komitet po Ispol'zovaniyu Atomnoj Ehnergii SSSR, 1974.
- [66] S. A. Kandil, B. Scholten, K. F. Hassan, H. A. Hanafi, and S. M. Qaim, "A comparative study on the separation of radioyttrium from Sr- and Rb-targets via ion-exchange and solvent extraction techniques, with special reference to the production of no-carrier-added ^{86}Y , ^{87}Y and ^{88}Y using a cyclotron," *Journal of Radioanalytical and Nuclear Chemistry*, vol. 279, pp. 823–832, mar 2009.
- [67] I. Verel, G. W. M. Visser, R. Boellaard, . Marijke, S.-V. Walsum, G. B. Snow, and G. A. M. S. Van Dongen, " ^{89}Zr Immuno-PET: Comprehensive Procedures for the Production of ^{89}Zr -Labeled Monoclonal Antibodies," *J Nucl Med*, vol. 44, pp. 1271–1281, aug 2003.
- [68] E. C. Dijkers, J. G. Kosterink, A. P. Rademaker, L. R. Perk, G. A. van Dongen, J. Bart, J. R. de Jong, E. G. de Vries, and M. N. Lub-de Hooge, "Development and Characterization of Clinical-Grade ^{89}Zr -Trastuzumab for HER2/neu ImmunoPET Imaging," *Journal of Nuclear Medicine*, vol. 50, pp. 974–981, jun 2009.
- [69] E. C. Dijkers, T. H. Oude Munnink, J. G. Kosterink, A. H. Brouwers, P. L. Jager, J. R. de Jong, G. A. van Dongen, C. P. Schröder, M. N. Lub-de Hooge, and E. G. de Vries, "Biodistribution of ^{89}Zr -trastuzumab and PET Imaging of HER2-Positive Lesions in Patients With Metastatic Breast Cancer," *Clinical Pharmacology & Therapeutics*, vol. 87, pp. 586–592, may 2010.
- [70] M. G. Mustafa, H. I. West, H. O'Brien, R. G. Lanier, M. Benhamou, and T. Tamura, "Measurements and a direct-reaction – plus – Hauser-Feshbach analysis of $\text{Y}^{89}(\text{p}, \text{n})\text{Y}^{89}\text{Zr}$, $\text{Y}^{89}(\text{p}, 2\text{n})\text{Y}^{88}\text{Y}$, and $\text{Y}^{89}(\text{p}, \text{pn})\text{Y}^{88}\text{Y}$ reactions up to 40 MeV," *Physical Review C*, vol. 38, pp. 1624–1637, oct 1988.
- [71] H. M. Omara, K. F. Hassan, S. A. Kandil, F. E. Hegazy, and Z. A. Saleh, "Proton induced reactions on ^{89}Y with particular reference to the production of the medically interesting radionuclide ^{89}Zr ," *Radiochimica Acta*, vol. 97, p. 467, jan 2009.
- [72] S. Busse, F. Rösch, and S. M. Qaim, "Cross section data for the production of the positron emitting niobium isotope ^{90}Nb via the $^{90}\text{Zr}(\text{p}, \text{n})$ -reaction," *Radiochimica Acta*, vol. 90, pp. 1–5, jan 2002.
- [73] V. Radchenko, H. Hauser, M. Eisenhut, D. J. Vugts, G. A. M. S. van Dongen, and F. Roesch, " ^{90}Nb – a potential PET nuclide: production and labeling of monoclonal antibodies," *Radiochimica Acta*, vol. 100, pp. 857–864, nov 2012.

- [74] Z. Kovács, F. Tárkányi, S. Qaim, and G. Stöcklin, “Production of 6.5 h ^{82}mRb via the $^{82}\text{Kr}(\text{p}, \text{n})$ -process at a low-energy cyclotron — A potential substitute for ^{82}Rb ,” *International Journal of Radiation Applications and Instrumentation. Part A. Applied Radiation and Isotopes*, vol. 42, pp. 831–834, jan 1991.
- [75] Y. E. Titarenko, V. F. Batyaev, A. Y. Titarenko, M. A. Butko, K. V. Pavlov, S. N. Florya, R. S. Tikhonov, V. M. Zhivun, A. V. Ignatyuk, S. G. Mashnik, S. Leray, A. Boudard, J. Cugnon, D. Mancusi, Y. Yariv, K. Nishihara, N. Matsuda, H. Kumawat, G. Mank, and W. Gudowski, “Measurement and simulation of the cross sections for nuclide production in ^{93}Nb and natNi targets irradiated with 0.04- to 2.6-GeV protons,” *Physics of Atomic Nuclei*, vol. 74, p. 537, may 2011.
- [76] M. R. Bhat, “Nuclear Data Sheets for $A = 57$,” *Nuclear Data Sheets*, vol. 85, no. 3, pp. 415–536, 1998.
- [77] R. Michel, R. Bodemann, H. Busemann, R. Daunke, M. Gloris, H.-J. Lange, B. Klug, A. Krins, I. Leya, M. Lüpke, S. Neumann, H. Reinhardt, M. Schnatz-Büttgen, U. Herpers, T. Schiekel, F. Sudbrock, B. Holmqvist, H. Condé, P. Malmborg, M. Suter, B. Dittrich-Hannen, P.-W. Kubik, H.-A. Synal, and D. Filges, “Cross sections for the production of residual nuclides by low- and medium-energy protons from the target elements C, N, O, Mg, Al, Si, Ca, Ti, V, Mn, Fe, Co, Ni, Cu, Sr, Y, Zr, Nb, Ba and Au,” *Nuclear Instruments and Methods in Physics Research Section B: Beam Interactions with Materials and Atoms*, vol. 129, no. 2, pp. 153–193, 1997.
- [78] F. Ditrói, F. Tárkányi, S. Takács, A. Hermanne, H. Yamazaki, M. Baba, and A. Mohammadi, “Activation cross-sections of longer lived products of proton induced nuclear reactions on cobalt up to 70 MeV,” *Journal of Radioanalytical and Nuclear Chemistry*, vol. 298, pp. 853–865, nov 2013.
- [79] R. Capote, M. Herman, P. Obložinský, P. Young, S. Goriely, T. Belgia, A. Ignatyuk, A. Koning, S. Hilaire, V. Plujko, M. Avrigeanu, O. Bersillon, M. Chadwick, T. Fukahori, Z. Ge, Y. Han, S. Kailas, J. Kopecky, V. Maslov, G. Reffo, M. Sin, E. Soukhovitskii, and P. Talou, “RIPL — Reference Input Parameter Library for Calculation of Nuclear Reactions and Nuclear Data Evaluations,” *Nuclear Data Sheets*, vol. 110, pp. 3107–3214, dec 2009.
- [80] M. Herman, R. Capote, B. V. Carlson, P. Obložinský, M. Sin, A. Trkov, H. Wienke, and V. Zerkin, “EMPIRE: Nuclear Reaction Model Code System for Data Evaluation,” *Nuclear Data Sheets*, vol. 108, no. 12, pp. 2655–2715, 2007.
- [81] A. Koning and J. Delaroche, “Local and global nucleon optical models from 1 keV to 200 MeV,” *Nuclear Physics A*, vol. 713, pp. 231–310, jan 2003.

- [82] M. Avrigeanu, A. Obreja, F. Roman, V. Avrigeanu, and W. von Oertzen, “Complementary optical-potential analysis of α -particle elastic scattering and induced reactions at low energies,” *Atomic Data and Nuclear Data Tables*, vol. 95, pp. 501–532, jul 2009.
- [83] T. Belgya, O. Bersillon, and R. Capote, “Handbook for calculations of nuclear reaction data, RIPL-2,” in *IAEA, Vienna*, . . ., no. June, 2006.
- [84] A. J. Koning and D. Rochman, “Modern Nuclear Data Evaluation with the TALYS Code System,” *Nuclear Data Sheets*, vol. 113, pp. 2841–2934, dec 2012.
- [85] T. Kawano, “CoH: The Hauser-Feshbach-Moldauer statistical model with the coupled-channels theory,” *Los Alamos National Laboratory, unpublished*, 2003.
- [86] T. Kawano, P. Talou, M. B. Chadwick, and T. Watanabe, “Monte Carlo Simulation for Particle and γ -Ray Emissions in Statistical Hauser-Feshbach Model,” *Journal of Nuclear Science and Technology*, vol. 47, pp. 462–469, may 2010.
- [87] V. Avrigeanu, P. E. Hodgson, and M. Avrigeanu, “Global optical potentials for emitted alpha particles,” *Physical Review C*, vol. 49, pp. 2136–2141, apr 1994.
- [88] M. S. Basunia, “Nuclear Data Sheets for $A = 22$,” *Nuclear Data Sheets*, vol. 127, no. Supplement C, pp. 69–190, 2015.
- [89] R. B. Firestone, “Nuclear Data Sheets for $A = 24$,” *Nuclear Data Sheets*, vol. 108, no. 11, pp. 2319–2392, 2007.
- [90] J. Wang and X. Huang, “Nuclear Data Sheets for $A = 51$,” *Nuclear Data Sheets*, vol. 144, no. Supplement C, pp. 1–296, 2017.
- [91] Y. Dong and H. Junde, “Nuclear Data Sheets for $A = 54$,” *Nuclear Data Sheets*, vol. 121, no. Supplement C, pp. 1–142, 2014.
- [92] H. Junde, “Nuclear Data Sheets for $A = 55$,” *Nuclear Data Sheets*, vol. 109, no. 4, pp. 787–942, 2008.
- [93] H. Junde, H. Su, and Y. Dong, “Nuclear Data Sheets for $A = 56$,” *Nuclear Data Sheets*, vol. 112, pp. 1513–1645, jun 2011.
- [94] C. M. Baglin, “Nuclear Data Sheets for $A = 59$,” *Nuclear Data Sheets*, vol. 95, no. 2, pp. 215–386, 2002.
- [95] E. Browne and J. K. Tuli, “Nuclear Data Sheets for $A = 60$,” *Nuclear Data Sheets*, vol. 114, no. 12, pp. 1849–2022, 2013.
- [96] K. Zuber and B. Singh, “Nuclear Data Sheets for $A = 61$,” *Nuclear Data Sheets*, vol. 125, pp. 1–200, 2015.

- [97] A. L. Nichols, B. Singh, and J. K. Tuli, “Nuclear Data Sheets for $A = 62$,” *Nuclear Data Sheets*, vol. 113, no. 4, pp. 973–1114, 2012.
- [98] E. Browne and J. K. Tuli, “Nuclear Data Sheets for $A = 65$,” *Nuclear Data Sheets*, vol. 111, pp. 2425–2553, sep 2010.
- [99] J. Tuli, “Nuclear Data Sheets for $A = 82$,” *Nuclear Data Sheets*, vol. 98, pp. 209–334, feb 2003.
- [100] E. A. McCutchan, “Nuclear Data Sheets for $A = 83$,” *Nuclear Data Sheets*, vol. 125, no. Supplement C, pp. 201–394, 2015.
- [101] A. Negret and B. Singh, “Nuclear Data Sheets for $A = 86$,” *Nuclear Data Sheets*, vol. 124, pp. 1–156, 2015.
- [102] E. McCutchan and A. Sonzogni, “Nuclear Data Sheets for $A = 88$,” *Nuclear Data Sheets*, vol. 115, pp. 135–304, jan 2014.
- [103] C. M. Baglin, “Nuclear Data Sheets for $A = 91$,” *Nuclear Data Sheets*, vol. 114, pp. 1293–1495, oct 2013.
- [104] C. M. Baglin, “Nuclear Data Sheets for $A = 92$,” *Nuclear Data Sheets*, vol. 113, pp. 2187–2389, oct 2012.
- [105] C. M. Baglin, “Nuclear Data Sheets for $A = 93$,” *Nuclear Data Sheets*, vol. 112, no. 5, pp. 1163–1389, 2011.
- [106] G. Albouy, J. P. Cohen, M. Gusakow, N. Poffé, H. Sergolle, and L. Valentin, “Réactions ($p, 3p3n$) entre 30 et 150 MeV,” *J. Phys. Radium*, vol. 24, no. 1, pp. 67–68, 1963.
- [107] I. R. Williams and C. B. Fulmer, “Excitation Functions for Radioactive Isotopes Produced by Protons below 60 MeV on Al, Fe, and Cu,” *Phys. Rev.*, vol. 162, pp. 1055–1061, oct 1967.
- [108] H. R. Heydecker, C. K. Garrett, and A. Van Ginneken, “Thin-Target Cross Sections for Some Cr, Mn, Fe, Co, Ni, and Zn Nuclides Produced in Copper by 82- to 416-MeV Protons,” *Phys. Rev. C*, vol. 6, pp. 1235–1240, oct 1972.
- [109] A. Grütter, “Excitation functions for radioactive isotopes produced by proton bombardment of Cu and Al in the energy range of 16 to 70 MeV,” *Nuclear Physics A*, vol. 383, no. 1, pp. 98–108, 1982.
- [110] L. R. Greenwood and R. K. Smith, “Measurement of Cu spallation cross sections at IPNS,” *U.S. Dept. of Energy, Fusion Energy Series*, vol. 18, no. 46, p. 11, 1984.

- [111] V. N. Aleksandrov, M. P. Semenova, and V. G. Semenov, "Production cross section of radionuclides in (p, x) reactions at copper and nickel nuclei," *Soviet Atomic Energy*, vol. 62, pp. 478–481, jun 1987.
- [112] M. Fassbender, Y. Shubin, V. P. Lunev, and S. M. Qaim, "Experimental studies and nuclear model calculations on the formation of radioactive products in interactions of medium energy protons with copper, zinc and brass: Estimation of collimator activation in proton therapy facilities," *Applied Radiation and Isotopes*, vol. 48, no. 9, pp. 1221–1230, 1997.
- [113] T. Ido, A. Hermanne, F. Ditrói, Z. SzÁcs, I. Mahunka, and F. Tárkányi, "Excitation functions of proton induced nuclear reactions on natRb from 30 to 70 MeV. Implication for the production of 82Sr and other medically important Rb and Sr radioisotopes," *Nuclear Instruments and Methods in Physics Research Section B: Beam Interactions with Materials and Atoms*, vol. 194, no. 4, pp. 369–388, 2002.
- [114] J. M. Sisterson and N. P. T. Center, "Selected radiation safety issues at proton therapy facilities," in *12th Biennial Topical Meeting of the Radiation Protection and Shielding Division of the American Nuclear Society*, 2002.
- [115] H. Yashima, Y. Uwamino, H. Iwase, H. Sugita, T. Nakamura, S. Ito, and A. Fukumura, "Measurement and calculation of radioactivities of spallation products by high-energy heavy ions," 2003.
- [116] F. Al-Saleh, A. Al-Harbi, and A. Azzam, "Excitation functions of proton induced nuclear reactions on natural copper using a medium-sized cyclotron," 2006.
- [117] F. Ditrói, S. Takács, F. Tárkányi, M. Baba, E. Corniani, and Y. Shubin, "Study of proton induced reactions on niobium targets up to 70MeV," *Nuclear Instruments and Methods in Physics Research Section B: Beam Interactions with Materials and Atoms*, vol. 266, no. 24, pp. 5087–5100, 2008.
- [118] F. Ditrói, A. Hermanne, E. Corniani, S. Takács, F. Tárkányi, J. Csikai, and Y. N. Shubin, "Investigation of proton induced reactions on niobium at low and medium energies," *Nuclear Instruments and Methods in Physics Research Section B: Beam Interactions with Materials and Atoms*, vol. 267, no. 19, pp. 3364–3374, 2009.
- [119] G. F. Steyn, C. Vermeulen, F. Szelecsenyi, Z. Kovacs, K. Suzuki, T. Fukumura, and K. Nagatsu, "Excitation functions of proton induced reactions on 89Y and 93Nb with emphasis on the production of selected radio-zirconiums," *Journal of the Korean Physical Society*, vol. 59, no. 23, pp. 1991–1994, 2011.
- [120] M. Shahid, K. Kim, H. Naik, M. Zaman, S.-C. Yang, and G. Kim, "Measurement of excitation functions in proton induced reactions on natural copper from their threshold to 43MeV," *Nuclear Instruments and Methods in Physics Research Section B: Beam Interactions with Materials and Atoms*, vol. 342, no. Supplement C, pp. 305–313, 2015.

- [121] E. Garrido, C. Duchemin, A. Guertin, F. Haddad, N. Michel, and V. Métivier, "New excitation functions for proton induced reactions on natural titanium, nickel and copper up to 70MeV," *Nuclear Instruments and Methods in Physics Research Section B: Beam Interactions with Materials and Atoms*, vol. 383, no. Supplement C, pp. 191–212, 2016.
- [122] P. W. Lisowski and K. F. Schoenberg, "The Los Alamos Neutron Science Center," *Nuclear Instruments and Methods in Physics Research Section A: Accelerators, Spectrometers, Detectors and Associated Equipment*, vol. 562, no. 2, pp. 910–914, 2006.
- [123] J. Koutský and J. Kocík, *Radiation Damage of Structural Materials*. Materials Science Monographs, Elsevier Science, 2013.
- [124] K. S. Krane, *Introductory Nuclear Physics*. Wiley, 3rd ed., 1987.
- [125] D. R. Olander, *Fundamental aspects of nuclear reactor fuel elements*. No. p. 1, Univ., 1990.
- [126] R. H. Pehl, "RADIATION DAMAGE OF GERMANIUM DETECTORS," in *Gamma Ray Spectroscopy in Astrophysics Symposium*, (Greenbelt, MD), 1978.
- [127] J. F. Shackelford, *Introduction to Materials Science for Engineers*. Pearson Prentice Hall, 7 ed., 2009.
- [128] N. T. Fourches, "Total Dose and Dose Rate Effects On Some Current Semiconducting Devices," in *Current Topics in Ionizing Radiation Research* (M. Nenoi, ed.), ch. 32, InTech, mar 2012.
- [129] A. Aframian, N. A. Askouri, and H. A. Khan, "Charged particle beam profile measurements," *Nuclear Instruments and Methods*, vol. 121, no. 3, pp. 421–424, 1974.
- [130] E. Reichmanis, C. W. Frank, and J. H. O'Donnell, *Irradiation of Polymeric Materials*, vol. 527. American Chemical Society, apr 1993.
- [131] O. Guven, R. Clough, S. Ahmed, S. Baccaro, V. Feldman, M. Gonzalez, S. Perera, F. Ranogajec, J. Sun, and M. Tavlet, *Stability and Stabilization of Polymers under Irradiation*. Vienna: International Atomic Energy Agency, 1999.
- [132] J. Davenas, I. Stevenson, N. Celette, S. Cambon, J. L. Gardette, A. Rivaton, and L. Vignoud, "Stability of polymers under ionising radiation: The many faces of radiation interactions with polymers," *Nuclear Instruments and Methods in Physics Research Section B: Beam Interactions with Materials and Atoms*, vol. 191, no. 1, pp. 653–661, 2002.
- [133] N. Azam, B. C. Robert, C. B. M., G. K. P., G. J. M., M. W. L., M. A. S., N. Ravinder, R. J. E., and S. C. G., "Radiochromic film dosimetry: Recommendations of AAPM Radiation Therapy Committee Task Group 55," *Medical Physics*, vol. 25, pp. 2093–2115, oct 1998.

- [134] M. Andre, L. D. F., and Y. Xiang, "Multichannel film dosimetry with nonuniformity correction," *Medical Physics*, vol. 38, pp. 2523–2534, may 2011.
- [135] L. David, M. Andre, Y. Xiang, and C. M. F., "An efficient protocol for radiochromic film dosimetry combining calibration and measurement in a single scan," *Medical Physics*, vol. 39, pp. 6339–6350, sep 2012.
- [136] C. T. Rueden, J. Schindelin, M. C. Hiner, B. E. DeZonia, A. E. Walter, E. T. Arena, and K. W. Eliceiri, "ImageJ2: ImageJ for the next generation of scientific image data," *BMC Bioinformatics*, vol. 18, no. 1, p. 529, 2017.
- [137] M. Furukawa, K. Shizuri, K. Komura, K. Sakamoto, and S. Tanaka, "Production of ^{26}Al and ^{22}Na from proton bombardment of Si, Al and Mg," *Nuclear Physics A*, vol. 174, no. 3, pp. 539–544, 1971.
- [138] J. R. Walton, D. Heymann, A. Yaniv, D. Edgerley, and M. W. Rowe, "Cross sections for He and Ne isotopes in natural Mg, Al, and Si, He isotopes in CaF_2 , Ar isotopes in natural Ca, and radionuclides in natural Al, Si, Ti, Cr, and stainless steel induced by 12-to 45-MeV protons," *Journal of Geophysical Research*, vol. 81, pp. 5689–5699, nov 1976.
- [139] I. Barchuk, V. Bulkin, V. Kuzmenkova, P. Kurilo, Y. Lobach, A. Ogorodnik, V. Procopenko, V. Sklyarenko, and V. Tokarevsky, "Excitation functions for reactions induced under interactions of protons upto 67 MeV with silicon and iron nuclei," *Atomnaya Ehnergiya*, vol. 63, no. 1, pp. 30–33, 1987.
- [140] V. N. Aleksandrov, M. P. Semenova, and V. G. Semenov, "Cross Sections of Radionuclide Production in (p, X)-Reactions," *Atomnaya Ehnergiya*, vol. 64, p. 445, 1988.
- [141] R. Bodemann, H.-J. Lange, I. Leya, R. Michel, T. Schiekel, R. Rösel, U. Herpers, H. Hofmann, B. Dittrich, M. Suter, W. Wölfl, B. Holmqvist, H. Condé, and P. Malmborg, "Production of residual nuclei by proton-induced reactions on C, N, O, Mg, Al and Si," *Nuclear Instruments and Methods in Physics Research Section B: Beam Interactions with Materials and Atoms*, vol. 82, pp. 9–31, jul 1993.
- [142] E. Browne and J. Tuli, "Nuclear Data Sheets for $A = 66$," *Nuclear Data Sheets*, vol. 111, pp. 1093–1209, apr 2010.
- [143] H. Herzog, F. Rösch, G. Stöcklin, C. Lueders, S. M. Qaim, and L. E. Feinendegen, "Measurement of Pharmacokinetics of Yttrium-86 Radiopharmaceuticals with PET and Radiation Dose Calculation of Analogous Yttrium-90 Radiotherapeutics," *Journal of Nuclear Medicine*, vol. 34, no. 12, pp. 2222–2226, 1993.
- [144] R. J. Nickles, A. D. Roberts, J. A. Nye, A. K. Converse, T. E. Barnhart, M. A. Avila-Rodriguez, R. Sundaresan, D. W. Dick, R. J. Hammas, and B. R. Thomadsen,

- “Assaying and PET imaging of yttrium-90: 1/spl Gt/34ppm \pm 0,” in *IEEE Symposium Conference Record Nuclear Science 2004.*, vol. 6, pp. 3412–3414 Vol. 6, 2004.
- [145] P.-E. Goethals and R. Zimmermann, “Cyclotrons used in Nuclear Medicine: World Market Report & Directory,” tech. rep., MEDraysintell, Louvain-la-Neuve, dec 2015.
- [146] T. G. J., S. Paul, H. Cornelia, R. T. J., and S. Vesna, “Manganese-52 positron emission tomography tracer characterization and initial results in phantoms and in vivo,” *Medical Physics*, vol. 40, p. 42502, mar 2013.
- [147] S. A. Graves, R. Hernandez, J. Fonslet, C. G. England, H. F. Valdovinos, P. A. Ellison, T. E. Barnhart, D. R. Elema, C. P. Theuer, W. Cai, R. J. Nickles, and G. W. Severin, “Novel Preparation Methods of 52Mn for ImmunoPET Imaging,” *Bioconjugate Chemistry*, vol. 26, pp. 2118–2124, oct 2015.
- [148] C. M. Lewis, S. A. Graves, R. Hernandez, H. F. Valdovinos, T. E. Barnhart, W. Cai, M. E. Meyerand, R. J. Nickles, and M. Suzuki, “52 Mn Production for PET/MRI Tracking Of Human Stem Cells Expressing Divalent Metal Transporter 1 (DMT1),” *Theranostics*, vol. 5, no. 3, pp. 227–239, 2015.
- [149] S. A. Graves, P. A. Ellison, H. F. Valdovinos, T. E. Barnhart, R. J. Nickles, and J. W. Engle, “Half-life of ^{51}Mn ,” *Physical Review C*, vol. 96, p. 014613, jul 2017.
- [150] A. L. Wooten, T. A. Aweda, B. C. Lewis, R. B. Gross, and S. E. Lapi, “Biodistribution and PET Imaging of pharmacokinetics of manganese in mice using Manganese-52,” *PLOS ONE*, vol. 12, p. e0174351, mar 2017.
- [151] R. Hernandez, S. A. Graves, T. Gregg, H. R. VanDeusen, R. J. Fenske, H. N. Wienkes, C. G. England, H. F. Valdovinos, J. J. Jeffery, T. E. Barnhart, G. W. Severin, R. J. Nickles, M. E. Kimple, M. J. Merrins, and W. Cai, “Radiomanganese PET Detects Changes in Functional β -Cell Mass in Mouse Models of Diabetes,” *Diabetes*, vol. 66, pp. 2163–2174, aug 2017.
- [152] J. Fitzgerald, “FitzPeaks gamma analysis and calibration software,” 2009.
- [153] A. Hermanne, A. Ignatyuk, R. Capote, B. Carlson, J. Engle, M. Kellett, T. Kibédi, G. Kim, F. Kondev, M. Hussain, O. Lebeda, A. Luca, Y. Nagai, H. Naik, A. Nichols, F. Nortier, S. Suryanarayana, S. Takács, F. Tárkányi, and M. Verpell, “Reference Cross Sections for Charged-particle Monitor Reactions,” *Nuclear Data Sheets*, vol. 148, pp. 338–382, feb 2018.
- [154] J. R. Cooper, L. Bernstein, M. A. McMahan, J. Powell, D. Wutte, L. Ahle, N. Benczer-Koller, D. Dashdorj, G. Kumbartzki, T. J. Mertzimekis, A. Schiller, C. Silver, and M. J. Taylor, “Production of a 76Kr radioactive ion beam using a batch mode method,” *Nuclear Instruments and Methods in Physics Research Section A: Accelerators, Spectrometers, Detectors and Associated Equipment*, vol. 533, no. 3, pp. 287–294, 2004.

- [155] D. Updegraff and S. A. Hoedl, "Nuclear Medicine without Nuclear Reactors or Uranium Enrichment," tech. rep., Center for Science, Technology, and Security Policy, American Association for the Advancement of Science, Washington, DC, jun 2013.
- [156] C. Waltz, M. Ayillon, T. Becker, L. Bernstein, K.-N. Leung, L. Kirsch, P. Renne, and K. V. Bibber, "Beam-induced Back-streaming Electron Suppression Analysis for an Accelerator Type Neutron Generator Designed for $^{40}\text{Ar}/^{39}\text{Ar}$ Geochronology," *Applied Radiation and Isotopes*, vol. 125, pp. 124–128, jul 2017.
- [157] C. Waltz, *Characterization of Deuteron-Deuteron Neutron Generators*. PhD thesis, University of California, Berkeley, 2016.
- [158] Q. Ji, A. Sy, and J. W. Kwan, "Radio frequency-driven proton source with a back-streaming electron dump," *Review of Scientific Instruments*, vol. 81, no. 2, p. 02B312, 2010.
- [159] T. W. Burrows, "Nuclear Data Sheets for $A = 47$," *Nuclear Data Sheets*, vol. 108, pp. 923–1056, may 2007.
- [160] S. M. Qaim, R. Capote, and F. Tarkanyi, "Nuclear Data for the Production of Therapeutic Radionuclides," Tech. Rep. 473, 2011.
- [161] K. L. Kolsky, V. Joshi, L. F. Mausner, and S. C. Srivastava, "Radiochemical purification of no-carrier-added scandium-47 for radioimmunotherapy," *Applied Radiation and Isotopes*, vol. 49, pp. 1541–1549, dec 1998.
- [162] L. F. Mausner, V. Joshi, and K. L. Kolsky, "Evaluation of chelating agents for radioimmunotherapy with scandium-47," *Journal of Nuclear Medicine*, vol. 36, no. CONF-950603, p. 104, 1995.
- [163] E. Browne and J. K. Tuli, "Nuclear Data Sheets for $A = 99$," *Nuclear Data Sheets*, vol. 112, pp. 275–446, feb 2011.
- [164] L. Deilami-nezhad, L. Moghaddam-Banaem, M. Sadeghi, and M. Asgari, "Production and purification of Scandium-47: A potential radioisotope for cancer theranostics," *Applied Radiation and Isotopes*, vol. 118, pp. 124–130, dec 2016.
- [165] K. S. Bhatki, A. T. Rane, and M. B. Kabadi, "Preparation of carrier-free copper-64, 67 nuclides by liquid-liquid extraction," *Journal of Radioanalytical Chemistry*, vol. 2, no. 1-2, pp. 73–77, 1969.
- [166] S. Mirzadeh and F. F. Knapp, "Spontaneous electrochemical separation of carrier-free copper-64 and copper-67 from zinc targets," *Radiochimica Acta*, vol. 57, no. 4, pp. 193–200, 1992.

- [167] H. F. Aly and M. A. El-Haggan, "Production of carrier-free scandium radioisotopes from a neutron-irradiated potassium titanium oxalate target," *Microchimica Acta*, vol. 59, no. 1, pp. 4–8, 1971.
- [168] T. H. Bokhari, A. Mushtaq, and I. U. Khan, "Separation of no-carrier-added radioactive scandium from neutron irradiated titanium," *Journal of Radioanalytical and Nuclear Chemistry*, vol. 283, no. 2, pp. 389–393, 2010.
- [169] L. Pietrelli, L. Mausner, and K. Kolsky, "Separation of carrier-free ^{47}Sc from titanium targets," *Journal of Radioanalytical and Nuclear Chemistry*, vol. 157, no. 2, pp. 335–345, 1992.
- [170] R. Capote, K. I. Zolotarev, V. G. Pronyaev, and A. Trkov, "Updating and Extending the IRDF-2002 Dosimetry Library," *Journal of ASTM International*, vol. 9, pp. 1–9, apr 2012.
- [171] E. M. Zsolnay, R. Capote, H. J. Nolthenius, and A. Trkov, "Summary Description of the New International Reactor Dosimetry and Fusion File (IRDFF release 1.0)," *IAEA Technical Report INDC (NDS)-0616*, 2012.
- [172] J. T. Goorley, M. R. James, T. E. Booth, F. B. Brown, J. S. Bull, L. J. Cox, J. W. J. Durkee, J. S. Elson, M. L. Fensin, R. A. I. Forster, J. S. Hendricks, H. G. I. Hughes, R. C. Johns, B. C. Kiedrowski, R. L. Martz, S. G. Mashnik, G. W. McKinney, D. B. Pelowitz, R. E. Prael, J. E. Sweezy, L. S. Waters, T. Wilcox, and A. J. Zukaitis, "Initial MCNP6 release Overview - MCNP6 version 1.0," *Los Alamos Report LA-UR-13-22934*, 2013.
- [173] J. Blachot, "Nuclear Data Sheets for $A = 115$," *Nuclear Data Sheets*, vol. 113, pp. 2391–2535, oct 2012.
- [174] D. C. Radford, "Notes on the use of the program gf3," 2000.
- [175] D. C. Radford, "ESCL8R and LEVIT8R: Software for interactive graphical analysis of HPGe coincidence data sets," *Nuclear Inst. and Methods in Physics Research, A*, vol. 361, pp. 297–305, jul 1995.
- [176] J. Rapaport and J. J. van Loef, "Excitation Function of the Reaction $\text{Zn-64}(n, p)\text{Cu-64}$ with Neutrons of Energies between 2 and 3.6 Mev," *Phys. Rev.*, vol. 114, pp. 565–569, apr 1959.
- [177] K. Nakai, H. Gotoh, and H. Amano, "Excitation Functions of $\text{Ni58}(n, p)\text{Co58}$ and $\text{Zn64}(n, p)\text{Cu64}$ Reactions in the Energy Region from 1.8 to 4.8 Mev," *Journal of the Physical Society of Japan*, vol. 17, no. 8, pp. 1215–1223, 1962.

- [178] A. Paulsen and H. Liskien, "Cross-sections for some (n, p) reactions near threshold," in *Nuclear data for reactors. Proceedings of a conference on nuclear data-microscopic cross-sections and other data basic for reactors.*, (Paris), pp. 217–224, 1967.
- [179] D. C. Santry and J. P. Butler, "Excitation Curves for the Reactions of Fast Neutrons with Zinc," *Canadian Journal of Physics*, vol. 50, no. 20, pp. 2536–2548, 1972.
- [180] D. L. Smith and J. W. Meadows, "Cross-Section Measurement of (n, p) Reactions for ^{27}Al , $^{46,47,48}\text{Ti}$, ^{58}Ni , ^{59}Co , and ^{64}Zn from Near Threshold to 10 MeV," *Nuclear Science and Engineering*, vol. 58, no. 3, pp. 314–320, 1975.
- [181] C. King, C. Ai, and J. Chou, "Cross-section measurement for the reaction Zn-64(n,p) Cu-64," *Nuclear Science, Taiwan*, vol. 16, no. 6, p. 71, 1979.
- [182] H. Hussain and S. Hunt, "Absolute neutron cross section measurements in the energy range between 2 and 5 MeV," *The International Journal of Applied Radiation and Isotopes*, vol. 34, pp. 731–738, apr 1983.
- [183] Y. Ikeda, C. Konno, M. Mizumoto, K. Hasegawa, S. Chiba, Y. Yamanouchi, and M. Sugimoto, "Activation cross section measurement at neutron energies of 9.5, 11.0, 12.0 and 13.2 MeV using H-1(B-11,n)C-12 neutron source at JAERI," in *Proceedings of an International Conference, held at the Forschungszentrum Jülich, Fed. Rep. of Germany, 13-17 May 1991* (S. M. Qaim, ed.), (Juelich, Germany), pp. 294–296, Springer-Verlag Berlin Heidelberg, 1990.
- [184] T. Shimizu, H. Sakane, S. Furuichi, M. Shibata, K. Kawade, and H. Takeuchi, "An improved pneumatic sample transport system for measurement of activation cross-sections with d-D neutrons in the energy range between 2.1 and 3.1 MeV," *Nuclear Instruments and Methods in Physics Research Section A: Accelerators, Spectrometers, Detectors and Associated Equipment*, vol. 527, no. 3, pp. 543–553, 2004.
- [185] L. González, A. Trier, and J. J. van Loef, "Excitation Function of the Reaction Ti-47(n, p)Sc-47 at Neutron Energies between 2.0 and 3.6 Mev," *Phys. Rev.*, vol. 126, pp. 271–273, apr 1962.
- [186] F. Armitage, "47Ti(n,p) Cross-section from 2.19 To 3.64 MeV," *Priv. Comm: J. Symonds (1967)*, 1967.
- [187] Y. Ikeda, C. Konno, K. Kosako, and K. Oishi, "Activation Cross Section Measurement at a Neutron Energy Range from 2.1 to 3.0 Mev by D-D Neutron Source at FNS," *Japanese Report to NEANDC*, vol. 155, p. 11, 1990.
- [188] T. Senga, H. Sakane, M. Shibata, H. Yamamoto, K. Kawade, Y. Kasugai, Y. Ikeda, H. Takeuchi, and T. Furuta, "Measurement of neutron activation cross sections in the energy range between 2. and 7. MeV by using a Ti-deuteron Target and a deuteron gas target," in *Proceedings of the JAERI Conference 2000*, (Japan), p. 5, 2000.

- [189] T. Shimizu, H. Sakane, M. Shibata, K. Kawade, and T. Nishitani, “Measurements of activation cross sections of (n, p) and (n, α) reactions with d-D neutrons in the energy range of 2.1-3.1 MeV,” *Annals of Nuclear Energy*, vol. 31, no. 9, pp. 975–990, 2004.
- [190] M. B. Chadwick, M. Herman, P. Oblozinsky, M. E. Dunn, Y. Danon, A. C. Kahler, D. L. Smith, B. Pritychenko, G. Arbanas, R. Arcilla, R. Brewer, D. A. Brown, R. Capote, A. D. Carlson, Y. S. Cho, H. Derrien, K. Guber, G. M. Hale, S. Hoblit, S. Holloway, T. D. Johnson, T. Kawano, B. C. Kiedrowski, H. Kim, S. Kunieda, N. M. Larson, L. Leal, J. P. Lestone, R. C. Little, E. A. McCutchan, R. E. MacFarlane, M. MacInnes, C. M. Mattoon, R. D. McKnight, S. F. Mughabghab, G. P. A. Nobre, G. Palmiotti, A. Palumbo, M. T. Pigni, V. G. Pronyaev, R. O. Sayer, A. A. Sonzogni, N. C. Summers, P. Talou, I. J. Thompson, A. Trkov, R. L. Vogt, S. C. van der Marck, A. Wallner, M. C. White, D. Wiarda, and P. G. Young, “ENDF/B-VII.1 nuclear data for science and technology: Cross sections, covariances, fission product yields and decay data,” *Nuclear Data Sheets*, vol. 112, pp. 2887–2996, dec 2011.
- [191] S.-C. Wu, “Nuclear Data Sheets for A = 46,” *Nuclear Data Sheets*, vol. 91, pp. 1–116, sep 2000.
- [192] M. Ayillon, P. A. Adams, J. D. Bauer, J. C. Batchelder, T. A. Becker, L. A. Bernstein, S.-A. Chong, J. James, L. E. Kirsch, K.-N. Leung, E. F. Matthews, J. T. Morrell, P. R. Renne, A. M. Rogers, D. Rutte, A. S. Voyles, K. V. Bibber, and C. S. Waltz, “Design, construction, and characterization of a compact DD neutron generator designed for 40 Ar/ 39 Ar geochronology,” *Nuclear Instruments and Methods in Physics Research Section A: Accelerators, Spectrometers, Detectors and Associated Equipment*, may 2018.
- [193] J. Meija, T. B. Coplen, M. Berglund, W. A. Brand, P. De Bièvre, M. Gröning, N. E. Holden, J. Irrgeher, R. D. Loss, T. Walczyk, and T. Prohaska, “Atomic weights of the elements 2013 (IUPAC Technical Report),” *Pure and Applied Chemistry*, vol. 88, p. 265, jan 2016.
- [194] D. L. Smith and J. W. Meadows, “Activation Cross Sections for 66Zn(n,p)66Cu,” *Nuclear Science and Engineering*, vol. 76, pp. 61–66, oct 1980.
- [195] E. A. McCutchan, “Nuclear Data Sheets for A = 68,” *Nuclear Data Sheets*, vol. 113, no. 6, pp. 1735–1870, 2012.
- [196] G. Gürdal and E. A. McCutchan, “Nuclear Data Sheets for A = 70,” *Nuclear Data Sheets*, vol. 136, pp. 1–162, 2016.
- [197] H. Junde, H. Xiaolong, and J. K. Tuli, “Nuclear Data Sheets for A = 67,” *Nuclear Data Sheets*, vol. 106, no. 2, pp. 159–250, 2005.
- [198] J. J. Van Loef, “Activation cross sections for (n, p) reactions in some medium-weight nuclei with D+D neutrons,” *Nuclear Physics*, vol. 24, no. 2, pp. 340–345, 1961.

- [199] M. Furuta, T. Shimizu, H. Hayashi, I. Miyazaki, H. Yamamoto, M. Shibata, and K. Kawade, “Measurements of activation cross sections of (n, p) and (n, α) reactions in the energy range of 3.5–5.9 MeV using a deuterium gas target,” *Annals of Nuclear Energy*, vol. 35, no. 9, pp. 1652–1662, 2008.
- [200] M. Bhike, A. Saxena, B. J. Roy, R. K. Choudhury, S. Kailas, and S. Ganesan, “Measurement of $^{67}\text{Zn}(n, p)^{67}\text{Cu}$, $^{92}\text{Mo}(n, p)^{92m}\text{Nb}$, and $^{98}\text{Mo}(n, \gamma)^{99}\text{Mo}$ Reaction Cross Sections at Incident Neutron Energies of $E_n = 1.6$ and 3.7 MeV,” *Nuclear Science and Engineering*, vol. 163, pp. 175–182, oct 2009.
- [201] T. W. Burrows, “Nuclear Data Sheets for $A = 49$,” *Nuclear Data Sheets*, vol. 109, no. 8, pp. 1879–2032, 2008.
- [202] J. Chen, J. Cameron, and B. Singh, “Nuclear Data Sheets for $A = 35$,” *Nuclear Data Sheets*, vol. 112, no. 11, pp. 2715–2850, 2011.
- [203] C. Ouellet and B. Singh, “Nuclear Data Sheets for $A = 32$,” *Nuclear Data Sheets*, vol. 112, no. 9, pp. 2199–2355, 2011.
- [204] D. C. Stupegia, M. Schmidt, C. R. Keedy, and A. A. Madson, “Neutron capture between 5 keV and 3 MeV,” *Journal of Nuclear Energy*, vol. 22, no. 5, pp. 267–281, 1968.

Appendix A

MCNP Input Files

THIS appendix contains the various MCNP6 input files used in the analysis of the work presented in this dissertation. They are provided for the purposes of both documentation and reproducibility, that anyone with a license for the code (version MCNP-6.1) might be able to run them. These models are in general used for the primary purpose of determining the energy distributions for each irradiation scenario, using the rigorous particle transport methods of the MCNP code. Since the energy assignment, and thus, particle fluence, for each of the experiments presented here are based upon these transport models, they represent a systematic factor in the magnitude of all cross sections reported in this work. By providing the transport models used, these input files allow for the renormalization of the reported cross sections, in the event of an error in the model inputs.

A.1 HFNG Irradiation Input

The following MCNP code simulates the operation of the UC Berkeley HFNG, as it existed at the time of the experiments described in the present work. This includes both the “single foil” (one target foil + one indium monitor foil, used for cross section measurements) and “nine foil” (3×3 indium foils, used for verifying that the beam is centered on the middle of mounted foils, as in Figure 4.8) modes of operation. These modes differ only in terms of which foils are “loaded” into the simulation — the “single foil” mode is used when Cells 11–18 are commented out and Cells 10 & 20 are uncommented. Similarly, the “nine foil” mode is used when Cell 20 is commented out and Cells 10–18 are uncommented. In the version presented here, the input is configured for a single-foil irradiation, using a zinc target foil and an indium monitor foil. This target configuration may be modified (to a titanium foil, or some other alternative) by modifying Cell 20 in the code.

The basic design characteristics and operation of the HFNG have been described in subsection 4.3.1, and a more detailed discussion of the generator may be found in the recent work of Unzueta *et al.* [192]. In short, the generator, running with only one of the

two available ion sources, extracts deuterium ions from an RF-heated deuterium plasma, forming a flat-profile beam, approximately 5 mm in diameter. This deuterium beam is incident upon a water-cooled, self-loading titanium-coated copper target [156, 157, 192], where the titanium layer acts as a reaction surface for DD fusion, producing a forward-focused neutron flux. Irradiation targets are inserted in the center of the titanium layer deuteron target, approximately 8 mm from the DD reaction surface, prior to startup. The following benchmarked MCNP model recreates the structural design and operation of the generator, for the configurations used in the work described in chapter 4. A rendering of the target chamber section of the HFNG model is seen in Figure 4.13. This model is used to simulate the production of DD neutrons according to the well-known energy distribution as a function of emission angle [1], and transport them throughout the generator. Using this transport model, the energy-differential neutron flux is calculated throughout the geometry of the HFNG, accounting for both attenuation and energy loss throughout the neutron production target, the irradiation target, and all structural components. These flux calculations are used (in subsection 4.3.3) to determine the effective neutron energy range subtended by the irradiation targets, which are used in the reporting of the measured cross sections.

```

TITLE - ETCHEVERRY HFNG IRRADIATION
C _____
C CELLS
C _____
10 100 -7.31      60 -70 -80          IMP:N,P=1 $ INDIUM
C 11 500 -1.31     60 -70 -81          IMP:N,P=1 $ INDIUM
C 12 500 -1.31     60 -70 -82          IMP:N,P=1 $ INDIUM
C 13 500 -1.31     60 -70 -83          IMP:N,P=1 $ INDIUM
C 14 500 -1.31     60 -70 -84          IMP:N,P=1 $ INDIUM
C 15 500 -1.31     60 -70 -86          IMP:N,P=1 $ INDIUM
C 16 500 -1.31     60 -70 -87          IMP:N,P=1 $ INDIUM
C 17 500 -1.31     60 -70 -88          IMP:N,P=1 $ INDIUM
C 18 500 -1.31     60 -70 -89          IMP:N,P=1 $ INDIUM
20 200 -7.134     70 -75 -80          IMP:N,P=1 $ ZINC
50 300 -8.92       5 -10 20 -30 40 -50 100 101 102 103
                    104 115 116 117 118 119          IMP:N,P=1 $ CU FRONT
60 300 -8.92       5 -10 20 -30 85 -90 105 106 107 108 109
                    110 111 112 113 114          IMP:N,P=1 $ CU BACK
62 300 -8.92       20 -54 -51 50 5 -10          IMP:N,P=1 $ CU LIP LOWER LEFT
63 300 -8.92       -30 55 -51 50 5 -10          IMP:N,P=1 $ CU LIP LOWER RIGHT
64 300 -8.92       20 -54 52 -85 5 -10          IMP:N,P=1 $ CU LIP LOWER LEFT
65 300 -8.92       -30 55 52 -85 5 -10          IMP:N,P=1 $ CU LIP LOWER LEFT
70 400 -1.00       -100 5 -10          IMP:N,P=1 $ WATER CHANNEL
71 400 -1.00       -101 5 -10          IMP:N,P=1 $ WATER CHANNEL
72 400 -1.00       -102 5 -10          IMP:N,P=1 $ WATER CHANNEL
73 400 -1.00       -103 5 -10          IMP:N,P=1 $ WATER CHANNEL
74 400 -1.00       -104 5 -10          IMP:N,P=1 $ WATER CHANNEL
75 400 -1.00       -105 5 -10          IMP:N,P=1 $ WATER CHANNEL
76 400 -1.00       -106 5 -10          IMP:N,P=1 $ WATER CHANNEL
77 400 -1.00       -107 5 -10          IMP:N,P=1 $ WATER CHANNEL
78 400 -1.00       -108 5 -10          IMP:N,P=1 $ WATER CHANNEL
79 400 -1.00       -109 5 -10          IMP:N,P=1 $ WATER CHANNEL
80 400 -1.00       -110 5 -10          IMP:N,P=1 $ WATER CHANNEL
81 400 -1.00       -111 5 -10          IMP:N,P=1 $ WATER CHANNEL
82 400 -1.00       -112 5 -10          IMP:N,P=1 $ WATER CHANNEL
83 400 -1.00       -113 5 -10          IMP:N,P=1 $ WATER CHANNEL
84 400 -1.00       -114 5 -10          IMP:N,P=1 $ WATER CHANNEL

```

```

85 400 -1.00    -115 5 -10          IMP:N,P=1 $ WATER CHANNEL
86 400 -1.00    -116 5 -10          IMP:N,P=1 $ WATER CHANNEL
87 400 -1.00    -117 5 -10          IMP:N,P=1 $ WATER CHANNEL
88 400 -1.00    -118 5 -10          IMP:N,P=1 $ WATER CHANNEL
89 400 -1.00    -119 5 -10          IMP:N,P=1 $ WATER CHANNEL
100 800 -4.54   -40 42 5 -10 54 -55 IMP:N,P=1 $ TI TARGET
550 0 -200 ((120 128 -130 131):(128 130 132):(128 -131 140)
           :(136 130 -128 129):(126 -129 -130 131):(134 130 -129)
           :(142 -129 -131):(138 -131 129 -128):(-124 129 -128)
           :(122 129 -128)) IMP:N,P=1
600 0 (-121 128 -130 131):(128 130 -133):(128 -131 -141)
           :(-137 130 -128 129):(-127 -129 -130 131):(-135 130 -129)
           :(-143 -129 -131):(-139 -131 129 -128) IMP:N,P=1
650 0 ((131 -130 125 -123 -128 129) (10: -5: -40: 90: -20: 30 )
           :(-144 123 -122):(-144 -125 124)) #100 IMP:N,P=1
675 600 -2.7 (5 -10 40 -90 20 -30) ((20 -30 75 -52):
           (55 -30 51 -75):(20 -54 51 -75)) #10 #20
           IMP:N,P=1 $ Al Holder if used
676 500 -1.00 ((5 -10 40 -90 20 -30)
           (20 -30 57 -75 54 -55) ) #10 #20 IMP:N,P=1 $ Poly Holder if used
680 0 (5 -10 40 -90 20 -30) ((54 -55 52 -85):(54 -55 50 -51):
           (54 -55 51 -57)) IMP:N,P=1
700 600 -2.7 (-120 121 128 -130 131) : (-122 123 -128 129 -130 131 144)
           : (124 -125 -128 129 -130 131 144)
           : (-126 127 -129 -130 131) : (-132 133 130 128)
           : (-134 135 -129 130) : (-136 137 130 -128 129)
           : (-140 141 -131 128) : (-142 143 -131 -129)
           : (-138 139 -131 -128 129) IMP:N,P=1 $ Al Shroud
900 0      200 -300 IMP:N,P=1 $ Concrete when used
999 0     300 IMP:N,P=0

```

C

C Surfaces

C

C

```

5   px -4.66
10  px  4.66 $ 9.32 cm total = 4.66 cm
20  py -4.445 $ 8.89 cm total = 4.445 cm
30  py  4.445
40  pz -0.6858
42  pz -0.6958
50  pz  0.
51  pz  0.1077 $ create 1/8" slot
52  pz  0.4252 $ create 1/8" slot
54  py -2.445 $ left interior of lip should be 2.08 cm
55  py  2.445 $ right interior of lip
57  pz  0.143 $ beginning of plastic holder
60  pz  0.194 $ front surface of Indium
70  pz  0.219 $ back surface of Indium 0.025 cm thick
75  pz  0.269 $ back surface of Zinc 0.05 cm thick
80  c/z 0. 0. 0.45
81  c/z 0. 1. 0.45
82  c/z 0. -1. 0.45
83  c/z 1. 0. 0.45
84  c/z 1. 1. 0.45
85  pz  0.5334 $Top Cu lower
86  c/z 1 -1. 0.45
87  c/z -1. 0. 0.45
88  c/z -1  1. 0.45
89  c/z -1 -1. 0.45
90  pz  1.2192 $Top Cu upper
91  py  -1.0
92  py  1.0

```

```

93 px -1.5
94 px 1.5
100 c/x 0.2413 -0.254 0.1778
101 c/x 0.7413 -0.254 0.1778
102 c/x 1.2239 -0.254 0.1778
103 c/x 1.7065 -0.254 0.1778
104 c/x 2.1891 -0.254 0.1778
C
105 c/x 0.2413 0.7874 0.1778
106 c/x 0.7413 0.7874 0.1778
107 c/x 1.2239 0.7874 0.1778
108 c/x 1.7065 0.7874 0.1778
109 c/x 2.1891 0.7874 0.1778
C
110 c/x -0.2413 0.7874 0.1778
111 c/x -0.7413 0.7874 0.1778
112 c/x -1.2239 0.7874 0.1778
113 c/x -1.7065 0.7874 0.1778
114 c/x -2.1891 0.7874 0.1778
C
115 c/x -0.2413 -0.254 0.1778
116 c/x -0.7413 -0.254 0.1778
117 c/x -1.2239 -0.254 0.1778
118 c/x -1.7065 -0.254 0.1778
119 c/x -2.1891 -0.254 0.1778
C _____ SHROUD SURFACES _____
C PLATES WITH CYLINDRICAL CAPS ON TOP, BOTTOM, AND SIDES, QUADRANTS OF SPHERES CAP CORNERS
C _____
120 C/Y 6.79 0. 3.24
121 C/Y 6.79 0. 2.98
122 PZ 3.23999
123 PZ 2.97999
124 PZ -3.23999
125 PZ -2.97999
126 C/Y -6.79 0. 3.24
127 C/Y -6.79 0. 2.98
128 PX 6.78999
129 PX -6.78999
130 PY 6.78999
131 PY -6.78999
132 S 6.79 6.79 0. 3.24
133 S 6.79 6.79 0. 2.98
134 S -6.79 6.79 0. 3.24
135 S -6.79 6.79 0. 2.98
136 C/X 6.79 0. 3.24
137 C/X 6.79 0. 2.98
138 C/X -6.79 0. 3.24
139 C/X -6.79 0. 2.98
140 S 6.79 -6.79 0. 3.24
141 S 6.79 -6.79 0. 2.98
142 S -6.79 -6.79 0. 3.24
143 S -6.79 -6.79 0. 2.98
144 CZ 2.032
C 145 CY 0.15875 $ hole in extraction plate
C
200 sph 0. 0. -0.696 30.
300 sph 0. 0. -0.696 133.

C _____
C Data
C _____
C _____
C Materials for Geometry

```

```

C _____
M100 49000      1.0
M101 49115      1.0
M115 49115      1.0
M200 30000.70c   1.0
M300 29063.70c   0.6915
          29065.70c   0.3085
M400 1001.70c   0.67
          8016.70c   0.33
M500 1001.70c   0.67
          6012       0.33
M600 13027.70c   1.0
M700 7014.70c    1.0
M800 22000       1.0
M850 1001.70c   -0.0221  $ Concrete
          6000.70c   -0.002484
          8016.70c   -0.574930
          11023.70c  -0.015208
          12000      -0.001266
          13027.70c  -0.019953
          14000.21c   -0.304627
          19000      -0.010045
          20000      -0.042951
          26000.21c   -0.006435
C Scattering Kernels
MT400 lwtr.11t $ Hydrogen in Light Water
MT500 poly.10t $ natural polyethylene
MT600 al27.12t $ Aluminum
C
F104:n 10
C FM104 -1 100 4
C FM104 -1 101 102
C F114:n 11
C FM114 0.03827 100 51
C F124:n 12
C FM124 0.03827 100 51
C F134:n 13
C FM134 0.03827 100 51
C F144:n 14
C FM144 0.03827 100 51
C F154:n 15
C FM154 0.03827 100 51
C F164:n 16
C FM164 0.03827 100 51
C F174:n 17
C FM174 0.03827 100 51
C F184:n 18
C FM184 0.03827 100 51
F194:n 10
E194 0. 1.0e-08 2.5e-08 1.0e-07 5.e-07 1.0e-06 1.0e-05 1.0e-04
          1.0e-03 1.0e-02 1.0e-01 0.25 0.5 0.75 1.0 1.25 1.5 1.75
          2.0 2.1 2.2 2.3 2.4 2.5 2.6 2.7 2.8 2.9 3.0 3.1 3.2
F21:n 200
F22:n 200
C21 -0.95 -0.9 -0.85 -0.8 -0.75 -0.7 -0.65 -0.6 -0.55 -0.5 &
          -0.45 -0.4 -0.35 -0.3 -0.25 -0.2 -0.15 -0.1 -0.05 0.0 &
          0.05 0.1 0.15 0.2 0.25 0.3 0.35 0.4 0.45 0.5 &
          0.55 0.6 0.65 0.7 0.75 0.8 0.85 0.9 0.95 1.0
FT21 FRV 0. 0. 1.
F32:n 200
F41:n 200
F51:n 60
FS51:n -80 -81 -82 -83 -84 -86 -87 -88 -89

```

```

F52:n 60
FS52:n -80 -81 -82 -83 -84 -86 -87 -88 -89
SD52 0.56745 0.56745 0.56745 0.56745 0.56745 0.56745 0.56745 0.56745 0.56745 1.
C F05:n 0. 0. 0.2 0.0 0. 0.2 0.2 0.0 0. -0.2 0.2 0.0
C F15:n 0. 1. 0.2 0.0 0. 1.2 0.2 0.0 0. 0.8 0.2 0.0
FMESH04:n geom=cyl origin=0. 0. 0.194
    axs = 0 0 1 vec = 1 0 0
    imesh=0.45 jmesh=0.025 kmesh=1
    iints=1 jint=1 kints=1
    emesh=3. eints=1200 enorm=yes
FMESH14:n geom=cyl origin=0. 10. 0.194
    axs = 0 1 0 vec = 1 0 0
    imesh=0.45 jmesh=0.025 kmesh=1
    iints=1 jint=1 kints=1
    emesh=3. eints=1200 enorm=yes
C FMESH14:n geom=cyl origin=0. 1. 0.194
C     axs = 0 0 1 vec = 1 0 0
C     imesh=0.425 jmesh=1.0e-04 kmesh=1
C     iints=1 jint=1 kints=1
C     emesh=3. eints=1200 enorm=yes
C FMESH24:n geom=cyl origin=0. -1. 0.194
C     axs = 0 0 1 vec = 1 0 0
C     imesh=0.425 jmesh=1.0e-04 kmesh=1
C     iints=1 jint=1 kints=1
C     emesh=3. eints=1200 enorm=yes
C FMESH34:n geom=cyl origin=1. 0. 0.194
C     axs = 0 0 1 vec = 1 0 0
C     imesh=0.425 jmesh=1.0e-04 kmesh=1
C     iints=1 jint=1 kints=1
C     emesh=3. eints=1200 enorm=yes
C FMESH44:n geom=cyl origin=1. 1. 0.194
C     axs = 0 0 1 vec = 1 0 0
C     imesh=0.425 jmesh=1.0e-04 kmesh=1
C     iints=1 jint=1 kints=1
C     emesh=3. eints=1200 enorm=yes
C FMESH54:n geom=cyl origin=1. -1. 0.194
C     axs = 0 0 1 vec = 1 0 0
C     imesh=0.425 jmesh=1.0e-04 kmesh=1
C     iints=1 jint=1 kints=1
C     emesh=3. eints=1200 enorm=yes
C FMESH64:n geom=cyl origin=-1. 0. 0.194
C     axs = 0 0 1 vec = 1 0 0
C     imesh=0.425 jmesh=1.0e-04 kmesh=1
C     iints=1 jint=1 kints=1
C     emesh=3. eints=1200 enorm=yes
C FMESH74:n geom=cyl origin=-1. 1. 0.194
C     axs = 0 0 1 vec = 1 0 0
C     imesh=0.425 jmesh=1.0e-04 kmesh=1
C     iints=1 jint=1 kints=1
C     emesh=3. eints=1200 enorm=yes
C FMESH84:n geom=cyl origin=-1. -1. 0.194
C     axs = 0 0 1 vec = 1 0 0
C     imesh=0.425 jmesh=1.0e-04 kmesh=1
C     iints=1 jint=1 kints=1
C     emesh=3. eints=1200 enorm=yes
C FMESH304:n geom=cyl origin=0. 0. 0.194
C     axs = 0 0 1 vec = 1 0 0
C     imesh=0.425 jmesh=0.025 kmesh=1
C     iints=1 jint=1 kints=1
C     emesh=3. eints=1200 enorm=yes
FMESH404:n geom=cyl origin=0. 0. 0.219
    axs = 0 0 1 vec = 1 0 0
    imesh=0.45 jmesh=0.05 kmesh=1

```

```

    iints=1  jint=1   kints=1
    emesh=3. eints=1200 enorm=yes
C FMESH204:n geom=xyz origin=-1.75 -1.75 0.192
C           imesh=1.75 jmesh=1.75 kmesh=0.217
C           iints=70 jint=70   kints=1
C FMESH214:n geom=xyz origin=-1.75 -1.75 0.192
C           imesh=1.75 jmesh=1.75 kmesh=0.217 emesh=3.
C           iints=70 jint=70   kints=1 eints=100
C FMESH404:n geom=cyl   origin=0. 0. 0.142
C           axs = 0 0 1 vec = 1 0 0
C           imesh=0.425 jmesh=1.0e-04 kmesh=1
C           iints=4 jint=1   kints=1
C
C *FMESH14:n geom=xyz origin=0. 0. 0. axs = 0 0 1 vec = 1 0 0
C           imesh=0.5 jmesh=0.0001 kmesh=1 emesh=5. eints=50
C           iints=1 jint=1   kints=1
C
C
C tmesh
C cmesh01:n flux
C cora01:n 0. 0.025
C corb01:n 0.142 0.167
C corc01:n 360.
C endmd
C
C Dose Cards for activation calculation Indium(n,n') is from IRDF-90
C
C 115In(n,n') 115mIn
C
FMESH504:N geom=cyl   origin=0. 0. 0.194
    axs = 0 0 1 vec = 1 0 0
    imesh=0.45 jmesh=0.025 kmesh=1
    iints=1 jint=1   kints=1
DE504 lin 1.e-11 0.32000 0.34000 0.36000 0.38000
    0.40000 0.42500 0.45000 0.47500 0.50000
    0.52500 0.55000 0.57500 0.60000 0.63000
    0.66000 0.69000 0.72000 0.76000 0.80000
    0.84000 0.88000 0.92000 0.96000 1.0000
    1.1000 1.2000 1.3000 1.4000 1.5000
    1.6000 1.7000 1.8000 1.9000 2.0000
    2.1000 2.2000 2.3000 2.4000 2.5000
    2.6000 2.7000 2.8000 2.9000 3.0000
DF504 lin 0.0e+00 0.0e+00 1.69e-05 5.24e-04 1.1e-03
    1.62e-03 2.06e-03 2.48e-03 3.1e-03 3.90e-03
    4.87e-03 6.01e-03 7.36e-03 8.93e-03 1.11e-02
    1.36e-02 1.65e-02 1.98e-02 2.48e-02 3.03e-02
    3.65e-02 4.33e-02 5.05e-02 5.82e-02 6.61e-02
    8.69e-02 1.08e-01 1.29e-01 1.50e-01 1.70e-01
    1.91e-01 2.12e-01 2.33e-01 2.54e-01 2.75e-01
    2.95e-01 3.13e-01 3.26e-01 3.35e-01 3.41e-01
    3.44e-01 3.45e-01 3.45e-01 3.44e-01 3.41e-01
C
C 64Zn(n,p)64Cu
C
FMESH604:N geom=cyl   origin=0. 0. 0.219
    axs = 0 0 1 vec = 1 0 0
    imesh=0.45 jmesh=0.05 kmesh=1
    iints=1 jint=1   kints=1
DE604 lin 1.e-11 0.144 0.25 0.32000 0.34000 0.36000 0.38000
    0.40000 0.42500 0.45000 0.47500 0.50000
    0.52500 0.55000 0.57500 0.60000 0.63000
    0.66000 0.69000 0.72000 0.76000 0.80000
    0.84000 0.88000 0.92000 0.96000 1.0000

```

```

1.1000  1.2000  1.3000  1.4000  1.5000
1.6000  1.7000  1.8000  1.9000  2.0000
2.1000  2.2000  2.3000  2.4000  2.5000
2.6000  2.7000  2.8000  2.9000  3.0000
DF604 lin 0.e+00 8.60e-08 4.45e-07 6.94e-07 7.65e-07 8.36e-07 9.08e-07
9.86e-07 1.10e-06 1.24e-06 1.37e-06 1.52e-06
1.67e-06 1.83e-06 2.02e-06 2.20e-06 2.43e-06
2.65e-06 2.88e-06 3.14e-06 4.44e-06 6.33e-06
8.22e-06 1.01e-05 1.29e-05 1.73e-05 2.74e-05
4.12e-05 8.36e-05 1.68e-04 3.22e-04 5.88e-04
1.03e-03 1.75e-03 2.84e-03 3.90e-03 5.38e-03
7.99e-03 1.09e-02 1.48e-02 2.00e-02 2.59e-02
3.42e-02 4.32e-02 5.38e-02 6.38e-02 7.37e-02
C
C Source - 0.25 cm radius disk sources located
C           outside the copper target holder
C
C SDEF POS=-0.05 -0.37 -0.686 &
C SDEF POS=0. 0. -0.686 &
C   AXS=0 0 1 VEC=0 0 1 RAD=D3 PAR=N DIR=D4 ERG=fdir D5 &
C   WGT=1.0 EXT=0
SDEF POS = 0.0 0.0 -0.696 &
AXS=0 0 1 VEC=0 0 1 RAD=D3 PAR=1 DIR=D4 ERG=fdir D5 &
WGT=1.0 EXT=0
C SI1 L 0 -1.1 0. 0 1.1 0.
C SP1 0.5 0.5
C Distribution for axs
C SIn L 0 1 0 0 -1 0
C SPn 0.5 0.5
C Distribution for vec
C DS2 L 0 0 1
C Distribution for rad
SI3 0 0.25
SP3 -21 1.0
C Distribution for dir
C This is cos(theta) in one-degree increments from 180 to 0 degreesou
C
SI4 -1 -0.99985 -0.99939 -0.99863 -0.99756 &
-0.99619 -0.99452 -0.99255 -0.99027 -0.98769 &
-0.98481 -0.98163 -0.97815 -0.97437 -0.9703 &
-0.96593 -0.96126 -0.9563 -0.95106 -0.94552 &
-0.93969 -0.93358 -0.92718 -0.9205 -0.91355 &
-0.90631 -0.89879 -0.89101 -0.88295 -0.87462 &
-0.86603 -0.85717 -0.84805 -0.83867 -0.82904 &
-0.81915 -0.80902 -0.79864 -0.78801 -0.77715 &
-0.76604 -0.75471 -0.74314 -0.73135 -0.71934 &
-0.70711 -0.69466 -0.682 -0.66913 -0.65606 &
-0.64279 -0.62932 -0.61566 -0.60182 -0.58779 &
-0.57358 -0.55919 -0.54464 -0.52992 -0.51504 &
-0.5 -0.48481 -0.46947 -0.45399 -0.43837 &
-0.42262 -0.40674 -0.39073 -0.37461 -0.35837 &
-0.34202 -0.32557 -0.30902 -0.29237 -0.27564 &
-0.25882 -0.24192 -0.22495 -0.20791 -0.19081 &
-0.17365 -0.15643 -0.13917 -0.12187 -0.10453 &
-0.087156 -0.069756 -0.052336 -0.034899 -0.017452 &
6.1232e-17 0.017452 0.034899 0.052336 0.069756 &
0.087156 0.10453 0.12187 0.13917 0.15643 &
0.17365 0.19081 0.20791 0.22495 0.24192 &
0.25882 0.27564 0.29237 0.30902 0.32557 &
0.34202 0.35837 0.37461 0.39073 0.40674 &
0.42262 0.43837 0.45399 0.46947 0.48481 &
0.5 0.51504 0.52992 0.54464 0.55919 &
0.57358 0.58779 0.60182 0.61566 0.62932 &

```

```

0.64279    0.65606    0.66913    0.682    0.69466  &
0.70711    0.71934    0.73135    0.74314    0.75471  &
0.76604    0.77715    0.78801    0.79864    0.80902  &
0.81915    0.82904    0.83867    0.84805    0.85717  &
0.86603    0.87462    0.88295    0.89101    0.89879  &
0.90631    0.91355    0.9205     0.92718    0.93358  &
0.93969    0.94552    0.95106    0.9563     0.96126  &
0.96593    0.9703     0.97437    0.97815    0.98163  &
0.98481    0.98769    0.99027    0.99255    0.99452  &
0.99619    0.99756    0.99863    0.99939    0.99985  &
1.0
C
C This is the secondary neutron angular distribution for incident deuterons of initial
C energy of 100keV - uses Cory's reaction # to weight slowing down spectrum
C (dsigma/domega)(theta)*domega normalized
C From Liskiien -Paulsen
C Error in previous computation - now corrected here
C
SP4 0. 9.5613e-05 0.00028675 0.00047762 0.00066804 &
0.00085784 0.0010468 0.0012349 0.0014218 0.0016073 &
0.0017914 0.0019738 0.0021545 0.0023331 0.0025097 &
0.002684 0.0028558 0.0030251 0.0031918 0.0033555 &
0.0035164 0.0036742 0.0038288 0.0039801 0.0041281 &
0.0042725 0.0044134 0.0045507 0.0046842 0.0048139 &
0.0049398 0.0050618 0.0051798 0.0052939 0.0054039 &
0.0055099 0.0056118 0.0057097 0.0058035 0.0058932 &
0.0059789 0.0060605 0.0061382 0.0062118 0.0062816 &
0.0063474 0.0064094 0.0064677 0.0065222 0.0065731 &
0.0066205 0.0066643 0.0067048 0.006742 0.0067761 &
0.006807 0.0068349 0.00686 0.0068823 0.006902 &
0.0069192 0.006934 0.0069466 0.006957 0.0069655 &
0.0069721 0.006977 0.0069803 0.0069822 0.0069827 &
0.0069821 0.0069805 0.006978 0.0069747 0.0069709 &
0.0069665 0.0069618 0.0069568 0.0069518 0.0069468 &
0.0069419 0.0069372 0.0069329 0.006929 0.0069257 &
0.006923 0.0069211 0.0069199 0.0069196 0.0069203 &
0.0069219 0.0069246 0.0069284 0.0069333 0.0069393 &
0.0069464 0.0069547 0.0069642 0.0069748 0.0069865 &
0.0069993 0.0070131 0.0070279 0.0070437 0.0070603 &
0.0070776 0.0070957 0.0071143 0.0071335 0.0071529 &
0.0071726 0.0071924 0.0072122 0.0072317 0.0072509 &
0.0072696 0.0072875 0.0073046 0.0073206 0.0073353 &
0.0073486 0.0073602 0.0073699 0.0073776 0.007383 &
0.0073859 0.0073861 0.0073834 0.0073776 0.0073684 &
0.0073556 0.0073391 0.0073187 0.007294 0.007265 &
0.0072315 0.0071932 0.00715 0.0071018 0.0070483 &
0.0069894 0.0069251 0.006855 0.0067792 0.0066975 &
0.0066099 0.0065162 0.0064164 0.0063104 0.0061982 &
0.0060798 0.0059551 0.0058242 0.0056871 0.0055438 &
0.0053944 0.0052389 0.0050774 0.0049101 0.004737 &
0.0045583 0.0043741 0.0041845 0.0039898 0.0037902 &
0.0035858 0.0033768 0.0031636 0.0029462 0.0027251 &
0.0025004 0.0022724 0.0020414 0.0018077 0.0015716 &
0.0013334 0.0010934 0.00085199 0.00060938 0.00036596 &
0.00012204
C
C Neutron energy vs angle wtd as above
C
DS5 2.1857 2.1858 2.186 2.1861 2.1863 &
2.1864 2.187 2.1876 2.1882 2.1887 &
2.1893 2.1903 2.1913 2.1923 2.1932 &
2.1942 2.1956 2.1971 2.1985 2.1999 &

```

```

2.2014 2.2032 2.205  2.2068 2.2086 &
2.2104 2.2125 2.2146 2.2167 2.2188 &
2.221  2.2235 2.2261 2.2286 2.2312 &
2.2337 2.2366 2.2395 2.2424 2.2453 &
2.2482 2.2514 2.2545 2.2577 2.2609 &
2.264  2.2676 2.2712 2.2747 2.2783 &
2.2818 2.2856 2.2895 2.2933 2.2971 &
2.3009 2.3051 2.3092 2.3134 2.3175 &
2.3216 2.326  2.3304 2.3348 2.3392 &
2.3436 2.3482 2.3527 2.3573 2.3618 &
2.3664 2.3712 2.376  2.3808 2.3856 &
2.3904 2.3954 2.4003 2.4052 2.4102 &
2.4151 2.4202 2.4254 2.4305 2.4356 &
2.4407 2.4459 2.4511 2.4563 2.4615 &
2.4667 2.4719 2.4772 2.4824 2.4876 &
2.4928 2.498  2.5033 2.5085 2.5137 &
2.5189 2.5242 2.5295 2.5348 2.5401 &
2.5454 2.5506 2.5557 2.5608 2.5659 &
2.571  2.5761 2.5812 2.5862 2.5913 &
2.5964 2.6013 2.6062 2.6111 2.616 &
2.6209 2.6256 2.6302 2.6349 2.6396 &
2.6442 2.6488 2.6533 2.6578 2.6623 &
2.6668 2.671  2.6751 2.6793 2.6835 &
2.6876 2.6915 2.6953 2.6991 2.703 &
2.7068 2.7104 2.714  2.7175 2.7211 &
2.7247 2.7277 2.7308 2.7339 2.737 &
2.7401 2.7428 2.7455 2.7482 2.7509 &
2.7535 2.7558 2.758  2.7602 2.7624 &
2.7647 2.7665 2.7683 2.7701 2.7719 &
2.7737 2.7749 2.7761 2.7773 2.7785 &
2.7797 2.7806 2.7814 2.7822 2.783 &
2.7839 2.7841 2.7843 2.7846 2.7848 &
2.785
C
C
FCL:n 1 1 0 34i 0
RAND GEN=2 STRIDE=152917 SEED=10899028731
NPS 1e8
C CUT:n j 2.2
MODE n
C PTRAC file=asc write=all event=src
C VOID $ 10 20 675 676
PRINT

```

A.2 IPF Nb(p,x) Target Stack Input

The following MCNP code simulates the irradiation of the $^{nat}Nb(p,x)$ target stack, used for the experiments described in chapter 2. The model consists of a 3D simulation of the full target stack, as outlined in subsection 2.3.1 and Table 2.1. This includes the stainless steel profile monitors, aluminum energy degraders, nominal 25 μm ^{nat}Nb target foils, and the nominal 25 μm ^{nat}Al and 50 μm ^{nat}Cu monitor foils. The target and monitor foils each include two pieces of of Kapton polyimide film tape, with each piece of tape consisting of 43.2 μm of a silicone adhesive (nominal 4.79 mg/cm²) on 25.4 μm of a polyimide backing (nominal 3.61 mg/cm²). The target stack also includes the target box's Inconel beam entrance window and aluminum chassis, its cooling water-filled cavity, and all other structural components

used for mounting the target box in the beamline. The target stack is not pumped down to the beamline vacuum, but exists at the local atmospheric pressure of approximately 77.6 kPa. A rendering of the target stack model is seen in Figure 2.19.

Incident upon the front of the stack is beam of protons in an elliptical beam spot, with a major axis 1.696 cm in diameter, and a minor axis 0.784 cm in diameter. This upstream spot size is determined from the radiochromic film developed by the stainless steel beam profile monitor at the front of the stack, seen in Figure 2.15. Based on historical beam characterization at LANSCE-IPF, the beam is modeled in MCNP as a circular pencil beam (no divergence/convergence) with a diameter of 1.696 cm, to avoid under-representing beam filling of target foils. The beam intensity has a linear radial $1/r$ intensity, and an average energy of 100 MeV with a Gaussian energy distribution width of 0.1 MeV. This beam definition is transported through the target stack, accounting for both attenuation, secondary reactions, and energy loss throughout the stack. The proton energy-differential flux is calculated in each stack element — as described in subsection 2.3.4, these distributions are used to assign energy bins to each foil, as well as for the variance minimization minimization techniques employed in this work. In addition, this transport model allows one to estimate the fluence loss down the stack, due to (p,x) reactions and scattering of the beam.

```

TITLE - 100 Mev Pencil Beam on Nb  Foil Stack mcnp6
C .
C Cell Definitions
C .
C ***** Inconel, Water, and SS Foil *****
1    7 -8.4446 -500 1 -2
2    6      -1 -500 2 -3
3    1     -2.8000 -500 3 -4
4    2 -7.788431 -500 4 -5
5    4     -1.42 -500 5 -6
6   10     -1.1100 -500 6 -7
7    8 -2.6076 -500 7 -8
8   10     -1.1100 -500 8 -9
9    4     -1.42 -500 9 -10
10   3 -0.000908 -500 10 -11
11   4     -1.42 -500 11 -12
12   10     -1.1100 -500 12 -13
13   9 -8.766068 -500 13 -14
14   10     -1.1100 -500 14 -15
15   4     -1.42 -500 15 -16
16   3 -0.000908 -500 16 -17
17   4     -1.42 -500 17 -18
18   10     -1.1100 -500 18 -19
19   5 -7.735 -500 19 -20
20   10     -1.1100 -500 20 -21
21   4     -1.42 -500 21 -22
22   3 -0.000908 -500 22 -23
23   1     -2.8000 -500 23 -24
24   4     -1.42 -500 24 -25
25   10     -1.1100 -500 25 -26
26   8 -2.542745 -500 26 -27
27   10     -1.1100 -500 27 -28
28   4     -1.42 -500 28 -29
29   3 -0.000908 -500 29 -30
30   4     -1.42 -500 30 -31

```

```

31      10    -1.1100 -500 31 -32
32      9     -8.71343 -500 32 -33
33      10    -1.1100 -500 33 -34
34      4     -1.42 -500 34 -35
35      3    -0.000908 -500 35 -36
36      4     -1.42 -500 36 -37
37      10    -1.1100 -500 37 -38
38      5     -7.436688 -500 38 -39
39      10    -1.1100 -500 39 -40
40      4     -1.42 -500 40 -41
41      3    -0.000908 -500 41 -42
42      1     -2.8000 -500 42 -43
43      4     -1.42 -500 43 -44
44      10    -1.1100 -500 44 -45
45      8     -2.508527 -500 45 -46
46      10    -1.1100 -500 46 -47
47      4     -1.42 -500 47 -48
48      3    -0.000908 -500 48 -49
49      4     -1.42 -500 49 -50
50      10    -1.1100 -500 50 -51
51      9     -8.777886 -500 51 -52
52      10    -1.1100 -500 52 -53
53      4     -1.42 -500 53 -54
54      3    -0.000908 -500 54 -55
55      4     -1.42 -500 55 -56
56      10    -1.1100 -500 56 -57
57      5     -7.389032 -500 57 -58
58      10    -1.1100 -500 58 -59
59      4     -1.42 -500 59 -60
60      3    -0.000908 -500 60 -61
61      1     -2.8000 -500 61 -62
62      4     -1.42 -500 62 -63
63      10    -1.1100 -500 63 -64
64      8     -2.473384 -500 64 -65
65      10    -1.1100 -500 65 -66
66      4     -1.42 -500 66 -67
67      3    -0.000908 -500 67 -68
68      4     -1.42 -500 68 -69
69      10    -1.1100 -500 69 -70
70      9     -8.721534 -500 70 -71
71      10    -1.1100 -500 71 -72
72      4     -1.42 -500 72 -73
73      3    -0.000908 -500 73 -74
74      4     -1.42 -500 74 -75
75      10    -1.1100 -500 75 -76
76      5     -7.321429 -500 76 -77
77      10    -1.1100 -500 77 -78
78      4     -1.42 -500 78 -79
79      3    -0.000908 -500 79 -80
80      1     -2.8000 -500 80 -81
81      4     -1.42 -500 81 -82
82      10    -1.1100 -500 82 -83
83      8     -2.444906 -500 83 -84
84      10    -1.1100 -500 84 -85
85      4     -1.42 -500 85 -86
86      3    -0.000908 -500 86 -87
87      4     -1.42 -500 87 -88
88      10    -1.1100 -500 88 -89
89      9     -8.710895 -500 89 -90
90      10    -1.1100 -500 90 -91
91      4     -1.42 -500 91 -92
92      3    -0.000908 -500 92 -93
93      4     -1.42 -500 93 -94

```

```

94      10    -1.1100 -500 94 -95
95      5     -7.178571 -500 95 -96
96      10    -1.1100 -500 96 -97
97      4     -1.42 -500 97 -98
98      3     -0.000908 -500 98 -99
99      1     -2.8000 -500 99 -100
100     4     -1.42 -500 100 -101
101     10    -1.1100 -500 101 -102
102     8     -2.461977 -500 102 -103
103     10    -1.1100 -500 103 -104
104     4     -1.42 -500 104 -105
105     3     -0.000908 -500 105 -106
106     4     -1.42 -500 106 -107
107     10    -1.1100 -500 107 -108
108     9     -8.683226 -500 108 -109
109     10    -1.1100 -500 109 -110
110     4     -1.42 -500 110 -111
111     3     -0.000908 -500 111 -112
112     4     -1.42 -500 112 -113
113     10    -1.1100 -500 113 -114
114     5     -7.067092 -500 114 -115
115     10    -1.1100 -500 115 -116
116     4     -1.42 -500 116 -117
117     3     -0.000908 -500 117 -118
118     2     -7.93 -500 118 -119
C  ***** Air surrounding stack *****
150     3     -0.000908 -200 500
C  ***** Universe Boundary *****
200     0             200

C .
C Surface Definitions
C .
C all distances represent the front of the listed object
1      px 0
2      px 0.064
3      px 0.786
4      px 0.8114
5      px 0.83638
6      px 0.83892
7      px 0.843238
8      px 0.845738
9      px 0.850056
10     px 0.852596
11     px 0.99388
12     px 0.99642
13     px 1.000738
14     px 1.006868
15     px 1.011186
16     px 1.013726
17     px 1.15138
18     px 1.15392
19     px 1.158238
20     px 1.161238
21     px 1.165556
22     px 1.168096
23     px 1.30888
24     px 1.80488
25     px 1.80742
26     px 1.811738
27     px 1.814288
28     px 1.818606
29     px 1.821146

```

```
30      px 1.96238
31      px 1.96492
32      px 1.969238
33      px 1.975418
34      px 1.979736
35      px 1.982276
36      px 2.11988
37      px 2.12242
38      px 2.126738
39      px 2.129818
40      px 2.134136
41      px 2.136676
42      px 2.27738
43      px 2.73238
44      px 2.73492
45      px 2.739238
46      px 2.741818
47      px 2.746136
48      px 2.748676
49      px 2.88988
50      px 2.89242
51      px 2.896738
52      px 2.902888
53      px 2.907206
54      px 2.909746
55      px 3.04738
56      px 3.04992
57      px 3.054238
58      px 3.057338
59      px 3.061656
60      px 3.064196
61      px 3.20488
62      px 3.55688
63      px 3.55942
64      px 3.563738
65      px 3.566368
66      px 3.570686
67      px 3.573226
68      px 3.71438
69      px 3.71692
70      px 3.721238
71      px 3.727368
72      px 3.731686
73      px 3.734226
74      px 3.87188
75      px 3.87442
76      px 3.878738
77      px 3.881818
78      px 3.886136
79      px 3.888676
80      px 4.02938
81      px 4.37638
82      px 4.37892
83      px 4.383238
84      px 4.385888
85      px 4.390206
86      px 4.392746
87      px 4.53388
88      px 4.53642
89      px 4.540738
90      px 4.546888
91      px 4.551206
92      px 4.553746
```

```

93      px 4.69138
94      px 4.69392
95      px 4.698238
96      px 4.701318
97      px 4.705636
98      px 4.708176
99      px 4.84888
100     px 5.19488
101     px 5.19742
102     px 5.201738
103     px 5.204368
104     px 5.208686
105     px 5.211226
106     px 5.35238
107     px 5.35492
108     px 5.359238
109     px 5.365438
110     px 5.369756
111     px 5.372296
112     px 5.50988
113     px 5.51242
114     px 5.516738
115     px 5.519868
116     px 5.524186
117     px 5.526726
118     px 5.66738
119     px 5.67982
C Outline of foil stack
500      rpp 0 5.67982 -1.27 1.27 -1.27 1.27
C Universe boundary - 50 cm radius sphere
200      so 50

mode n h
C Al-2014
m1   13027.      0.05878645
      29063.      0.000812285 29065.      0.000363564 14028.      0.00050382
      14029.      2.34429e-005 14030.      1.69972e-005 25055.      0.000247294
      12024.      0.000349358
C 316 SS
m2   24050.      0.000672865
      24052.      0.01296789 24053.      0.001466307 24054.      0.000368568
      26054.      0.003518959 26056.      0.05522496 26057.      0.001271974
      26058.      0.000171578 28058.      0.006585093 28060.      0.002535278
      28061.      0.000108758 28062.      0.000351592 28064.      8.88507e-005
C Simple Air, O, N, Ar
m3   7014.      3.81269e-005
      8016.      9.50145e-006 18040.      1.66404e-007
C Kapton
m4   1001.      0.02256188
      6012.      0.04967341 7014.      0.004513215 8016.      0.01128638
C Niobium
m5   69000.      1
C Water
m6   1001.      0.007835711
      1002.      1.17553e-006 8016.      0.00559252
C Inconel
m7   28058.      0.03033345
      28060.      0.0112996 28061.      0.000482982 28062.      0.001514818
      28064.      0.000369887 26054.      0.00093471 26056.      0.01413661
      26057.      0.000320903 26058.      4.16534e-005 24050.      0.000715839
      24052.      0.01325908 24053.      0.001474897 24054.      0.000359615
      41093.      0.004247543 42092.      0.000390557 42094.      0.000238502
      42095.      0.000406153 42096.      0.000421111 42097.      0.000238612

```

```

        42098.      0.000596747 42100.      0.000233382 22048.      0.000749566
C   Aluminum
m8    13000.          1
C   Copper
m9    29000.          1
C   Silicone adhesive
m10   1001.          0.6
       6012.          0.2 8016.          0.1 14000.          0.1
imp:n  1 118r      0          $ 1, 200
imp:h  1 118r      0          $ 1, 200
C 100 MeV proton pencil beam at -0.1,0,0 (x,y,z)
C sdef erg=100 par=h vec=1 0 0 dir=1 pos=-0.10 0.0 0.0
sdef pos=-0.10 0.0 0.0 axs=1 0 0 ext=0 rad=d1 par=h vec=1 0 0 dir=1 erg=d2
si1 0 0.848101      $ radial sampling range: 0 to Rmax (=0.848cm)
sp1 -21 1           $ radial sampling weighting: r^-1 for disk
C si2 H 99.9 19I 100.1      $ 20 energy bins between X and Y
C sp2 D 0 0.05 19R      $ equal weighting for each bin
sp2 -41 0.1 100      $ Gaussian energy profile, mean 100 MeV,
C                      $ 0.1 MeV FWHM
phys:n 101
phys:h 101 j 0
prdmp 1+8 1+8 -1
nps 1+8
C ++++++
C Add tally below
C ++++++
C CINDER90 activation cross sections provided in
C 63 group LaBauve neutron energy group structure
histp 7 13 19 26 32 38 45 51 57 64 70 76 83 89 95 102 108 114
f4:n 7 13 19 26 32 38 45 51 57 64 70 76 83 89 95 102 108 114
e4 1 9999I 101
f14:h 7 13 19 26 32 38 45 51 57 64 70 76 83 89 95 102 108 114
e14 1 9999I 101

```

A.3 88-Inch Cyclotron 55 MeV Fe(p,x) Target Stack Input

Update references and specifics here!

The following MCNP code simulates the irradiation of the 55 MeV $^{nat}\text{Fe}(p,x)$ target stack, used for the experiments described in chapter 3. The model consists of a 3D simulation of the full target stack, as outlined in subsection 3.3.1 and Table 3.1. This includes the stainless steel profile monitors, aluminum energy degraders, nominal 25 μm ^{nat}Nb target foils, and the nominal 25 μm ^{nat}Al and 50 μm ^{nat}Cu monitor foils. The target and monitor foils each include two pieces of Kapton polyimide film tape, with each piece of tape consisting of 43.2 μm of a silicone adhesive (nominal 4.79 mg/cm²) on 25.4 μm of a polyimide backing (nominal 3.61 mg/cm²). The target stack also includes the target box's Inconel beam entrance window and aluminum chassis, its cooling water-filled cavity, and all other structural components used for mounting the target box in the beamline. The target stack is not pumped down to the beamline vacuum, but exists at the local atmospheric pressure of approximately 77.6 kPa. A rendering of the target stack model is seen in Figure 3.20.

Incident upon the front of the stack is beam of protons in an elliptical beam spot, with a major axis 1.696 cm in diameter, and a minor axis 0.784 cm in diameter. This upstream spot size is determined from the radiochromic film developed by the stainless steel beam profile monitor at the front of the stack, seen in [Figure 2.15](#). Based on historical beam characterization at LANSCE-IPF, the beam is modeled in MCNP as a circular pencil beam (no divergence/convergence) with a diameter of 1.696 cm, to avoid under-representing beam filling of target foils. The beam intensity has a linear radial $1/r$ intensity, and an average energy of 100 MeV with a Gaussian energy distribution width of 0.1 MeV. This beam definition is transported through the target stack, accounting for both attenuation, secondary reactions, and energy loss throughout the stack. The proton energy-differential flux is calculated in each stack element — as described in [subsection 3.3.4](#), these distributions are used to assign energy bins to each foil, as well as for the variance minimization minimization techniques employed in this work. In addition, this transport model allows one to estimate the fluence loss down the stack, due to (p,x) reactions and scattering of the beam.

```

MCNPX Visual Editor Version X.24E
c
c   Cell Definitions
c
c ***** SS, Fe, Ti, and Cu Foils *****
1   2 -7.728923 -500 1 -2
2   4 -1.42 -500 2 -3
3   8 -1.18 -500 3 -4
4   5 -8.0884 -500 4 -5
5   8 -1.18 -500 5 -6
6   4 -1.42 -500 6 -7
7   3 -1.58e-009 -500 7 -8
8   4 -1.42 -500 8 -9
9   8 -1.18 -500 9 -10
10  6 -4.436 -500 10 -11
11  8 -1.18 -500 11 -12
12  4 -1.42 -500 12 -13
13  3 -1.58e-009 -500 13 -14
14  4 -1.42 -500 14 -15
15  8 -1.18 -500 15 -16
16  7 -8.9616 -500 16 -17
17  8 -1.18 -500 17 -18
18  4 -1.42 -500 18 -19
19  3 -1.58e-009 -500 19 -20
20  1 -2.672688 -500 20 -21
21  4 -1.42 -500 21 -22
22  8 -1.18 -500 22 -23
23  5 -7.964 -500 23 -24
24  8 -1.18 -500 24 -25
25  4 -1.42 -500 25 -26
26  3 -1.58e-009 -500 26 -27
27  4 -1.42 -500 27 -28
28  8 -1.18 -500 28 -29
29  6 -4.374 -500 29 -30
30  8 -1.18 -500 30 -31
31  4 -1.42 -500 31 -32
32  3 -1.58e-009 -500 32 -33
33  4 -1.42 -500 33 -34
34  8 -1.18 -500 34 -35
35  7 -8.928 -500 35 -36

```

```

36      8    -1.18  -500 36  -37
37      4    -1.42  -500 37  -38
38      3   -1.58e-009 -500 38  -39
39      1   -2.677295 -500 39  -40
40      4    -1.42  -500 40  -41
41      8    -1.18  -500 41  -42
42      5   -8.0016  -500 42  -43
43      8    -1.18  -500 43  -44
44      4    -1.42  -500 44  -45
45      3   -1.58e-009 -500 45  -46
46      4    -1.42  -500 46  -47
47      8    -1.18  -500 47  -48
48      6    -4.5   -500 48  -49
49      8    -1.18  -500 49  -50
50      4    -1.42  -500 50  -51
51      3   -1.58e-009 -500 51  -52
52      4    -1.42  -500 52  -53
53      8    -1.18  -500 53  -54
54      7   -8.9964  -500 54  -55
55      8    -1.18  -500 55  -56
56      4    -1.42  -500 56  -57
57      3   -1.58e-009 -500 57  -58
58      1   -2.69567  -500 58  -59
59      4    -1.42  -500 59  -60
60      8    -1.18  -500 60  -61
61      5   -7.9704  -500 61  -62
62      8    -1.18  -500 62  -63
63      4    -1.42  -500 63  -64
64      3   -1.58e-009 -500 64  -65
65      4    -1.42  -500 65  -66
66      8    -1.18  -500 66  -67
67      6   -4.3628  -500 67  -68
68      8    -1.18  -500 68  -69
69      4    -1.42  -500 69  -70
70      3   -1.58e-009 -500 70  -71
71      4    -1.42  -500 71  -72
72      8    -1.18  -500 72  -73
73      7   -9.35   -500 73  -74
74      8    -1.18  -500 74  -75
75      4    -1.42  -500 75  -76
76      3   -1.58e-009 -500 76  -77
77      1   -2.697443 -500 77  -78
78      4    -1.42  -500 78  -79
79      8    -1.18  -500 79  -80
80      5   -8.0084  -500 80  -81
81      8    -1.18  -500 81  -82
82      4    -1.42  -500 82  -83
83      3   -1.58e-009 -500 83  -84
84      4    -1.42  -500 84  -85
85      8    -1.18  -500 85  -86
86      6   -4.3948  -500 86  -87
87      8    -1.18  -500 87  -88
88      4    -1.42  -500 88  -89
89      3   -1.58e-009 -500 89  -90
90      4    -1.42  -500 90  -91
91      8    -1.18  -500 91  -92
92      7   -8.9396  -500 92  -93
93      8    -1.18  -500 93  -94
94      4    -1.42  -500 94  -95
95      3   -1.58e-009 -500 95  -96
96      1   -2.697299 -500 96  -97
97      4    -1.42  -500 97  -98
98      8    -1.18  -500 98  -99

```

```

99      5 -8.0832 -500 99 -100
100     8 -1.18 -500 100 -101
101     4 -1.42 -500 101 -102
102     3 -1.58e-009 -500 102 -103
103     4 -1.42 -500 103 -104
104     8 -1.18 -500 104 -105
105     6 -4.458 -500 105 -106
106     8 -1.18 -500 106 -107
107     4 -1.42 -500 107 -108
108     3 -1.58e-009 -500 108 -109
109     4 -1.42 -500 109 -110
110     8 -1.18 -500 110 -111
111     7 -8.97 -500 111 -112
112     8 -1.18 -500 112 -113
113     4 -1.42 -500 113 -114
114     3 -1.58e-009 -500 114 -115
115     1 -2.698031 -500 115 -116
116     4 -1.42 -500 116 -117
117     8 -1.18 -500 117 -118
118     5 -7.972 -500 118 -119
119     8 -1.18 -500 119 -120
120     4 -1.42 -500 120 -121
121     3 -1.58e-009 -500 121 -122
122     4 -1.42 -500 122 -123
123     8 -1.18 -500 123 -124
124     6 -4.466 -500 124 -125
125     8 -1.18 -500 125 -126
126     4 -1.42 -500 126 -127
127     3 -1.58e-009 -500 127 -128
128     4 -1.42 -500 128 -129
129     8 -1.18 -500 129 -130
130     7 -8.9344 -500 130 -131
131     8 -1.18 -500 131 -132
132     4 -1.42 -500 132 -133
133     3 -1.58e-009 -500 133 -134
134     4 -1.42 -500 134 -135
135     8 -1.18 -500 135 -136
136     1 -2.711024 -500 136 -137
137     8 -1.18 -500 137 -138
138     4 -1.42 -500 138 -139
139     3 -1.58e-009 -500 139 -140
140     2 -7.788692 -500 140 -141
c ***** Air surrounding stack *****
141     3 1.58e-009 -200 500
c ***** Universe Boundary *****
200     0          200

1      px 0
2      px 0.013
3      px 0.01554
4      px 0.01935
5      px 0.02185
6      px 0.02566
7      px 0.0282
8      px 0.17175
9      px 0.17429
10     px 0.1781
11     px 0.1806
12     px 0.18441
13     px 0.18695
14     px 0.3305
15     px 0.33304
16     px 0.33685

```

```
17      px 0.33935
18      px 0.34316
19      px 0.3457
20      px 0.48925
21      px 0.71325
22      px 0.71579
23      px 0.7196
24      px 0.7221
25      px 0.72591
26      px 0.72845
27      px 0.872
28      px 0.87454
29      px 0.87835
30      px 0.88085
31      px 0.88466
32      px 0.8872
33      px 1.03075
34      px 1.03329
35      px 1.0371
36      px 1.0396
37      px 1.04341
38      px 1.04595
39      px 1.1895
40      px 1.4135
41      px 1.41604
42      px 1.41985
43      px 1.42235
44      px 1.42616
45      px 1.4287
46      px 1.57225
47      px 1.57479
48      px 1.5786
49      px 1.5811
50      px 1.58491
51      px 1.58745
52      px 1.731
53      px 1.73354
54      px 1.73735
55      px 1.73985
56      px 1.74366
57      px 1.7462
58      px 1.88975
59      px 1.98675
60      px 1.98929
61      px 1.9931
62      px 1.9956
63      px 1.99941
64      px 2.00195
65      px 2.1455
66      px 2.14804
67      px 2.15185
68      px 2.15435
69      px 2.15816
70      px 2.1607
71      px 2.30425
72      px 2.30679
73      px 2.3106
74      px 2.3131
75      px 2.31691
76      px 2.31945
77      px 2.463
78      px 2.56
79      px 2.56254
```

```
80      px 2.56635
81      px 2.56885
82      px 2.57266
83      px 2.5752
84      px 2.71875
85      px 2.72129
86      px 2.7251
87      px 2.7276
88      px 2.73141
89      px 2.73395
90      px 2.8775
91      px 2.88004
92      px 2.88385
93      px 2.88635
94      px 2.89016
95      px 2.8927
96      px 3.03625
97      px 3.13325
98      px 3.13579
99      px 3.1396
100     px 3.1421
101     px 3.14591
102     px 3.14845
103     px 3.292
104     px 3.29454
105     px 3.29835
106     px 3.30085
107     px 3.30466
108     px 3.3072
109     px 3.45075
110     px 3.45329
111     px 3.4571
112     px 3.4596
113     px 3.46341
114     px 3.46595
115     px 3.6095
116     px 3.7065
117     px 3.70904
118     px 3.71285
119     px 3.71535
120     px 3.71916
121     px 3.7217
122     px 3.86525
123     px 3.86779
124     px 3.8716
125     px 3.8741
126     px 3.87791
127     px 3.88045
128     px 4.024
129     px 4.02654
130     px 4.03035
131     px 4.03285
132     px 4.03666
133     px 4.0392
134     px 4.18275
135     px 4.18529
136     px 4.1891
137     px 4.2018
138     px 4.20561
139     px 4.20815
140     px 4.3517
141     px 4.3647
```

c Outline of foil stack

```

500      rpp 0 4.3647 -1.27 1.27 -1.27 1.27
c Universe boundary - 50 cm radius sphere
200      so 50

mode n h
c Al-2014
m1    13027.      0.05878645
      29063.      0.000812285 29065.      0.000363564 14028.      0.00050382
      14029.      2.34429e-005 14030.      1.69972e-005 25055.      0.000247294
      12024.      0.000349358
c 316 SS
m2    24050.      0.000672865
      24052.      0.01296789 24053.      0.001466307 24054.      0.000368568
      26054.      0.003518959 26056.      0.05522496 26057.      0.001271974
      26058.      0.000171578 28058.      0.006585093 28060.      0.002535278
      28061.      0.000108758 28062.      0.000351592 28064.      8.88507e-005
c Simple Air, O, N, Ar
m3    7014.      3.81269e-005
      8016.      9.50145e-006 18040.      1.66404e-007
c Kapton
m4    1001.      0.02256188
      6012.      0.04967341 7014.      0.004513215 8016.      0.01128638
c Iron
m5    26000.      1
c Titanium
m6    22000.      1
c Copper
m7    29000.      1
c Acrylic adhesive
m8    1001.      0.8
      6012.      0.5 8016.      0.2
imp:n 1 140r      0      $ 1, 200
imp:h 1 140r      0      $ 1, 200
c 55 MeV proton pencil beam at -0.1,0,0 (x,y,z)
sdef pos=-0.10 0.0 0.0 axs=1 0 0 ext=0 rad=d1 par=h vec=1 0 0 dir=1 erg=d2
si1 0 0.440348      $ radial sampling range: 0 to Rmax (=0.44 cm)
sp1 -21 1      $ radial sampling weighting: r^-1 for disk
si2 H 53.9 19I 55      $ 20 energy bins between X and Y
sp2 D 0 0.05 19R      $ equal weighting for each bin
phys:n 56
phys:h 56 j 0
prdmp 1+7 1+7 -1
nps 1+7
c ++++++
c Add tally below
c ++++++
c CINDER90 activation cross sections provided in
c 63 group LaBauve neutron energy group structure
histp 4 10 16 23 29 35 42 48 54 61 67 73 80 86 92 99 105 111 118 124 130
f4:n 4 10 16 23 29 35 42 48 54 61 67 73 80 86 92 99 105 111 118 124 130
e4 1 5000I 56
f14:h 4 10 16 23 29 35 42 48 54 61 67 73 80 86 92 99 105 111 118 124 130
e14 1 5000I 56
c e4 1.000e-11 5.000e-09 1.000e-08 1.500e-08 2.000e-08 2.500e-08
c 3.000e-08 3.500e-08 4.200e-08 5.000e-08 5.800e-08 6.700e-08
c 8.000e-08 1.000e-07 1.520e-07 2.510e-07 4.140e-07 6.830e-07
c 1.125e-06 1.855e-06 3.059e-06 5.043e-06 8.315e-06 1.371e-05
c 2.260e-05 3.727e-05 6.144e-05 1.013e-04 1.670e-04 2.754e-04
c 4.540e-04 7.485e-04 1.234e-03 2.035e-03 2.404e-03 2.840e-03
c 3.355e-03 5.531e-03 9.119e-03 1.503e-02 1.989e-02 2.554e-02
c 4.087e-02 6.738e-02 1.111e-01 1.832e-01 3.020e-01 3.887e-01
c 4.979e-01 0.639279 0.82085 1.10803 1.35335 1.73774
c 2.2313 2.86505 3.67879 4.96585 6.065 10.00

```

```
c      14.9182   16.9046   20.0      25.0
```

A.4 88-Inch Cyclotron 25 MeV Fe(p,x) Target Stack Input

Update references and specifics here!

The following MCNP code simulates the irradiation of the 25 MeV $^{nat}Fe(p,x)$ target stack, used for the experiments described in chapter 3. The model consists of a 3D simulation of the full target stack, as outlined in subsection 3.3.1 and Table 3.1. This includes the stainless steel profile monitors, aluminum energy degraders, nominal 25 μm ^{nat}Nb target foils, and the nominal 25 μm ^{nat}Al and 50 μm ^{nat}Cu monitor foils. The target and monitor foils each include two pieces of Kapton polyimide film tape, with each piece of tape consisting of 43.2 μm of a silicone adhesive (nominal 4.79 mg/cm²) on 25.4 μm of a polyimide backing (nominal 3.61 mg/cm²). The target stack also includes the target box's Inconel beam entrance window and aluminum chassis, its cooling water-filled cavity, and all other structural components used for mounting the target box in the beamline. The target stack is not pumped down to the beamline vacuum, but exists at the local atmospheric pressure of approximately 77.6 kPa. A rendering of the target stack model is seen in Figure 3.21.

Incident upon the front of the stack is beam of protons in an elliptical beam spot, with a major axis 1.696 cm in diameter, and a minor axis 0.784 cm in diameter. This upstream spot size is determined from the radiochromic film developed by the stainless steel beam profile monitor at the front of the stack, seen in Figure 2.15. Based on historical beam characterization at LANSCE-IPF, the beam is modeled in MCNP as a circular pencil beam (no divergence/convergence) with a diameter of 1.696 cm, to avoid under-representing beam filling of target foils. The beam intensity has a linear radial $1/r$ intensity, and an average energy of 100 MeV with a Gaussian energy distribution width of 0.1 MeV. This beam definition is transported through the target stack, accounting for both attenuation, secondary reactions, and energy loss throughout the stack. The proton energy-differential flux is calculated in each stack element — as described in subsection 3.3.4, these distributions are used to assign energy bins to each foil, as well as for the variance minimization minimization techniques employed in this work. In addition, this transport model allows one to estimate the fluence loss down the stack, due to (p,x) reactions and scattering of the beam.

```
MCNPX Visual Editor Version X_24E
c
c  Cell Definitions
c
c ***** SS, Fe, Ti, and Cu Foils *****
1      2  -7.736384 -500 1 -2
2      4   -1.42 -500 2 -3
3      8   -1.18 -500 3 -4
4      5  -7.8772 -500 4 -5
5      8   -1.18 -500 5 -6
```

```

6      4    -1.42  -500 6  -7
7      3   -1.58e-009 -500 7  -8
8      4    -1.42  -500 8  -9
9      8    -1.18  -500 9  -10
10     6   -4.3488  -500 10 -11
11     8    -1.18  -500 11 -12
12     4    -1.42  -500 12 -13
13     3   -1.58e-009 -500 13 -14
14     4    -1.42  -500 14 -15
15     8    -1.18  -500 15 -16
16     7   -6.9956  -500 16 -17
17     8    -1.18  -500 17 -18
18     4    -1.42  -500 18 -19
19     3   -1.58e-009 -500 19 -20
20     1   -2.684134 -500 20 -21
21     4    -1.42  -500 21 -22
22     8    -1.18  -500 22 -23
23     5   -7.958   -500 23 -24
24     8    -1.18  -500 24 -25
25     4    -1.42  -500 25 -26
26     3   -1.58e-009 -500 26 -27
27     4    -1.42  -500 27 -28
28     8    -1.18  -500 28 -29
29     6   -4.3872  -500 29 -30
30     8    -1.18  -500 30 -31
31     4    -1.42  -500 31 -32
32     3   -1.58e-009 -500 32 -33
33     4    -1.42  -500 33 -34
34     8    -1.18  -500 34 -35
35     7   -8.081   -500 35 -36
36     8    -1.18  -500 36 -37
37     4    -1.42  -500 37 -38
38     3   -1.58e-009 -500 38 -39
39     1   -2.711024 -500 39 -40
40     4    -1.42  -500 40 -41
41     8    -1.18  -500 41 -42
42     5   -7.9364  -500 42 -43
43     8    -1.18  -500 43 -44
44     4    -1.42  -500 44 -45
45     3   -1.58e-009 -500 45 -46
46     4    -1.42  -500 46 -47
47     8    -1.18  -500 47 -48
48     6   -4.3828  -500 48 -49
49     8    -1.18  -500 49 -50
50     4    -1.42  -500 50 -51
51     3   -1.58e-009 -500 51 -52
52     4    -1.42  -500 52 -53
53     8    -1.18  -500 53 -54
54     7   -6.8864  -500 54 -55
55     8    -1.18  -500 55 -56
56     4    -1.42  -500 56 -57
57     3   -1.58e-009 -500 57 -58
58     4    -1.42  -500 58 -59
59     8    -1.18  -500 59 -60
60     5   -7.9824  -500 60 -61
61     8    -1.18  -500 61 -62
62     4    -1.42  -500 62 -63
63     3   -1.58e-009 -500 63 -64
64     4    -1.42  -500 64 -65
65     8    -1.18  -500 65 -66
66     6   -4.3516  -500 66 -67
67     8    -1.18  -500 67 -68
68     4    -1.42  -500 68 -69

```

```

69      3 -1.58e-009 -500 69 -70
70      4 -1.42 -500 70 -71
71      8 -1.18 -500 71 -72
72      7 -8.7628 -500 72 -73
73      8 -1.18 -500 73 -74
74      4 -1.42 -500 74 -75
75      3 -1.58e-009 -500 75 -76
76      4 -1.42 -500 76 -77
77      8 -1.18 -500 77 -78
78      5 -8.0132 -500 78 -79
79      8 -1.18 -500 79 -80
80      4 -1.42 -500 80 -81
81      3 -1.58e-009 -500 81 -82
82      4 -1.42 -500 82 -83
83      8 -1.18 -500 83 -84
84      6 -4.3996 -500 84 -85
85      8 -1.18 -500 85 -86
86      4 -1.42 -500 86 -87
87      3 -1.58e-009 -500 87 -88
88      4 -1.42 -500 88 -89
89      8 -1.18 -500 89 -90
90      7 -8.9336 -500 90 -91
91      8 -1.18 -500 91 -92
92      4 -1.42 -500 92 -93
93      3 -1.58e-009 -500 93 -94
94      4 -1.42 -500 94 -95
95      8 -1.18 -500 95 -96
96      5 -8.0184 -500 96 -97
97      8 -1.18 -500 97 -98
98      4 -1.42 -500 98 -99
99      3 -1.58e-009 -500 99 -100
100     4 -1.42 -500 100 -101
101     8 -1.18 -500 101 -102
102     6 -4.4056 -500 102 -103
103     8 -1.18 -500 103 -104
104     4 -1.42 -500 104 -105
105     3 -1.58e-009 -500 105 -106
106     4 -1.42 -500 106 -107
107     8 -1.18 -500 107 -108
108     7 -8.9284 -500 108 -109
109     8 -1.18 -500 109 -110
110     4 -1.42 -500 110 -111
111     3 -1.58e-009 -500 111 -112
112     4 -1.42 -500 112 -113
113     8 -1.18 -500 113 -114
114     5 -8.0456 -500 114 -115
115     8 -1.18 -500 115 -116
116     4 -1.42 -500 116 -117
117     3 -1.58e-009 -500 117 -118
118     4 -1.42 -500 118 -119
119     8 -1.18 -500 119 -120
120     6 -4.4232 -500 120 -121
121     8 -1.18 -500 121 -122
122     4 -1.42 -500 122 -123
123     3 -1.58e-009 -500 123 -124
124     4 -1.42 -500 124 -125
125     8 -1.18 -500 125 -126
126     7 -8.9352 -500 126 -127
127     8 -1.18 -500 127 -128
128     4 -1.42 -500 128 -129
129     3 -1.58e-009 -500 129 -130
130     2 -7.709313 -500 130 -131

```

c ***** Air surrounding stack *****

```
131      3 1.58e-009 -200 500
c  ***** Universe Boundary *****
200      0      200

1      px 0
2      px 0.013
3      px 0.01554
4      px 0.01935
5      px 0.02185
6      px 0.02566
7      px 0.0282
8      px 0.17175
9      px 0.17429
10     px 0.1781
11     px 0.1806
12     px 0.18441
13     px 0.18695
14     px 0.3305
15     px 0.33304
16     px 0.33685
17     px 0.33935
18     px 0.34316
19     px 0.3457
20     px 0.48925
21     px 0.51465
22     px 0.51719
23     px 0.521
24     px 0.5235
25     px 0.52731
26     px 0.52985
27     px 0.6734
28     px 0.67594
29     px 0.67975
30     px 0.68225
31     px 0.68606
32     px 0.6886
33     px 0.83215
34     px 0.83469
35     px 0.8385
36     px 0.841
37     px 0.84481
38     px 0.84735
39     px 0.9909
40     px 1.0036
41     px 1.00614
42     px 1.00995
43     px 1.01245
44     px 1.01626
45     px 1.0188
46     px 1.16235
47     px 1.16489
48     px 1.1687
49     px 1.1712
50     px 1.17501
51     px 1.17755
52     px 1.3211
53     px 1.32364
54     px 1.32745
55     px 1.32995
56     px 1.33376
57     px 1.3363
58     px 1.47985
59     px 1.48239
```

```
60      px 1.4862
61      px 1.4887
62      px 1.49251
63      px 1.49505
64      px 1.6386
65      px 1.64114
66      px 1.64495
67      px 1.64745
68      px 1.65126
69      px 1.6538
70      px 1.79735
71      px 1.79989
72      px 1.8037
73      px 1.8062
74      px 1.81001
75      px 1.81255
76      px 1.9561
77      px 1.95864
78      px 1.96245
79      px 1.96495
80      px 1.96876
81      px 1.9713
82      px 2.11485
83      px 2.11739
84      px 2.1212
85      px 2.1237
86      px 2.12751
87      px 2.13005
88      px 2.2736
89      px 2.27614
90      px 2.27995
91      px 2.28245
92      px 2.28626
93      px 2.2888
94      px 2.43235
95      px 2.43489
96      px 2.4387
97      px 2.4412
98      px 2.44501
99      px 2.44755
100     px 2.5911
101     px 2.59364
102     px 2.59745
103     px 2.59995
104     px 2.60376
105     px 2.6063
106     px 2.74985
107     px 2.75239
108     px 2.7562
109     px 2.7587
110     px 2.76251
111     px 2.76505
112     px 2.9086
113     px 2.91114
114     px 2.91495
115     px 2.91745
116     px 2.92126
117     px 2.9238
118     px 3.06735
119     px 3.06989
120     px 3.0737
121     px 3.0762
122     px 3.08001
```

```

123      px 3.08255
124      px 3.2261
125      px 3.22864
126      px 3.23245
127      px 3.23495
128      px 3.23876
129      px 3.2413
130      px 3.38485
131      px 3.39795
c Outline of foil stack
500      rpp 0 3.39795 -1.27 1.27 -1.27 1.27
c Universe boundary - 50 cm radius sphere
200      so 50

mode n h
c Al-2014
m1    13027.      0.05878645
      29063.      0.000812285 29065.      0.000363564 14028.      0.00050382
      14029.      2.34429e-005 14030.      1.69972e-005 25055.      0.000247294
      12024.      0.000349358
c 316 SS
m2    24050.      0.000672865
      24052.      0.01296789 24053.      0.001466307 24054.      0.000368568
      26054.      0.003518959 26056.      0.05522496 26057.      0.001271974
      26058.      0.000171578 28058.      0.006585093 28060.      0.002535278
      28061.      0.000108758 28062.      0.000351592 28064.      8.88507e-005
c Simple Air, O, N, Ar
m3    7014.      3.81269e-005
      8016.      9.50145e-006 18040.      1.66404e-007
c Kapton
m4    1001.      0.02256188
      6012.      0.04967341 7014.      0.004513215 8016.      0.01128638
c Iron
m5    26000.      1
c Titanium
m6    22000.      1
c Copper
m7    29000.      1
c Acrylic adhesive
m8    1001.      0.8
      6012.      0.5 8016.      0.2
imp:n 1 130r      0      $ 1, 200
imp:h 1 130r      0      $ 1, 200
c 25 MeV proton pencil beam at -0.1,0,0 (x,y,z)
sdef pos=-0.10 0.0 0.0 axs=1 0 0 ext=0 rad=d1 par=h vec=1 0 0 dir=1 erg=d2
s1l 0 0.440348      $ radial sampling range: 0 to Rmax (=0.44 cm)
sp1 -21 1      $ radial sampling weighting: r^-1 for disk
si2 H 24.5 19I 25      $ 20 energy bins between X and Y
sp2 D 0 0.05 19R      $ equal weighting for each bin
phys:n 26
phys:h 26 j 0
prdmmp 1+7 1+7 -1
nps 1+7
c ++++++
c Add tally below
c ++++++
c CINDER90 activation cross sections provided in
c 63 group LaBauve neutron energy group structure
histp 4 10 16 23 29 35 42 48 54 60 66 72 78 84 90 96 102 108 114 120 126
f4:n 4 10 16 23 29 35 42 48 54 60 66 72 78 84 90 96 102 108 114 120 126
e4 1 2500I 26
f14:h 4 10 16 23 29 35 42 48 54 60 66 72 78 84 90 96 102 108 114 120 126
e14 1 2500I 26

```

```
c e4      1.000e-11 5.000e-09 1.000e-08 1.500e-08 2.000e-08 2.500e-08
c      3.000e-08 3.500e-08 4.200e-08 5.000e-08 5.800e-08 6.700e-08
c      8.000e-08 1.000e-07 1.520e-07 2.510e-07 4.140e-07 6.830e-07
c      1.125e-06 1.855e-06 3.059e-06 5.043e-06 8.315e-06 1.371e-05
c      2.260e-05 3.727e-05 6.144e-05 1.013e-04 1.670e-04 2.754e-04
c      4.540e-04 7.485e-04 1.234e-03 2.035e-03 2.404e-03 2.840e-03
c      3.355e-03 5.531e-03 9.119e-03 1.503e-02 1.989e-02 2.554e-02
c      4.087e-02 6.738e-02 1.111e-01 1.832e-01 3.020e-01 3.887e-01
c      4.979e-01 0.639279 0.82085 1.10803 1.35335 1.73774
c      2.2313    2.86505   3.67879  4.96585  6.065     10.00
c      14.9182   16.9046   20.0      25.0
```